UNIVERSITY OF CALIFORNIA, IRVINE

Molecular composition and chemical transformation of secondary organic aerosols from biogenic precursors

DISSERTATION

Submitted in partial fulfillment of the requirements
for the degree of

DOCTOR OF PHILOSOPHY

in Chemistry

by

Tran Bao Nguyen

Ph.D. dissertation committee:
Professor Sergey A. Nizkorodov, UCI, Chair
Professor Barbara J. Finlayson-Pitts, UCI
Professor Donald R. Blake, UCI
Dr. Alexander Laskin, PNNL

2012

"One day, in retrospect, the years of struggle will strike you as the most beautiful."
— Sigmund Freud

Table of Contents

List of Terminology and Acronyms

- **AI:** Aromaticity index – describes the degree of aromaticity in a molecule, introduced by Koch et al (2006) [1]. For $C_cH_hO_oN_n$ molecules, $AI = (1 + c - o - 0.5h) / (c - o - n)$.

- **Alkyl nitrate:** a compound with molecular formula $R-ONO_2$ where R is an alkyl group.

- **AM:** Adjusted mass – introduced in this dissertation as the product of the neutral mass with the hydrogen to carbon ratio (molecular mass x H/C).

- **Aging**: When referring to aerosols, further reaction of condensed-phase compounds in the atmosphere by light (photoaging), oxidants (oxidative aging), or other chemicals.

- **AS:** Ammonium sulfate – $(NH_4)_2SO_4$.

- **Brown carbon**: a general definition for organic compounds in environmental samples that absorb light in the visible region and visually appear to be brown.

- **CCN**: Cloud condensation nuclei – small particles in the atmosphere, e.g., aerosols, that water vapor can condense onto and form cloud droplets.

- **Da**: Dalton – a unit of atomic or molecular mass equivalent to atomic mass unit (amu), defined as $1/12^{th}$ of the mass of an unbound neutral atom of ^{12}C in its ground state.

- **DBE:** Double bond equivalency – a formalism to characterize the number of double bonds and rings in molecule, introduced by Badertscher et al (2001) [2]. For $C_cH_hO_oN_n$ molecules with *trivalent* nitrogen, $DBE = 1 - h/2 + n/2 + c$. For $C_cH_hO_oN_n$ molecules with *pentavalent* nitrogen, $DBE = 1 - h/2 + 3n/2 + c$.

- **ESI**: Electrospray ionization – a soft-ionization technique where solvent-dissolved analytes are ionized by passing through a highly-charged capillary tip. The solvent is then dispersed into a fine aerosol and the charged analytes that are dissolved within the droplets become gas-phase ions through evaporation and droplet fission.

- **GB:** Gas-phase basicity (kJ mol^{-1}) – the change in Gibbs free energy (Δ G, *kJ mol^{-1}*) of a gaseous compound by accepting a proton.

- **H/C**: hydrogen to carbon ratio of a molecule.

- **HR-MS**: High-resolution mass spectrometry – usually defined as mass spectrometry methods with mass resolving power in excess of 10^4 m/Δm. in this dissertation, HR-MS refers to techniques with mass resolving power 60,000 – 100,000 m/Δm at *m/z* 400.

- **Isoprene**: An aliphatic VOC (C_5H_8) emitted mainly by deciduous trees. Isoprene emissions are greater than 500 Tg per year, approximately one-third of all hydrocarbons emitted into the atmosphere. Many natural compounds, e.g., carotenes, terpenes, certain vitamins, squalene, are formed from isoprene units and are called isoprenoids.

- **KM**: Kendrick mass – IUPAC masses (relative to ^{12}C) that are renormalized to a different unit, e.g. CH_2 such that KM_{CH2} = (mass)$_{IUPAC}$ x [(nominal mass)$_{CH2}$ / (exact mass)$_{CH2}$]

- **KMD**: Kendrick mass defect – the difference between the nominal mass and the KM.

- **KLA**: Keto-limononaldehyde – a second-generation ozonolysis product of limonene with molecular formula of $C_9H_{14}O_3$.

- **LA**: Limononaldehyde – a first-generation ozonolysis product of limonene with molecular formula of $C_{10}H_{16}O_2$.

- **Limonene**: A cyclic monoterpene ($C_{10}H_{16}$) emitted from citrus trees and commonly used in household cleaning products and air fresheners.

- **LOD**: Limit of detection – the analyte concentration where the analyte signal is observed over the noise threshold.

- **LTQ**: Linear trap quadrupole – a linear ion trap used in the hybrid ion trap-Orbitrap instrument (Thermo Corp.) used for HR-MS analyses in this dissertation.

- **MAC**: Mass absorption coefficient – a metric for quantifying absorption of a material at a particular wavelength. Calculated as suggested by Ref [3]: MAC (λ, g cm^{-2}) = Abs (λ) x ln(10) / [b (cm) x C (g cm^{-3})]

- **MAC**: Methacrolein (C_4H_6O) – an unsaturated aldehyde that is a first generation oxidation (both O_3 and OH) product of isoprene.

- **Mass resolving power**: The ability to distinguish between ions differing slightly in accurate masses. This parameter may be characterized by the ratio of the mass with respect to the peak width measured at that mass (m/Δm).

- **Monoterpenes**: Organic compounds with chemical formula $C_{10}H_{16}$, comprised of 2 isoprene units. Examples include limonene and alpha-pinene.

- **MOUDI**: Micro-Oriface Uniform Deposition Impactor – a rotating multistage impactor (MSP Corp.) used to size-separate collected aerosols.

- **MS**: Mass spectrometry.

- **MS^n**: Tandem multistage mass spectrometry – in this work MS^n refers to collision-induced dissociation (CID) of ions of interest selected in a linear ion trap. The MS stages used for experiments in this dissertation are typically n = 2 – 4 due to signal availability. The ejected fragments are neutral species and the product fragments are ionic.

- **MVK**: Methyl vinyl ketone (C_4H_6O) – an unsaturated ketone that is a first generation oxidation (both O_3 and OH) product of isoprene.

- **MW**: Molecular weight (g mol^{-1}).

- **m/z**: mass to charge ratio – the ratio of detected mass of an ion relative to the charge of the ion. In the assigned mass spectra in this work, the charge of the ions are +1 in the positive ionmode and -1 in the negative ion mode.

- **Nano-DESI**: Nanospray desorption electrospray ionization – a technique developed by Roach et al (2010) [4] where analytes are simultaneously desorbed an ionized on a surface without prior extraction.

- **N/C**: nitrogen to carbon ratio of a molecule.

- **NOC**: Nitrogen-containing organic compounds.

- **Nominal mass**: (of a molecule) the sum of all the integer masses of its components, e.g. nominal (CO_2) = 44.

- **NOx**: General term for mono-nitrogen oxides – defined as the sum of nitric oxide (NO) and nitrogen dioxide (NO_2).

- **NOy**: "Odd" nitrogen – defined as the sum of NOx and all nitrogen compounds produced from NOx, including nitric acid (HNO_3) and organic nitrates.

- **Oligomers**: A larger molecule comprised of a few to several identical (homologous) or different (heterogeneous) covalently-bonded monomer units.

- **O_3**: Ozone – the second most important atmospheric oxidant globally. Typical concentrations are approximately 50 ppb in urban areas.

- **O/C**: oxygen to carbon ratio of a molecule.

- **OH**: Hydroxyl radical – the dominant atmospheric oxidant. Rate constants of OH with organics in the gas phase are on the order of 1×10^{-10} cm^3 $molec^{-1}$ s^{-1}. Typical atmospheric concentrations are approximately 1×10^6 molec cm^{-3}.

- **Orbitrap**: a high resolution mass analyzer with up to 100,000 m/Δm mass resolution at *m/z* 400 that measures masses of ions through the frequencies of their orbiting oscillations around a "spindle-like" electrode. Orbitrap developed by Alexander Makarov in 2000 [5].

- **Organic nitrate**: more general than alkyl nitrate – a compound with molecular formula R′-ONO$_2$ where R′ can be an alkyl group or a functionalized alkyl chain.

- **Photooxidation:** Oxidation induced by light, e.g., when photolysis is used to create OH radicals during reaction.

- **POA**: Primary organic aerosols – aerosols that are emitted into the atmosphere, most commonly in urban environments from vehicle exhaust, industrial processes, biomass burning, or cooking.

- **PTR-ToF-MS**: Proton transfer reaction time-of-flight mass spectrometry – an online mass spectrometry technique used to monitor gas-phase organic compounds. PTR-ToF-MS utilizes soft ionization by proton transfer of hydronium ions (H$_3$O$^+$) to the analyte; therefore, any analyte with proton affinity greater than water will be detected.

- **RH**: Relative humidity – the ratio of the partial pressure of water vapor in a mixture relative to the saturation water vapor pressure.

- **SMPS**: Scanning mobility particle sizer – a continuously scanning instrument that measures particle diameter and count.

- **SOA**: Secondary organic aerosols – aerosols that are formed via chemical reactions in the atmosphere. Most commonly SOA are formed by the reaction of alkanes or alkenes with OH and O$_3$, which produces less volatile organic compounds that can condense onto pre-existing particles or self nucleate.

- **SOC**: Sulfur-containing organic compounds.

- **SVOC**: Semi-volatile organic compounds – defined by the US EPA as organic molecules with boiling point range 240-260°C to 380-400°C. Usually formed through the first- or second-generation oxidation of VOC.

- **TOF**: time-of-flight – a mass analyzer with mass resolution up to 8000 m/Δm at m/z 150 that measures the masses of ions by correlating to their velocity in an electric field.

- **VK diagram**: Van-Krevelen diagram – a 2D representation of degree of oxidation of the organic mixture by plotting the H/C vs. O/C of each compound detected by HR-MS.

- **VOC**: Volatile organic compounds – defined by the US EPA as organic molecules with boiling point range 50-100°C to 240-260°C. Generally directly emitted from the biosphere (e.g., isoprene) or from human activities (e.g., toluene).

List of Tables

List of Figures

measured concentrations of O_3 (ozone photometer) and isoprene (PTR-ToF-MS). The rate of the OH + isoprene reaction could then be calculated as the difference, $R_{OH} = -d[ISO]/dt - R_{O3}$. The results show that ozone did not make a significant contribution to isoprene oxidation under present conditions.

Figure 6.2: Time evolution of (a) oxidants and particles and (b) select VOC in the high-NOx photooxidation reaction including: isoprene (ISO), the sum of isobaric methylvinylketone and methacrolein (MVK+MAC), methacrylic acid (MAA), glycolaldehyde (GLYCOL), hydroxyacetone (HAC), and methylglyoxal (MGLY). Gray shading represents the error between repeated experiments.

Figure 6.3: Characterization of (a) the flux from the photolysis lamp compared modeled solar flux under summer clear-sky conditions and (b) the temperature change of an aqueous sample under the lamp for the $0 - 4$ h photolysis time period used in this work. The solar flux was calculated using the "Quick TUV" calculator, available at the UCAR website http://cprm.acd.ucar.edu, using the following parameters: SZA = 0, 300 Dobson overhead ozone, surface albedo of 0.1, ground elevation and altitude = 0 km.

Figure 6.4: Mass spectra of the aqueous SOA extract detected in ESI positive ion mode and converted to neutral molecular formulas for the dark control (panels on the left) and photolysis (panels on the right) experiments for 0 h and 4 h time intervals. Peaks are normalized with respect to the total mass concentration (200 μg mL^{-1}) in the sample. The most abundantly observed compound is sodiated $C_{10}H_{16}O_8$. Mass spectra are also plotted with respect to normalized signal-to-noise in the supporting information (Fig. S4). Note the breaks in the vertical axis.

List of Schemes

Acknowledgments

I have a lot of kind and intelligent people to thank for helping me along the road to obtaining my Ph.D. Without the people mentioned here, this dissertation would not be possible. I am grateful for their contribution, big or small, concrete or intangible.

I owe the largest debt of gratitude to my advisor, Professor Sergey Nizkorodov. I hope he knows how much I appreciate all that he has done for me, in particular his unyielding support, and how much I look up to him. Sergey was accommodating to my style of learning and working, which enabled me to be more efficient in graduate school. I'm thankful that he entrusted me with the responsibility of building a photochemical chamber in my first year with little supervision. It was something I had no experience in doing and in the end, remains one of my proudest accomplishments. While ready with helpful suggestions, he allowed me a long intellectual leash to design experiments and pursue my own ideas. This autonomy gave me the confidence I needed to continue on in academia.

Sergey is a great teacher and mentor. I have learned so much from him over the years: about atmospheric chemistry, photochemistry, and all aspects of science. It is rare to see someone so dedicated to helping his students. I enjoyed our many scientific discussions. Often they would lead to new ideas that he would encourage me to try, and these ideas have been the basis of many of my published works. I sincerely appreciate his efforts in providing a supportive atmosphere for me to develop into an independent thinker and scientist. I will look back at my graduate school experience as a fond time in my life.

I am also indebted to Sergey for giving me the opportunity to go to major scientific conferences and, more importantly, visit Pacific Northwest National Laboratory (PNNL) approximately once every six months as a user of the Environmental Molecular Science

Laboratory (EMSL) facility. My graduate education was enriched for having spent time working at a national lab with state-of-the-art equipment and with fantastic collaborators like Drs. Alex Laskin and Julia Laskin. These two people were instrumental in the development of my career and I consider them to be secondary advisors.

Alex was a great co-advisor to me. I am fortunate to have such a encouraging, friendly and knowledgeable mentor. He hosted all of my visits to PNNL and made himself available to assist me. I used the LTQ-Orbitrap mass spectrometer in his lab and, without this collaboration, indeed this dissertation would be very different as most of my publications heavily depend on high-resolution mass spectrometry. In the lab, he has taught me a lot about taking mass spectra. On occasion, he performed some analyses that I ran out of time to do. I greatly appreciate the work he has done to help me, the scientific insights he has provided on all of my projects, and the excellent advice he has given me over the years.

I also want to sincerely thank Julia for all her guidance and support. During my PNNL trips, Julia often helped me troubleshoot the mass spectrometer, and while I was at UCI, she answered complicated questions over email and guided me toward useful literature. It was through these interactions that I gained a deeper understanding of the instrument design and methods. Julia is also a gifted writer and editor. I am grateful that my own writing has improved significantly through working with her.

Other collaborators with whom I've had productive partnerships include: Dr. Patrick Roach from PNNL (now at Roach & Associates, LLC), Dr. Norbert Staimer and Professor Ralph Delfino from the UCI School of Medicine, David Fooshee and Professor Pierre Baldi from UCI School Computer Sciences, and Rachel O'Brien and Professor Allen Goldstein from UC Berkeley Department of Engineering. In particular, I appreciate Pat taking the time to train me

on the nano-DESI technique that he developed. I also want to thank Norbert, David and Rachel for drafting very nice manuscripts for publication and including me in their projects.

I'd also like to acknowledge the members of my Ph.D. committee, who have significantly shaped my experience at UCI. Professor Barbara J. Finlayson-Pitts taught the first atmospheric chemistry course I've ever taken and I could not have had a better introduction to atmospheric chemistry. As the director of AirUCI, her energy and excitement toward science are inspirational. Professor Donald Blake is also a wonderful teacher and a continual source of positivity. I was lucky to have taken a great chromatography class with him. I appreciate both of these committee members taking the time to write me letters of recommendation in the past. In addition, they have both given me excellent advice about how to structure a research plan and how to critically read the scientific literature.

I regard myself as privileged to have worked as part of AirUCI, which is comprised of a wonderful group of scientists who are always happy to collaborate, provide expertise, or share equipment. I'm thankful for the assistance and friendship of everyone at AirUCI. In particular I'd like acknowledge those that have spent a significant amount of time with me discussing both important and mundane things over the years: Dr. Emily Bruns, Dr. Veronique Perraud, and Dr. Lisa Wingen from the Finlayson-Pitts Group; Dr. Ming Cheng, Dr. Guofeng Sun, Dr. Theresa McIntire, Safa Khan, and Allie Margarella from the Hemminger Group; and Dr. Paul Nissenson, Dr. Wayne Chang, and Alex Cohan from the Dabdub Group.

Of course I cannot leave out the members of the Nizkorodov group that have been such an integral part of my Ph.D. experience. I deeply appreciate Dr. Xiang Pan and Dr. Adam Bateman putting in the effort to help me get established when I first joined the group. Xiang taught me basic aerosol techniques and showed me where things were kept in the lab. Although

he was writing his dissertation at the time, Xiang generously offered his assistance every time I needed it. Adam taught me what he knew about high-resolution mass spectrometry data analysis and helped me get acquainted with doing research at PNNL. Also, Adam readily answered questions I had about research. I believe without these two group-mates, I would have had a much rockier start in graduate school. I'm also grateful for the current and past Nizkorodov group members who have shared the day-to-day triumphs and trials of academic life with me over the last few years. In particular, interacting with Dr. Scott Epstein, Dr. David Bones, and Amanda Macmillan made my experience here very enjoyable. I also had the opportunity to mentor some outstanding undergraduate students: Katelyn Updyke, Lucas Nguyen, and Paula Lee. I enjoyed working with all of you and hope to continue our friendships in the future.

In addition, I want to thank the following UCI graduate students, postdocs, faculty and staff for their kindness in facilitating my research. There are many things I would have missed out on learning and incorporating into my dissertation if not for them. These people include: Dr. David Martin from the Vanderwal group for teaching me basic organic chemistry preparatory techniques; Dr. John DeLorbe of the Overman group for being a consultant on synthesis methods; Linda Tseng of the Rosso Group (Engineering) for troubleshooting the ion chromatography instrument; Dr. Jean Elkoury of the Detwiler group (Engineering) for teaching me about various water-based analytical techniques; Professor William Cooper (Engineering) for sharing his lab equipment, serving as the fifth member of my oral exam committee, and sponsoring my participation in many conference events; Dr. Philip Dennison of the NMR Facility for helping with difficult NMR experiments and writing custom codes for me when none were available; Professor Richard Chamberlain for letting me use his lab space and equipment;

Dr. Jiri Misek of the Luptak group for helpful discussions; and Emeritus Professor Jim Pitts and Professor Benny Gerber for their stimulating conversation.

Before beginning my Ph.D. research, I had the fantastic opportunity to work for the National Institute for Water and Air (NIWA) in Wellington, New Zealand. This was my first experience working in atmospheric chemistry and I will always cherish it. I am deeply grateful to the people at the NIWA atmospheric chemistry team: particularly Chief Scientist Dr. Keith Lassey for creating a position for me at NIWA, Mr. Gordon Brailsford for training me to analyze greenhouse samples with the GC-FID/ECD, and Dr. Antony Gomez for teaching me how to collect "background" gas samples from the Baring Head site. I gained so much practical knowledge and a deep appreciation for the science and history of environmental monitoring.

Looking back, I'm confident that I would not have developed an interest in chemistry nor the drive to pursue graduate school if not for the exceptional faculty and staff at USC. First off, I have to thank the professors who gave me the opportunity to work for them: Professor Mark Thompson, Professor Surya Prakash and Professor Robert Wu. I'm grateful that Prof. Thompson took a chance on hiring a sophomore who just switched majors to chemistry. This early experience set the foundation for my future research by allowing me to learn basic laboratory skills. Prof. Prakash and Prof. Wu were both excellent advisors and great role models. They were determined to see me succeed. I appreciate them setting aside time to talk to me in-depth about research, help me acquire fellowships like the NSF REU, and discuss the most appropriate job options for me after college.

In addition to undergraduate supervisors, other USC professors and staff members put in significant amounts of effort to open up paths for me in science. Professor Thomas Flood encouraged me to pursue graduate school and wrote me letters of support. Professor Darryl

Judge and Emeritus Professor William Weber both went out of their way to ensure that I was accepted to research labs by securing me interviews with their colleagues. As I had a late start in chemistry, many concepts were at first difficult for me to grasp. I owe special thanks to Dr. Michael Quinlan for keeping his office door open, making sure I understood the course material taught in general chemistry, and giving me some great chemistry books upon my graduation.

I also sincerely appreciate the continual love and support from my parents Tan and Chau, my sister Angie, my brother Kevin, and my friends-for-life Kay and Michelle. Specifically, I want to thank my parents for supporting my education throughout the years. Lastly, I am so grateful for my loving husband and best friend Robert for being a motivational force by my side throughout this journey. Robert has played many supportive roles in my graduate career, including: test audience, camera man, cheering squad, psychiatrist, and chauffer. I'm lucky to have such a wonderful partner with whom to share life's adventures.

Curriculum Vitae

Appointments:

| 2012 – | **Stanback Postdoctoral Fellow**, California Institute of Technology |

Education and Research:

2012   **Ph.D. in Chemistry**, University of California – Irvine

2008 – 2012   **Visiting Scholar** to the Environmental Molecular Sciences Laboratory, Pacific Northwest National Laboratory

2008 – 2012   **Graduate Research Assistant** in the Sergey A. Nizkorodov Research Group, University of California – Irvine

2007   **Atmospheric Technician** at the National Institute for Water and Air, Wellington, New Zealand

2007   **B.S. in Chemistry** *cum laude*, University of Southern California

2006 – 2007   **Undergraduate Research Assistant** in the G.K. Surya Prakash Group, University of Southern California

2006 – 2007   **Undergraduate Research Assistant** in the Space Sciences Laboratory, University of Southern California

2005   **Undergraduate Research Assistant** in the Mark E. Thompson Group, University of Southern California

Awards and Honors:

2012   **California Institute of Technology,** *Stanback Postdoctoral Fellowship*

2012   **UC Irvine Department of Chemistry,** *E.K.C. Lee Fellowship*

2011   **UC Irvine Graduate Division,** *Chancellor's Club Fellowship*

2011	**UC Irvine Department of Chemistry,** *Regent's Dissertation Fellowship*
2010	**UC Irvine Department of Chemistry,** *Michael E. Gebel Award*
2009, 2011	**PNNL Office of Science & Engineering Education,** *Alternate Sponsored Fellowship*
2010	**American Association for Aerosol Research,** *- Student Poster Competition Winner*
2009	**UC Irvine Department of Chemistry,** *Outstanding Contribution to Teaching from a First Year Student*
2009	**National Science Foundation,** *Graduate Research Fellowship, Honorable Mention*
2006 – 2007	**National Science Foundation,** *Research Experience for Undergraduates (REU) Fellowship*
2005	**Women in Science and Engineering,** *Undergraduate Research Grant*
2003-2007	**University of Southern California,** *Undergraduate Leadership Scholarship*

Publications:

11. **T.B. Nguyen**, S.A. Nizkorodov, A. Laskin, and J. Laskin, "An approach toward the quantification of organic compounds in environmental samples using high-resolution electrospray mass spectrometry" *Submitted to Analytical Methods (2012)*

10. K.M. Updyke, **T.B. Nguyen**, P.B. Lee, J. Laskin, A. Laskin, and S.A. Nizkorodov, "Extent of visible light absorption by model biogenic and anthropogenic organic aerosols aged with gaseous ammonia" *Submitted to Atmospheric Environment (2012)*

9.   **T.B. Nguyen**, A. Laskin, J. Laskin, and S.A. Nizkorodov, "Direct aqueous photolysis of isoprene secondary organic aerosol" *Phys. Chem. Chem. Phys.* (2012), advanced article online; doi:10.1039/C2CP40944E

8.   D.R. Fooshee[†], **T.B. Nguyen**[†], J. Laskin, A. Laskin, S.A. Nizkorodov, and P. Baldi, "COBRA: A computational brewing application for predicting the molecular composition of organic aerosols" *Environ. Sci. Tech.* **46** (2012) 6048 – 6055 [†] *These authors contributed equally.*

7.   N. Staimer, **T.B. Nguyen**, S.A. Nizkorodov, and R.J. Delfino, "Glutathione peroxidase inhibitory assay for electrophilic pollutants in diesel exhaust and tobacco smoke," *Anal. Bioanal. Chem.* **403** (2012) 431- 441

6.   **T.B. Nguyen**, P.B. Lee, K.M. Updyke, D.L. Bones, J. Laskin, A. Laskin and S.A. Nizkorodov, "Formation of nitrogen- and sulfur-containing light-absorbing compounds accelerated by evaporation of water from secondary organic aerosols," *J. Geophys. Res. – Atmos.* **117** (2012) D01207; doi:10.1029/2011JD016944

5.   **T.B. Nguyen**, J. Laskin, A. Laskin, and S.A. Nizkorodov, "Nitrogen-containing organic compounds and oligomers in secondary organic aerosol formed by photooxidation of isoprene" *Environ. Sci. Tech.* **45** (2011*)* 6908–6918

4.   **T.B. Nguyen,** P.J. Roach, J. Laskin, A. Laskin, and S.A. Nizkorodov, "Effect of humidity on the composition of isoprene photooxidation secondary organic aerosol" *Atmos. Chem. Phys.* **11** (2011) 6931-6944

3.   **T.B. Nguyen**, A.P. Bateman, D.L. Bones, J. Laskin, A. Laskin, and S.A. Nizkorodov, "High-resolution mass spectrometry analysis of secondary organic aerosol generated by ozonolysis of isoprene," *Atmos. Environ.* **44** (2010) 1032-1042

2.   D.L. Bones, D.K. Henricksen, S.A. Mang, M. Gonsior, A.P. Bateman, **T.B. Nguyen**, W.J. Cooper, and S.A. Nizkorodov, "Appearance of strong absorbers and fluorophores in limonene-O_3 SOA due to NH_4^+-mediated chemical aging over long time scales," *J. Geophys. Res. – Atmos.* **115** (2010) D05203; doi:10.1029/2009JD012864

1.   C.Y.R. Wu, **T.B. Nguyen**, D.L. Judge, H.C. Lu, H.K. Chen, and B.M. Cheng, "Destruction yields and half-lives of NH_3 in various mixed cosmic ice systems by EUV photolysis," *Adv. Geosciences– Planet. Sci.***7** (2007) 101- 113

Publications in Preparation:

3.   R. O'Brien**, T.B. Nguyen**, A. Laskin, J. Laskin, S.A. Nizkorodov, and A.H. Goldstein, "A comparison of the composition of urban SOA from the 2010 CalNex Campaign and SOA generated in a photochemical chamber." *Preparation for Environ. Sci. Tech. (2012)*

2.   **T.B. Nguyen,** A. Laskin, and S.A. Nizkorodov, "Brown carbon formation from reactions of limonene-derived ketoaldehydes with $NH_4^+$and amino acids." *Preparation for Atmos. Chem. Phys. (2012)*

1.   L. Q. Nguyen, D. Shemesh, **T.B. Nguyen**, D.B.C. Martin, C.D. Vanderwal, R.B. Gerber, and S.A. Nizkorodov, "Absorption spectra, photochemistry, and mass spectrometry of beta-hydroxynitrates of atmospheric interest" *Preparation for J. Phys. Chem. A (2012)*

Abstract of the Dissertation

Molecular composition and chemical transformation of secondary organic aerosols from

biogenic precursors

Tran B. Nguyen

Doctor of Philosophy in Chemistry

University of California, Irvine, 2012

Professor Sergey A. Nizkorodov, Chair

There are large gaps surrounding our understanding of secondary organic aerosols (SOA), which represent a significant fraction of fine particulate matter globally. One of the most difficult aspects of SOA to characterize is the molecular composition, because it is both complex and dynamic. However, the composition of SOA determines to a large extent the impact SOA has on climate, atmospheric chemistry, and human health. The main focus of this dissertation is the detailed composition analysis of SOA generated from important biogenic precursors and the characterization of chemistry induced by their simulated interaction with clouds, anthropogenic pollutants, and solar radiation. In particular, the gas- and aerosol-phase compounds associated with SOA from isoprene, the most abundant volatile organic compound emitted from the biosphere, are studied with the advanced technique of high-resolution mass spectrometry (HR-MS). Many SOA compounds, particularly nitrogen-containing organics, are reported for the first time. Spectroscopy tools like UV-Vis, FT-IR and NMR are also used to characterize optical properties and molecular structures of SOA compounds. A secondary focus of this dissertation is to describe brown carbon formation from the ammonium- and amino acid-mediated aging of

limonene SOA. Brown carbon changes the optical properties of SOA, but the sources are poorly understood. The experiments presented in this dissertation aim to elucidate the previously-unknown precursors, kinetics and products of the reaction. The molecular detail gained from the HR-MS and spectroscopic analyses provides tremendous insight into the formation mechanism and further atmospheric reactions of SOA.

Chapter 1: Introduction

1.1. Background and motivation

1.1.1. Secondary organic aerosols (SOA)

Aerosols, small particles comprised of liquid or solid material suspended in air, interact extensively with solar radiation (direct effect) by scattering and absorbing light, and with clouds (indirect effect) by nucleating cloud droplets and modifying the cloud albedo (reflectivity) and lifetime [6, 7]. They are generally ascribed to have a cooling effect on climate by reducing the amount of solar radiation reaching the surface. However, there is a large degree of uncertainty in describing the radiative forcing potential of aerosols [8], primarily surrounding their interaction with clouds and coupling between biogenic aerosols and human-induced pollution. The impact of aerosols on visibility, climate and health are pronounced. Aerosols are responsible for the urban haze (dramatically reduced visibility) in rapidly-growing megacities [9]. They are associated with major climate anomalies; for example, smaller than expected increase in warming of the 2000 – 2010 decade is coupled to an increase in the aerosol burden of the same period [10]. Additionally, mounting epidemiological evidence attribute certain adverse cardiovascular and respiratory effects to chronic fine aerosols exposure [11], in particular, exposure to organic aerosols [12].

The compositions of aerosols are highly variable worldwide, and often contain both organic and inorganic material. The dominant form of aerosols in many parts of the world is secondary organic aerosols (SOA) [13], comprising up to half the total aerosol mass at mid-latitudes and up to 90% in forested regions. Furthermore, SOA account for most of the cloud condensation nuclei (CCN) fraction in forested regions [14]. SOA are formed by atmospheric reactions of volatile organic compounds (VOC) with oxidants like the hydroxyl radical (OH) and ozone (O_3). The lower-volatility products produced from the first- and later-generation chemistry

2

can form SOA through gas-particle partitioning onto preexisting particles or through self-nucleation [15, 16]. More importantly, anthropogenic pollution like nitrogen oxides (NOx = NO + NO$_2$) and sulfur dioxide (SO$_2$) significantly affects the production and chemical composition of SOA through complex mechanisms, and may have either an enhancement or inhibitory role [9, 17, 18]. The net SOA burden is documented to have increased approximately 200% since pre-industrial times [19] due to perturbations of the biosphere by human activities. Therefore, it is important to thoroughly understand the sources, mechanism of formation, and fate of SOA.

1.1.2. Biogenic SOA precursors

VOC with intact C=C double bonds are quickly oxidized in the atmosphere to generate SOA. These unsaturated VOC may be emitted from both biogenic and anthropogenic sources. However, the quantity of VOC emitted from the biosphere, e.g., from continental plant-based and oceanic sources, exceed anthropogenic emissions by an order of magnitude [20, 21] and often dominate SOA production. The biogenic VOC discussed in this work include two important SOA precursors: isoprene (C$_5$H$_8$) and limonene (C$_{10}$H$_{16}$).

Isoprene alone has emissions exceeding 600 teragrams of carbon (TgC) per year [22], making it the most abundant non-methane hydrocarbon in the atmosphere comprising an estimated 44 % of the total global VOC flux. Isoprene is most dominantly emitted by broad-leafed and deciduous trees, and its mixing ratio in forested areas is approximately 4 – 10 parts-per-billion (ppb) by volume [23, 24]. The SOA formation potential from isoprene has been re-evaluated in the last few years due to the detection of low-volatility isoprene-derived oxidation products in the aerosols sampled in a forest environment [24]. Previously described as negligible [25], SOA mass yields (defined as [(SOA formed)$_{mass}$/(VOC reacted)$_{mass}$)]) from the photooxidation of isoprene is now estimated to be in the range of 0.2 – 5.3 %, depending on

3
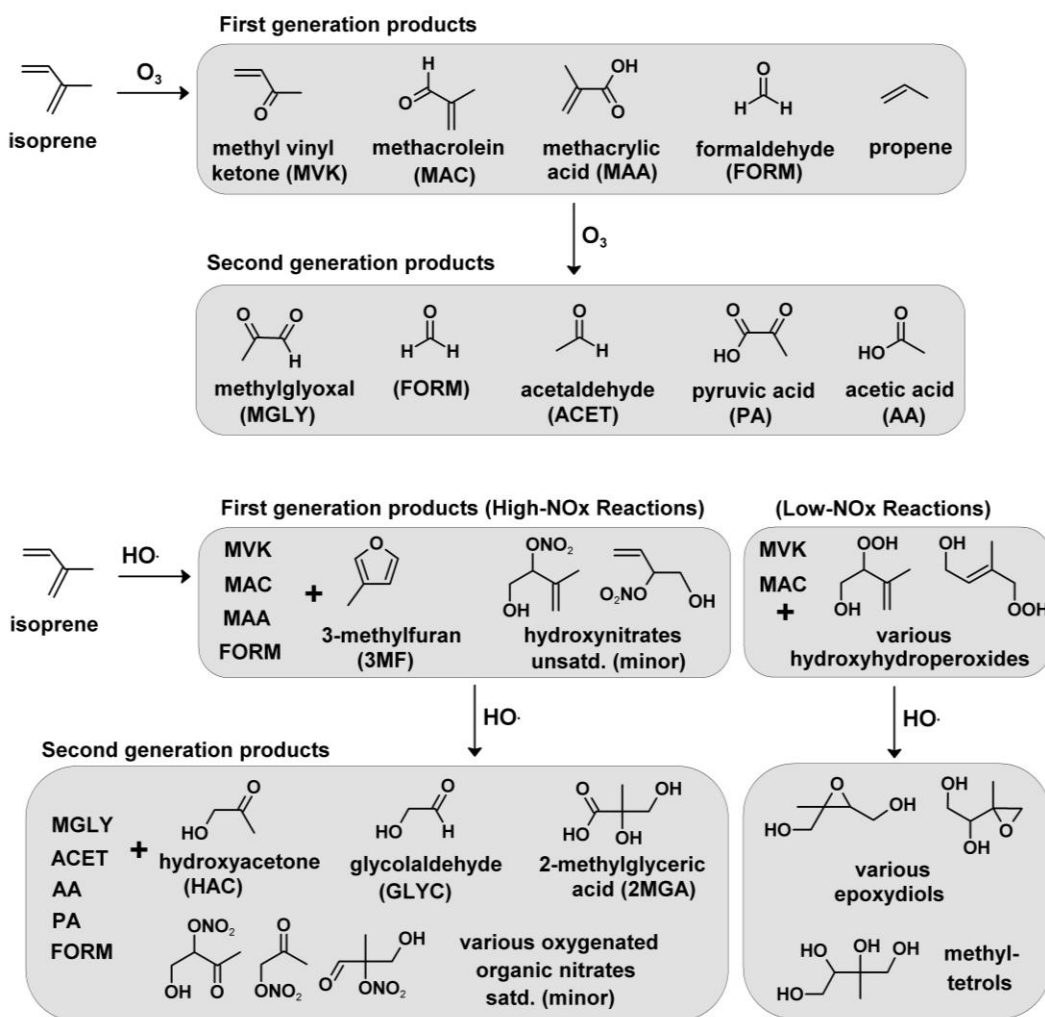
Figure 1.1: Notable monomeric products from the O_3- and OH-initiated oxidation of isoprene. Both low- and high-NOx products are featured for the OH-initiated pathway.

oxidation conditions (see ref. [18], and references therein). The SOA mass yield from the ozone oxidation is estimated to be 1% [26]. These SOA yields are much lower than the yields from most other VOC; however, the low yields are well-compensated by the high atmospheric abundance of isoprene relative to all other SOA precursors. In fact, the oxidation reactions of isoprene are estimated to contribute approximately 50% to the global SOA budget, with OH being the primary oxidant [27, 28]. The reaction of isoprene and its first generation products with

OH dominate during the daytime, as these reactions are several orders of magnitude faster than their reaction with O_3 [29].

The reaction of isoprene with O_3 and OH [21, 24, 26, 29-35] to produce monomer products are shown in Figure 1.1. Note that most of the initial oxidation products are small in size and too volatile to partition in the particle phase without additional chemistry. For a low-MW molecule like isoprene, oligomerization reactions of monomers and heterogeneous-phase reactions are important to generate larger compounds with sufficiently low vapor pressure to condense onto aerosols. The first-generation oxidation chemistry from OH and O_3 result in similar semivolatile products such as methacrolein (MAC) and methylvinylketone (MVK). However, there are also significant differences. In the O_3-initiated reaction, the addition of O_3 to one of the isoprene double bonds creates a primary ozonide intermediate, a five-member C_2O_3 ring. Cleavage of primary ozonides, followed by isomerization of the resulting carbonyl oxides, generates carbonyl and acid stable products that do not retain the C_5 skeleton of isoprene [32]. In the OH-initiated reaction, the reaction proceeds predominantly through addition of the OH radicals to one of the double bonds of isoprene (R 1.1) [31]. As result, C_5 products are more common in OH-oxidation of isoprene and many products are functionalized with hydroxyl moieties.

In urban environments, the isoprene is oxidized in the presence of high nitric oxide (NO) and nitrogen dioxide (NO_2) mixing ratios, termed "high-NOx" oxidation and in more pristine environments, the oxidation occurs with low NOx mixing ratios. The differences in the low and high NOx-mediated regimes lie in the fate of the alkylperoxy radicals (RO_2) that are produced from Reaction (1.2) after the rapid addition of oxygen to alkyl radicals [21]:

$$RHC=CHR' + OH \rightarrow RHC(OH)-\dot{C}HR' \qquad (R\ 1.1)$$

$$RHC(OH)–\dot{C}HR' + O_2 \rightarrow RHC(OH)–C(OO·)HR' \qquad (R\ 1.2)$$

$$RHC(OH)–C(OO·)HR' + NO \rightarrow RHC(OH)–C(O·)HR' + NO_2 \qquad (R\ 1.3a)$$

$$RHC(OH)–C(OO·)HR' + NO \rightarrow RHC(OH)–C(ONO_2)HR' \qquad (R\ 1.3b)$$

$$RHC(OH)–C(O·)HR' + O_2 \rightarrow RHC(OH)–C(=O)R' + HO_2 \qquad (R\ 1.4)$$

$$RHC(OH)–C(O·)HR' \rightarrow \textit{Decomposition and/or isomerization products} \qquad (R\ 1.5)$$

$$RHC(OH)–C(OO·)HR' + HO_2 \rightarrow \textit{peroxide, carbonyl or alcohol} + O_2 \qquad (R\ 1.6)$$
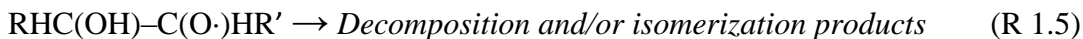
Reaction (1.3a) of RO_2 with NO to produce an alkoxy radical (RO) is preferential to (1.3b), and RO will undergo further reaction to form stable products. These stable products include carbonyls, acids, and organic nitrates. A particularly dominant product in the aerosol phase is 2-methylglyceric acid (2MGA). 2MGA is a hydroxyacid that is notable for its ability to participate in homogeneous oligomerization [36-40] . It is a useful tracer molecule for the ambient source-apportionment measurements of isoprene/OH SOA [41].

However, in the low-NOx regime, where NO is not available to participate in Reaction (1.3a), the RO_2 reacts with the hydroperoxy radical (HO_2) to form hydroperoxides (ROOH), alcohols and other products alongside molecular oxygen (R 1.6). Reaction (1.6) terminates the radical chain. Further reaction of first-generation hydroperoxides in low-NOx chemistry has been reported to form epoxydiols (Fig. 1.1) and recycle the OH [34]. A perhaps more dominant fate of isoprene hydroperoxides in forested environments is their direct photolysis to recycle OH and generate RO radicals [42]. Tetrols are also formed more favorably in the low-NOx reactions of isoprene by OH, possibly from the epoxydiol precursors, and are used as tracers of isoprene/OH SOA in forested areas [43].

Monoterpene emissions are estimated to comprise 11% of the total VOC flux at 130 TgC per year [44]. Distributions of the monoterpene emissions vary by region, but limonene is estimated to contribute up to 20 % of the total monoterpene emissions [45]. Limonene is also extensively used as an additive to household products and is one of the most abundant VOC in the indoor atmosphere [46]. Its reaction with O_3 generates particles inside buildings and residences, places where people spend the majority of their lives [47]. SOA from limonene is considerably less well-studied than pinene; yet, this monoterpene has substantial atmospheric significance in both the indoor and outdoor environments due to its large SOA yield (~50% [48]) and the distinctive chemistry of its aerosol-phase products (Section 1.1.4).
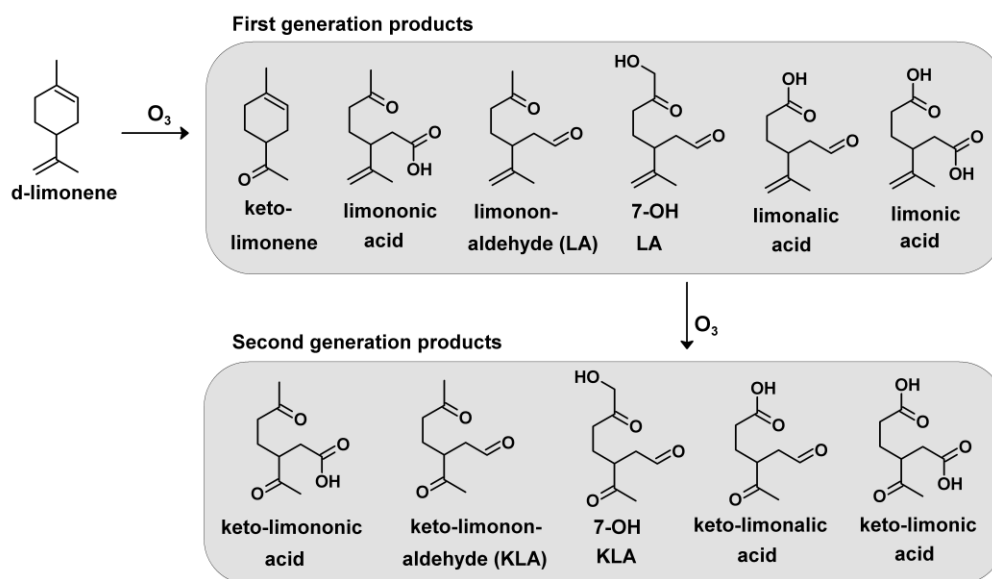
Figure 1.2: Notable monomeric products from the O_3- initiated oxidation of d-limonene. Naming convention is taken from Ref. [49].

This dissertation will only discuss chemistry stemming from the O_3-initated oxidation of limonene. Major products from this oxidation pathway are shown in Figure 1.2, which are believed to account for up to ~ 60% of the total aerosol mass [50]. Unlike isoprene, the higher-

MW skeleton of limonene produces condensable first-generation products. The endocyclic double bond of limonene is estimated to be 10 times more reactive toward O_3 than the exocyclic double bond [51]; therefore first generation products all retain the exocyclic double bond and most are C_{10} compounds due to the ozonolysis ring-opening reaction. The only product of oxidation of the exocyclic double bond is a C_9 ketone and formaldehyde. Thus, the second generation products of limonene all contain an additional ketone functional group.

Gas chromatography analysis shows that limononaldehyde (LA) is the most abundant compound in the gas phase and keto-limononaldehyde (KLA) is the most abundant compound in the particle phase [50]. The high abundance of KLA in the particle phase is expected because both keto-limonene and LA, two first-generation products with the highest yield [52], produce KLA through ozonolysis. The high aerosol-phase abundance of these ketoaldehydes were corroborated in other studies [53, 54], which additionally suggest a sizable contribution from higher-MW oligomers.

1.1.3. Composition analysis

The SOA composition provides important information about sources and chemistry of SOA. For example, the detection of tracer compounds in ambient SOA can suggest identities of VOC precursors and oxidants [55-57]. The composition also determines many of the physical, optical, and chemical characteristics of the SOA. The ability for the SOA to act as CCN largely depends on the particle size, but it is also strongly modulated by the presence of organic material near the surface [58, 59]. Furthermore, the mechanism with which SOA "age," or chemically evolve in the atmosphere, depend on its initial composition. In the aerosol-phase, the photolabile compounds like carbonyls will absorb solar radiation and fragment [60, 61] whereas unsaturated hydrocarbons are more likely to react with OH leading to further oxidation, thus enhancing their

chemical functionality [62]. Certain chemical groups present in SOA also have the ability to interact with reduced nitrogen compounds [63-65], which may change their light-absorbing properties. Despite the importance of the SOA composition, it remains poorly understood on the molecular level.

The last decade witnessed significant progress toward the characterization of SOA; however, the scientific understanding of SOA composition is still quickly evolving due to advances in analytical techniques. In particular, the SOA composition was discovered to be quite complex. Investigations within the last 10 years revealed many previously-unknown compounds in SOA, some of which are present in substantial quantity: oligomers [39, 54, 66-68], organic sulfur compounds [69-74], epoxides [34, 75, 76], high molecular-weight (MW) organic nitrates [36, 38, 40], and reduced organic nitrogen compounds [63, 77, 78]. In fact, a relatively simple gas-phase reaction such as ozonolysis of isoprene may give rise to thousands of aerosol-phase products [79]. Furthermore, most of the compounds in SOA contain more than one chemical functionality [80], which favors their partitioning into the condensed phase. The multifunctional and dynamic nature of SOA composition poses significant challenges to its chemical analysis.

Fortunately, these challenges can be addressed relatively comprehensively by modern analytical tools. Mass spectrometry is the most common technique used to measure SOA composition due to its ability to simultaneously detect a wide range of chemical species. The application of mass spectrometry to organic aerosols is a rapidly developing field. A query of "*atmospheric aerosol mass spectrometry*" in the Thomson Reuters Web of Science[TM] search engine in January 2012 reveals that out of ~ 1900 publications, approximately half are published

in the last three years. The gaining popularity of mass spectrometry aerosol measurements is a testament to the wealth of information afforded by mass spectra.
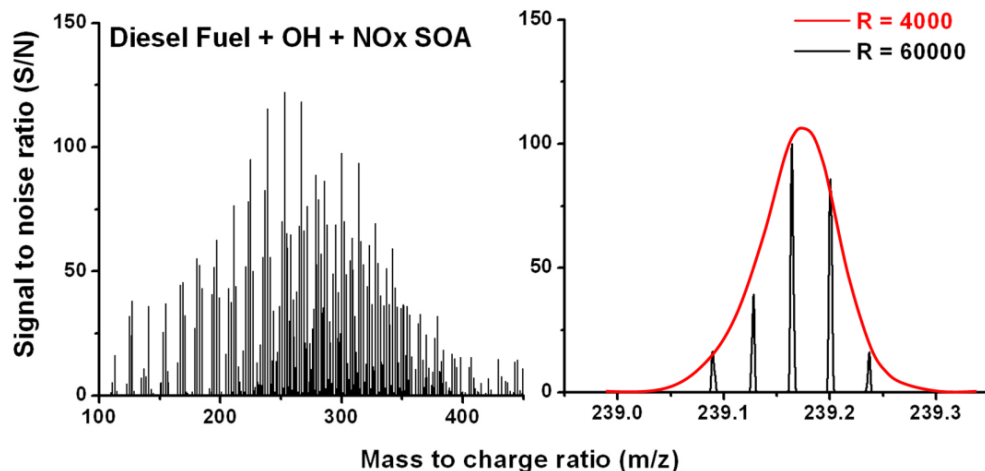
Figure 1.3: Demonstration of mass resolving power in a full mass spectrum of complex diesel-fuel SOA (left panel). The left panel is the full HR mass spectrum, and the right panel zooms in around m/z 239 peaks. The right panel shows that HR-MS ($R \sim 10^5\text{-}10^6$) is able to resolve all the molecular components, whereas lower-resolution mass analyzers like ToF ($R \sim 4000 - 8000$) will show the same cluster of compounds as one convoluted peak.

Two particularly promising techniques for the composition analysis of aerosols are aerosol mass spectrometry (AMS) [81] and high-resolution mass spectrometry (HR-MS) [82]. AMS is a convenient *online* technique that offers high temporal resolution of aerosol composition and size. The online characteristic of AMS makes it a valuable tool for the rapid detection of aerosols in the field. However, AMS has some shortcomings that renders it unsuitable for measurements of the detailed composition of SOA: (1) the extensive fragmentation of organic compounds due to the electron impact ionization method complicates the identification of neutral parent compounds and (2) the mass resolving power, defined as the ratio of the mass of a detected ion with respect to its peak width (m/Δm) is too low for the unambiguous assignment of most SOA compounds. The red trace in Figure 1.3 shows that the

mass resolution (~ 4000 m/Δm at *m/z* 200) [83] of even the most sophisticated mass analyzer for the AMS (time-of-flight (ToF)) analyzer may not resolve the masses for many types of organics present in SOA. Therefore ToF-AMS is better suited for the analysis of the average composition, e.g., speciation of the compounds into organic vs. inorganic or nitrate vs. amines, rather than detailed composition, e.g., molecular identification of individual organic compounds.

HR-MS, which include mass analyzers like Orbitrap [84] and Fourier-transform ion-cyclotron-resonance (FT-ICR) [85], is currently an *offline* technique that offers excellent mass resolution (mass resolving power from 10^5-10^6 m/Δm at *m/z* 400). Figure 1.3 shows a particularly complex HR-MS spectrum of SOA generated from the oxidation of multicomponent diesel fuel recorded by the author of this dissertation. The right panel of Figure 1.3 illustrates the full molecular speciation of organic components achieved with high mass resolution techniques. With Orbitrap-based HR-MS (currently available resolving power ~ 10^5), accurate-mass assignments of SOA compounds can be made unambiguously up to approximately *m/z* 500 [86] and more cautiously at higher masses. With further improvements and lowering costs of the HR-MS technology, instruments with higher mass resolving power will be broadly available to the aerosol scientists in the near future. HR-MS is especially advantageous in analyzing molecules with heteroatoms in their composition (e.g., $C_cH_hO_oN_nS_s$). The offline characteristic of HR-MS may be its biggest disadvantage, as SOA collection and further sample preparation may introduce artifacts in analysis. However, it is anticipated that the current development of HR-MS methods will make it possible to use HR-MS for online analysis of aerosols in the near future. At present time, the artifacts can be mediated by appropriate choice of solvent and minimal sample preparation [87]. Additionally, there are extraction-free methods of HR-MS that can be employed if sample preparation introduces impurities or suppresses signal.

HR-MS is coupled to soft-ionization techniques that do not significantly fragment the parent compound, facilitating straightforward identification of SOA compounds. This dissertation will focus on the popular electrospray ionization (ESI) technique [88], where a solvent-dissolved organic mixture is sprayed via a high-voltage capillary tip into the MS inlet, and nanospray desorption electrospray ionization (nano-DESI) [4], an alternative technique to ESI where no solvent extraction of the SOA is necessary. Section 1.3.3 describes these techniques in more detail.

1.1.4. Secondary brown carbon

Aerosols are generally known to scatter light, providing a net cooling effect on climate; however, there are a few classes of aerosols that also absorb visible light, which changes their radiative forcing potential. The three classes of light-absorbing carbon compounds include: elemental black carbon, organic brown carbon, and mineral dust aerosol. The recently-discovered fraction of organic brown carbon [89], with absorption cross sections in the visible wavelengths ($\lambda > 400$ nm), significantly modify the optical properties of aerosols and impact visibility and climate in urban areas [90]. Brown carbon can have both primary sources, e.g., vehicle and biomass burning, and secondary sources coupled with SOA formation and aging. To date, the identification of brown carbon species from biomass burning [91], aqueous chemistry of pure monomer compounds [63, 65, 92-95], and chemistry of dissolved SOA [64, 96] provide important clues to the chemical nature of brown carbon. For some species of brown carbon, the C=N bond appear to be an important moiety[63, 77]. Other types of organic brown carbon include conjugated compounds [97], possibly with sulfur in the molecule formula [96]. However, the full structures and formation mechanism of brown carbon are still open questions in the literature.

Specifically, secondary brown carbon can contribute up to 30% of the light-absorbing properties of water-soluble organic compounds sampled in the field [98]. Given that their mass absorption coefficients (MAC) are an order of magnitude smaller than black carbon [99], the 30% contribution to light absorption by brown carbon represents a substantial amount of total organic mass. An important group of secondary brown carbon originates from the reaction of organic compounds with reduced nitrogen species like ammonia (NH_3), ammonium (NH_4^+), amines (RNH_2) and amino acids. So far, brown carbon are reported to formed from reactions of reduced nitrogen with 1,2-dicarbonyls like glyoxal [93, 95] and methylglyoxal [63, 94], and unknown components of limonene ozonolysis SOA [64, 96]. More than one type of precursor must exist, because 1,2-dicarbonyls are not expected to be formed in known oxidation mechanisms of limonene with OH and O_3 (Figure 1.2). Studies on elucidating the identities of unknown brown carbon precursors, in limonene SOA or otherwise, will greatly aid in the understanding of secondary brown carbon formation and in the identification of ambient sources.

1.2. Goals and organization of the dissertation

The foremost goal of this dissertation is to comprehensively describe the pool of molecular formulas, characterize various effects on formation chemistry, and investigate the aqueous photochemistry of organic compounds in SOA derived from the oxidation of isoprene. Figure 1.4 shows the process with which SOA are generated and studied in most of the works presented in this dissertation. SOA are produced under controlled laboratory settings in a photochemical Teflon chamber constructed at UCI (hereinafter, UCI Chamber). Precise tuning of conditions relevant to aerosol formation, e.g., mixing ratios of water vapor, VOC, NOx, O_3, and oxidants, allow the isolation and detailed investigations of several factors that affect SOA

formation and aging chemistry. The composition studies are performed offline with HR-MS techniques on SOA collected on filters.
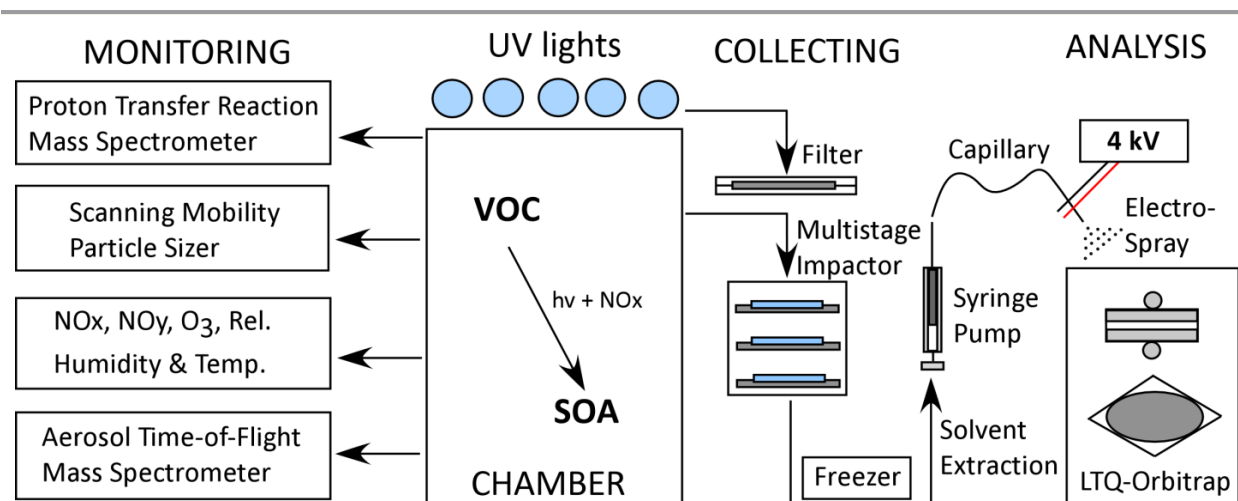
Figure 1.4: Diagram showing SOA generation, monitoring, collection and offline analysis.

Chapter 2 outlines the first HR-MS studies on the O_3-initated oxidation of isoprene and represents the first data collected from the UCI chamber after its construction. The results demonstrate the utility of HR-MS to deducing chemistry based on repeating mass units and implicate the importance of heterogeneous reactions to SOA formation. This chapter outlines mass sorting tools like Kendrick [100] and van Krevelen [101] analyses in more detail than the subsequent chapters.

Chapter 3 builds upon the framework of common HR-MS techniques to study SOA formation from the OH-initiated oxidation of isoprene in the high- and low-NOx chemical regimes. Oligomerization is important for the SOA formation from isoprene, and repeating monomer units are suggested as homogenous building blocks for oligomers. Additionally this chapter introduces high-resolution tandem multistage mass spectrometry (MS^n) and demonstrates the technique with organic nitrates found in high-NOx isoprene/OH SOA.

Chapter 4 describes the role of water vapor on the initial stages of aerosol formation chemistry for the isoprene/OH high-NOx SOA. These studies represent the first humid experiments done in the UCI chamber as the capabilities of the chamber grow with time. The composition is characterized in dry and humid environments and HR-MS is used to study the carbon length and abundance of oligomers in each environment. Important reactions and particularly reactive monomers leading to SOA formation are discussed.

Chapter 5 presents an original approach to the assignment of mass concentrations in HR-ESI-MS data via the implementation of a novel calibration axis. The effect of structure and molecular size in the ESI ionization mechanism is discussed in detail, which aid in the interpretation of ESI-MS data presented in the dissertation. The methodology described in this chapter lays the foundation for certain analyses done in Chapter 6.

Chapter 6 outlines the first direct photolysis study of isoprene high-NOx SOA organics and the second direct photolysis study on complex mixtures relevant to aerosols. A thorough introduction to aqueous photochemistry can be found in this chapter. The results demonstrate significant changes in both the average (bulk) and detailed (molecular) properties of the dissolved SOA undergoing photolysis. Interesting photo-induced reactions of organic nitrates and detailed MS^n studies of chemical structures are discussed. The work presented here demonstrates of the power of HR-MS to study organic chemistry and not just composition.

The following two chapters of the dissertation shifts the focus onto brown carbon formation from limonene SOA, motivated by the reasons outlined in Section 1.1.4. Chapter 7 adds to the understanding of the aqueous-phase reaction of limonene/O_3 SOA with NH_4^+ and amino acids, work started by *Bones et al (2010)*, by illustrating the rate enhancing capability of simulated cloud and fog processing and the ability of the SOA mixture to undergo acid-

15

catalyzed aldol condensation when prompted by evaporation. This chapter utilizes UV-Vis and HR-MS to measure the light absorbance and composition, respectively, in order to characterize the general nature of the chromophoric organic material and the rates of formation.

Chapter 8 presents unpublished work on the identification of chromophore precursors present in limonene/O_3 SOA. The work presented here is the first description of chemistry stemming from individual compounds present in limonene/O_3 SOA. This chapter discusses the synthetic and analytical methods used to obtain pure precursor compounds and resultant chromophoric material. Spectroscopy tools like UV-Vis, FT-IR and NMR are heavily utilized to determine rates of formation, visualize key products and comment on secondary brown carbon formation from realistic SOA compounds.

Chapter 9 concludes this dissertation by discussing the knowledge gained by molecular identification of SOA compounds and commenting on work yet to be done on the topic of SOA formation, composition and chemistry.

1.3. General Methods

1.3.1. SOA generation and collection in the UCI Chamber

This section describes the most common methods for conducting the SOA experiments described in the dissertation. Deviations from the general scheme will be described in the appropriate chapters. SOA were synthesized by oxidation of VOC in a 5 m^3 Teflon™ (Dupont FEP) rectangular prism chamber, designed by the author of this dissertation and built in 2008 in the Nizkorodov Laboratory at UCI. The chamber is surrounded by a 20 m^3 enclosure made of black acrylic and sealed with silicone gaskets. Figure 1.5 shows a picture of the UCI Chamber.

Figure 1.5: Picture of the UCI Photochemical Chamber with UV-B lights turned on.

The chamber is attached to an FT-IR purge air generator (Parker Balston, Model 75-62) as an air source for experiments. The purge gas generator dries the ambient air with a membrane air drier, removes CO_2 and particulate impurities, and flows into the chamber at rates of $0 - 70$ standard liters per minute (SLM). The outflow from the chamber is directed toward a high-flow vent. Before each experiment, the chamber is purged for at least 12 hours at 70 SLM until particle concentrations decrease below 0.01 μg m^{-3}. All SOA experiments described in this dissertation were performed in the absence of seed particles in order to obtain particle compositions that are entirely organic to facilitate HR-MS analysis.

Reagents, e.g., pure VOC, OH precursors or OH scavengers, were added to the chamber by evaporation at room temperature. The liquid reagents were injected with a gas-tight microliter syringe (Halmilton Inc.) into a clean custom-made glass bulb with a low flow (< 5 SLM) of dry

air. The chamber is equipped with a small electric fan inserted into the interior for mixing VOC. The fan mixed the reagents within the chamber during injection/equilibration of VOC and was then turned off when oxidant is injected or created in order to minimize particle wall losses. Both isoprene and d-limonene were obtained from Sigma Aldrich with 99% and 97 % purity, respectively. In some experiments, hydrogen peroxide (H_2O_2, Sigma Aldrich, 30% in water) is used as an OH precursor through its photolysis reaction. In other "precursor-free" experiments, only the UV photochemistry of O_3/NOx with water vapor is used to produce OH. The presence/absence of OH precursors will be indicated in the appropriate chapters. Typically the evaporation of high-volatility VOC is instantaneous, confirmed by gas-phase spectrometry techniques (Section 1.3.2), and the evaporation of H_2O_2 solution takes ~ 20 minutes.

Experiments in Chapters 2 and 3 were performed under dry conditions with relative humidity (RH < 2%). All other experiments were performed under higher RH (50 − 90 %) conditions that are more prevalent in the atmosphere. For the "humid" experiments, water vapor was introduced by flowing dry purge air through a Nafion™ membrane humidifier attached to a water bath circulator (Julabo Corp.) operating at 35°C. The RH in the chamber, as well as the temperature (± 1°C), was monitored by a Vaisala HMT330 probe (accuracy ± 2 %RH). It took approximately 2 hours at ~ 40 SLM to reach RH = 60 %. At RH > 99%, visibly foggy conditions were obtained in the chamber and water condensed on the chamber walls.

For O_3 reactions, a 1 SLM flow of oxygen (99.994% purity) was sent through an UV O_3 generator into the chamber. In the O_3 experiments, an OH scavenger is used because OH is a side product of the O_3 reaction [102]. O_3 is also a side product of the OH reaction, but as its reaction rates with alkenes are several orders of magnitude slower than the OH reaction, no O_3 scavenger is necessary. For high-NOx experiments, NO was introduced by adding a calibrated volume of a

primary standard (Praxair, 5000 ppm NO in N_2) into the chamber at approximately 100 SLM. Some NO_2 was usually produced when the NO standard was injected in the chamber. The order of injection of reagent is as follows: water vapor (if used), oxidant or OH precursor (if any), OH scavenger (if any), NOx (if used) and VOC. All these compounds are monitored by the analytical techniques discussed in Section 1.3.2.
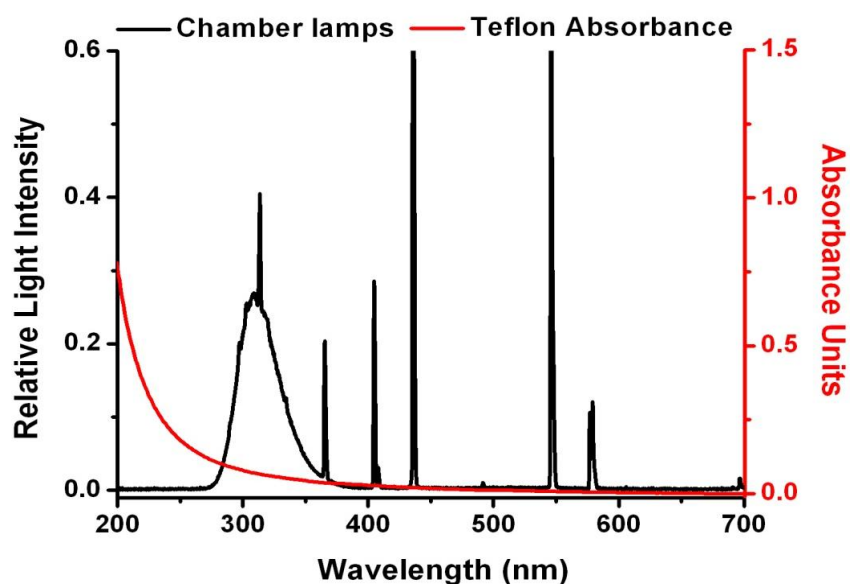
Figure 1.6: Absorbance spectrum of 5 mil Teflon FEP film superimposed on the emission spectrum of the chamber UV-B lamps.

The chamber is equipped with approximately 40 UV-B lamps (Philips T12, 40 W) mounted on three chamber walls. These lamps have broadband emissions with maximum intensity centered around 310 nm (Fig. 1.6) which does not overlap significantly with the absorbance of the chamber wall material so that light with wavelengths above $\lambda \sim 280$ nm are available for photooxidation. The lamp spectrum was taken with a fiber optic hand-held spectrometer (Ocean Optics, USB4000) and the absorption spectrum was recorded with a UV-Vis spectrophotometer (Shimadzu UV-2450). The lamps were placed at least 0.5 meters away

from the chamber walls to minimize heating at the Teflon surface. The chamber is not temperature controlled and after approximately 3 hours of reaction, the temperature rises approximately 5°C within the enclosure walls. Although this changes the RH values somewhat, there is no significant effect to the photooxidation reactions as deduced from analytical measurements. After injection and verification that the concentrations of all reagents stabilized, UV-B lamps were turned on to initiate the photochemistry. The photooxidation times were on the order of a few hours.

Aerosols were collected through an activated charcoal denuder (Sunset Laboratories Inc.) to remove VOC and residual oxidants. Typically SOA were collected onto 47 mm diameter Teflon filter substrates (Millipore 0.2 μm pore size) either through a home-built aerosol filter holder or using a rotating multistage micro-orifice uniform deposition impactor (MOUDI 110-R) operated at 30 standard liters per minute. For collection with size-selected MOUDI, the stages with the most SOA (typically the 0.056 – 0.32 μm size stages for isoprene SOA) were combined if solvent extraction was done for analysis. The collection lasted for a few hours. Collected samples were placed in plastic holders, vacuum-sealed in polyethylene bags, and frozen at -20°C pending offline analysis. Blank samples were usually generated under the same experimental conditions, but in the absence of either UV radiation or VOC. Particle mass concentrations in the blank samples were < 0.01 μg/m^3.

1.3.2. Monitoring of particles and gases during SOA formation

The UCI chamber is equipped with a suite of online analytical instrumentation to monitor the evolution of particles and gaseous species during photooxidation reactions. The size distribution and concentration of SOA particles were monitored by a scanning mobility particle sizer (SMPS, TSI Inc.). SMPS is comprised of a differential mobility analyzer (DMA, TSI model

3081) and condensation particle counter (CPC, TSI model 3775). Polydisperse aerosol (with various diameters) enter the DMA through an [85]Krypton neutralizer where they obtain a Fuchs equilibrium charge distribution (equal number of singly charged positive and negative ions). The positively charged particles move through 1 atm air towards a negatively charged rod in the center of the DMA with a velocity that is directly proportional to the particle cross-sectional area. For a fixed DMA rod potential, only particles of certain size can exit the DMA at the bottom. From scanning the potential on the rod, monodispersed populations of aerosol are selected and exit the DMA to be counted by the CPC. The CPC counts the number of particles by first enlarging their diameters with supersaturated butanol vapor and measuring their light scattering.

The main sheath (aerosol free) flow rate on the SMPS was 3 SLM and the aerosol sampling flow rate was 0.3 SLM. The sheath RH was kept below 10 %. It was assumed that with this dry sheath flow, measurements of particles even from very humid experiments correspond to their dry diameters. To convert the observed particle number concentration (particles m^{-3}) to a mass concentration ($\mu g \ m^{-3}$), a particle density of 1.2 g cm^{-3} was assumed for the biogenic SOA studied here based on density information available for alpha-pinene SOA[103]. The particles were assumed to be spherical, a reasonable assumption for SOA produced in a chamber without seed particles. The range of particle diameters that can be monitored were 15 – 660 μm. The time resolution for SMPS scans were 4 minutes. In typical experiments, SOA mass concentrations at the time of collection were on the order of 100 $\mu g \ m^{-3}$.

O_3 and NOy (NO_x + any NO_x-derived products) were monitored by photometric methods and both the O_3 and NO_y inlet flows from the chamber were filtered to remove the scattering contribution of particles in the photometric analyses. O_3 was monitored by a Thermo Model 49i

UV dual-cell photometric analyzer with a 1 ppb precision. The detection method is based on the attenuation of light at 254 nm due to O_3 in an absorption cell. NO and NOy were measured with Thermo Model 42iy analyzer. The analyzer measures the chemiluminescence of the following reaction with a photomultiplier:

$$NO + O_3 \rightarrow NO_2 + O_2 + h\upsilon \qquad (R\ 1.7)$$

The inlet flow from the chamber is split into two equal flows: the first one is used to analyze the total NO concentration and the second flow is directed across a heated (325 °C) Molybdenum catalyst to convert all higher oxides of nitrogen into NO. The second flow is then measured for NO and the difference between the first and second flow is the NOy concentration. It is important to note that the catalytic conversion method is not equally sensitive to all NOy, e.g., there are differences in the NO conversion of NO_2 vs. HNO_3 vs. $RONO_2$. Therefore in experiments where an NOy species that is efficiently-converted reacts to form a species that is poorly-converted, the nitrogen balance will appear to not be conserved. This is the case for many high-NOx SOA experiments where initially there is only NO and NO_2, and as the reaction proceeds, the fraction of the initial NOx is converted to HNO_3, $RONO_2$, HONO and other species increases. The stated detection limit for both of these instruments was 0.05 ppb and the detection time resolution was 1 min.

An online proton-transfer-reaction time-of-flight mass spectrometer (PTR-ToF-MS, Ionicon Analytik) was used to follow the decay of VOC and the production of the gas-phase photooxidation products. The benefits of PTR-ToF-MS include: high sensitivity (detection limit approaching 1 ppt), high (1 s) time resolution, and lower degrees of fragmentation compared to electron impact ionization techniques. The instrument has sufficient theoretical mass resolving power (8000 m/Δm at *m/z* 200) to accurately identify most gas-phase species during the

photooxidation. The instrument was operated at R = 4000 – 5000 (V mode). Gaseous compounds have lower MW (< 200 Da) compared to aerosol-phase compounds and the resolution necessary for accurate-mass assignments is lower; however, structural isomers still cannot be resolved with this (or any mass spectrometry) method.

PTR at the operation conditions used for our studies (V_{drift} = 600 V, E/N ~ 130 Td) is a relatively soft-ionization mechanism. The VOC are ionized by proton transfer from hydronium ions (H_3O^+) that are produced from water in the hollow cathode ion source:

$$e^- + H_2O \rightarrow H_2O^+ + 2e^- \qquad \text{(R 1.8)}$$

$$H_2O^+ + H_2O \rightarrow H_3O^+ + OH \qquad \text{(R 1.9)}$$

$$H_3O^+ + VOC \rightarrow VOC\text{-}H^+ + H_2O \qquad \text{(R 1.10)}$$
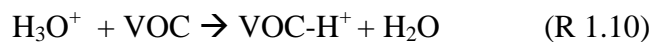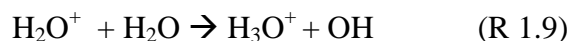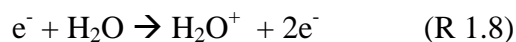
Therefore, only VOC whose proton affinity (PA) is greater than that of water (166.5 kcal mol^{-1}) will be protonated. This convenient feature of PTR-ToF-MS simplifies the detected mass spectra because the spectra will not include interferences from abundant atmospheric species like N_2, O_2, CO_2, CO, H_2, Ar and He. Consequently, some compounds relevant to SOA formation have low PA and will not be detected with PTR-ToF-MS until the analyte molecule is relatively large, because PA increases with molecular size [104]. For example, alkanes cannot be detected PTR-ToF-MS with until approximately octane or decane [105]. Some compounds have PA similar to water, e.g., formaldehyde (171.8 kcal mol^{-1}) and its detection is RH-dependent. Therefore, in high RH experiments, a correction was performed based on methods described in Ref. [106] to obtain accurate mixing ratios of formaldehyde.

The detected signal in the MS come primarily from protonated (VOC-H$^+$) ions. At low E/N, some VOC will also be detected as protonated water clusters (VOC-$(H_2O)_n$-H$^+$) and at high E/N, more VOC will undergo fragmentation, which complicate analysis. Even at relatively mild

ionization conditions, some classes of compounds undergo almost exclusively dissociative PTR. For example halogenated hydrocarbons (RX, where X = F, Cl, Br, I) will lose HX, larger alcohols will lose H_2O, and alkyl nitrates will lose NO_2 or HONO. In some cases, fragments like NO_2^+ are also detected in the MS and are distinctive enough to be used as a qualitative tracer for organic nitrates.
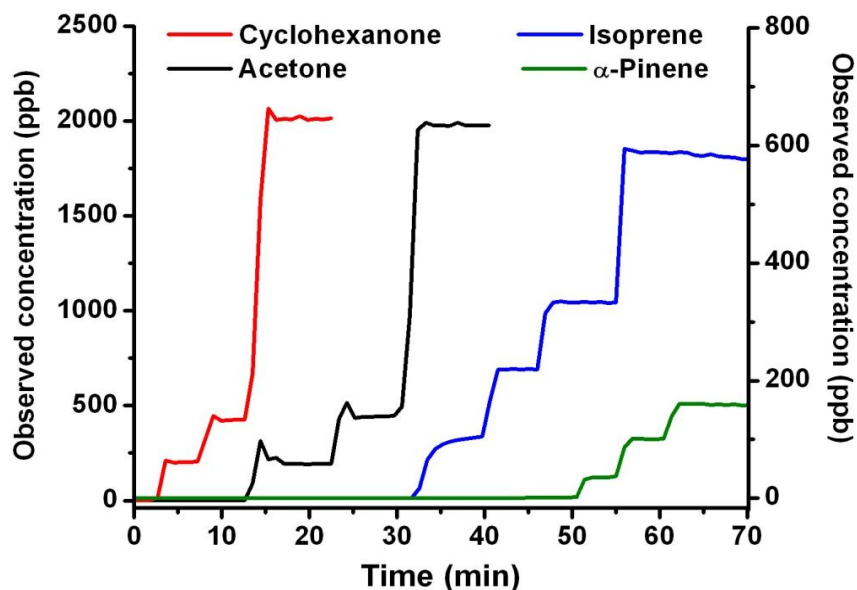
Figure 1.7: PTR-ToF-MS calibration traces for select compounds. Cyclohexanone/acetone and isoprene/α-pinene concentrations are shown on the left and right axes, respectively.

VOC concentrations are monitored by the ToF Viewer program. The program calculates gas-phase concentration (in ppb) by a specific algorithm that is based on the raw VOC-H^+ signal, the H_3O^+ signal and the proton-transfer rate (PTR) constant for each VOC. A PTR rate constant of 2 x 10^{-9} cm^3 s^{-1} $molec^{-1}$ is assumed for most VOC unless empirical data are available in the literature or if standards are available for calibration at the specific PTR conditions to manually adjust the response. Fortunately the PTR constant does not vary greatly for most VOC. For

uncalibrated VOC, the absolute quantity may be off by, at most, a factor of ~ 3 as the PTR rate

constants for oxygenated VOC typically range from $1x\ 10^{-9}$ to 5×10^{-9} $cm^3\ s^{-1}\ molec^{-1}$ [107].

Calibration was performed for a few groups of compounds: alcohols (methanol and

pentanol), aldehydes (formaldehyde), ketones (acetone and cyclohexanone), and alkenes

(isoprene and α-pinene). Many VOC, especially multifunctional compounds, are not available as

standards for calibration. The calibration was performed by injecting known amounts of VOC

into the chamber allowing the mixing ratios to stabilize. Figure 1.7 shows the PTR-ToF-MS

traces for select compounds during calibration, demonstrating the rapid response of the

instrument and the stability of VOC signal. At least three concentrations of VOC were injected

for each calibration compound, and the ratio $[VOC]_{observed}/[VOC]_{theoretical}$ was used as a

multiplicative factor in adjusting the PTR-ToF-MS response for each type of compounds.

1.3.3. HR-MS composition analysis with LTQ-Orbitrap

The SOA samples collected on filters were analyzed using a high-resolution linear ion

trap (LTQ) Orbitrap™ (Thermo Corp.) mass spectrometer available at the Wiley Environmental

Molecular Sciences Laboratory (EMSL) user facility at Pacific Northwest National Laboratory

(PNNL). LTQ-Orbitrap is a hybrid mass analyzer that offers high mass resolving power (100,000

m/Δm at *m/z* 400), high mass accuracy (1-2 ppm), and a large mass range *m/z* 50 – 2000 [84].

HR-MS analyses presented in this work were performed in collaboration with PNNL scientists

Drs. Alexander Laskin, Patrick Roach, and Julia Laskin.

Figure 1.8 shows a diagrammatic representation of LTQ-Orbitrap and the trajectory of

the ions in the mass analyzer. Ions that are produced in the source (discussed below) are

transferred via multipole ion guides into the LTQ, where they are initially analyzed with lower

mass resolution (± 0.01). The instrument can operate in both the LTQ mode (lower mass

resolution, higher ion signal) and Orbitrap mode (higher mass resolution, lower ion signal). The instrument was typically run with R= 60,000 in order to obtain higher ion signal at sufficiently high resolution. Fragmentation studies using collision-induced dissociation (CID) are also performed in the LTQ, and product ions are analyzed in the Orbitrap.
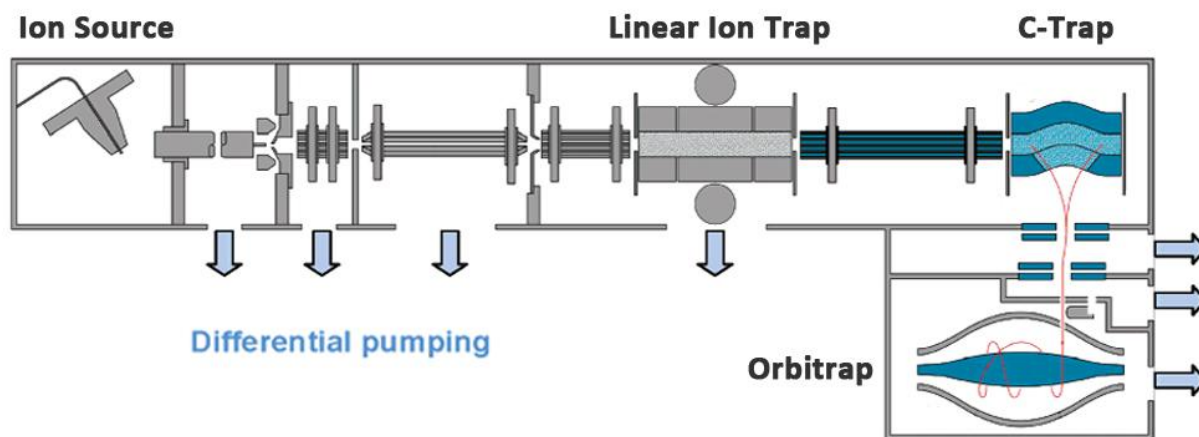
Figure 1.8: Diagram of LTQ-Orbitrap instrument, remixed and reused with permission from Ref: Makarov, A., et al., *Anal. Chem.* 2006. Copyright American Chemical Society.

Ions from the LTQ are transferred to the Orbitrap by transmission through an octopole ion guide into a curved C-trap, where they are cooled by collision with molecular nitrogen and held with RF-only potential. The C-trap injects tight packets of ions orthogonally at an offset (Fig. 1.8), in pulses, into the pinhole opening of the Orbitrap. The Orbitrap is maintained under ultra-high vacuum (~ 10^{-10} mbar) and captures the injected ion packets by rapidly scanning the electric field axially along the inner electrode. Ions with exact masses selected by the Orbitrap potential will orbit the inner electrode perfectly in thin rings and others will collide with the outer electrode. The frequencies corresponding to the axial oscillation of ions along the Orbitrap are recorded as a frequency spectrum, which is then converted to a mass spectrum through a fast Fourier-transform done in the Xcalibur software available from Thermo Electron Corp.
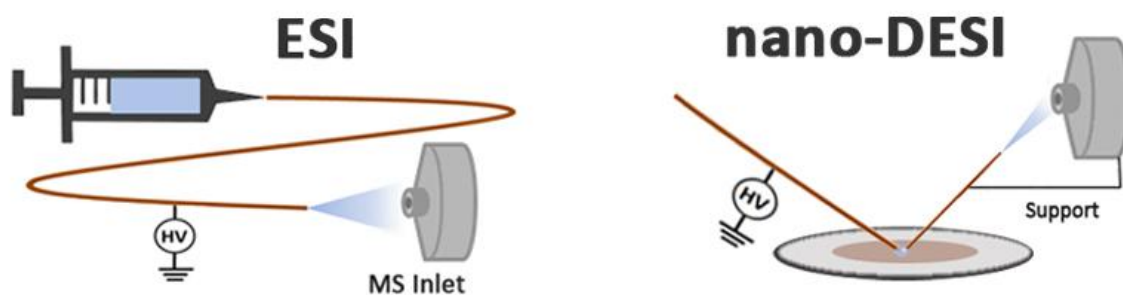
Figure 1.9: The two HR-MS ionization sources discussed in this dissertation: electrospray ionization (ESI) and nano-desorption electrospray ionization (nano-DESI).

The instrument is equipped with either a direct-infusion electrospray ionization (ESI) or a nanospray desorption electrospray ionization (nano-DESI) source [4, 108]. Both are soft-ionization techniques that do not fragment even high-MW molecules. These techniques were used, sometimes in conjunction, to obtain spectra in the works presented in the following chapters. ESI is well-suited for the analysis of dissolved organics, and is the common technique for the analysis of natural and biological organic matter [109, 110]. Nano-DESI is a sensitive ambient ionization technique that can detect nanograms of SOA material on surfaces without sample preparation prior to analysis. Nano-DESI is better suited for the analysis of chemically labile molecules that potentially react with solvent molecules or very small quantities of collected organic material where dilution would be detrimental to the observed signal [108].

The schematic representation of the ESI procedure is shown in the left panel of Figure 1.9. For ESI analysis, SOA material collected on a filter is first extracted in a small volume (1 – 3 mL) of solvent. Typical solvents used for ESI are methanol, H_2O, and acetonitrile (ACN). However, as carbonyls in SOA may form hemiacetals and acetals with methanol in the timescale of the analysis [87], the solvents used in the subsequent works exclude methanol. The dissolved sample is injected at low flow rates (0.5 – 1 μL min^{-1}) with a microliter syringe. The solvent-

dissolved analytes travel through a fused-silica capillary (50 μm I.D.) that has a pulled conical

tip, onto which a high potential (~ 4 kV) is applied. The potential at the capillary tip disperses the

liquid sample into a fine charged aerosol through solvent evaporation and Coulomb fission. The

final gas-phase ion formation mechanism of ESI is still debated, but the Ion Evaporation Model

suggests that, upon solvent evaporation, the electric field strength of a droplet with a certain

critical diameter becomes sufficiently large to field desorb the solvated ions [111]. The

ionization efficiencies of different classes of analytes depend on the ionization mode and a

variety of inter-dependent factors. Factors affecting ionization in positive ion mode ESI will be

discussed in detail in Chapter 5.

Figure 1.9 also shows a schematic representation of the nano-DESI procedure, developed

in the laboratory of our collaborators Alexander and Julia Laskin at PNNL in 2010 [4]. A

traditional DESI procedure, developed in the laboratory of R. Graham Cooks at Purdue in 2004

[112, 113], electrosprays the solvent onto the sample surface with the aid of a gas jet. The

simultaneous ionization and desorption of ions occurs on the surface and the desorbed ion flow is

directed from the surface to the inlet of the MS. However, under normal operating conditions

there may be indirect transfers of analyte away from the MS, splashing of the solvent, and other

undesirable effects in DESI.   The nanospray variation of DESI comprises two capillaries joined

by a small solvent bridge (Fig. 1.9). The solvent is continuously fed from the primary capillary

and aspirates through the secondary capillary into the MS inlet from capillary action, minimizing

indirect transfer effects and solvent splashing. The solvent bridge may be a very small droplet,

which amplifies analyte signal by reducing solvent dilution. The solvent-analyte contact time in

nano-DESI on the substrate surface is in the range of 1 − 3 min for a typical experiment. This

shorter contact time decreases undesirable solvent-analyte side reactions. *Laskin et al. (2010)*

demonstrated that nano-DESI is more sensitive to nitrogen-containing organic compounds (NOC) [91]; thus nano-DESI is used as an auxiliary technique to ESI in this dissertation for those samples that are expected to contain a sizable fraction of NOC.

The analyte molecules (M) ionized in ESI and nano-DESI are detected primarily as protonated ($[M+H]^+$) and/or sodiated ($[M+Na]^+$) ions in the positive ion mode and as deprotonated ($[M-H]^-$) ions in the negative ion mode. Fragmentation of the primary ions may occur in some cases, and ion complex formation may also occur with highly concentrated solutions. Generally, the "neutral" molecular formulas are presented in the following sections, and can be obtained by subtracting or adding the exact mass of a proton or a sodium ion. Data were taken in the ionization modes most appropriate for the sample. Most compounds ionize well in the positive ion mode; however, moderately acidic organic compounds, e.g., organic nitrates, sulfates, and acids, will be more efficiently ionized via deprotonation. Instrumental mass calibrations were performed at least twice daily with a commercial standard mixture of caffeine, the protein MRFA, and the Ultramark 1621 polymer series (MSCAL5, Aldrich) to maintain high mass accuracy (1 ppm at m/z 500). The calibration standard molecules have masses spanning the range of 130 – 2000 Da, which is sufficiently wide for SOA analysis.

1.3.4. Data processing and accurate-mass assignments

Mass spectra similar to the one shown in Figure 1.3 are extracted from the Xcalibur program of the LTQ-Orbitrap and were analyzed according to the scheme presented in Figure 1.10. Peaks were first "deconvoluted" in the Decon2LS program developed at PNNL [http://ncrr.pnl.gov/software/] by replacing the initial signal distribution of each peak with a single value representing the signal-to-noise ratio (S/N) at the maximum m/z value. Peaks with S/N lower than 4 – 10 times the background S/N were not included in the analyses, and the

discriminatory background ratio chosen is proportional to the total signal of the sample. This step typically removes smaller peaks with relative intensities below 1 %. Deconvolution is performed for all spectra, including those of the blank samples.
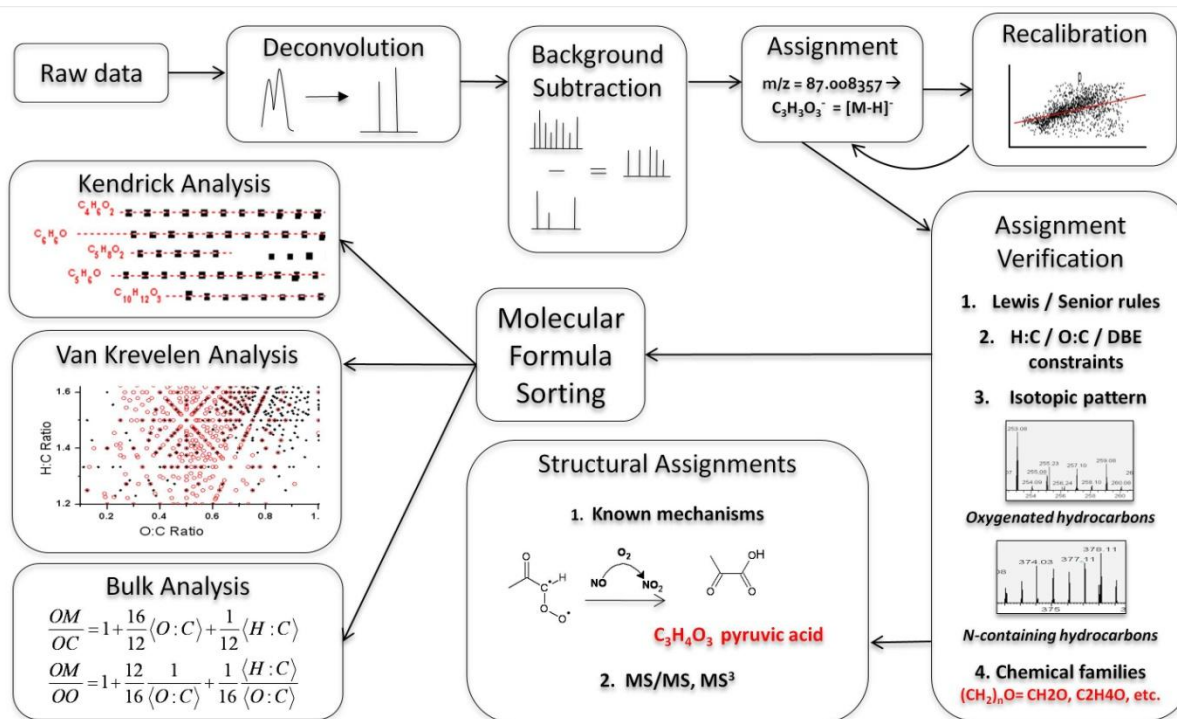
Figure 1.10: HR-MS data analysis steps: from raw accurate-mass peaks to assigned and sorted molecular formulas.

The deconvoluted sample spectra are then "aligned" (i.e., matched with respect to the m/z values) with the blank spectra using a custom Labview 7.0 program in order to subtract background peaks. The peaks in two spectra are defined as a match if they are within a tolerance range of $m/z \pm 0.001$, and the peaks in the sample that also appear in blank experiments were removed. The Labview alignment program also labels peaks corresponding to ^{13}C isotopes of organic compounds based on the expected ratio of the $^{13}C/^{12}C$ peaks and the exact-mass positions. ^{13}C peaks are clearly differentiable from single-nitrogen NOC that are also nominally

even in mass by observing their isotopic patterns (isotopic patterns of oxygenated organics vs. NOC are shown in Fig. 1.10 under the "Assignment verification" panel). The ^{13}C peaks were also removed from further analyses.

The background-subtracted and de-isotoped peaks are then processed with a separate Labview 7.0 program that assigns a molecular formula to each peak based on their measured m/z values. In the positive ion mode, ions are assigned to sodiated ($C_cH_hN_nO_oNa^+$) or protonated ($C_cH_{h+1}N_nO_o^+$) molecular formulas and in the negative ion mode, they are assigned to deprotonated ($C_cH_{h-1}N_nO_o^-$) molecular formulas. The assignments consider a specified tolerance ($m/z \pm 0.001$) and constraints imposed on the elemental ratios (e.g., $0 \leq O/C \leq 3.0$, $0.8 \leq H/C \leq 2.5$), number of atoms ($C \leq 40$, $O \leq 80$, $H \leq 80$, $N \leq 2$, and $Na \leq 1$), and parities (odd m/z only or all m/z) in the molecular formulas [114, 115]. The atomic parameters are chosen to represent a broad range of organic compounds and the parity constraints are used to assign NOC and oxygenated organics in an iterative manner.

After the assignment, the theoretical masses of each assigned molecule are computed based on their assigned molecular formulas. A linear least-squares analysis is used for recalibration to minimize the deviation between observed and theoretical m/z. Recalibrated masses typically change on the order of $m/z \pm 0.0001 - 0.001$. The recalibrated m/z axis for each sample is re-processed in the Labview assignment program, and the number of assignable peaks typically increases ~ $10 - 20\%$ after recalibration. Assignments are verified based on valency, parity, and isotopic patterns built into the Labview codes. The peaks that can be assigned based on programmed parameters typically comprise $60 - 80$ % of the total peaks. Unassigned peaks are minor components, with relative abundances of less than 5% of the maximum peak.

At this point, assigned molecular formulas can be converted to that of the neutral species for further data processing. The S/N values of compounds detected as both protonated and sodiated species in the positive ion mode are typically summed. The molecular formulas of compounds contain a rich array of information, which can be revealed following various sorting methods that will be expanded upon in Chapter 2. However, the molecular formulas themselves do not unequivocally characterize the chemical structure of molecules because isomeric compounds share molecular formulas. Structure determinations can be aided by a comparison of structures expected based on mechanisms reported in the scientific literature and, more straightforwardly, by structure analysis techniques like tandem mass spectrometry, which will be expanded upon in Chapter 3.

Chapter 2: Composition of Isoprene Ozonolysis SOA

2.1. Abstract

The chemical composition of SOA generated from the ozonolysis of isoprene in the presence of an OH scavenger was examined using high-resolution electrospray ionization mass spectrometry (ESI-MS) in the mass range $m/z = 50\text{-}1000$. The chemical composition of SOA is complex, with more than 1000 assigned peaks observed in the positive and negative ion mode spectra. Only a small fraction of peaks correspond to known products of isoprene oxidation, such as pyruvic acid, glycolic acid, methylglyoxal, etc. The absolute majority of the detected peaks correspond to highly oxidized oligomeric constituents of SOA, with an average O/C molar ratio of 0.6. The corresponding organic mass (OM) to organic oxygen (OO) ratio is 2.4. Approximately 8% of oxygen atoms in SOA are in the form of peroxides, as quantified with an iodide test. Double bond equivalency (DBE) factors, representing the sum of all double bonds and rings, increase by 1 for every 1-2 additional carbon atoms in the molecule. The number of unoxidized C=C double bonds is estimated to be less than 10%; the remaining DBE is due to C=O carbonyl groups. Kendrick analysis suggests that the prevalent oligomer building blocks are small carbonyls with a C_1-C_2 skeleton. Formaldehyde (CH_2O) is identified as the most common repetitive building block in the observed oligomeric compounds.

2.2. Introduction

Ozonolysis of isoprene is an important daytime and intra-canopy pathway for SOA formation [116]. The ozonolysis mechanism and major products from the ozonolysis of isoprene were presented in Section 1.1.2. The ozonolysis of isoprene has been the subject of a large number of studies [117-125]. However, the detection of oxidation products was usually limited to gas-phase products using gas chromatographic (GC) and/or infrared (IR) spectroscopic analysis. Major products identified in previous studies included volatile and semivolatile compounds such as methyl vinyl ketone (MVK), methacrolein (MAC), propene, methylglyoxal, acetaldehyde, acetone, and formaldehyde.

Condensed-phase and multi-phase chemistry can make a significant contribution to the yield of SOA from isoprene oxidation. Important oxidative processes for isoprene (and its volatile and semivolatile products) occurring in the aerosol phase include acid-catalyzed heterogeneous reactions leading to humic-like products [126], formation of tetrols and polyfunctional acids in the presence of peroxides [35, 36, 41, 127, 128], and cloud processing of isoprene oxidation products [129-133]. It is speculated that these semivolatile products are further oxidized in the particle phase to form lower-volatility species, further promoting their affinity for the particle phase and providing a sink for the vast majority of semivolatile compounds. Therefore, the composition of particle-phase oxidation products can be very complex. This study will investigate the non-volatile and semivolatile components of SOA generated from the dark ozonolysis of isoprene (designated isoprene/O_3 SOA for the remainder of the paper) using high-resolution electrospray ionization mass spectrometry (ESI-MS).

Recent modeling and laboratory studies provided evidence that H_2O_2 and organic peroxides (ROOH) are important components of biogenic SOA, especially in SOA produced by

ozone reactions [36, 134-141]. The fraction of water soluble peroxides in isoprene/O_3 SOA was measured in this work with an iodometric test. In combination with the high-resolution mass spectrometry data, these measurements make it possible to estimate the fraction of the organic oxygen mass residing in the peroxidic form.

2.3. Experimental

2.3.1.   SOA generation and mass spectrometry

Isoprene/O_3 aerosol was generated by an ozone-initiated oxidation of isoprene in the UCI Chamber (Section 1.3.1) under dry (RH < 2 %) conditions. The initial concentrations of isoprene (Aldrich, 99% purity) were 500 ppb and 1 ppm, chosen to yield sufficient quantity of aerosol necessary for ESI-MS analysis. The ratio of ozone to isoprene was limited to unity to avoid over-oxidation [120]. The typical SOA mass concentrations for the 500 ppb and 1 ppm experiments were 15 μg/m^3 and 40 μg/m^3, respectively. The reaction time and ozone to isoprene ratio were not sufficient to completely oxidize the first generation products MVK, MAC, and methacrylic acid (MAA), given that their reactivity with ozone is almost an order of magnitude lower than that of isoprene [142]. An excess of cyclohexane (45 ppm, Fisher, >99% purity) was added as an OH scavenger. Without an OH scavenger, it is estimated that up to 50% of the oxidation products are formed through the OH-initiated oxidation [125].

Initial particle formation occurred within 30 minutes. The mixture was allowed to react for 1 hour, after which, the particles were collected on a Teflon-coated filter (Millipore, 0.2 μm pore) at a flow rate of 20 standard liters per minute (SLM). The filters were extracted with 10 minutes sonication in 1 mL of acetonitrile (EMD 99.8% purity). The extracts were not pre-concentrated to avoid thermal decomposition and/or polymerization effects. Assuming all SOA

on the filter was dissolved, the extracts had typical concentrations of 10-100 µg/mL. Blank experiments were conducted using the same experimental procedure except isoprene was not injected into the chamber. Mass spectra from blank experiments contained reproducible peaks attributed to contamination from the filter and acetonitrile solvent. These peaks were subtracted from the sample mass spectra during the data analysis stage.

Extracted SOA samples were analyzed with LTQ-Orbitrap MS. The ESI flow rate was 0.3 - 0.5 µL min^{-1} and the spray voltage was 4.0 kV. The system was operated in both positive and negative ion modes with a mass range of m/z 50 - 1000. Data analysis was performed as outlined in Section 1.3.4. Because no NO_x was introduced into the chamber and because of the inertness of acetonitrile with respect to SOA compounds [143], we did not expect to find any nitrogen-containing species in the mass spectra. Intensities of peaks with even nominal m/z values were consistent with ^{13}C isotopic substitution and such peaks were therefore excluded from the analysis. Approximately 30% of the total peaks could not be assigned, most of which had relative abundance of less than 5%. The fraction of unassigned peaks was higher at higher m/z values, as expected. Molecular formulas of the corresponding neutral molecules, M, were calculated by subtracting the exact atomic weights of Na and H atoms from [M+Na]$^+$ and [M+H]$^+$, respectively, and adding the mass of the proton to the measured m/z of the [M-H]$^-$ species. All molar ratios, double bond equivalency factors, and chemical formulas presented in this chapter refer to the neutral molecules.

2.3.2. Peroxide test

The peroxide test was performed as described by [134]. Isoprene/O$_3$ SOA samples were prepared as described above and collected on pre-weighed filters. The loaded filters were weighed to ±2 µg accuracy with Sartorius ME5-F filter balance, and extracted in nanopure water

37

(18.0 MΩ cm^{-1}). The extract was filtered using a syringe filter. As this test is sensitive only to water-soluble peroxides, solubility of SOA is an important variable in this method. In several separate experiments, SOA was collected on CaF$_2$ windows by impaction and extracted in water and in several organic solvents. SOA appeared to be fully soluble in polar solvents like water, acetonitrile, and methanol (there was no visible residue on the window or colloidal particles in the solution) and poorly soluble in nonpolar solvents chloroform and toluene. This implies that isoprene/O$_3$ SOA is dominated by polar, water-soluble species. The peroxide test should therefore measure the total peroxide content in isoprene/O$_3$ SOA.
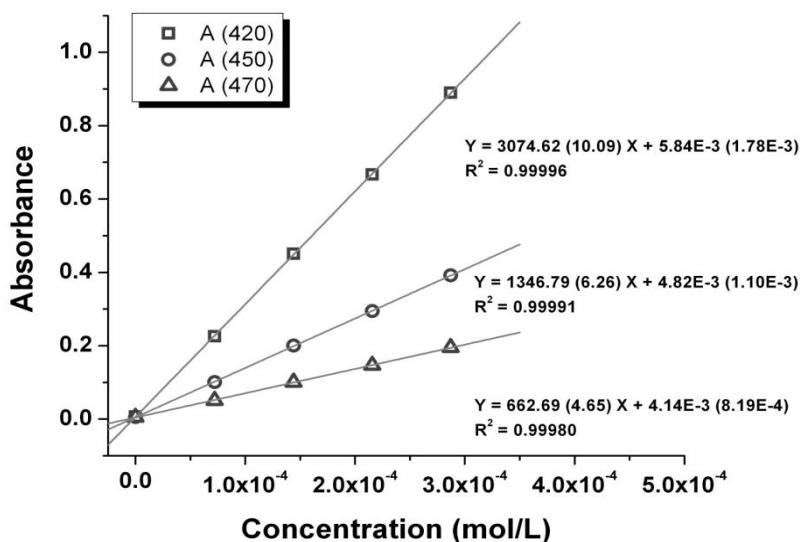
Figure 2.1: Absorbance of I$_3^-$ chromophore in peroxide test as a function of concentration of the H$_2$O$_2$ calibrant.

The colorimetric test is based on the reaction of H$_2$O$_2$ or water-soluble organic peroxides with excess potassium iodide (KI) in the presence of acetic acid, which produces I$_3^-$ ion with a characteristic absorption spectrum in the visible range:

$$3\ I^-(aq) + H_2O_2\ (aq) + 2\ H^+(aq) \rightarrow I_3^-(aq) + 2\ H_2O \qquad (R\ 2.1)$$
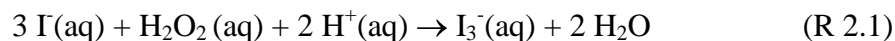
Figure 2.1 shows calibration of the peroxide test using aqueous H_2O_2 solutions (Fluka, ACS certified at 3.4% w/w) with 0.6 M solution of KI (EMD, 99.0%). The calibration was linear at several wavelengths (λ = 420, 450 and 470 nm). Aqueous samples were allowed to react, with continuous stirring, for 1 hour at room temperature before being analyzed with a Shimadzu UV-Visible dual-beam spectrophotometer (UV-2450, Shimadzu Corp.) in 1.0 cm quartz cells at three wavelengths, 420 nm, 450 nm, and 470 nm. Although [134] used benzoyl peroxide for the calibration purposes, H_2O_2 is a more convenient calibrant for this study because the SOA is water soluble.

2.4. Results and discussion

2.4.1. Mass spectra
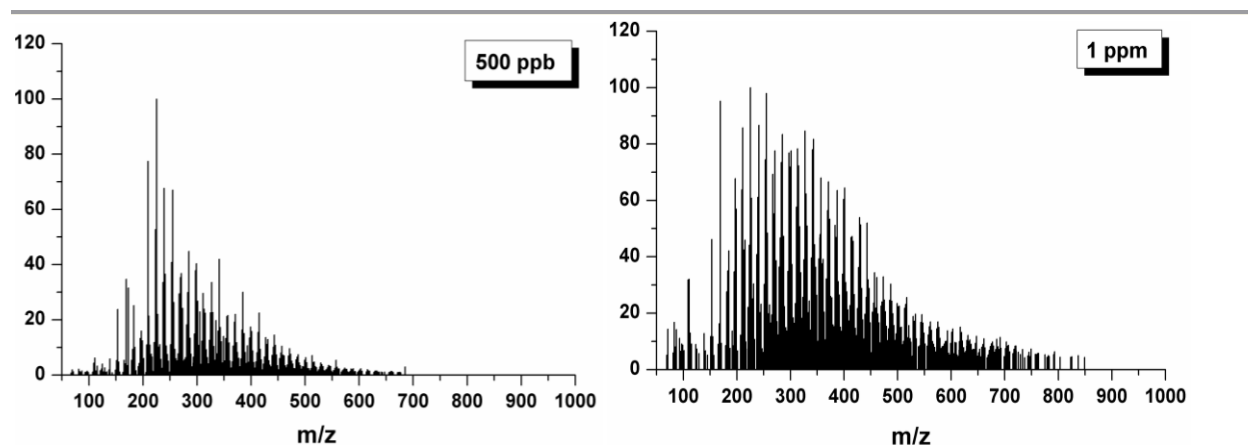
Figure 2.2: Representative high-resolution mass spectra of isoprene/O_3 SOA in the positive ion mode. No peaks were detected above *m/z* =1000. The initial concentrations of isoprene are shown in the boxes.

The mass spectra of isoprene/O_3 SOA at both initial reactant concentrations of 500 ppb and 1 ppm are shown in Figure 2.2 (positive ion mode) and Figure 2.3 (negative ion mode). Background peaks attributed to solvent and filter impurities, as well as peaks with signal-to-noise

ratio below 4, are excluded from these plots. There are more than 1500 peaks in the positive ion mode spectra and more than 1000 total peaks in the negative ion mode spectra. In both detection modes, the majority of the observed peaks are assignable to specific formulas by the method described above.

In contrast to the mass spectra of limonene/O_3 SOA, which contain well-defined clusters of peaks corresponding to monomeric, dimeric, trimeric and tetrameric products [53], the mass spectra of isoprene/O_3 SOA cannot be clearly divided into obvious oligomeric subgroups. The peak intensity distribution varies between the negative and positive ion mode spectra, with the positive mode spectra exhibiting a larger number of peaks in the high m/z region. In contrast, the negative and positive ion mode spectra of limonene/O_3 SOA were quite similar [53]. Expected first generation isoprene oxidation products (C_1-C_5), from oxidation with ozone or incompletely-scavenged OH radicals, are observed in both modes. However, the dominance of C_6-C_{40} compounds observed in the positive ion spectra cannot be explained solely by the gas-phase oxidation of isoprene, suggesting a high degree of oligomerization in the aerosol.
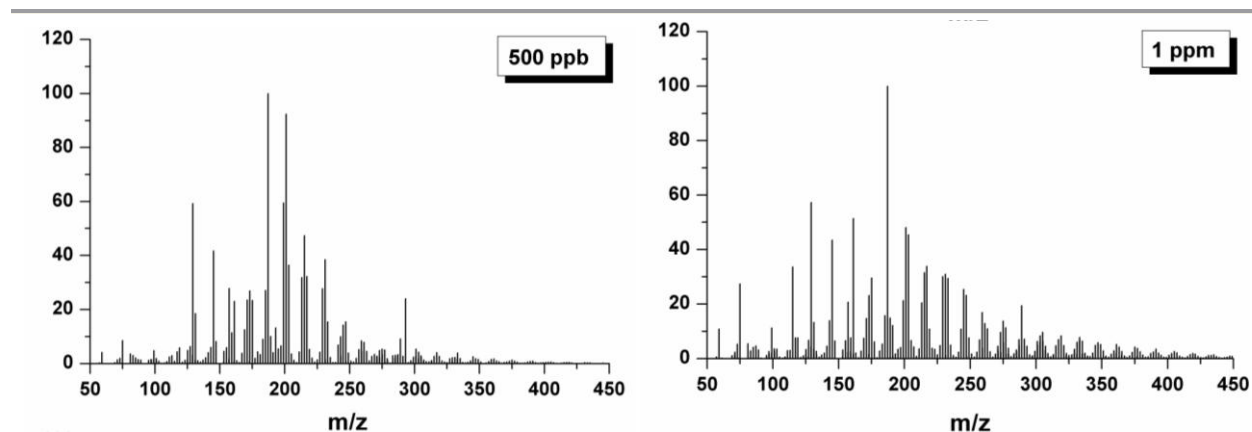
Figure 2.3: Representative high-resolution mass spectra of isoprene/O_3 SOA in the negative ion mode. No peaks were detected above $m/z = 450$. The initial concentrations of isoprene are shown in the boxes.

The major visual differences between the positive and negative ion mode spectra can be explained by the mechanism of ESI. Sodiation and protonation become more efficient with increasing molecular size of the oligomer [144, 145], which effectively shifts the intensity distribution in the positive ion mode spectra to higher *m/z* values with respect to the negative ion mode spectra. Therefore oligomeric molecules may be overrepresented in the positive ion mode spectra and underrepresented in the negative ion mode spectra. This effect is clearly visible in Figures 2.2 and 2.3. The fraction of oligomeric products produced by the limonene + O_3 reaction is similarly higher in the positive ion mode spectra [53]. These detection biases mean that each ionization mode provides complementary information.

The complexity of mass spectra arising from the oxidation of the C_5 skeleton of isoprene is truly unexpected, given the number of constraints imposed on this system: the OH oxidation channel was inhibited with a scavenger, there was no NO_x in the chamber, and the reaction took place in the dark, preventing any photochemistry. Therefore, most of the observed peaks must have resulted from secondary reactions involving the first-generation products. Because ozonolysis of an isolated isoprene molecule can only produce C_1-C_4 compounds, it is clear that a high level of oligomerization has occurred either in the aerosol phase or in the extraction solution prior to ESI/MS analysis.

2.4.2. Van Krevelen vs. DBE representation of mass spectra

Van Krevelen (VK) diagrams are useful for the visualization and analysis of HR-MS spectra of complex organic mixtures [146]. VK diagrams take advantage of the exact elemental assignments to recast mass-spectral data in terms of oxygen-to-carbon (O/C), hydrogen-to-carbon (H/C), and other appropriate molar ratios. In this work, we use an approach to the visualization of mass spectral data, which slices the VK diagrams into segments corresponding to

different values of the double bond equivalency (DBE) factors, also known as the degree of unsaturation. DBE is equal to the number of double bonds and/or rings in a closed-shell organic molecule [147, 148]. For a molecule that consists of h hydrogen atom, c carbon atoms, o oxygen atoms, and no other kinds of atoms, DBE is calculated as follows [2]:

$$DBE = 1 - h/2 + c \qquad\qquad\qquad (E\ 2.1)$$

Figure 2.4 shows a VK diagram for isoprene/O_3 SOA in both positive and negative modes. The sizes of the symbols are logarithmically scaled by the corresponding peak intensities and color coded by the DBE values. Because of ionization biases discussed earlier, peak intensities are not necessarily representative of actual concentrations of individual compounds. However, they serve as a good indication of the general distribution of peaks in the mass spectra. The VK diagrams corresponding to the positive and negative ion modes provide complimentary information because the lists of molecular formulas derived from the positive and negative ion mode spectra do not fully overlap.
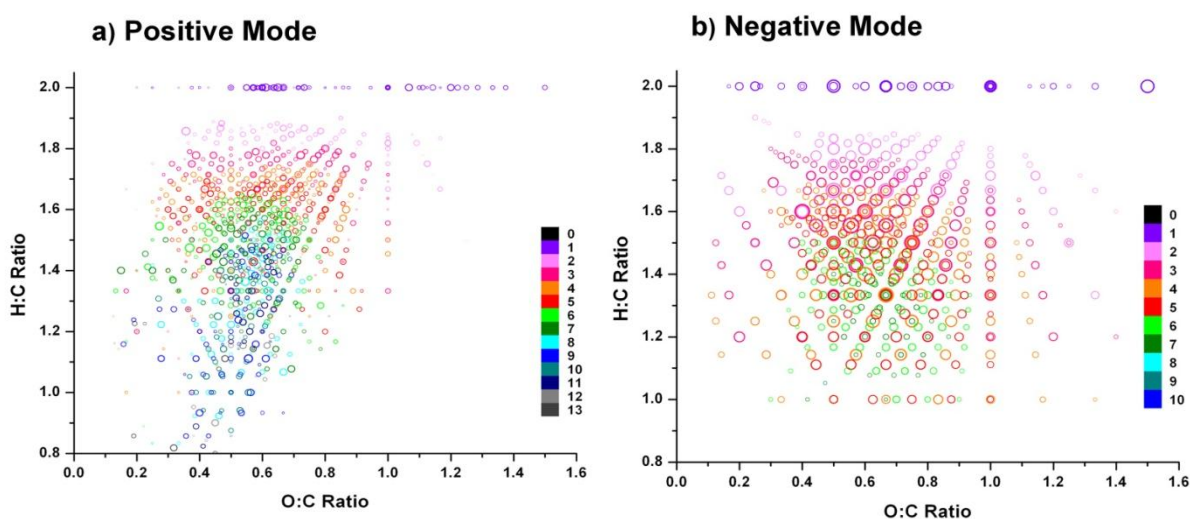
Figure 2.4: Van Krevelen diagrams for positive and negative ion mode spectra. Sizes of points are weighted by an adjusted mass-spectral intensity scale and color-mapped by DBE values. Values next to the color code are the DBE values.

VK diagrams can be used to qualitatively identify different composition domains in natural organic samples [146, 149]. The upper left portion of the diagram with high H/C ratio (~2), low O/C ratio (<1), and a DBE of 1 corresponds to smaller aliphatic (C_2-C_5) aldehydes and alcohols. The upper right portion of the diagram with high H/C (~2), high O/C (1-2), and low DBE (1-2) represents small (C_1-C_2) aliphatic oxygenated compounds (e.g. carboxylic acids, esters, and peroxides). Oligomeric SOA constituents with high DBE values cluster in the center of the diagram (H/C ~ 1.5, O/C ~ 0.6). Highly oxidized (O/C > 1) oligomeric compounds are detected only in the negative ion mode and appear at the lower right region, with DBE values exceeding 4. This region likely represents multifunctional acids, which are known to constitute a sizable fraction of total organic mass [80].
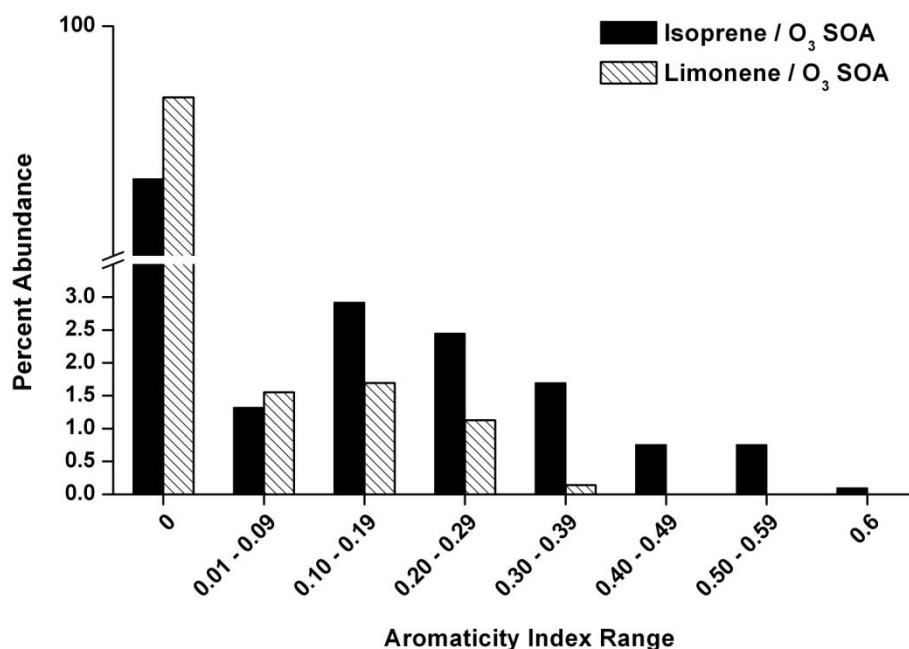
Figure 2.5: Histogram of the distribution of AI values in isoprene/O_3 SOA (this work) and in the limonene/O_3 SOA [54]. The majority of the peaks had AI = 0 necessitating a break in the vertical axis.

The lower left corner of the VK diagram contains the most unusual and least characterized products of isoprene ozonolysis, which have low H/C ratios, low O/C ratios, and large DBE values greater than 10. Some of these compounds contain unsaturated C=C bonds or rings built entirely from carbon atoms as evidenced by their positive aromaticity indexes (AI). The definition of AI specifically excludes C=O bonds and cyclic ethers from contributing to the degree of unsaturation [1],

$$AI = (1 + c - o - h/2) / (c - o) \qquad\qquad (E\ 2.2)$$

where AI values are defined as zero for $c - o \leq 0$. Ref. [1] recommended a threshold of AI > 0.5 for aromatic compounds and AI > 0.67 for condensed aromatic compounds. The range of AI for isoprene/O_3 SOA and limonene/O_3 SOA are presented in Figure 2.5.
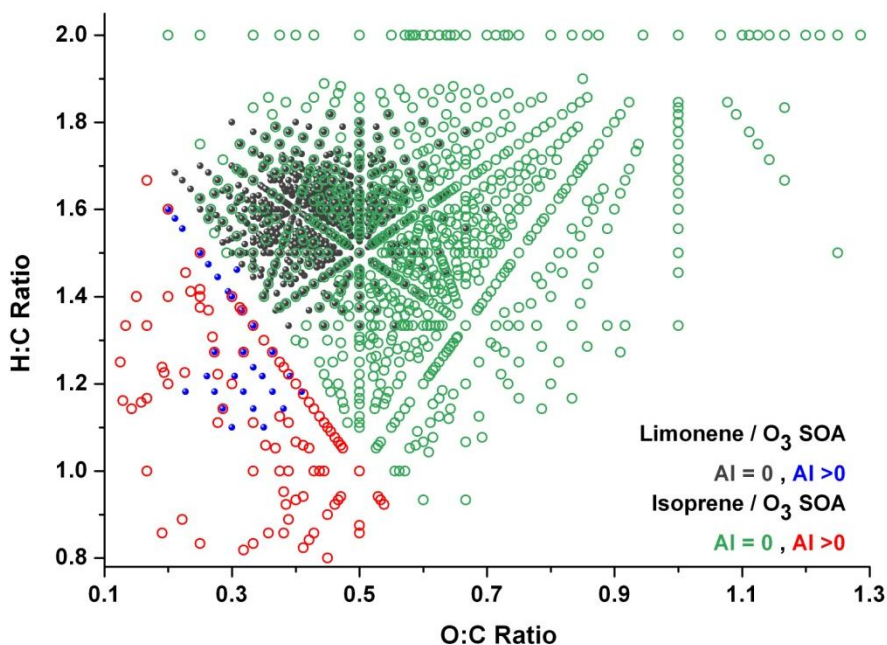
Figure 2.6: Comparison of Van Krevelen diagrams for limonene/O_3 and isoprene/O_3 SOA based on data from the positive ion mode mass spectra. Points in the bottom left corner of the diagram are characterized by positive aromaticity index (AI) values, which indicate the presence of unoxidized C=C bonds.

Figure 2.6 compares the positive ion mode data for isoprene/O_3 SOA and limonene/O_3 SOA extracts [54]. Both types of SOA contain molecular formulas with positive values of AI (in the case of isoprene/O_3 SOA, ~10% of formulas detected in the positive ion mode and ~6% of formulas detected in the negative ion mode had AI>0). It is important to note that while a positive value of AI suggests there may be aromatic characteristics in the compound, it does not necessitate this. As the majority of the observed positive AI values are below the suggested thresholds for aromatic or condensed aromatic structures (Fig. 2.5), the positive AI values likely arise from non-aromatic C=C bonds that were incompletely oxidized by ozone or formed through secondary oligomerization processes such as aldol condensation.

Figure 2.6 demonstrates that O/C ratios in isoprene/O_3 span a considerably larger range than O/C ratios in limonene/O_3 SOA [53, 54]. The large difference in the appearance of the VK plots for limonene/O_3 and isoprene/O_3 SOA demonstrates that one cannot ascribe a unique region of the VK plot to SOA as has been attempted, for example, by [150]. This difference is in part due to the disparity in the number of unsaturated carbon atoms in the precursors. Limonene ($C_{10}H_{16}$) contains four sp^2 and six sp^3 hybridized carbon atoms. Isoprene (C_5H_8) also contains four sp^2 hybridized atoms but only one sp^3 hybridized carbon atom. One of the double bonds in limonene is endocyclic, in contrast to isoprene, which only has vinylic double bonds. Addition of ozone to an endocyclic double bond generally leads to ring-opening without loss of carbon atoms from the molecule. On the contrary, ozonolysis of vinylic bonds leads to a loss of atoms from the carbon skeleton. Assuming that ozonolysis adds 1-2 oxygen atoms to each non-terminal sp^2 carbon atom, and removes all terminal sp^2 carbon atoms, the O/C ratios should range from 0.3-0.7 and 0.7-1.3 in limonene/O_3 and isoprene/O_3 SOA, respectively. This is consistent with the

observed increase in the average O/C values from 0.45 for limonene/O_3 SOA to 0.62 for isoprene/O_3 SOA.

2.4.3. Oligomers in Isoprene/O_3 SOA

A large fraction of observed peaks in both ionization modes appear at high *m/z* values (*m/z* >200, Figures 2.2 and 2.3). These compounds must result from fairly extensive oligomerization, as the largest monomeric products of isoprene ozonolysis have masses below 150 Da. The large fraction of products observed in the oligomeric form is not unprecedented. For example, a significant fraction of oligomeric compounds were found in the ozonolysis of limonene [53, 151, 152], ozonolysis and photooxidation of α-pinene [149, 152-157], photooxidation of isoprene [36, 158], trimethylbenzene [159, 160], toluene [161], and in aqueous mixtures of simple isoprene oxidation products [130, 131, 162, 163]. The fraction of higher molecular weight species generally increases with increasing initial precursor concentrations. However, oligomers have been observed in laboratory-generated SOA with initial VOC loadings approaching atmospheric levels [164]and in ambient SOA [155].

Possible monomeric units have been routinely deduced from mass spectrometric evidence [36, 130, 131, 157, 163], by examining the distribution of Δ*m/z* separations between various product peaks. From these methods, carboxylic acids (pyruvic acid, oxalic acid, glycolic acid, 2-methylglyceric acid, and glyoxylic acid) and aldehydes have been suggested as possible monomeric units of oligomers found in isoprene SOA. Kendrick representation of high-resolution mass spectrometric data [165] can similarly be used to search for potential oligomeric units. The standard IUPAC scale sets the atomic mass of ^{12}C to exactly 12 Da. Kendrick redefined the mass scale by choosing a different base, most commonly by setting the molar mass of CH_2 group to exactly 14 Da [166]. Any combination of atoms can serve as the base for

calculating Kendrick mass (KM). The Kendrick mass defect (KMD) is then defined as the difference between the nominal mass and KM. For example, if formaldehyde is used as the base, KM_{CH_2O} and KMD_{CH_2O} are obtained by setting the molar mass of CH_2O to exactly 30 Da.

$$KM_{CH_2O} = mass \times \frac{\left[mass_{CH_2O} \right]}{mass_{CH_2O}} \qquad \text{(E 2.3)}$$

$$KMD_{CH_2O} = mass - KM_{CH_2O} \qquad \text{(E 2.4)}$$

Square brackets refer to the nominal mass obtained by rounding the mass to the nearest integer. When KMD_{CH_2O} values are plotted versus the nominal m/z values, homologous series of compounds differing only by the number of CH_2O units fall on horizontal lines and are clearly distinguishable as shown in Figure 2.7. Identification of the elemental composition of one compound in the homologous series enables assignment of all peaks in the series. We have relied on this method to either confirm or reject ambiguous assignments of peaks at high m/z values.

The choice of formaldehyde as the Kendrick base in this work is not arbitrary. A computer program was used to systematically evaluate different Kendrick bases for their ability to give series with the largest average number of homologous compounds. The Kendrick bases that yielded the longest families were CH_2O, O, CH_2, C_2H_4O, C, $C_3H_4O_2$, and CO, in descending order. Using this analysis we identified CH_2O as the most common building block of isoprene/O_3 SOA. In contrast, CH_2 and O were the best Kendrick bases for identification of homologous series in limonene/O_3 SOA [53].

The prominence of the Kendrick base CH_2O suggests that formaldehyde acts as one of the monomeric building blocks for oligomeric growth. Kendrick bases C_2H_4O, and $C_3H_4O_2$ may correspond to neutral compounds like acetaldehyde and methylglyoxal, respectively, acting as monomer building blocks. The esterification process has also been shown to add repetitive

47

$C_3H_4O_2$ units in the oligomerization of condensed-phase compounds [36, 131, 155, 162, 167-170]. Aldehydes like formaldehyde, acetaldehyde, and methylglyoxal were also recognized as possible oligomeric building blocks in the analysis of high resolution mass spectra of ozonolysis of alpha and beta pinene [149]. These three compounds are important by-products of isoprene gas-phase ozonolysis and can be produced in substantial yields via multiple reaction pathways [117, 121, 171].
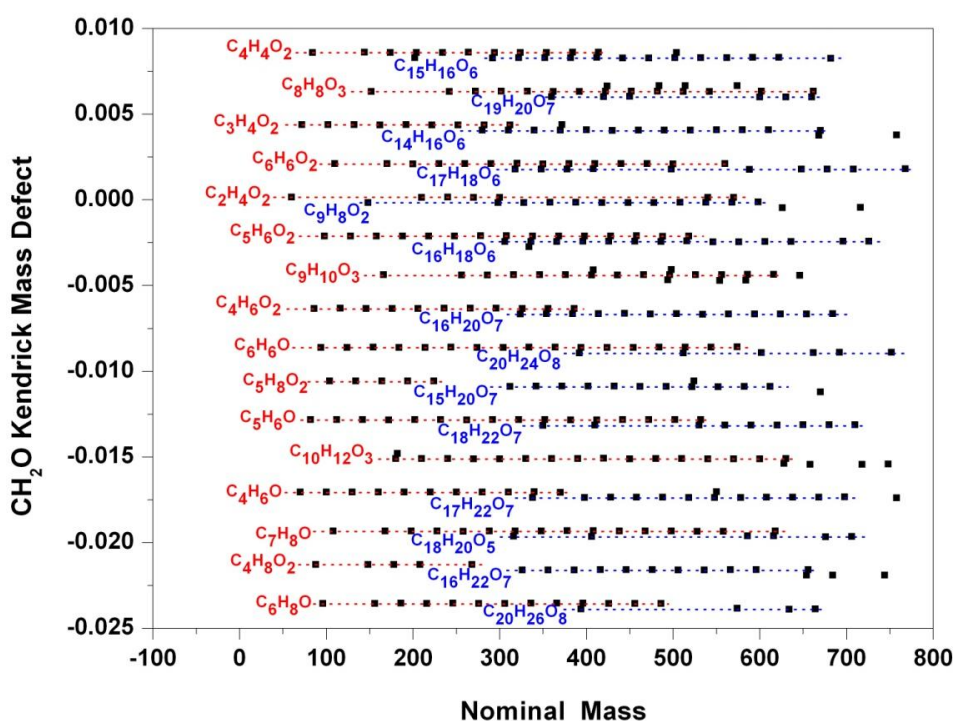
Figure 2.7: A magnified portion of the Kendrick mass defect plot of isoprene/O_3 SOA with CH_2O as the Kendrick base. Families $M(CH_2O)_n$ with n=0,1,2,3… appear on the same horizontal line. Dashed lines serve as visual guides. The red and blue colors are used to distinguish between Kendrick families in close proximity. Adjacent points differ by the mass of one CH_2O molecule. The first member of each family (M) is labeled.

Because of the high initial concentrations of reactants in our experiments, the aldehydes are present in sufficient quantities in the chamber to participate in reversible and irreversible uptake into the particle phase. Such uptake of semivolatile compounds (e.g. glyoxal,
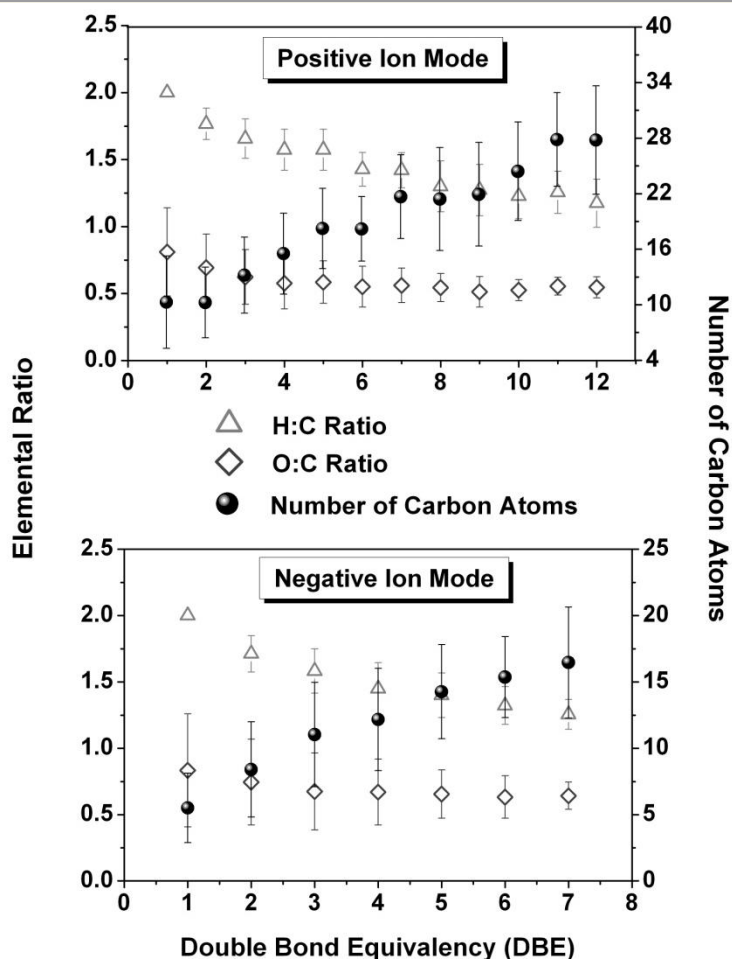
Figure 2.8: Correlation between the average number of C atoms, O/C ratio, H/C ratio and DBE in the isoprene/O_3 SOA. For all molecules with the same DBE values, the weighted-average elemental ratios and their uncertainties (one standard deviation) were calculated from Eqs. (2.5) and (2.6).

methylglyoxal, etc.) has been shown to occur with much greater efficiency than predicted by gas-to-particle partition theory [167, 168, 172-175]. This is not to say that all oligomeric compounds in isoprene/O_3 SOA have resulted from polymerization of aldehydes. More likely, these simple aldehydes contributed to SOA via gas-to-particle uptake reactions with hydroxyl and carbonyl functional groups of involatile molecules that had already condensed in SOA. Mechanisms for

these uptake processes include hydration, aldol condensation, hemiacetal formation, esterification, etc., [36, 131, 155, 162, 167-170].

The distribution of DBE values in SOA products can be used to impose further constraints on the oligomerization mechanism. Figure 2.8 shows the average values of O/C ratio, H/C ratio, and c (the number of carbon atoms in the molecule) calculated for each subset of DBE values for both positive and negative ion mode spectra. There is a linear correlation between DBE and the average values of c. The slopes of the $<c>$ vs. DBE dependence are 1.8 (R^2=0.961) and 1.7 (R^2=0.968) in the negative and positive ion mode, respectively. This is consistent with a C_1 to C_2 molecule acting as the oligomer building block, wherein each oligomerization step adds either a new double bond or a ring in the molecule.

2.4.4. Low molecular weight species in Isoprene/O_3 SOA

For sufficiently small m/z values, tentative structural assignments are also possible with HR-MS. Table 2.1 shows the most likely assignments of several prominent low-m/z peaks based on their accurate masses. Not all assignments in Table 2.1 are unique; for example, structural isomers methylglyoxal and acrylic acid cannot be distinguished based on their mass alone. The compounds detected in highest abundance were pyruvic acid ($C_3H_4O_3$) and glycolic acid ($C_2H_4O_3$), both important aqueous-phase higher-generation products of isoprene oxidation [132, 176]. Gas-phase measurement of pyruvic acid by [121] produced a relatively small yield of 0.02. The high abundance of pyruvic acid observed in this work suggests that its total yield (gas-phase + particle-phase) should be considerably larger. Model simulations show that glycolic acid is a prominent product in the aqueous-phase oxidation of isoprene and its carbonyl products under a variety of atmospheric conditions. It is speculated to be the intermediate species for the formation of other hygroscopic acids [129].

Table 2.1: Tentative assignments of low molecular weight species observed in the positive and negative ion mode ESI-MS spectra of isoprene/O₃ SOA. These compounds likely exist in SOA in the form of esters or aldol condensates, which reversibly decompose upon extraction of SOA in the solvent for ESI-MS analysis. The relative abundance column shows the corresponding peak intensities in percentages relative to the largest peak in the mass spectrum.

Tentative Assignment	Molecular Structure	Detection Mode	Relative Abund. (%)	Chemical Formula	Neutral Mass
Formic Acid		[+]	2.6	CH_2O_2	46.0055
Acetic Acid /		[+/-]	2.6 / 7.5*	$C_2H_4O_2$	59.0133
Glycolic Acid		[-]	17.9	$C_2H_4O_3$	76.0160
Acrylic acid / Methylglyoxal		[+/-]	2.9 / 1.2	$C_3H_4O_2$	71.0133
Pyruvic Acid		[+/-]	16.1 / 3.1	$C_3H_4O_3$	87.0082
Malonic Acid		[-]	1.2	$C_3H_4O_4$	104.0110
Propanoic Acid		[-]	3.2	$C_3H_6O_2$	74.0368
Lactic Acid		[-]	2.2	$C_3H_6O_3$	90.0317
Methacrolein / Methylvinylketone		[+/-]	7.2 / 0.75	C_4H_6O	69.0340
Methacrylic acid		[+/-]	7.1 / 3.2	$C_4H_6O_2$	85.0290
Acetic anhydride		[+/-]	3.7 / 2.7	$C_4H_6O_3$	101.0239
Succinic Acid		[+/-]	3.3 / 6.0	$C_4H_6O_4$	117.0188
Malic Acid		[+/-]	2.9 / 1.9	$C_4H_6O_5$	133.0137
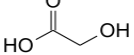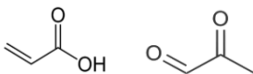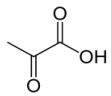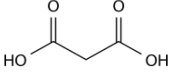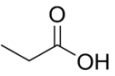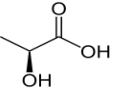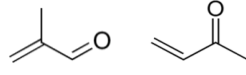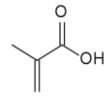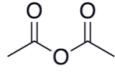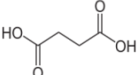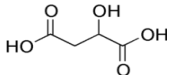
* Positive / Negative ion mode abundances, respectively

Several organic acids appearing in Table 2.1 are not first-generation products of isoprene ozonolysis. They may arise from oxidation of the first generation products by incompletely-scavenged OH radical and other reactive species formed in the decomposition of Criegee intermediates. Criegee intermediates with a C-H bond in the alpha position have a small activation barrier to H migration (on the order of 10 kJ mol^{-1}) to form an energetically favored hydroperoxide [124]. This hydroperoxide decomposes to form a hydroxyl radical and an alkyl or alkoxy radical. The OH yield in ozonolysis of isoprene through the hydroperoxide channel was determined to be 19-27% [118, 122, 124, 177, 178]. Pathways for the formation of some of the assigned products via the hydroperoxide channel are depicted in Figure 2.9.
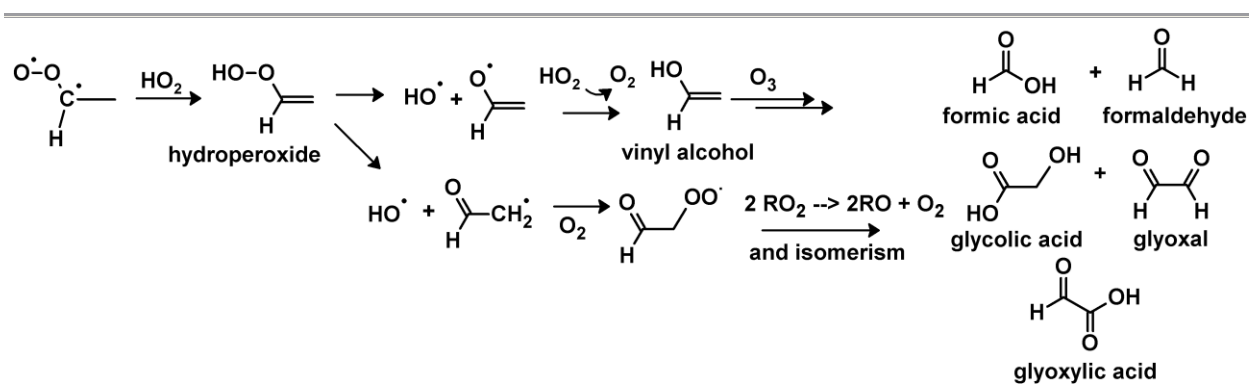
Figure 2.9: Example of hydroperoxide formation and subsequent photodecomposition to give OH, R, and RO radicals. Further chemistry leads to some products shown in Table 2.1.

Some of the compounds listed in Table 2.1 are not expected to partition into the aerosol phase because they are too volatile. However, we are able to observe molecules like MAC and MVK in the mass spectra, which are known volatile products of isoprene ozonolysis in NO$_x$-free experiments [117, 120, 121]. Acetic acid, another important gas-phase product of isoprene ozonolysis [179, 180], also shows up in the mass spectra. The detection of these volatile compounds in ESI-MS spectra may be an artifact of the collection and detection process. As

chamber air is pulled through the filter, collected organic matter on the filter may uptake "sticky" semivolatile compounds [181-183]. For example, it has been demonstrated that glyoxal, a relatively volatile oxidation product of biogenic VOCs, has a measured uptake coefficient several orders of magnitude higher than can be predicted by typical gas-particle partitioning theory [167]. Once partitioned into the aerosol phase, semivolatile compounds may undergo reversible acid-catalyzed processes, such as esterification or aldol condensation. Following extraction of the SOA sample into acetonitrile solution, the equilibria are shifted, releasing the semivolatile species in the solution. As a result, these semivolatiles are detected by ESI-MS even though they were not necessarily present in the airborne SOA in an unbound form. Similarly, the monomer acids described previously (pyruvic acid, glycolic acid, etc.) may be present in the SOA in the oligomeric form and observed in ESI-MS after reversible decomposition processes.

2.4.5. Elemental and mass ratios between C, H, and O atoms

Organic aerosol samples are routinely analyzed to determine the total mass of organic carbon (OC) and elemental carbon (EC) in the sample. The total organic mass (OM) can then be estimated from OC by multiplying it by a prescribed OM/OC ratio, which ranges from about 1.4 to 2.3 depending on the type of organics present in the aerosol [184, 185]. The ratio of the mass of organic oxygen (OO) to OC is another useful metric in classifying different types of organic aerosol [185]. In the case of fully soluble SOA samples, the OM/OC ratio can be directly calculated from high resolution ESI mass spectra data once assumptions about relative detection sensitivities are made. It is convenient to first define the average molar ratio <O/C> as the total number of oxygen atoms divided by the total number of carbon atoms in the sample. The average $\langle H:C \rangle$ ratio can be defined in a similar way.

$$< O/C > = \sum_i x_i o_i \ / \sum_i x_i c_i \qquad\qquad \text{(E 2.5)}$$

$$< H/C > = \sum_i x_i h_i \ / \sum_i x_i c_i \qquad\qquad \text{(E 2.6)}$$

Here, h_i, c_i, and o_i are the numbers of H, C, and O atoms in the ith compound, $C_{c_i} H_{h_i} O_{o_i}$, and x_i is the intensity of the corresponding peak in the mass spectrum. Equations (2.5) and (2.6) rely on the assumption that all SOA compounds can be detected by the ESI-MS method with equal sensitivity, which is certainly a simplification [54]. In Chapter 5 of this dissertation, a sensitivity calibration of HR-ESI-MS will demonstrate the disparate sensitivities of organic molecules, especially at lower masses. However, these weighted-average ratios still provide useful qualitative information about the degree of oxidation of SOA constituents formed from different precursors. These ratios can be converted into the OM/OC, OO/OC and OM/OO ratios after scaling by proper atomic weights. For organic samples containing only hydrogen, oxygen, and carbon atoms, as is the case for isoprene/O_3 SOA or limonene/O_3 SOA, these ratios are [54]:

$$< \frac{OM}{OO} > = \ 1 + \frac{12}{16} \frac{1}{<O/C>} + \frac{1}{16} \frac{<H/C>}{<O/C>} \qquad\qquad \text{(E 2.7)}$$

$$< \frac{OM}{OC} > = \ 1 + \frac{16}{12} < O/C > + \frac{1}{12} < H/C > \qquad\qquad \text{(E 2.8)}$$

$$< \frac{OO}{OC} > = \ \frac{16}{12} < O/C > \qquad\qquad \text{(E 2.9)}$$

The calculated values of all these ratios for isoprene/O_3 SOA and limonene/O_3 SOA are listed in Table 2.2.

Despite the differences in intensity distribution and detection range of the positive and negative ion mode spectra (Figures 2.1 and 2.2), the values of OM/OC, OO:OC and OM/OO ratios derived from these spectra are quite similar. This level of agreement is perhaps fortuitous

Table 2.2. Molar- and mass- weighted elemental ratios in isoprene/O_3 SOA calculated from Equations (2.5-2.9). Calculations are done separately for data from the positive and negative ion mode mass spectra of isoprene/O_3 SOA. Data from our earlier study of limonene/O_3 SOA [54] are provided for comparison.

	\<O/C\>	\<H/C\>	OM/OC	OM/OO	OO/OC
Isoprene/O_3 SOA (+) Ion Mode	0.61 (±0.20)	1.53 (±0.28)	1.94 (±0.27)	2.38 (±0.59)	0.82 (±0.27)
Isoprene/O_3 SOA (-) Ion Mode	0.63 (±0.26)	1.51 (±0.25)	1.97 (±0.35)	2.34 (±0.73)	0.84 (±0.35)
Limonene/O_3 SOA (+) Ion Mode	0.45 (±0.09)	1.58 (±0.11)	1.73 (±0.11)	2.88 (±0.42)	0.60 (±0.11)

as positive ion mode spectra are dominated by various oligomeric species, whereas negative ion mode spectra are dominated by molecules with carboxylic acid functional groups. We want to point out, however, that the average elemental ratios are remarkably *insensitive* to the method of their calculation. For example, for data from the positive ion mode spectra of isoprene/O_3 SOA, the average O/C ratio calculated form Equation (2.5) is 0.61. The ratio becomes 0.58 if all the weights in Equation (2.5) are set to 1. If the weights are arbitrarily set to $(m/z)^{-1}$ to approximately account for the higher ionization efficiency of higher molecular weight species the average O/C ratio becomes 0.57. Finally, the unweighted average of all individual O/C ratios shown in Figure 2.3(a) is 0.60. Similar types of calculations for data from the negative ion mode spectra result in the following values for the average O/C ratios: 0.63, 0.65, 0.64, 0.68, respectively. This lack of sensitivity of the average O/C ratio to the method of its calculation was also observed in the case of α-pinene SOA [149]and increases our degree of confidence in the elemental and mass ratios listed in Table 2.2.

The data in Table 2.2 reveals that the degree of oxidation in isoprene/O_3 SOA is quite high, with OO accounting for more than 40% of SOA mass (OM/OO~2.4). A substantial fraction

of this oxygen is likely present in the form of organic peroxides (see next section). The fraction of carbonyls and carboxyls should also be substantial as evidence by the large DBE values (Figure 2.4). In comparison, limonene/O_3 SOA is characterized by a smaller OO content, with OM/OO~2.9, for the reasons described in Section 2.4.2.

2.4.6. Peroxides in Isoprene/O_3 SOA

Organic peroxides measured in this experiment were assumed to be stable on the timescale it took to generate, collect, and extract the sample (approximately 3 hours). The measured amount of peroxidic groups, normalized with respect to the SOA mass, was 1.0 ($\pm$0.1)$\times10^{-6}$ mol mg^{-1}. As most SOA constituents have multiple functional groups and high O/C ratios, it is convenient to report the percentage of organic oxygen residing in peroxy groups (f_{peroxy}) as a measure of the peroxide content of SOA:

$$f_{\text{peroxy}}(\%) = \frac{mw_{O2}n_{\text{peroxy}}}{m_{\text{SOA}}} \times \frac{OM}{OO} \times 100\% \qquad (11)$$

Here n_{peroxy} is the molar amount of peroxy groups measured by the iodometric test, m_{SOA} is the mass of SOA sample, and mw_{O2} is the molecular weight of the peroxy group (32 g mol^{-1}). Using the OM/OO ratio from Table 2.2 (~2.4), we found that oxygen in peroxy groups accounted for $f_{peroxy} = 8 \pm 2$ % by mass of all oxygen in isoprene/O_3 SOA. This number has to be treated as approximate because of the uncertainties involved in the estimation of the OO/OM ratio, and because of the restriction of the peroxide test to water soluble SOA compounds. Nevertheless, the fraction of peroxides in the isoprene/O_3 SOA is quite substantial. This result agrees reasonably well to measurements done by *Hasson et al* (2001) [119], who reported approximately 6 wt% total hydroperoxide yield in their isoprene/O_3 SOA formed under dry conditions. *Docherty et al (2005)* [134] reported very high peroxide fractions, 47, 85, 34 and 98

wt%, in the ozonolysis of α-pinene, β-pinene, Δ^3carene, and sabinene, respectively. In their calculations, *Docherty et al (2005)* assumed an average organic peroxide molar mass of 300 g mol^{-1}. If we were to use this value with our data, we would get a similarly high organic peroxide yield, in excess of 30%. We believe that expressing the peroxide fraction from Eq. (2.11) is more practical as it does not have to rely on the assumed molecular weight of a representative SOA species, and it accounts for the polyfunctional nature of SOA compounds.

2.5. Summary

Results of this HR-MS study are consistent with the following qualitative picture of SOA formation in the isoprene/O$_3$ system. During the initial stages of oxidation, ozone reacts with isoprene via established gas-phase reaction pathways producing a number of low-molecular weight products, including formaldehyde, formic acid, methylglyoxal, MAC, MVK, MAA, etc. As these first-generation products build up in the reaction chamber they undergo further oxidation or react with Criegee intermediates. This leads to the appearance of second-generation products that are subsequently partitioned into the particle phase. The second-generation products can grow further by gas-to-particle reactive uptake of the first-generation products, especially small aldehydes and carboxylic acids.

Multiple clues about the chemistry leading to SOA formation are encoded in the distribution of the molecular formulas from SOA species; this is the sort of information that high-resolution mass spectrometry can provide directly. For example, the large values of double bond equivalency factors (DBE) shown in Figure 2.4 are indicative of the prevalence of carbonyl and carboxyl functionalities in the SOA species. Observation of SOA species with positive aromaticity index values (Figures 2.5 and 2.6) indicates that a small fraction (~10%) of the products still retain unsaturated C=C bonds. The increase in the average value of DBE with the

number of carbon atoms in the molecular skeleton (Figure 2.7) reveals that the most common building blocks for the SOA oligomers contain 1-2 carbon atoms. The prominence of the CH_2O Kendrick base (Figure 2.6) suggests an efficient gas-to-particle reactive uptake of formaldehyde by the SOA species. The direct observation of a number of highly volatile species in the mass spectra of the SOA extracts (Table 2.1) suggests that this uptake is at least partly reversible. Finally, the values of the elemental and mass ratios are consistent with highly oxidized SOA species, with an estimated average O/C ratio of about 0.6 (Table 2.2) and maximal O/C ratio exceeding 1 for some of the molecules (Figure 2.4). These results clearly demonstrate that the isoprene/O_3 SOA is a complicated and dynamic mixture of highly oxygenated organic compounds.

Chapter 3: Composition of Isoprene Photooxidation SOA Generated in Low- and High-NOx Environments

3.1. Abstract

High-resolution electrospray ionization mass spectrometry (HR-ESI -MS) was used to probe molecular structures of oligomers in SOA generated in laboratory experiments on isoprene photooxidation at low- and high-NOx conditions. Up to 80-90% of the observed products are oligomers and up to 33% by number are nitrogen-containing organic compounds (NOC). We observe oligomers with up to 8 monomer units in length. Tandem mass spectrometry (MS^n) confirms NOC compounds are organic nitrates and elucidates plausible chemical building blocks contributing to oligomer formation. Most organic nitrates are comprised of methylglyceric acid units. Other important multifunctional C_2-C_5 monomer units are identified including methylglyoxal, hydroxyacetone, hydroxyacetic acid, glycolaldehyde, and 2-methyltetrols. The majority of the NOC oligomers contain only one nitrate moiety resulting in a low average N/C ratio of 0.019. Average O/C ratios of the detected SOA compounds are 0.54 under the low-NOx conditions and 0.83 under the high-NOx conditions. Our results underscore the importance of isoprene photooxidation as a source of NOC in organic particulate matter.

3.2. Introduction

Photooxidation of isoprene produces low-volatility compounds that end up in SOA, including tracer molecules 2-methylglyceric acid (2MGA) and 2-methyltetrols [24, 36, 41, 43, 186, 187]. Oligomer formation by particle-phase accretion reactions is significant in isoprene SOA [158, 188]. The initial concentrations of nitrogen oxides (NO+NO$_2$ = NOx) in chamber photooxidation experiments affects the semivolatile and nonvolatile products produced from isoprene and, therefore, the yield and composition of the SOA [36]. Under high-NOx conditions, relevant to urban environments, the chemistry of alkylperoxy radicals (RO$_2$) is controlled by the RO$_2$ + NO $\rightarrow$ RO + NO$_2$ reaction, and favors production of carbonyl compounds in the gas phase [21]. Furthermore, under high-NOx conditions, the yield of gas-phase organic nitrates from isoprene is significant, in the range of 8-13% [30, 189, 190]. As these organic nitrates are expected to be large (C$_4$-C$_5$) and bifunctional [191], they can enter the particle phase through gas/particle partitioning, reactive uptake, and oligomerization. In contrast, under low-NOx conditions, relevant to more pristine environments like the Amazon basin, the RO$_2$ + HO$_2$ $\rightarrow$ ROOH + O$_2$ reaction becomes the dominant fate of RO$_2$ radicals, and organic nitrates are expected to have negligible yields. Figure 1.1 in Section 1.1.2 shows the major expected products from both low- and high-NOx photooxidation.

The SOA yield from the photooxidation of isoprene has been extensively investigated in laboratory chamber studies over a broad range of NOx concentrations [18]. However, the particle-phase composition has not been studied in detail until the work of *Surratt et al (2006)* [36]. That study identified ~ 22-34% of the high-NOx aerosol mass as oligomers and suggested 2MGA to be a key monomer unit forming oligomers by esterification reactions. (Herein, we use the term oligomers and high-MW compounds interchangeably for constituents of isoprene SOA

with molecular weights in excess of 200 g/mol, which corresponds to at least two monomeric products bound together.) Gas chromatography ion-trap MS studies by *Szmigielski et al (2007)* confirmed that 2MGA is a prominent oligomer building block [37]. In addition, the nitrogen-containing organic compounds (NOC) in isoprene SOA formed under high-NOx were shown to be organic mono-nitrates. A recent study of the photooxidation of methacrolein (MAC) further confirmed 2MGA as a key monomer in SOA oligomerization reactions [40]. The overall conclusion from these studies is that more acidic products are formed under high-NOx conditions with a greater contribution from dihydroxyacids like 2MGA. However, a large fraction of the oligomeric compounds remains uncharacterized because the highly diverse nature of oligomer building blocks in isoprene SOA complicates the molecular level analysis of SOA.

In this work, we use HR-MS to overcome this limitation and provide additional insights into the compositional differences, which control the physical and chemical properties of SOA formed under the high- and low-NOx oxidation regimes. An emphasis is placed on the organic nitrate fraction (both mono- and poly-nitrates), comparing the atomic elemental ratios (H/C, O/C and N/C ratios) of the detected SOA compounds, and studying a large pool of oligomer building blocks in low-NOx and high-NOx SOA generated from the photooxidation of isoprene.

3.3. Experimental

Photooxidation of isoprene was performed in the UCI Chamber under dry (RH < 2%) conditions, as described by Section 1.3.1. In all experiments, the starting mixing ratios of isoprene and H_2O_2 were 250 ppb and 2 ppm, respectively. For high-NOx experiments, the initial mixing ratios of NO and NO_2 were 600 ppb and 100 ppb, respectively. For low-NOx experiments, the initial mixing ratios of NO and NO_2 were < 1 ppb and < 3 ppb, respectively.

Figure 3.1 shows that in the high-NOx oxidation, NO decreased to zero after approximately 40 minutes and in the low-NOx oxidation, NO decreased to zero quickly and remained at zero for throughout the oxidation period. After the concentrations of all reagents stabilized the UV lamps were turned on to initiate the photochemistry. The photooxidation time was two hours.
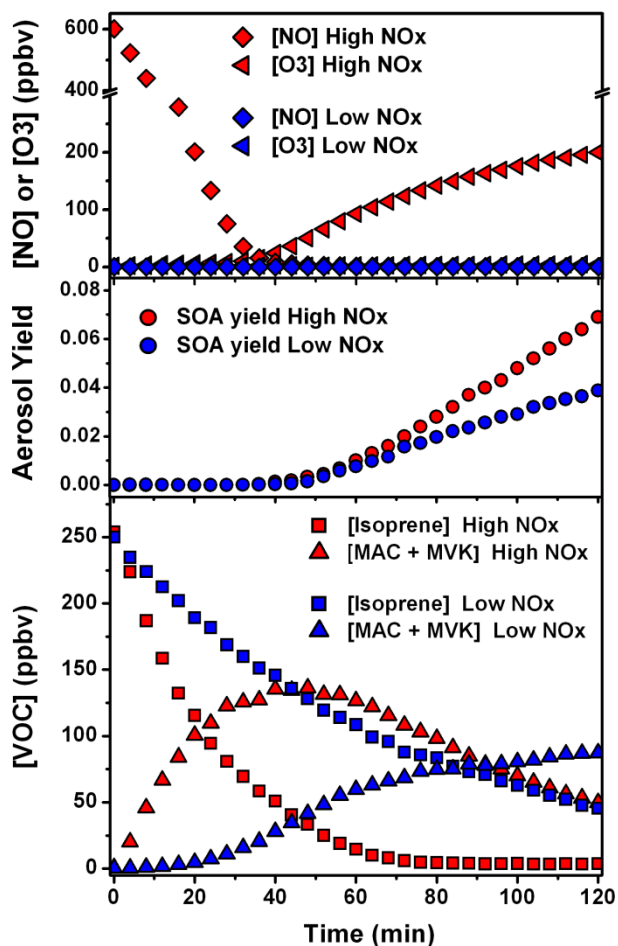
Figure 3.1: Representative time dependences of difference species in the chamber under high- and low-NOx conditions. Photooxidation starts at t=0. (a) Nitric oxide and ozone; (b) the time-dependent SOA yield; (c) PTR-ToF-MS measurements of isoprene and its first-generation products methacrolein (MAC) and methylvinylketone (MVK), observed as isobaric species.

PTR-ToF-MS was used to follow the decay of isoprene and the production of the first-generation photooxidation products MAC and methylvinylketone (MVK). The PTR-ToF-MS

was operated with a resolving power (ratio of the peak position to its full width at half maximum) of around 1,500 at *m/z* 69 (the nominal mass of the protonated isoprene). The difference in SOA yield, production of VOC and decay of isoprene observed using PTR-ToF-MS is in good agreement with previous accounts of isoprene gas-phase oxidation and are shown in Figures 3.1. The initial OH concentration was estimated from the decay rate of isoprene, and it was 2×10^7 and 4×10^7 molec cm^{-3} under the low-NOx and high-NOx conditions, respectively. The OH concentration was higher in the high-NOx photooxidation due to OH recycling from NO + HO$_2$ → OH + NO$_2$ reaction [21].

The first panel in Figure 3.1 shows the time-dependence of NO, O$_3$, SOA yield, and selected VOC mixing ratios in the chamber. The higher OH concentration at high-NOx conditions leads to a faster decay of isoprene and its first-generation products resulting in correspondingly higher SOA yields. Based on the PTR-ToF-MS time profile of the reactions, we expect a higher contribution of second-generation oxidation products in the high-NOx oxidation SOA. In the high-NOx reaction, the concentration of O$_3$ starts to build up after a large fraction of isoprene is consumed. Based on the reaction rates of the first generation products, e.g. MVK with O$_3$ [192] and OH [193], and the estimated concentrations of OH and O$_3$ in our chamber, the maximum contribution of O$_3$-oxidation chemistry to the total product formation is *ca.* 10%. From structure-based volatility estimations [194], the O$_3$ + isoprene products are expected to be more volatile than OH + isoprene products. Therefore, the contribution of O$_3$ + isoprene to the particle-phase fraction is predicted to be minor under the present experimental conditions.

The SOA loadings after two hours of reaction were 20 and 40 μg/m^3, under the low-NOx and high-NOx conditions, respectively. Aerosols were collected onto Teflon filter substrates (Millipore 0.2 μm pore size) using MOUDI operated at 30 standard liters per minute. The

collection lasted for 3 hours, which allowed oligomerization reactions to occur in the dark. Blank samples were generated under the same experimental conditions, but in the absence of the UV radiation.

SOA samples were extracted with 10 minutes sonication in a mixture (1:1 v/v) of acetonitrile and water (both Acros Organics, HPLC grade) at a concentration of *ca.*100 µg/mL before analysis with HR-ESI-MS as outlined in Section 1.3.3. The mass spectrometer was operated in the negative ion mode to optimize detection of organic nitrates. Analyte molecules are detected as [M-H]$^-$ in the mass range of *m/z* 50-2000. The spray voltage was 4 kV and the solvent flow rate was 0.5 µL/min. Data analysis on all samples was performed as described in Section 1.3.4. All mass spectra were processed to exclude peaks present in the spectra obtained from blank experiments. The peaks were assigned elemental formulas $C_cH_hO_oN_n$. Because deprotonation was assumed to be the major ionization mechanism, formulas of neutral SOA compounds were obtained by adding one hydrogen atom to the ionic formulas. Typically >1,000 distinct peaks were detected in the SOA samples and 60-70% peaks were unambiguously assigned to a molecular formula. The unassigned peaks were low in ion abundance with the signal-to-noise < 1% of the main peak.

3.4. Results and discussion

3.4.1. Mass spectra and elemental ratios

Figures 3.2a and 3.2b show characteristic HR negative ion mode ESI mass spectra for isoprene photooxidation SOA, with NOC peaks marked in red. Approximately 700 compounds were assigned for the low-NOx sample and 900 compounds were assigned for the high-NOx sample. 80-90% of detected peaks corresponded to high-MW compounds (> 200 Da). We detect

a higher contribution from oligomers in our work compared to the work of *Surratt et al (2006)*. In our work, oligomers are ionized with higher efficiency and may be overestimated. In contrast, in the work of *Surratt et al (2006)*, higher-MW oligomers may hydrolyze or otherwise decompose in the chromatographic separation. Therefore, one should consider the 80-90% value reported in our study as upper bounds and the 22-34% value reported in the *Surratt et al (2006)* study as lower bounds.
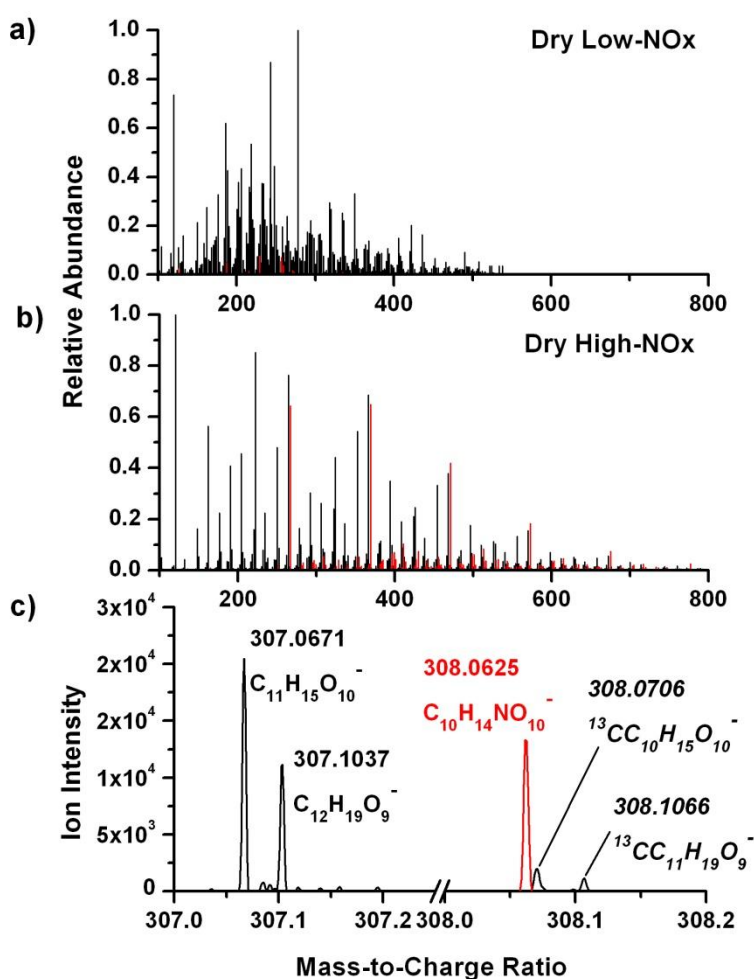
Figure 3.2: Representative high-resolution (-) ESI mass spectra of SOA obtained from photooxidation of isoprene under dry conditions in the (a) low- and (b) high-NOx experiments. NOC peaks are shown in red. Panel (c) is a magnified view of the high-NOx mass spectrum, illustrating the unambiguous resolution of peaks belonging to nitrogen-containing molecules and those of ^{13}C satellites around *m/z* 308.

Spectra of SOA generated under two NOx conditions are clearly different. In the low-NOx sample, the mass range of observed molecules is approximately *m/z* 80-600, consistent with MALDI-MS observations of *Surratt et al (2006)*, and the spectrum is dominated by dimer and trimer peaks clustered around *m/z* 200. Peaks with even nominal masses have relatively small intensities suggesting that most ions have no nitrogen atoms in them. The corresponding carbon numbers of the compounds range from C_2 to C_{29}.
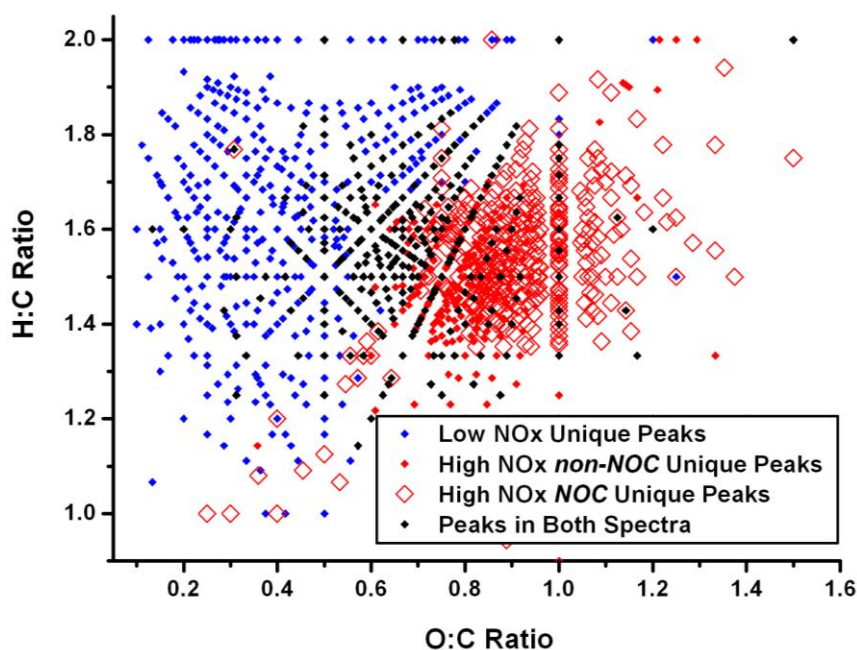
Figure 3.3: Van Krevelen diagram of SOA obtained from photooxidation of isoprene. Peaks corresponding to NOC observed in the high-NOx spectra are shown with open blue markers. Filled markers correspond to Nitrogen-free products observed either uniquely under low-NOx (blue) and high-NOx (red) conditions or under both conditions (black). Average elemental ratios were determined as: O/C = 0.54, H/C = 1.61, N/C < 0.002 for low-NOx SOA, and O/C = 0.83, H/C = 1.55, N/C = 0.019 for high-NOx SOA.

In contrast, the high-NOx mass spectrum spans a wider range of masses indicating more extensive oligomerization under these conditions. The mass range of observed molecules is *m/z* 80-900, consistent with ESI-MS observations of *Surratt et al (2006),* with corresponding carbon

numbers of C_2-C_{35}. A number of abundant peaks in the spectrum have even nominal masses characteristic of molecules containing an odd number of nitrogen atoms. The mass resolving power of the Orbitrap is sufficient to resolve the NOC peaks from the ^{13}C satellite peaks at the same nominal mass (Fig. 3.2c). The mass difference between ^{13}C and N is 0.008 Da, and the peak width at half maximum is 0.005 Da at m/z 300. Even though the NOC and ^{13}C peaks start to merge above m/z 500, we can still confidently assign the NOC peaks in cases when the peak intensities exceed those predicted from the natural abundance of ^{13}C.

Figure 3.3 shows the graphical representation of the degree of alkylation and oxidation of the isoprene SOA formed in the low-NOx vs. high-NOx samples in the form of a Van Krevelen (VK) diagram [101, 146], where the H/C ratios of the individual SOA compounds are plotted against the O/C ratios. Elemental ratios shown in Figure 3.3 are those of individual molecules that were assigned based on HR-MS analysis. Each coordinate on the VK diagram may represent more than one molecule due to graphical overlap. The low-NOx and high-NOx data were separated into three categories: peaks observed in both data sets, peaks observed uniquely in the low-NOx data, and peaks observed uniquely in the high-NOx data. Compounds observed under both conditions span a broad range of the O/C and H/C ratios. In contrast, the elemental ratios of compounds unique to the low-NOx SOA sample are clustered around the low O/C ratio region and those of the high-NOx SOA compounds tend to have higher O/C values. The intensity-weighted average O/C ratios of the detectable compounds, calculated in an identical manner to our previous work [79], are 0.54 and 0.83 under low-NOx and high-NOx conditions, respectively. The higher average O/C in the high-NOx experiments is attributed to more extensive oxidation in the gas-phase (the OH concentrations are higher by at least a factor of two compared to the low-NOx experiments) and higher incorporation of organic nitrates, as we will

discuss in Section 3.4.2. Each $-ONO_2$ group contributes 3 oxygen atoms to the molecular formula, thus resulting in higher O/C values.

It is useful to compare the O/C ratios determined in this work with the existing field and laboratory measurements reported by aerosol mass spectrometry (AMS) methods [195]. One caveat in making such comparisons is bias towards preferential detection of oxygenated organic and organic nitrate species in the ESI negative ion mode, which may lead to an overestimation of the actual O/C value. However, the disparity of O/C values obtained in positive vs. negative ion mode ESI is not expected to be large, for example, the O/C values measured for ozone-isoprene SOA in the positive and negative ion mode ESI [79] were 0.61 and 0.63, respectively. The O/C and N/C ratios quantified by AMS are affected by the opposite problem: they may underestimate the true values [196, 197]. Despite these limitations, the low-NOx O/C ratio of 0.54 obtained in this study compares favorably to the AMS O/C values of 0.41-0.77 measured in chamber studies [196] and 0.39-0.45 measured in low-sulfate aerosol particles in the Amazon basin [198]. The lower O/C ratio obtained in the field experiments may be attributed to the contribution from monoterpenes. For example, the average O/C values are lower for alpha-pinene/O_3 and photooxidation SOA (0.29-0.45) [199-201] and for limonene/O_3 SOA (0.43-0.50) [53, 54].

The O/C ratio of the high-NOx SOA may be compared to those from aerosols sampled in forested sites affected by urban NOx emissions, e.g. Whistler Mountain, Canada, which is close to major highways. The high-NO_x O/C value of 0.83 obtained in this study compares well with the O/C range of 0.43-0.81 obtained in chamber studies [196] and value of 0.83 measured on the Whistler Mountains in Canada [202 2562]. A comparison to a predominantly urban site can also be made; however, this comparison is more ambiguous because of the presence of multiple SOA precursors and contributions from primary aerosols. Nevertheless, the O/C value of 0.83 falls in

between that of urban "fresh" organic aerosol (OA) (0.52–0.64) and urban "aged" OA (0.8 - 1.02) [203] measured in Mexico City.

3.4.2. Nitrogen-containing organic compounds in the aerosol phase
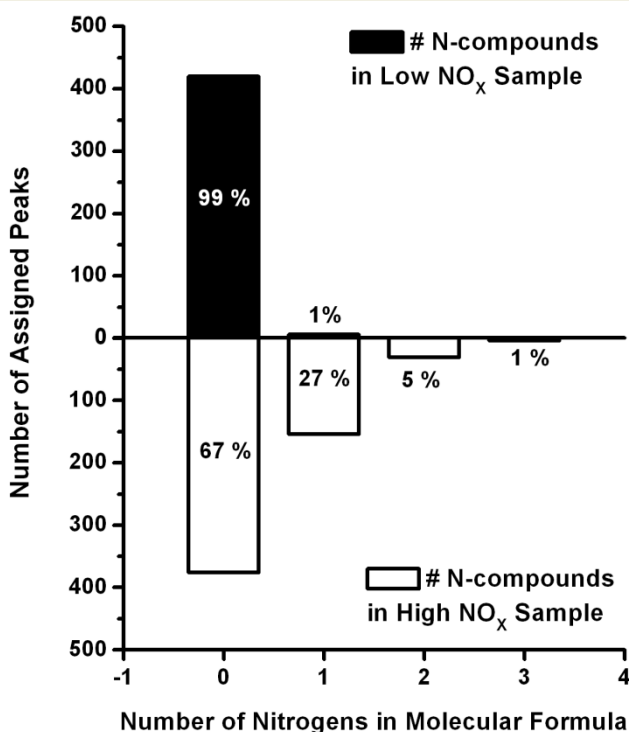
Figure 3.4: The distribution of NOC compounds in SOA generated from the low- and high-NOx photooxidation of isoprene. Most particle-phase compounds do not contain nitrogen even when generated under high initial NOx concentrations; however, a significant fraction of high-NOx SOA molecules contain one (27%), two (5%), and three (1%) nitrogen atoms.

A significant fraction of SOA compounds formed under high-NOx conditions are NOC species. Figure 3.4 shows the distribution of assigned molecules containing zero-, one-, two- and three-nitrogen atoms. Approximately 33% (by count) of all peaks in the high-NOx mass spectrum are assigned to NOC, with 27% containing one, 5% containing two, and less than 1% containing three nitrogen atoms. In the high-NOx sample, the smallest NOC molecule detected by (-) ESI-MS was the nitrate ester of 2-methylglyceric acid (2MGA nitrate, henceforth). In

70

contrast, only 1% of peaks are assigned to NOC in the low-NOx samples; they likely result from the reactions of the residual NO (< 1 ppb).
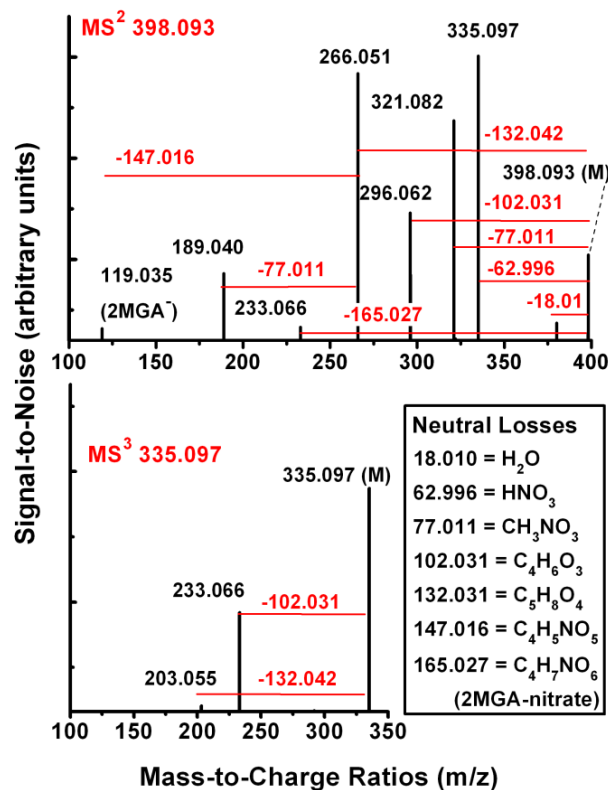
Figure 3.5: Representative MS^2 spectrum of m/z 398.093 ($C_{13}H_{20}NO_{13}^-$) and MS^3 spectrum of its largest ionic fragment m/z 335.097 ($C_{13}H_{19}O_{10}^-$). Neutral loss masses are shown in red. The corresponding neutral fragment formulas shown in the legend are the most abundant neutral losses observed in CID of all oligomeric NOC studied in this work. These data are also shown in tabular form in Table 3.1.

Figure 3.5 and Table 3.1 show the high resolution MS^n data for select NOC observed in this work. A distinct CID (collision induced dissociation) pattern confirms the identity of NOC in high-NOx isoprene SOA as hydroxy organic nitrates based on the even-electron losses of 62.996 Da (HNO_3) and 77.011 Da (CH_3NO_3) [36]. This fragmentation pattern is shown for a representative molecular ion $C_{13}H_{20}NO_{13}^-$ in figure 3.6. Most of the organic nitrates are derived

Table 3.1: MS^2 and MS^3 tables of select NOC oligomers. MS^2 product ions (a,b,c, etc.) are observed after CID of the parent ion (M). MS^3 ions (I, II, III, etc.) are the CID products of selected high-abundance MS^2 ions. Relative abundances are normalized to the most abundant ion observed within a certain level of CID. Losses are observed as neutral molecules. HNO_3 and CH_3NO_3 losses are characteristic of organic nitrates.

MS^2	m/z = 266.051 (M)		Ionic Product		Abundance	Neutral Fragment	
	$C_8H_{12}NO_9^-$		m/z	Formula	(%)	Mass	Formula
		a	189.040	$C_7H_9O_6$	100.0	M - 77.011	CH_3NO_3
		b	119.035	$C_4H_7O_4$	2.9	M - 147.016	$C_4H_5NO_5$
		c	164.020	$C_4H_6NO_6$	1.2	M - 102.031	$C_4H_6O_3$
		d	203.056	$C_8H_{11}O_6$	1.0	M - 62.995	HNO_3
MS^3	m/z = 189.040 (a)	I	87.009	$C_3H_3O_3$	100.0	102.031	$C_4H_6O_3$

MS^2	m/z = 368.083 (M)		Ionic	Product	Abundance	Neutral	Product
	$C_{12}H_{18}NO_{12}^-$		m/z	Formula	(%)	Mass	Formula
		a	291.072	$C_{11}H_{15}O_9$	100.0	M-77.012	CH_3NO_3
		b	305.088	$C_{12}H_{17}O_9$	99.6	M-62.996	HNO_3
		c	266.051	$C_8H_{12}NO_9$	55.2	M-102.032	$C_4H_6O_3$
		d	292.079	$C_{11}H_{16}O_9$	14.2	M-76.004	CH_2NO_3
MS^3	m/z = 291.072 (a)	I	159.066	$C_7H_{11}O_4$	100.0	a - 132.006	$C_4H_4O_5$
	$C_{11}H_{15}O_9^-$	II	119.035	$C_4H_7O_4$	97.0	a - 172.037	$C_7H_8O_5$
		III	189.040	$C_7H_9O_6$	39.6	a - 102.032	$C_4H_6O_3$
		IV	203.056	$C_8H_{11}O_6$	35.2	a - 88.016	$C_3H_4O_3$
		V	192.027	$C_6H_8O_7$	20.1	a - 99.045	$C_5H_7O_2$
MS^3	m/z = 305.088 (b)	I	203.056	$C_8H_{11}O_6$	100.0	b - 102.032	$C_4H_6O_3$
	$C_{12}H_{17}O_9^-$	II	101.024	$C_4H_5O_3$	12.6	I - 102.032	$C_4H_6O_3$
MS^4	m/z = 189.040 (aIII)	a	87.009	$C_3H_3O_3$	100.0	c - 102.032	$C_4H_6O_3$
	$C_7H_9O_6^-$						
MS^2	m/z = 398.093 (M)		Ionic	Product	Abundance	Neutral	Product
	$C_{13}H_{20}NO_{13}^-$		m/z	Formula	(%)	Mass	Formula
		a	335.097	$C_{13}H_{19}O_{10}$	100.0	M-62.996	HNO_3
		b	266.051	$C_8H_{12}NO_9$	95.5	M-132.042	$C_5H_8O_4$
		c	321.082	$C_{12}H_{17}O_{10}$	78.7	M-77.011	CH_3NO_3
		d	296.062	$C_9H_{14}NO_{10}$	48.4	M-102.031	$C_4H_6O_3$
		e	189.040	$C_7H_9O_6$	28.5	b - 77.011	CH_3NO_3
		f	380.083	$C_9H_{18}NO_{12}$	12.3	M-18.010	H_2O
		g	233.066	$C_9H_{13}O_7$	10.9	M-165.027	$C_4H_7NO_6$

			Ionic m/z	Product Formula	Abundance (%)	Neutral Mass	Product Formula
	h		119.035	$C_4H_7O_4$	9.6	b - 147.016	$C_4H_5NO_5$
MS^3 m/z = 335.097 (a)		I	233.066	$C_9H_{13}O_7$	100.0	a - 102.031	$C_4H_6O_3$
$C_{13}H_{19}O_{10}^-$		II	203.055	$C_7H_9O_6$	22.2	a - 132.042	$C_5H_8O_4$
MS^3 m/z = 266.051 (b)		I	189.040	$C_7H_9O_6$	100.0	b - 77.011	CH_3NO_3
$C_8H_{12}NO_9^-$							

MS^2 m/z = 400.109 (M)		Ionic m/z	Product Formula	Abundance (%)	Neutral Mass	Product Formula
$C_{13}H_{22}NO_{13}^-$						
	a	298.077	$C_9H_{16}NO_{10}$	100.0	M - 102.032	$C_4H_6O_3$
	b	337.113	$C_{13}H_{21}O_{10}$	94.9	M - 62.996	HNO_3
	c	263.077	$C_{10}H_{15}O_8$	73.5	M – 137.032	$C_3H_6O_2$
	d	161.045	$C_6H_9O_5$	28.3	c - 102.032	$C_4H_6O_3$
	e	323.098	$C_{12}H_{19}O_{10}$	15.2	M - 77.011	CH_3NO_3
	g	119.035	$C_4H_7O_4$	13.7	c - 144.042	$C_6H_8O_4$
MS^3 m/z = 298.077 (a) I		235.082	$C_9H_{15}O_7$	100.0	a - 62.996	HNO_3
$C_9H_{16}NO_{10}^-$						

MS^2 m/z = 410.0935 (M)		Ionic m/z	Product Formula	Abundance (%)	Neutral Mass	Product Formula
$C_{14}H_{20}NO_{13}^-$						
	a	308.062	$C_{10}H_{14}NO_{10}$	100.0	M - 102.032	$C_4H_6O_3$
	b	347.098	$C_{14}H_{19}O_{10}$	31.2	M - 62.996	HNO_3
	c	307.067	$C_{11}H_{15}O_{10}$	14.8	M - 103.027	$C_3H_5NO_3$
	d	333.082	$C_{13}H_{17}O_{10}$	11.0	M - 77.011	CH_3NO_3

MS^2 m/z = 470.115 (M)		Ionic m/z	Product Formula	Abundance (%)	Neutral Mass	Product Formula
$C_{16}H_{24}NO_{15}^-$						
	a	393.104	$C_{15}H_{21}O_{12}$	100.0	M - 77.011	CH_3NO_3
	b	368.083	$C_{12}H_{16}NO_{12}$	9.7	M - 102.032	$C_4H_6O_3$
	c	407.119	$C_{16}H_{23}O_{12}$	8.3	M - 62.996	HNO_3
MS^3 m/z = 393.104 (a)	I	291.072	$C_{11}H_{15}O_9$	100.0	a - 102.032	$C_4H_6O_3$
$C_{15}H_{21}O_{12}^-$	II	221.067	$C_8H_{13}O_7$	50.0	a - 172.037	$C_7H_8O_5$
	III	189.041	$C_7H_9O_6$	35.3	II- 32.026	CH_3OH
	IV	273.061	$C_{11}H_{13}O_8$	8.7	I - 18.011	H_2O
	V	305.088	$C_{12}H_{17}O_9$	7.0	a - 88.016	$C_3H_4O_3$
	VI	261.098	$C_{11}H_{17}O_7$	5.8	V - 43.990	CO_2

73

from 2MGA oligomer esters, consistent with previous observations [36, 40, 204]. However, notably, a neutral fragment corresponding to the dehydrated nitrate ester of a 2-methyltetrol ($C_5H_{11}NO_6$) was also inferred from the CID spectra as a loss of 163.047 Da ($C_5H_9NO_5$). This CID pattern suggests that 2-methyltetrol nitrates are produced in the high-NOx photooxidation and are incorporated into the SOA constituents through oligomerization. Different fragmentation patterns would be observed if the NOC compounds contained nitro groups (-NO_2), nitrites (-ONO), aliphatic amines (-NH-), imines (=N-) or N-heterocyclic compounds [205-207].

In addition to the losses of N-containing fragments, the most common neutral loss fragment for all NOC oligomers observed in MS^n experiments is 102.032 Da ($C_4H_6O_3$). Based on the present observation of product ions and previous work by *Surratt et al (2006)*, the $C_4H_6O_3$ neutral loss is used as a signature of 2MGA-based esters. However, it is important to note that $C_4H_6O_3$ is not unique to either isoprene SOA oligomers or to aliphatic esters in general. $C_4H_6O_3$ fragment has been also observed in the MS^n spectra of fused sugar rings [208-212] that have little in common with the 2MGA oligomerization products. The MS^n ions produced from CID of the selected peaks are listed in Table 3.1; examples include *m/z* 119.035 Da ($C_4H_7O_4^-$, deprotonated 2MGA), 189.040 Da ($C_7H_9O_6^-$, deprotonated 2MGA+ pyruvic acid), and 164.0198 Da ($C_4H_6NO_6^-$, deprotonated 2MGA nitrate).

The incorporation of -ONO_2 groups in 33% of the compounds contributes to the relatively high O/C ratio in the high-NOx data (Fig. 3.3). The majority of the NOC have more than 10 C-atoms, but even large (C > 20) compounds have just one nitrate group. As a result, the intensity-weighted average N/C ratio in high-NOx SOA is relatively low (0.019). This value is comparable to the N/C ratio of ambient OA measured by AMS both in Mexico City (~ 0.02)

[203] - a site dominated by urban OA, and on Whistler Mountain, Canada (~0.03) [202] - a site affected by both biogenic and anthropogenic emissions.

In the atmosphere, the NOC fraction in $PM_{2.5}$ is significant [213, 214, 215]. More than 20% of the particulate mass observed in Atlanta, Georgia, a site with high isoprene mixing ratios, is attributed to organic nitrates based on single particle mass spectrometry [216]. Our results underscore the importance of isoprene photooxidation as a source of atmospheric NOC. The mixing ratio of isoprene in an urban atmosphere can range from 2 ppb [217] to 6 ppb [218]. An SOA mass yield of 3% from the photooxidation of isoprene [219, 220] will produce an estimated $0.08 - 0.25$ $\mu g/m^3$ aerosol mass. Therefore, a 33% organic nitrate yield from our work, applied to the $0.08 - 0.25$ $\mu g/m^3$ aerosol mass estimated from isoprene, corresponds to $0.03 - 0.08$ $\mu g/m^3$ of particulate organic nitrates in the atmosphere. For comparison, the total airborne particulate organic nitrate mass measured in the afternoon in Pasadena, CA is 0.12 $\mu g/m^3$[221]. The above estimation suggests that a substantial fraction (30-70%) of these nitrates may come from isoprene. We note, however, that the contribution of isoprene loading in Pasadena, CA is much less than anthropogenic VOC loading.

3.4.3. Oligomer building blocks

A unique aspect of (-) ESI-MS is the soft ionization of very large oligomers. MS^n studies (Section 3.4.2) verified that these oligomers are real molecules, opposed to ionic clusters formed in ESI, due to the high (>10 units) CID threshold energy necessary for fragmentation. Oligomer esters of 2MGA [36, 37, 40] appear in the mass spectra as families of peaks differing in mass units of 102.032 Da ($C_4H_6O_3$ - dehydrated 2MGA). The long homologous chemical families found in isoprene SOA are best showcased with a Kendrick analysis [79, 100, 222], where the masses of the observed compounds are renormalized from a ^{12}C-based mass adopted by the

IUPAC system to another base commonly repeated in the mass spectra, e.g. by setting the mass of $C_4H_6O_3$ to the integer value of 102 Da. The renormalized masses are now termed the $C_4H_6O_3$ Kendrick mass (KM) and the difference between the KM and the nominal mass is termed the Kendrick mass defect (KMD). Homologous series of peaks differing in one $C_4H_6O_3$ unit, arising from repetitive incorporation of the monomer 2MGA will have identical values of KMD. An assignment of any member in the series is sufficient for assigning molecular formulas to the remaining homologous peaks.
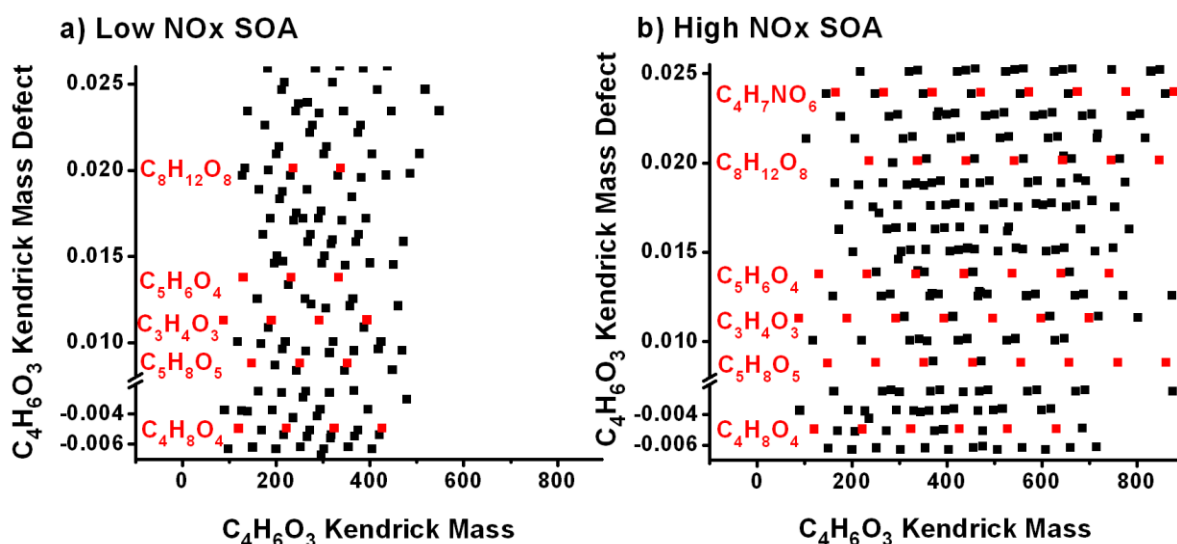
Figure 3.6: Magnified view of the $C_4H_6O_3$ Kendrick diagram for SOA obtained from photooxidation of isoprene under (a) low NOx and (b) high NOx conditions. Homologous series differing in repetitive $C_4H_6O_3$ units fall on the same horizontal lines with identical Kendrick mass defects. Selected families are shown in red to highlight especially long homologous series of 2MGA esters.

Figure 3.6 shows a $C_4H_6O_3$-based Kendrick diagram of isoprene SOA formed under high- and low-NOx conditions. Based on the KMD analysis, important molecules that produce long oligomer ester series with 2MGA are: $C_3H_4O_3$ (pyruvic acid), $C_4H_8O_3$, $C_4H_8O_4$ (2MGA), $C_4H_7NO_6$ (2MGA nitrate), $C_5H_6O_4$, $C_5H_8O_5$, $C_6H_{10}O_5$, and $C_8H_{12}O_8$ (likely a hemiacetal dimer of

2MGA). The lines shown in red correspond to the longest observed homologous series, including the 2MGA nitrates ($C_4H_7NO_6+$ ($C_4H_6O_3)_{[0-3]}$) reported by *Surratt et al (2006)* for high-NOx SOA. Some of the observed NOC oligomers include up to 8 units of $C_4H_6O_3$ in high-NOx SOA. In combination, the 2MGA-based NOC oligomers contribute significantly to the overall signal (~7% in abundance). In comparison, the contribution of the most prominent non-NOC family of 2MGA oligomer esters ($C_4H_8O_4+$ ($C_4H_6O_3)_{[0-6]}$) is about ~5%. Figure 3.6 also illustrates that the lengths of both NOC and nitrogen free oligomer series are shorter in low-NOx SOA. For example, for the $C_5H_8O_5+$ ($C_4H_6O_3)_n$ series, n ranged up to 7 and the oligomers with n=2,3 were the most abundant in the high-NOx mass spectra. For the same series in the low-NOx case, the oligomers with n=0, 1 were the most abundant, and the longest observed oligomer corresponded to n=2.

We performed a mass difference analysis to sift through the distributions of peaks and identify oligomeric units of primary importance in SOA growth reactions. In Chapter 4, we demonstrate that isoprene photooxidation SOA generated under two RH conditions had different prevailing mass differences in the spectra: under dry conditions, 102.032 Da ($C_4H_6O_3$) was the most prominent mass difference from the prevalence of 2MGA oligomer esters, and under humid conditions 15.995 Da (O-atom) was the most prominent mass difference [39, 223], which is consistent with *Zhang et al (2011)* [223]. Because we are interested in multifunctional oligomer building units, we limit our mass difference analysis in this study to units containing at least 2 carbon atoms. We have examined all bases of the type $C_{(2-10)}H_{(2-20)}O_{(0-10)}$ using both the mass difference analysis (to find the most common mass differences) and Kendrick analysis (to identify long chemical families).

Table 3.2: Three most abundant repeating units in isoprene photooxidation SOA, ranked by the frequency of their repetition in the mass spectra. In the high-NOx case, two separate rankings are provided for the NOC and non-NOC compounds. Literature references refer to observation of these monomers amongst products of isoprene photooxidation.

High-NOx Sample

Repeating Units	Frequency	Monomer	Monomer Name	Proposed Structure	Ref.
		NOC			
$C_4H_6O_3$ and $C_4H_8O_4$	204	$C_4H_8O_4$	2-methylglyceric acid (2MGA)		[36, 40, 41]
$C_3H_4O_2$	178	$C_3H_6O_3$ or $C_3H_4O_2$	lactic acid or methylglyoxal		[131, 176, 224, 225]
C_2H_2O and $C_2H_4O_2$	174	$C_2H_4O_2$	glycolaldehyde		[226-228]
		Nitrogen free			
$C_3H_4O_2$	369	$C_3H_6O_3$ or $C_3H_4O_2$	lactic acid or methylglyoxal		[131, 176, 224, 225]
$C_4H_6O_3$ and $C_4H_8O_4$	368	$C_4H_8O_4$	2-methylglyceric acid (2MGA)		[36, 40, 41]
C_2H_4O	**350**	**$C_2H_6O_2$ or C_2H_4O**	**acetaldehyde or ethylene glycol**		**[82]**

Low-NOx Sample

Repeating Units	Frequency	Monomer	Monomer Name	Proposed Structure	Ref.
		Nitrogen free			
C_2H_4O	438	$C_2H_6O_2$ or C_2H_4O	acetaldehyde or ethylene glycol		[82]
C_2H_2O and $C_2H_4O_2$	417	$C_2H_4O_2$	glycolaldehyde		[226-228]
C_3H_4O and $C_3H_6O_2$	**404**	**$C_3H_6O_2$**	**hydroxyacetone**		**[29, 227]**
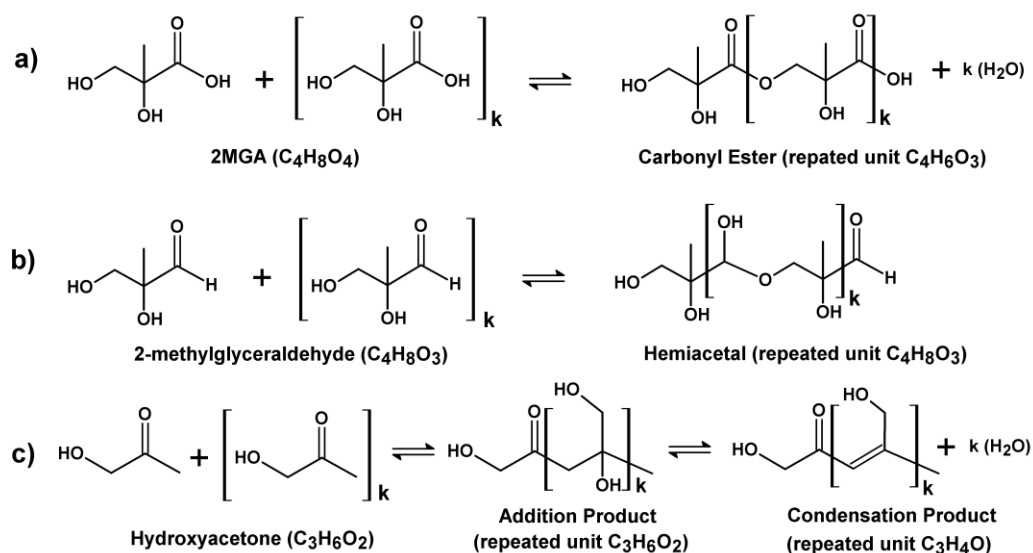
Figure 3.8: As illustrative examples, self oligomerization reactions are shown of (a) 2-methylglyceric acid (2MGA) producing carbonyl esters through condensation chemistry from repeated integration of $C_4H_6O_3$ units (b) 2-methylglyceraldehyde producing linear hemiacetals through addition chemistry from repeated integration of $C_4H_8O_3$ units and (c) hydroxyacetone producing an aldol through addition chemistry from repeated integration of $C_3H_6O_2$ units, then subsequently producing an aldol condensation product through condensation chemistry from repeated integration of C_3H_4O units.

Nitrogen was not included in the analysis for ease of comparison between the high-NOx and low-NOx data and because of the low N/C ratio for majority of SOA molecules. The resulting bases were considered as oligomer building blocks if they corresponded to an expected stable isoprene oxidation product capable of undergoing condensation or addition reactions resulting in the formation of oligomers [36, 97, 131, 168, 172, 229, 230]. Important condensation reactions include: esterification, aldol condensation, and anhydride formation, and important addition reactions include: hemiacetal formation, oxidative ring opening, and related reactions. Condensation reactions between two monomers (M and M') will produce molecular formulas of the type (M + M' - H_2O) and addition reactions will produce molecular formulas of the type (M + M'). With addition reactions, the oligomer building block and the corresponding monomer are

the same. Examples of condensation and addition reactions of repeated units to produce oligomers is shown in Figure 3.7.

The three most important oligomer building blocks and the corresponding monomers, sorted by their frequency of occurrence in the respective data, are shown in Table 3.2. The high-NOx data is divided into two NOC and nitrogen-free components. There is a significant degree of overlap between the oligomer building blocks found in each type of SOA. However, the frequencies of occurrence for the building blocks are different. The most prominent monomeric building blocks in the low-NOx sample are smaller in size than those found in the high-NOx sample. In the low-NOx sample, the top two monomers are C_2 compounds derived from aldehydes, whereas in the high-NOx sample, the top two monomers are C_3-C_4 compounds derived from organic acids. It appears that low-NOx conditions generally favor the production of aldehydes and polyols leading to the dominance of addition-type oligomerization in aerosol, and high-NOx conditions favor the production of multifunctional acids making the condensation-type chemistry more important [36].

As expected, all the monomers shown in Table 3.2 represent multifunctional compounds capable of self- or cross-oligomerization such as hydroxy carboxylic acids, keto carboxylic acids, or hydroxy carbonyls. The similarity in incorporation of oligomer building blocks between the low- and high-NOx data may be due to similar low-volatility reaction products entering and reacting with each other in the aerosol phase and common heterogeneous uptake mechanisms (like reactive uptake of methylglyoxal) [231]. Our analysis revealed several C_4-C_5 oligomer building blocks that are highly oxidized and functionalized but generally retain the carbon skeleton of isoprene. Larger monomers have low vapor pressure (e.g., the vapor pressure of 2MGA is estimated to be 4 x 10^{-5} Torr at 25° C using the group contribution method by Pankow

80

and Ascher [194]) and enter the particle-phase by physical condensation, after which, they partake in slow oligomerization reactions. It is likely that these molecules are not present in the monomeric form in particles due to their high reactivity.

Small (C_2-C_3) monomers in Table 3.2, which were observed in a number of isoprene oxidation studies as gas-phase products, are not expected to partition into the particle phase in their monomeric forms. They likely participate in oligomerization reactions through heterogeneous (surface) uptake. Heterogeneous reactions of glyoxal and methyglyoxal have been extensively investigated and their gas/particle partitioning is much greater than can be predicted based on their solubility in organic phase alone [232-235]. Methylglyoxal in particular, may contribute to organic particulate mass through reactions in weakly-acidic instead of strongly-acidic (e.g. sulfuric acid) media [231]. Our data, correspondingly, suggest that methylglyoxal is an important contributor to isoprene SOA growth.

The prevalence of the mass differences $C_2H_2O/C_2H_4O_2$, $C_2H_2O_2$, and $C_3H_6O_2$ between SOA individual constituents suggest that glycolaldehyde, hydroxyacetic acid, and hydroxyacetone, respectively, are also involved in oligomerization reactions either in the gas phase followed by gas-particle partitioning or by reactive uptake onto organic aerosols. These small carbonyl compounds are present in significant quantity in the isoprene + OH reaction [193, 236, 237]. Glycolaldehyde was also suggested by *Lim et al (2005)* to be an important cloud-processing source of SOA through aqueous uptake [238]. However, uptake experiments of several carbonyl compounds on inorganic seed particles concluded that equilibrium partitioning and acid-catalyzed uptake was not significant for methylglyoxal and hydroxyacetone [234]. The disagreement between the predictions derived from HR-MS with the observations by *Kroll et al.* [234] may be due to differences in surface reactions of these molecules on pre-existing SOA

organics vs. inorganic seed particles. In our experiments, inorganic seeds were not used and the aerosol particles were comprised entirely of organic material. Further investigation of heterogeneous reactions of methylglyoxal, glycolaldehyde, and hydroxyacetone on model aerosol surfaces is warranted because they are important isoprene photooxidation products [226, 227, 237, 239-242].

In summary, an array of molecular information, e.g., formation of complex organic nitrates, distribution of functional groups in the molecules (from MS^n studies), insights into the mechanism of oligomer formation (from repeating units), can be extracted from the HR-MS data. The average elemental composition in the form of the O/C, H/C and N/C ratios can also be extracted, and it is in good agreement with the information obtained by online methods such as AMS. However, such averaged quantities do not fully convey the heterogeneity of the molecular structures of the SOA compounds. Detailed molecular information provided by high resolution methods helps us better understand and predict the fundamental chemistry and physics of SOA , e.g., how molecules in SOA react with each other and with atmospheric radicals, how they absorb solar radiation, and how they interact with water vapor.

Chapter 4: Effect of Relative Humidity on the Composition of Isoprene High-NOx Photooxidation SOA

4.1. Abstract

The effect of relative humidity (RH) on the composition and concentrations of gas-phase products and secondary organic aerosol (SOA) generated from the photooxidation of isoprene under high-NOx conditions was investigated. The yields of most gas-phase products were the same regardless of initial water vapor concentration with exception of hydroxyacetone and glycolaldehyde, which were considerably affected by RH. A significant change was observed in the SOA composition, with many unique condensed-phase products formed under humid (90% RH) vs. dry (<2% RH) conditions, without any detectable effect on the rate and extent of the SOA mass growth. There is a 40% reduction in the number and relative abundance of distinct particle-phase nitrogen-containing organic compounds (NOC) detected by high resolution mass spectrometry. The suppression of condensation reactions, which produce water as a product, is the most important chemical effect of the increased RH. For example, the total signal from oligomeric esters of 2-methylglyceric acid was reduced by about 60% under humid conditions and the maximum oligomer chain lengths were reduced by 7-11 carbons. Oligomers formed by addition mechanisms, without direct involvement of water, also decreased at elevated RH but to a much smaller extent. The observed reduction in the extent of condensation-type oligomerization at high RH may have substantial impact on the phase characteristics and hygroscopicity of the isoprene aerosol. The reduction in the amount of organic nitrates in the particle phase has implications for understanding the budget of NOC compounds.

4.2. Introduction

Water is ubiquitous in the atmosphere, and relative humidity (RH) may affect the mechanism of SOA formation, chemical composition and physical properties of SOA [243-245]. RH controls the liquid water content (LWC) of the aerosol [246], and therefore any chemical reaction or physical process that involves water as a reactant, product, or solvent may be affected. With a typical hygroscopic growth factor of 1.1 at 85% RH for biogenic SOA [247], the particle LWC should be of the order of 30% by volume. This may be sufficient to have a substantial fraction of organic compounds partition in the aqueous phase.

Isoprene photooxidation SOA has been studied under a variety of RH conditions [18]. *Dommen et al (2006)* studied SOA yields from isoprene photooxidation generated without inorganic seeds in the RH range of 2-84% and found that high RH does not considerably change the SOA yields and gas-particle partitioning in the SOA formation process [158]. However, a recent study by *Zhang et al (2011)* found an approximately 2-fold increase in SOA yield in the dry vs. humid conditions when using ammonium sulfate seed aerosol [223]. Similarly, modeling studies predict that isoprene SOA yield is enhanced under humid conditions [248]. The disagreement between the isoprene SOA yields measured under different RH conditions in *Dommen et al (2006) vs. Zhang et al (2011)* experiments is likely due to the absence and presence of seed particles, but other factors could also contribute. The present work does not use seed particles and therefore is more comparable to the work of *Dommen et al (2006)* with respect to the RH effect on the SOA yields.

The role of RH in determining the SOA composition and yield is difficult to predict a priori as there are several types of processes that may be induced by LWC. One possible consequence of LWC is an increase in reactive uptake kinetics of volatile organic compounds

(VOC) into the aerosol phase because gas-phase carbonyls, like glyoxal and methylglyoxal, may

hydrate on particles containing adsorbed water, and subsequently polymerize into less volatile

products [131, 233, 235, 249-256]. In this case, water serves as a reactant during the hydration

stage and accelerates oligomerization of the hydrated carbonyls, leading to an increase in the

aerosol yield and increased abundance of aerosol-phase hemiacetal products. Even without

hydration, the presence of surface water may significantly alter the efficiency of reactive uptake

of VOC [257].
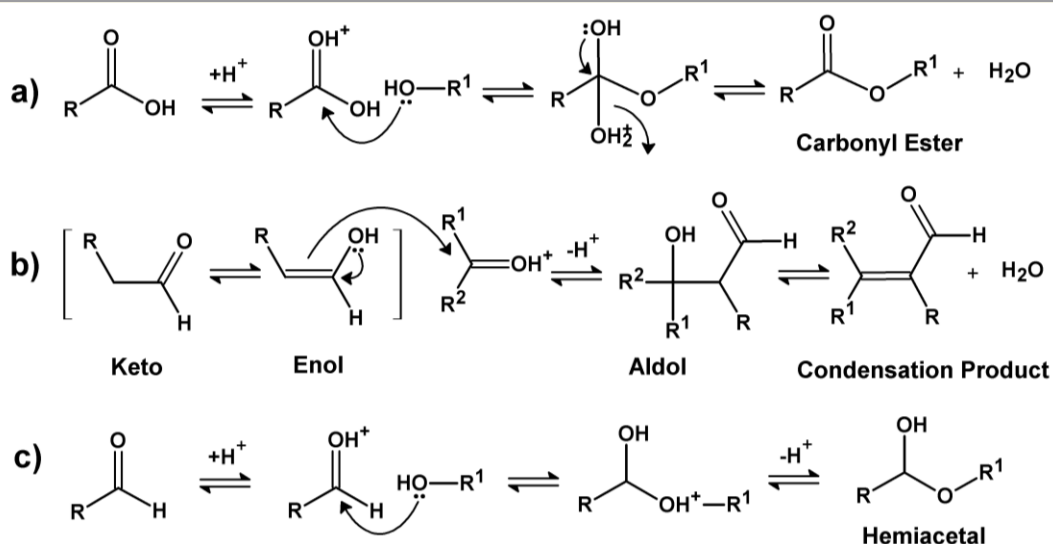
Figure 4.1: Mechanisms of acid-catalyzed oligomeric growth by (a) esterification, (b) aldol condensation and (c) hemiacetal formation. Aldol condensation involves two steps: an addition step to yield the aldol and a condensation step to yield a β-unsaturated aldehyde. The nucleophiles in reactions (a-c) may be the enol tautomers of carbonyls. Each reaction is affected by liquid water content either directly or indirectly through solvation.

Figure 4.1 shows the most common chemical equilibria involving SOA constituents

which may be affected by the increased LWC. Condensation reactions like esterification (Fig.

4.1a) and the aldol condensation (Fig. 4.1b), which produce a water molecule as reaction

product, have been shown to be important in biogenic SOA formation, especially under high-

NOx conditions [36, 37, 68, 131, 168, 258]. Addition reactions including hemiacetal formation

(Fig. 4.1c) and aldol formation (intermediate in Fig. 1b), where the molecular formula of the product is a simple result of adding the reactant formulas, are also important in the formation of SOA from biogenic precursors, especially under the low-NOx conditions [172, 259, 260]. The addition products may stem from heterogeneous uptake; for example: hemiacetals derived from isoprene have been demonstrated to form in the acid-catalyzed reactive uptake of gas-phase epoxydiols [204].

The increase of LWC will likely impede esterification and aldol condensation by shifting the chemical equilibrium towards the reactants but have little effect on the formation of hemiacetal, which does not involve water directly. However, an enhancement of aldol formation due to increased LWC is also possible in special cases due to shifts in the keto-enol tautomerism. For example, in malonic acid particles, the concentration of the reactive enol form increased by an order of magnitude for particles exposed to 90% vs. 2% RH [261]. The suppression of oligomerization results in more volatile aerosol constituents, which may reduce the SOA yield.

Due to the different effects of high RH – enhancement in the reactive uptake of VOC and suppression of condensation oligomerization reactions – the composition of SOA will likely be affected by RH and the change in the extent of oligomerization may be positive or negative depending on which type of reaction is dominant. For the same reason, the aerosol mass may also change. The changes in composition affects the physical characteristics of the SOA, e.g. hygroscopicity, viscosity, etc., which may have profound implications in the atmosphere. In this work, we investigate the effect of RH on the molecular composition of SOA produced by isoprene photooxidation using high-resolution mass spectrometry and the effect of RH on the SOA mass yield by traditional techniques.

4.3. Experimental

SOA was generated under high-NOx conditions (isoprene: $NO_x \approx 1{:}3$) in the absence of seed aerosol in the UCI Chamber as described in Section 1.3.1. Prior to each experiment, the Teflon chamber was filled with zero air humidified to desired value of RH using a Nafion multi-channel humidifier (Perma Pure FC125). The initial mixing ratio of NO was 600 ppb. There was also up to 100 ppb of NO_2 present initially. Approximately 2 ppm H_2O_2 was used as an OH precursor. The initial mixing ratio of isoprene was 250 ppb. After all the precursors were injected, the mixture was exposed to the UV-B radiation, producing OH by photolysis of H_2O_2. The OH concentration of $\sim 4 \times 10^7$ molec/cm^3 was estimated from the observed decay rate of isoprene.

Under high RH conditions, H_2O_2 may partition into the adsorbed water on particles and potentially contribute to aqueous photochemistry [219]. We estimate that the contribution of aqueous photochemistry to the production of OH is negligible under our experimental conditions, largely because we do not use inorganic seeds. The hygroscopic growth factors (GF) for model biogenic OA are in the range of 1.05-1.10 [262], which are much smaller than the corresponding GF of 1.5-2.1 reported [262, 263] for inorganic salts typically used as seeds in aerosol chamber experiments. This helps suppress the particle LWC, and minimize the rate of the aqueous photochemistry. The rates of gas-phase oxidation of isoprene and its derivatives do not change between dry and humid conditions (Fig. 4.2a) confirming that the gas-phase OH is not significantly depleted due to partitioning of H_2O_2 in the particle aqueous phase.

Experiments were performed in the temperature range of 22-26°C. The initial values of RH were < 2% for "dry" experiments and ~ 90% for "humid" experiments. These values were chosen to maximize the differences in the SOA composition induced by the particle LWC

without the risk of water condensation in the chamber. The actual RH experienced by the reacting mixture was lower at the end of the reaction period (70-80% RH) due to a slight rise in temperature (3-5 °C) in the chamber during the photooxidation. For the remainder of the article, we will be referring to these conditions as "dry" and "humid".

The sheath flow in the SMPS's differential mobility analyzer (DMA) column was maintained at low RH (<10% when DMA was connected to the humidified chamber). We assumed that most water evaporated quickly upon contact of aerosol flow (0.3 SLM) with the sheath flow (3 SLM). Therefore, the SMPS measurements could be converted into the dry aerosol mass concentration. A particle density of 1.2 g/cm^3 typical of biogenic SOA was assumed for the dry SOA material [103, 199, 264, 265], regardless of the humidity in the chamber during the SOA formation. We note that it is not necessary to know the absolute density value as we will be comparing the relative SOA yields between the dry and humid experiments.

The photooxidation time was 2 hours, after which the SOA loading was ~ 40 μg/m^3. At that time, isoprene completely decayed and first generation products (methyl vinyl ketone (MVK), methacrolein (MAC), and 3-methylfuran (3MF)) were also nearly completely removed. The concentration of O$_3$ increased to about 200 ppb during the experiments. The experiments were performed in an identical manner, within a span of several days, with the only difference being the initial chamber RH. At least three samples were generated for each set of conditions. PTR-ToF-MS spectra showed excellent reproducibility in the time dependence of concentrations of isoprene and its major oxidation products. Blank experiments were performed identically to the sample experiments, but in the absence of UV radiation. The blank and background particle mass concentrations were < 0.01 μg/m^3. Aerosols were collected using MOUDI on aluminum foils and PTFE substrates (Whatman 2 μm). Samples from stages 6-10 (covering the particle size

range of 0.056-0.56 μm) were used in the analysis. The substrates with collected samples were placed in plastic holders, vacuum-sealed in polyethylene bags, and frozen in anticipation of off-line analysis.

The SOA samples were analyzed using a high-resolution linear ion trap (LTQ) - Orbitrap™ (Thermo Corp.) mass spectrometer, using electrospray ionization (ESI) and nanospray desorption electrospray ionization (nano-DESI) as described in Section 1.3.3. In this work, both techniques were used to obtain spectra in both positive and negative ionization modes. Analyte molecules are detected as $[M+H]^+$ and $[M+Na]^+$ ions in the positive ion mode and as $[M-H]^-$ in the negative ion mode. A mixture (1:1 v/v) of HPLC-grade acetonitrile and water served as the solvent in ESI and the eluent in nano-DESI. The concentration of analyte in ESI was *ca.* 40 μg/mL (resulting from extraction of substrates into 1 mL of the solvent). Background mass spectra were taken on substrates obtained from blank experiments; they were not significantly different from pure solvent spectra. Data analyses were performed as described in Section 1.3.4.

4.4. Results

4.4.1. SOA yield and gas-phase reaction products

PTR-ToF-MS was used to simultaneously track all VOC, including isoprene, with 18 s time-resolution. The humidity of the sampled air affects the extent of the PTR ionization. Under normal operation conditions, humidity will alter the PTR ion concentrations by less than 5% [266]. However, the ion signal of VOC with PA similar to the PA of water, like formaldehyde (718 kJ/mol), may be affected by more than 5% due to the backward protonation of H_3O^+ primary ions at higher sample inlet humidity. This RH effect theoretically decreases ion signal

90

under higher inlet flow RH. The ion signals for formaldehyde were corrected at the relevant drift

potential (U_{drift} = 600 V) using the procedure reported by *Inomata et al. (2008)* [106].
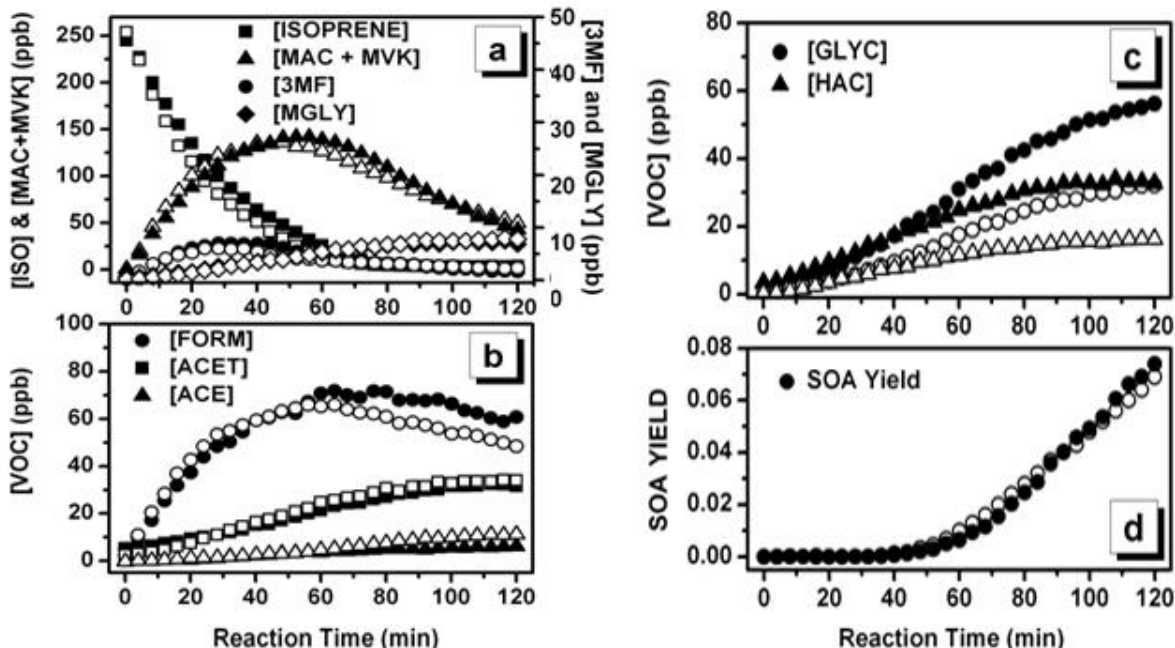
Figure 4.2: Time dependent concentrations of selected species in the chamber during the photooxidation. Open markers refer to dry conditions and filled markers refer to humid conditions. PTR-ToF-MS mixing ratios of (a) isoprene, methylvinylketone (MVK) + methacrolein (MAC) , 3-methylfuran (3MF), methylglyoxal (MGLY) (b) formaldehyde (FORM), acetaldehyde (ACET), acetone (ACE) (c) glycolaldehyde (GLYC) and hydroxyacetone (HAC). (d) The time-dependent SOA yield from isoprene photooxidation does not change with respect to initial concentration of water vapor in the chamber. The time-dependent SOA yield in panel (d) is defined as [(mass)$_{SOA}$/(mass)$_{Reacted\ Isoprene}$] (note: oxidation of MAC and MVK also contributes to SOA mass).

We generally do not observe significant differences in the PTR-ToF-MS time-dependent

traces of the major VOC products monitored between the dry and humid conditions. Figure 4.2a

shows the decay of isoprene and the formation of the first- and second-generation products

methacrolein (MAC), methylvinylketone (MVK), 3-methylfuran (3MF), and methylglyoxal

(MGLY). MAC and MVK are detected as an isobaric pair. The time-dependent traces of

formaldehyde (FORM), acetaldehyde (ACET) and acetone (ACE) are shown in Figure 4.2b. The

time-dependent trace of FORM shows that at approximately the 60 minute mark, after almost all isoprene has been reacted, the decay of FORM is reduced in the presence of water vapor. However, as gas-phase FORM has both photolysis loss channels [267] and sources due to isoprene photooxidation [268], it is not clear which mechanism is affected by RH. Non-volatile products like 2-methlyglyceric acid (2MGA) were not detected by PTR-ToF-MS.

However, there are notable exceptions to this observation: the production of glycolaldehyde (GLYC, m/z 61.03) and hydroxyacetone (HAC, m/z 75.04) increased under humid conditions (Fig. 4.2c). At the end of the photooxidation period, the concentration of GLYC was 33 ppb (dry) and 56 ppb (humid) in the representative samples. Similarly, the concentration of HAC was 16 ppb (dry) and 33 ppb (humid). The signal at m/z 61.03 and at m/z 75.04 may have interferences from acetic acid and lactaldehyde, respectively. However, acetic acid is not expected to be a significant product on the timescale of the experiment [30, 228]. Furthermore, lactaldehyde is not observed from the oxidation of isoprene in laboratory experiments or in field observations, so we do not expect these interferences to be significant. Conversely, GLYC and HAC are important water-soluble isoprene oxidation products commonly observed in the field [226, 227, 237, 240-242]. GLYC is produced in the OH+MVK reaction [193, 236] and HAC is produced in the OH+MAC reaction [237] following the photooxidation of isoprene. GLYC and HAC may also be formed from prompt sources like the decomposition of alkenoxy radicals [269, 270] or from the degradation of hydroxy alkenyl nitrates [30]. The increase in signal of these second-generation VOC at higher RH is unexpected, and cannot be explained by backward reactions in the PTR ion source.

The effect of RH on the resulting SOA mass in the chamber was insignificant. Figure 4.2d shows the time-dependent SOA yield defined as the ratio of the dry SOA mass ($\mu g/m^3$)

produced over the concentration of isoprene reacted. This yield definition is not ideal as a large contribution to SOA mass arises from the oxidation of first generation products after all of the isoprene has already reacted [271]. However, for the sake of comparison, the traditional definition of SOA yield was used to gauge the relative differences between the two sets of data, without an emphasis on the absolute yield quantification.

Figure 4.2d demonstrates that RH does not substantially affect the SOA yield from isoprene photooxidation in the absence of inorganic seeds. This result qualitatively agrees with conclusions of *Dommen et al (2006)* who reported no significant change in the SOA yields at different RH [158], also for SOA generated in the absence of inorganic seeds. However, our observations are different from the recent study of *Zhang et al (2011)* who reported an enhancement of the SOA yield under dry conditions from isoprene photooxidation in $(NH_4)_2SO_4$-seeded experiments [223]. The presence of inorganic seeds in the chamber is an important difference between the seeded and non-seeded experiments. $(NH_4)_2SO_4$ particles exhibit significant hygroscopic growth at elevated RH (GF~ 1.5 at 85% RH for $(NH_4)_2SO_4$ seeds [262, 263]), compared to organic particles (GF~ 1.0-1.1 for biogenic SOA [247, 262]). The increased LWC in the seeded experiments likely has an effect on the SOA formation, and may account for the different conclusions of *Zhang et al (2011) vs. Dommen et al (2006)* and this work.

Under humidified conditions, the use of H_2O_2 as an OH precursor may lead to aqueous photochemistry occurring directly inside the wetted particles, potentially affecting the final SOA yield. This would be more of an issue for the seeded experiments, which have higher LWC. *Dommen et al (2006)* performed "classical photooxidation" experiments without OH precursors. The good agreement between this work and that of *Dommen et al (2006)* with respect to the RH

effect on the SOA yields suggests that the specific choice of OH precursor and presence of H_2O_2 in the chamber is not important for the non-seeded experiments.

4.4.2. Mass spectrometry analysis of SOA samples
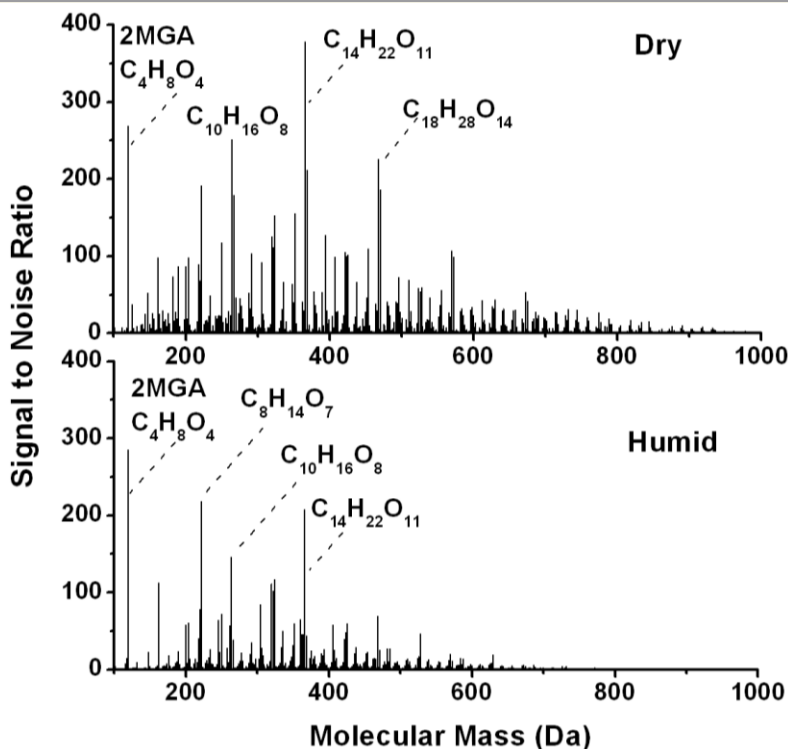
Figure 4.3: Stick spectra of all assigned compounds in high-NOx isoprene SOA samples generated under two humidity conditions. The spectra represent a merged set of ESI and nano-DESI data. The horizontal axis corresponds to molecular weights of the neutral SOA compounds, and the vertical axis corresponds to the mass spectra intensities. High-MW oligomeric species in the dry sample are significantly more abundant.

Figure 4.3 shows the stick mass spectra for isoprene photooxidation SOA generated under dry (RH <2%) and humid (RH 90%) conditions. The horizontal axis corresponds to molecular weights of the neutral SOA compounds, which could be unambiguously assigned to $C_cH_hO_oN_n$ molecules from the corresponding measured m/z values. We are interested in the most complete set of compounds for our analysis regardless of their mode of detection. Mass spectra

shown in Figure 4.3 represent a merged set of ESI and nano-DESI data, which plots the average abundance of each feature detected in different ionization modes. The background peaks from blank samples were removed.

The negative and positive mode data with ion peak assignments in *m/z* are converted to neutral masses and merged because negative and positive modes ionize different subsets of SOA compounds, and nano-DESI is more sensitive to labile compounds compared to ESI. Although the averaged mass spectral intensities do not represent the relative molecular abundances in the aerosol, they can still be used for qualitative comparison between the dry and humid samples. To ensure that the intensities in the mass spectra of dry and humid SOA samples can be compared, we recorded the mass spectra under identical instrumental settings. Approximately 750 peaks were assigned in each mass spectrum, representing ~70% of all the observed peaks.
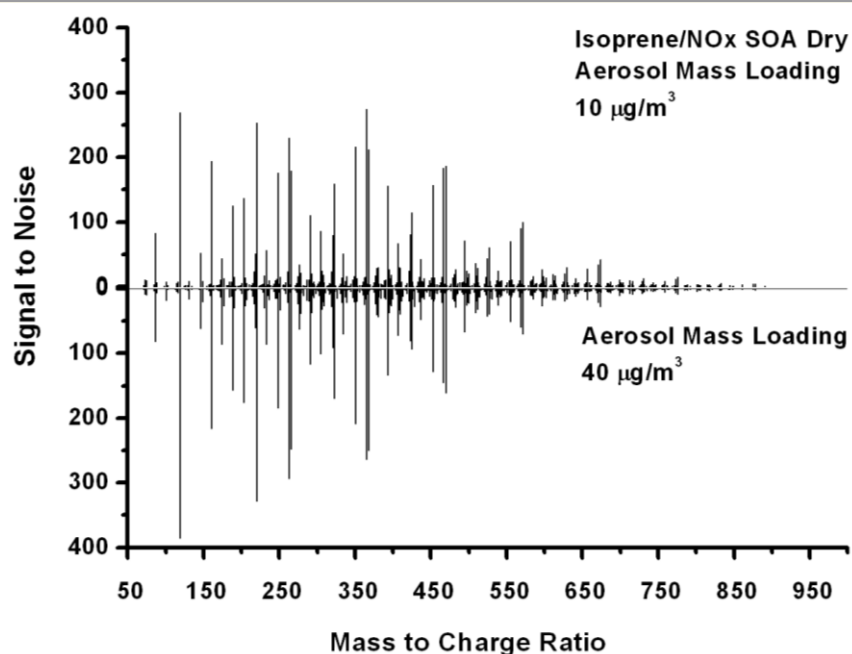
Figure 4.4: Different SOA mass loading on sample filters do not significantly change the peak intensity distribution of SOA compounds in the electrospray experiments.

The monomer form of 2MGA was observed with high abundance in both dry and humid spectra, indicating that the formation pathway to produce 2MGA is not significantly affected by RH. For example, one formation pathway for 2MGA and its oligomers is the photooxidation of a second-generation product from isoprene methacryloylperoxynitrate (MPAN) [40, 204]. Methyltetrols were not observed in the high-NOx data, consistent with the findings of *Surratt et al (2006)*. Figure 4.3 shows that the components of SOA generated under dry vs. humid conditions were quite different. Differences in peak intensities in the dry vs. humid samples did not result from an experimental artifact as in both cases the filters contained about the same amount of deposited SOA material. Furthermore, experiments with different filter loadings, 10 μg/m^3 vs. 40 μg/m^3 estimated by SMPS data, under a specific RH condition resulted in similar intensity distributions (Fig. 4.4).

Isoprene has a relatively low molecular weight (68.063 Da) and even the heaviest products of isoprene oxidation that retain its original carbons have molecular weights under 200 Da (for example, 2-methyltetrol nitrate ester weighs 181.058 Da). Figure 4.3 shows that 80-90% of the observed isoprene SOA constituents have molecular weights in excess of 200 Da and therefore correspond to oligomeric molecules. In the mass spectrum of the SOA generated under dry conditions, more peaks are observed in the 400-1000 Da region, whereas for the SOA formed under humid conditions most peaks are clustered around 200-400 Da. We note that oligomers may be overrepresented in our work as larger, multifunctional molecules are more efficient charge acceptors and are easier to ionize in the electrospray. Nevertheless, it is clear that oligomerization plays an important role in the SOA formation chemistry.

The highest abundance peaks, including those explicitly labeled in Fig. 4.3, are generally found in both dry and humid spectra. There are ~ 550 common peaks observed in both samples,

corresponding to approximately 73% of the assigned peaks. However, there are significant and reproducible differences in the signal-to-noise (S/N) ratios of these peaks between the dry vs. humid spectra. The S/N differences in the common peaks, under identical analytical conditions, suggest that RH affects the rate of production of these compounds. The amount of overlap between the two spectra decreased with an increase in *m/z*. For example, the overlap was 85% for molecular weights between 100- 600 Da but only 36% for the 600-1000 Da region. This trend logically implies that the formation of larger oligomers is hindered by high initial chamber RH (the discussion of the oligomers will be expanded upon in Section 4.5).
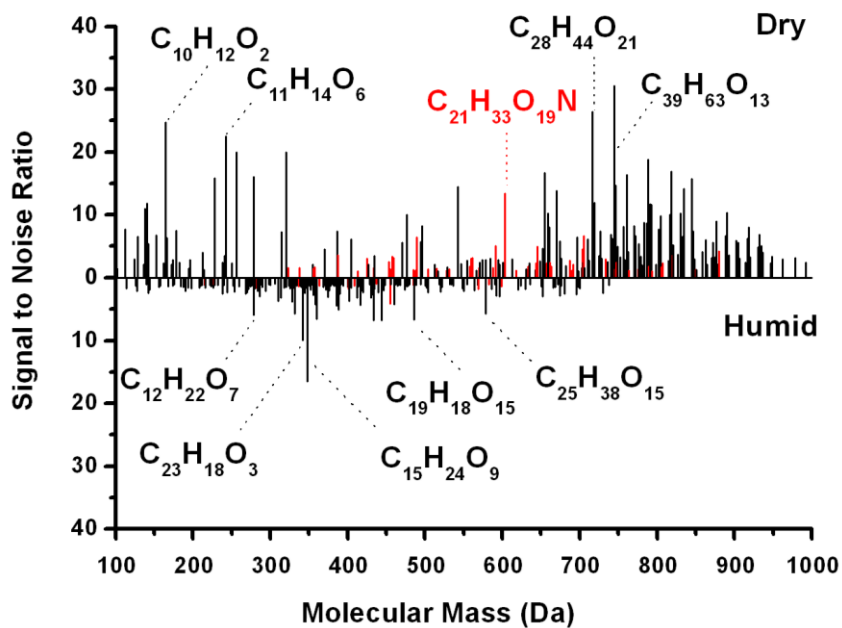
Figure 4.5: Stick spectra of assigned compounds that are unique to either dry or humid conditions. The axes are defined in the same way as in Figure 3. There are approximately 200 formulas unique to the dry conditions and 225 formulas unique to the humid conditions out of 750 assigned formulas in each sample. Unique formulas with higher abundances are labeled. NOC species are shown in red.

Approximately 20% and 12% of the total number of peaks were assigned to NOC molecules in the dry and humid sample, respectively. In addition to the reduction in the total

number of the observed NOC species, the S/N of the NOC peaks in the humid mass spectra was greatly reduced. For example, $C_{12}H_{19}O_{12}N$ (369.091 Da) was detected with a S/N of 212 in the dry sample vs. S/N of 44 in the humid sample. Similar drastic reduction in signal (>80%) was observed for $C_8H_{13}O_9N$ (267.059 Da), $C_{16}H_{25}O_{15}N$ (471.122 Da), $C_{20}H_{31}O_{18}N$ (573.154 Da), and several other NOC species. Most of these NOC are oligomers. The only monomer nitrate observed is $C_4H_7O_3NO_3$ (the nitrate ester of 2MGA) and its signal is similarly low in both the dry and humid data (S/N of 1.6 and 1.5, respectively). The structural identities of selected NOC were probed with high-resolution tandem mass spectrometry (MS^n) and the detailed discussion was presented in Chapter 3. Briefly, most of the NOC molecules that are affected by RH are oligomeric organic nitrates with several 2MGA units incorporated into the structure. As an example, MS^n revealed $C_8H_{13}O_9N$ to be a condensation dimer of 2MGA and its nitrate ester ($C_4H_7O_3NO_3$+ $C_4H_6O_3$).

Figure 4.5 compares peaks observed uniquely in samples generated under dry or humid conditions, with those of higher abundances explicitly labeled. There were approximately 220 unique peaks in the dry dataset and 225 unique peaks in the humid dataset, representing ~ 37% of all the assigned 750 peaks by count. Because all of the unique peaks were of relatively low abundance (S/N < 40), their MS^n analysis could not be performed. However, a visual comparison shows that a large fraction of compounds formed uniquely under dry conditions belong to the higher-MW oligomers and NOC species. Some of these molecules could be attributed to high-MW condensation oligomers whose formation was hindered under the humid conditions. For example $C_{28}H_{44}O_{21}$ (Fig. 4.5) is likely a 7-unit homologous 2MGA oligomer from the $C_4H_8O_3$+ $(C_4H_6O_3)_n$ family (Table 4.1).

Table 4.1: Total abundances of oligomers in the condensation and addition reactions from selected homologous families. Each condensation family is generated by a repeated addition of $C_4H_6O_3$ to the $C_xH_yO_z$ precursor listed in the first column. The addition families are built by repeated addition of $C_2H_4O_2$ to a $C_xH_yO_z$ precursor. k_{max} is defined as the maximum number of homologous oligomer units attached to the parent molecule, used as indicators of oligomer length, and ΔC is the change in the total number of carbon atoms in the oligomer, calculated based on the number of carbon in the monomer unit and the change in k_{max}.

Condensation $C_cH_hO_oN_n +$ $(C_4H_6O_3)_k$	Dry Total Signal	Dry k_{max}	Humid Total Signal	Humid k_{max}	ΔSignal (%)	ΔC
$C_2H_4O_3$	114	7	34	5	-70	-8
$C_3H_4O_3$	455	8	106	6	-77	-8
$C_3H_6O_2$	225	9	107	6	-52	-12
$C_3H_6O_3$	140	8	35	6	-75	-8
$C_4H_6O_3$	445	8	137	6	-69	-8
$C_4H_8O_3$	100	8	28	5	-72	-12
$C_4H_8O_4$	598	8	467	6	-22	-8
$C_4H_7O_6N$	736	7	126	6	-83	-4
$C_5H_8O_4$	291	8	124	5	-57	-12
$C_5H_8O_5$	491	7	167	5	-66	-8
$C_6H_8O_4$	165	7	88	4	-47	-12
$C_6H_{10}O_5$	1053	8	451	6	-57	-8
$C_7H_{10}O_4$	166	7	77	5	-54	-8
Average	383	8	150	5	**-63 ($\pm$16)**	**-9 ($\pm$2)**

Addition $C_cH_hO_oN_n +$ $(C_2H_4O_2)_k$	Dry Total Signal	Dry k_{max}	Humid Total Signal	Humid k_{max}	ΔSignal (%)	ΔC
$C_3H_4O_2$	32	3	21	3	-34	0
$C_5H_6O_2$	131	4	69	4	-48	0
$C_5H_6O_4$	212	4	101	4	-52	0
$C_6H_8O_3$	49	3	40	3	-19	0
$C_6H_8O_4$	502	3	324	3	-35	0
$C_7H_8O_4$	161	6	81	5	-50	-2
$C_7H_8O_5$	282	5	108	5	-62	0
$C_7H_{10}O_5$	83	3	39	3	-53	0
$C_8H_{10}O_3$	74	5	61	5	-18	0
$C_8H_{10}O_5$	599	6	388	5	-35	-2
$C_8H_{10}O_6$	165	4	122	4	-26	0
$C_9H_{12}O_4$	51	5	143	5	+177	0
$C_9H_{12}O_5$	194	4	148	5	-24	+2
Average	195	4	127	4	**-21 ($\pm$61)**	**0 ($\pm$1)**

Other molecules like $C_{11}H_{14}O_6$ are formed from heterogeneous (comprised of different monomeric units) oligomerization because their molecular formulas are not linked to repeating units of any one monomer. These molecules are less likely to form in the humid conditions because high RH may hinder the formation of certain monomers. Although the number of observed unique peaks is similar for both the dry and humid data, the total ion signal for unique peaks in the dry data is much higher. This may suggest either higher physical abundance of those unique compounds in the sample or higher ionization efficiency in the electrospray.

4.5. Discussion

The similarity in the time-dependent concentrations of reaction products and SOA yields in the dry and humid experiments suggests that the initial gas-phase oxidation chemistry was similar. The OH yield from the photolysis of H_2O_2 was likely minimally affected by the additional water vapor. However, the increase in signal of GLYC and HAC indicates that water vapor indeed affected a certain subset of photochemical reactions. As GLYC and HAC are both water-soluble, they should be lost more easily to the walls with higher initial water vapor in the chamber. Therefore, the increase in the abundances of these products in the gas phase under higher RH conditions is unexpected. Due to the multiple sources of GLYC and HAC, the reason behind this particular RH effect is unclear and a more systematic investigation is necessary to implicate specific reactions.

The observed reduction of the organic nitrates in the particle phase under humid conditions may be due to the following reasons. First, the total organic nitrates formed in the gas phase may be reduced, which would limit the number of particle-phase nitrates by gas-particle partitioning. Typically, VOC do not fragment in the PTR ion source; however, volatile organic nitrates ($RONO_2$) may lose nitrous acid (- HONO), nitric acid ($-HNO_3$) or fragment into NO_2^+

[272, 273]. As the identities of the individual nitrates are unknown, we cannot use carbon-based fragment ions formed in the PTR ion source, e.g. $[M\text{-}HONO]^+$ or $[M\text{-}HNO_3]^+$, to trace the time evolution of the total amount of organic nitrates. We do observe a 40% decrease in the signal of NO_2^+ under humid conditions, which may in principle be used as a tracer ion for the total organic nitrates in PTR-ToF-MS. Unfortunately, due to strong interferences from nitric acid (HNO_3) [274], the NO_2^+ signal cannot be exclusively assigned to organic nitrate fragmentation. In addition, the yield of NO_2^+ from larger alkyl nitrates is small (e.g. 3% yield for a branched C_3 nitrate [272]). The yield of NO_2^+ from HNO_3 is not known, however, we expect a significant build up of HNO_3 during photooxidation. That HNO_3 is the dominant cause of the reduction in the NO_2^+ signal is consistent with the exceptional water solubility of HNO_3. However, a humidity-induced reduction in gas-phase organic nitrates cannot be completely ruled out based on the PTR-ToF-MS observations.

The second possibility for the observed reduction of the organic nitrates in the particle phase is that the formation of condensation organic oligomers containing a $-ONO_2$ group may decrease under humid conditions. This, in turn, may lead to a reduction in the ion current for the NOC compounds. The SOA may still contain monomer nitrates, but as monomers are likely to be less ionizable than oligomers, the observed total NOC signal should decrease with a decrease in the degree of oligomerization. The negligible RH-induced change in observed signal of the monomer nitrate of 2MGA (Section 4.4.2), the only observed monomer NOC species, is consistent with a similar concentration of monomeric nitrates in the aerosol and decreased oligomerization.

Finally, the particle-phase nitrates may be reduced in the humid conditions by a suppression of direct esterification of alcohols by nitric acid (HNO_3), also a condensation-type

process. Nitric acid concentration in these experiments may be sufficient for the efficient partitioning of HNO_3 into the particle phase. If esterification of alcohols by HNO_3 is the main reason for the suppression of NOC in humid experiments, the reduction in the yield of organic nitrates should be smaller under more realistic atmospheric conditions with much lower NO_2 and HNO_3 concentrations as compared to the chamber. Nevertheless, this process has implications for the total budget of NOC compounds in particles, especially in highly-polluted urban air environments.

The high resolution mass spectra shown in Figure 4.3 suggest that 2MGA is formed in comparably high abundance in both dry and humid conditions. However, the oligomerization arising from 2MGA is significantly affected by RH. For systematic assessment of the oligomerization patterns in SOA formed under the dry and humid conditions, we conducted a statistical molecular weight (MW) difference analysis for all the assigned compounds. For x different compounds, there are x^2-x non-zero mass differences that can be grouped in a histogram to identify the most common MW differences. Each such difference can be assigned to a formula $C_cH_hO_oN_n$, where c, h, o, and n can be positive or negative depending on the chemical process responsible for propagating this particular fragment through the distribution of formulas. It is possible to trace high-MW formulas to lower-MW ones by generating chemical "families" of the type $C_xH_yO_zN_w+[C_cH_hO_oN_n]_k$ where $C_xH_yO_zN_w$ is the smallest member of the family and k is the number of times the difference formula is repeated. This type of analysis, which in essence identifies the most frequently repeated base formulas to use for a given distribution of compounds, is routinely performed in high resolution mass spectrometry [79, 131, 222, 275] to find monomer units that form long oligomer "families". Our criteria for identifying monomer units using this method are: (1) observation of a large number of families which have a broad

range of k values; (2) ability to link the formula difference to an expected product of isoprene oxidation. It is important to note that non-homologous oligomers, i.e. those including different monomer building blocks, may also be present in large numbers but they are harder to track down with statistical tools.
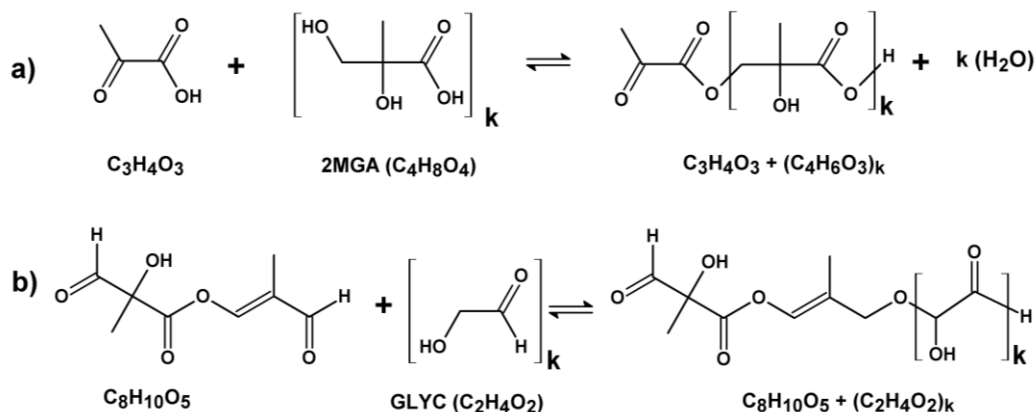
Figure 4.6: (a) Condensation oligomerization from repeated esterification by 2MGA produces MW differences equivalent to $C_4H_6O_3$ (b) Addition oligomerization from repeated hemiacetal formation with GLYC produces MW differences equivalent to $C_2H_4O_2$.

MW differences corresponding to O-atom and CH_2 are usually the most common differences for natural complex mixtures as these groups are present in the majority of organic molecules. Indeed for humid isoprene high-NOx data, the most common mass differences were O-atom followed by CH_2. However, the most common difference in dry isoprene high-NOx data was a more complex unit: $C_4H_6O_3$ (102.032 Da). This mass difference must correspond to the formation of oligomers via condensation reactions involving 2MGA, [37, 259] a very abundant molecule in both humid and dry SOA samples. However, the prevalence of this mass difference in only the dry sample supports that 2MGA-based oligomers are much more important when the SOA is generated under dry conditions. The polyfunctional nature of 2MGA (carboxylic acid and alcohol functionality) enables the formation of very long oligomers similar to the poly-

condensation of glycolic acid to make polyesters in industrial applications (Fig. 4.6a). The molecular formula of 2MGA is $C_4H_8O_4$ but with an H_2O loss at every condensation step the repeated unit becomes $C_4H_6O_3$.

The unit $C_2H_4O_2$ was also identified as a prominent repeating motif in our analysis and assigned as the addition unit of GLYC (HO-CH_2-C(O)H). GLYC is similar to 2MGA in that it is bifunctional (it is the simplest hydroxyaldehyde) and can produce relatively long homologous oligomers (Fig. 4.6b). Like any hydroxyaldehyde, GLYC can oligomerize by addition to form hemiacetals, and its hydrated form HO-CH_2-C$(OH)_2$H can oligomerize by condensation. However, with the relatively low amount of water present in the particle (about 30% by volume under humid conditions) the contribution of the hydrated form should be small.

Therefore, the unit $C_4H_6O_3$ was used in our analysis to represent homologous condensation with 2MGA, and $C_2H_4O_2$ was used to represent homologous addition with GLYC. We examined these two important types of oligomer families in detail to discern differences in oligomerization due to the additional water vapor present in the chamber at the time of aerosol formation. We note that while these two types of oligomers are among the most abundant, there are other types of condensation and addition oligomers in isoprene SOA that respond to RH in a qualitatively similar way.

Oligomers produced from 2MGA condensation chemistry are very large and generally homologous (k_{max} = 4 - 9). The homologous nature of 2MGA oligomers, which dominate the signal abundance from the SOA samples generated at both high and low RH conditions may account for the semi-solid nature of biogenic SOA [276, 277]. A number of long homologous families of the type $C_xH_yO_z$ + $(C_4H_6O_3)_k$, with k ranging from 1 up to 9 were identified (Table 4.1 and Table A1 of Appendix A). Table 4.1 reports the summed ion signal from all oligomers

identified from a particular family under both dry and humid conditions. The total signals are reported as the sum of the signal-to-noise ratios within the entire chemical family. The change in signal is defined as the absolute difference between the humid and dry total signal relative, divided by the maximum of the two total signals. As expected, RH affects the condensation oligomer chain length significantly. Homologous families of 2MGA are 2-3 monomer units shorter under humid conditions, corresponding to 7-11 fewer carbon atoms per molecule. The average decrease of condensation oligomers in SOA generated under humid conditions is $63 \pm 16\%$, where the error in this case is the statistical spread in oligomer ion abundance between the thirteen homologous families included in Table 4.1.

Figure 4.7a shows the representative abundance distribution of the oligomers with molecular formulas $C_xH_yO_zN_w+ (C_4H_6O_3)_k$. The trend of decreasing signal for each oligomer in the family, as well as a decrease in the length of the oligomers, at higher initial chamber RH is clearly observable. The distribution of oligomer signal shows that the most abundant oligomer in the family is not the same when SOA is generated under dry and humid conditions. For example, Figure 4.7a reveals the most abundant oligomer in the family $C_3H_4O_3+ (C_4H_6O_3)_k$ is the tetramer (k=3) under dry conditions and the trimer under humid conditions (abundances reported in Table A1 of Appendix A). In general, the most abundant oligomer decreases by one monomer length in the chemical families and the signal distribution and oligomer length trends are similar for all the 2MGA-based families studied in this work.

Figure 4.7b shows a family of the type $C_xH_yO_z + (C_2H_4O_2)_k$ formed by the repeated addition of GLYC $(C_2H_4O_2)$. The signal distribution in Figure 6b is not significantly affected by RH (abundances of chemical family members reported in Table A2 of Appendix A). The observed addition-type oligomers had k_{max} ranging from 3 to 6. In contrast to the condensation-

type oligomers, which uniformly decreased in abundance at high RH, the addition-type oligomers did not display a clear trend (-21 ± 61%) in the total oligomer signal. However it is clear that, unlike the condensation oligomers, the oligomer chain length and number of carbon atoms are not affected by RH due to this type of addition reactions.
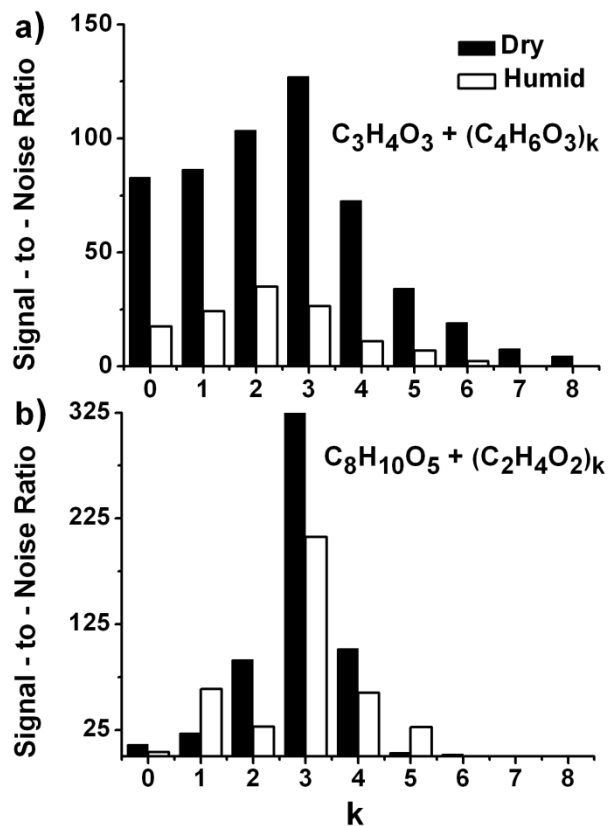
Figure 4.7: Representative distributions of homologous oligomeric compounds in high-NOx SOA under dry (filled bars) and humid (open bars) conditions. (a) Condensation-type oligomers from repeated esterification by 2MGA ($C_4H_8O_4$ with one H_2O lost per oligomerization step). (b) Addition-type oligomers incorporating homologous units of glycolaldehyde ($C_2H_4O_2$).

The evidence from high resolution mass spectrometry offers an important conclusion: the composition of isoprene photooxidation SOA changes considerably with RH even though the SOA yield appears to be unaffected. The rate of production of most of the volatile oxidation products in isoprene photooxidation remained the same regardless of RH, with an important

exception of GLYC and HAC (40-50% increase with high RH). The total number of aerosol-phase NOC compounds also decreased by 40% in the humid mass spectra, and is most consistent with a reduction of oligomerization reactions involving monomeric NOC species. There are visible differences in the mass spectra with ~ 37% unique products formed in either dry or humid conditions.

The common products observed under dry and humid conditions correspond mostly to condensation and addition oligomers and their relative abundance varies considerably between the two RH conditions. Our observations suggest that isoprene SOA formed under high RH conditions contain a significantly smaller number of high-MW homologous oligomers compared to the dry conditions due to a shift in chemical equilibria of the condensation reactions. The overall yield of all condensation oligomers decreased and the oligomers may be three monomer units shorter in SOA generated in humid air. In contrast, there is only a weak reduction in the number of addition-type oligomers obtained from our analysis but the data suggest the length of addition oligomers remain unchanged.

4.6. Atmospheric implications

The shorter chain length of oligomer esters produced under humid conditions (~5-7 monomer residues, including parent) compared to those produced under dry conditions (~ 8-10 monomer residues) has important implications for the physical properties of the SOA. Consider for example, the solubility behavior of straight-chain oligomer esters of hydroxyacids, such as 2-methylglyceric acid (2MGA), where an inverse relationship between oligomer length and solubility is observed [278]. Capillary electrophoresis experiments by *Braud et al (1996)* determined that hydroxybutyric acid oligomers were no longer water-soluble at 5 monomer units

107

long and glycolic acid oligomers were no longer water-soluble at 3 monomer units. Additionally, the viscosity of condensation oligomers increases with oligomer chain length [279].

As the water-solubility and viscosity of condensation oligomers is higher in SOA produced under dry conditions, the phase characteristics of the SOA may also change; for example, more viscous organic materials may be more "glassy" than less-viscous organic materials in their amorphous state. The less-viscous SOA can absorb water into the bulk, while the water uptake of the more-viscous SOA is limited by the surface [59]. Therefore, the water solubility and viscosity of the isoprene SOA, influenced by the total concentration of long-chain oligomers, may affect its hygroscopicity, or CCN ability. The hygroscopicity and morphology of particles were found to be important factors in the prediction and interpretation of CCN results [280]. Isoprene SOA generated under dry conditions, where the composition is dominated by long oligomer esters, may exhibit reduced CCN activity compared to those generated under humid conditions. This prediction based on mass spectrometry data is in agreement with observations made by *Poulain et al (2010)* that the hygroscopicity of α-pinene ozonolysis SOA is directly proportional to the water mixing ratio present in the chamber during SOA formation [245]. Although the hygroscopicity of isoprene photooxidation products generated with a variety of VOC/NOx ratios have been investigated [281], no hygroscopic growth factor or CCN activity measurements have been reported for isoprene SOA generated under humid vs. dry conditions. As biogenic SOA represents a large fraction of the tropospheric aerosol budget, a systematic study of the hygroscopic properties of SOA from isoprene, for example, as a function of initial chamber RH is warranted.

Chapter 5: Estimation of Organic Compound Concentrations in Complex Mixtures Using High-Resolution Electrospray Mass Spectrometry

5.1. Abstract

Quantitative analysis of individual compounds in complex mixtures using high-resolution electrospray ionization mass spectrometry (HR-ESI-MS) is complicated by differences in the ionization efficiencies of analyte molecules in the mixture, resulting in signal suppression during ionization. However, the ability to obtain concentration estimates of compounds in an environmental sample is important for data interpretation and comparison. We introduce an approach for estimating mass concentrations of analytes observed in a multicomponent mixture by HR-ESI-MS, without prior separation. The approach relies on a calibration of the instrument using appropriate standards added to the mixture of studied analytes. An illustration of how the proposed calibration can be applied in practice is provided for aqueous extracts of isoprene photooxidation organic aerosol, with multifunctional organic acids standards. We show that the observed ion sensitivities in ESI-MS are positively correlated with the "adjusted mass," defined as a product of the molecular mass and the H/C ratio in the molecule (adjusted mass = H/C x molecular mass). The correlation of the observed ESI sensitivity with adjusted mass is justified by considering trends of the physical and chemical properties of organic compounds that affect ionization in the positive ion mode, i.e., gas-phase basicity, polarizability, and molecular size.

5.2. Introduction

High-resolution electrospray ionization mass spectrometry (HR-ESI-MS) is a powerful technique for the identification and characterization of compounds in complex mixtures including aqueous natural organic matter (NOM) [110, 282], cloud and fog samples [283], peptide mixtures [284], crude oil [285], and organic aerosol extracts [82, 286]. In these applications, it is desirable to convert raw ion intensities into absolute concentrations or at the very least determine the relative abundances of compounds in the mixture. Even modest accuracy provided by the estimation would be invaluable for the interpretation of the experimental results. However, ionization efficiencies in ESI vary with spray conditions (e.g., voltage, solvent, flow rate), analyte chemical properties, and the presence of charge competitors (see Ref. [111] and references therein), making quantitative analysis in ESI-MS challenging. As a result, ESI-MS is typically used for detection and identification of compounds in complex mixtures while quantitative measurement studies rely on HPLC separation, stable isotope labeling, and/or intensity calibration using internal standards [287].

Most studies on the quantification of analytes using ESI-MS focus on relative ionization efficiency measurements of two standards in pure solvents. This approach is informative, but two-component mixtures may have different ESI responses compared to multicomponent mixtures, because the ionization response depends on the concentration and chemical properties of all solutes in the mixture [288]. Environmental samples are often a complex mixture of dissolved organics, which simultaneously compete for charge. Nevertheless, quantitative analyses of analytes in polymer matrices have been performed for a few compounds using internal standards [289]. This approach can be expanded to all observable compounds in

the mixture if there is a good correlation between the peak intensities and other parameters that can be directly obtained from the mass spectra.

One direction of current research in mass spectrometry is focused on prediction of ESI ionization efficiencies based on the physico-chemical properties of the analyte molecules [290-293]. In positive ion mode HR-ESI-MS, analyte molecules are typically observed as protonated $[M+H]^+$ or sodiated $[M+Na]^+$ species. Therefore, positive mode ionization in ESI enables chemical characterization of molecules that readily form and stabilize a positive charge. Many parameters, often related, affect ionization efficiencies within separate compound classes: polarizability, gas-phase basicity (GB, related to proton affinity (PA) by an entropic term – $T\Delta S^o$), sodium affinity, and surface activity that may be estimated based on the octanol-water partitioning constant [290, 291, 293, 294]. These properties, and therefore ionization efficiencies, are affected by both the molecular size and the structure of the analyte.

It is well-established that for homologous series of compounds, GB and average polarizability of compounds are proportional to molecular size [104, 295] . Furthermore, as analyte molecules approach higher molecular masses, their ability to form sodium adducts increase [296]. However, GB and sodium binding energy are also intrinsically related to structural characteristics like the ionization site or degree of unsaturation [297-301]. Specifically, GB increases with degree of unsaturation in molecules ionized on carbon atoms such as aliphatic hydrocarbons [104], carbonyls [301], and cyclic ethers [299, 300] because the additional π-electrons offer resonance stabilization of the positive charge. However, when ionization occurs on more basic atoms such as N, S or O, the GB decreases between the sp^3 to sp^2 hybridization states of the basic atoms, e.g., going from an amine to an enamine, because sp^3 atoms are more electronegative [104]. As the dependence of the ionization efficiency to degree of unsaturation

may vary by compound class and be either positive or negative, the effect of molecular size alone will not accurately describe ionization efficiencies. Therefore, a combination of factors should be considered when estimating ionization efficiencies, perhaps with one factor describing the size (e.g., mass) and another relating to the structure of the molecule. Calibrations that utilize easily-accessible parameters from the mass spectra, as opposed to approaches relying on physico-chemical properties that may not be available in the literature, will facilitate the processing of large HR-ESI-MS datasets. Yet, the simplicity of the calibration should not significantly compromise analytical accuracy.

In this work, we characterized the positive ion mode HR-ESI-MS response of a few multifunctional organic acids in authentic complex organic aerosol (OA) sample matrices, generated from the OH-oxidation of isoprene, without chromatographic separation as a calibration method. Organic acid species are common in OA [30, 57] and other environmental samples [302, 303], which are often highly oxidized and comprised of multifunctional polar compounds. We introduce an approach for estimating concentrations of analyte compounds based on a novel *"adjusted mass"* axis that explicitly considers the contribution of both analyte molecular size and degree of unsaturation. We show that degree of unsaturation, parameterized by the H/C ratios that are conveniently obtained from HR-MS, adequately represents the structural effects on ionization within separate compound classes. The known total mass concentration of organics is used to normalize the calculated analyte concentrations. Our approach provides convenient concentration estimates of organic compounds from raw ion intensities and can be practically applied to environmental samples. The accuracy of the method is greater if the total concentration is known or can be determined using an alternative method (such as total organic carbon analysis).

5.3. Experimental

Organic aerosol (OA) were synthesized as described in Section 1.3.1 and used as a matrix for ESI sensitivity calibrations. OA were generated from the 5 hour OH radical initiated photooxidation of 500 ppb isoprene (C_5H_8, Aldrich purity 99%) in the presence of 700 ppb nitrogen oxides (NO + NO_2) at 70% relative humidity in the UCI Chamber. No additional OH radical precursors were added and no inorganic seed particles were used. OA samples were collected on PTFE filters (0.2 μm) and extracted with 10 min sonication in 1.5 – 2.0 mL water to a mass concentration of 200 μg mL^{-1} (or 10^{-3} M assuming an average MW of 200 g mol^{-1} for OA compounds), which is comparable to polluted environmental water samples [304].

Table 5.1: Positive ion mode ESI calibration using organic mono- and di-acid standards in aqueous isoprene OA sample matrix. Effective sensitivity is the slope of the dependence of the signal-to-noise ratio on the mass concentration (μg/mL) of the added standard. Effective limit-of-detection (LOD) is the minimum concentration of standard necessary for its detection by ESI-MS within the aqueous OA matrix.

Standard Name (Formula)	Detected Ion	Exact Molecular Mass (Da)	Molecular Structure	Effective Sensitivity (mL $μg^{-1}$)	Effective LOD (μg mL^{-1})
Malic acid ($C_4H_6O_5$)	Na^+	134.022		0.60 (±0.02)	8.83 (±2.42)
3,5-Dihydroxy benzoic acid ($C_7H_6O_4$)	H^+	154.027		0.011 (±0.001)	25.18 (±8.58)
Pinonic acid ($C_{10}H_{16}O_3$)	Both Na^+ and H^+	184.110		Na^+ ion: 2.86 (±0.42) H^+ ion: 2.25 (±0.25)	Na^+ ion: 0.30 (±0.10) H^+ ion: 0.74 (±0.14)
5-Oxoazelaic acid ($C_9H_{14}O_4$)	Na^+	186.089		5.48 (±0.14)	0.02 (±0.01)
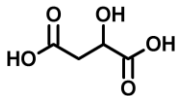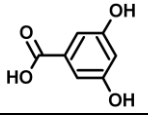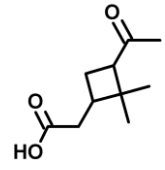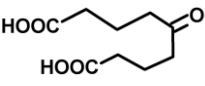
Ionization sensitivity calibrations were performed by adding four to five concentrations of organic acid standard stock solutions ($10^{-5} - 10^{-3}$ M) to the aqueous OA matrix to achieve total organic acid concentrations of $0.1 - 100$ μg mL^{-1}) and recording HR-ESI-MS spectra. Table 5.1 shows the chemical structures and properties of the standards: malic acid ($C_4H_6O_5$), 3,5-dihydroxybenzoic acid ($C_7H_6O_4$), pinonic acid ($C_{10}H_{16}O_3$) and 5-oxoazelaic acid ($C_9H_{14}O_4$). All standards were purchased from Sigma-Aldrich, Inc., with the highest possible chemical grade. Standards varied in size and chemical functionality (diacids vs. monoacids, aromatic vs. aliphatic). When picking the standards, we required that they had different molecular formulas from the compounds already present in OA. The volume of added standards did not exceed 10 % of the total volume, and therefore did not significantly dilute OA compounds.

OA mixtures in water, spiked with known amounts of the organic acid standards, were electrosprayed into a high-resolution linear-ion-trap (LTQ) Orbitrap™ mass spectrometer in the positive ion mode. The mass range of m/z $100 - 2000$ was used for experiments, although analyte compounds in the OA did not exceed 600 Da in size. Samples were introduced with direct infusion using a flow rate of $0.5 - 1$ μL min^{-1} and ionized with a spray voltage of 4 kV. Analyte compounds were detected as sodiated $[M+Na]^+$ and/or protonated $[M+H]^+$ species. The HR-ESI-MS analysis and data processing was performed as described in Sections 1.3.3 and 1.3.4, respectively. The molecular formulas of the ions were converted to "neutral" molecular formulas (M) by subtracting the exact mass of a proton or sodium cation. The individual calibration curves were fit to an appropriate model using least-squares analyses. The degree of deviation from a linear fit were used as a comparison metric and is reported as the correlation coefficient R^2, ranging from 0 (poor fit) to 1 (perfect fit).

5.4. Results and discussion

5.4.1. Calibration of organic acid standards in complex OA mixtures.
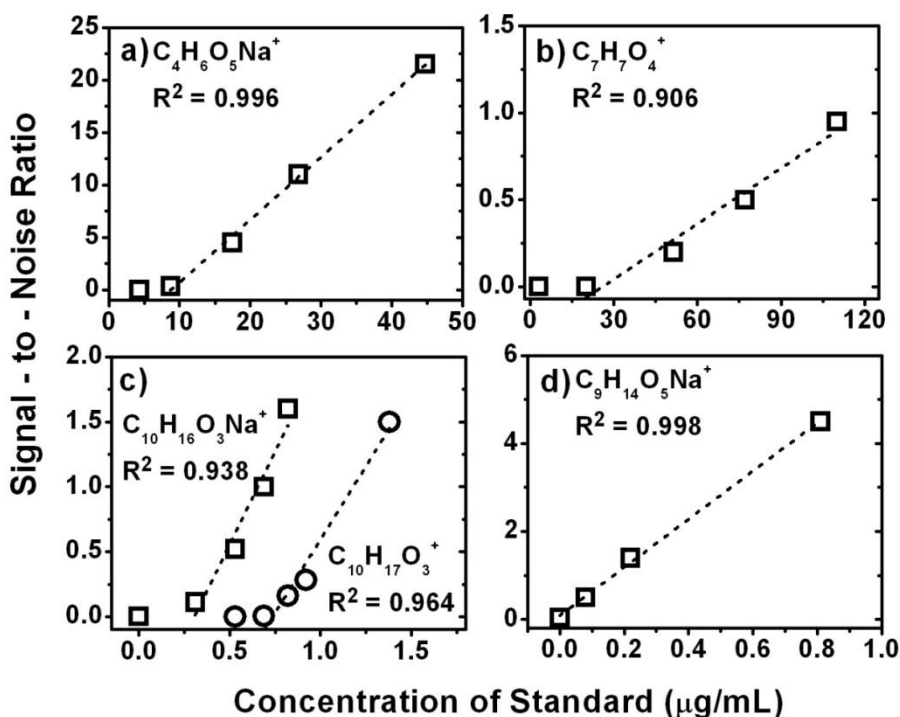
Figure 5.1: Sensitivity response for protonated and/or sodiated peaks from (a) malic acid (b) 3,5-dihydroxybenzoic acid (c) pinonic acid and (d) 5-oxoazelaic acid. See Table 5.1 for additional information about the standards. Only data above the LOD are included in the linear fit.

A calibration was performed to establish the sensitivity of the HR-ESI-MS technique in detecting molecules of varying size and structure in complex OA mixture. The OA matrix includes multifunctional organic acids, organic nitrates, carbonyls, and other types of oxygenated compounds present as monomeric and oligomeric structures [36, 38, 40]. The OA composition is dominated by aliphatic molecules (average H/C ~ 1.6) that are highly oxidized (average O/C ~ 0.8) with a wide distribution of molecular weights (MW = 100-600 g mol^{-1}). Although the MW of the standard compounds (MW < 200 g mol^{-1}) are lower, the degree of oxidation (O/C = 0.3 − 1.2) exhibits good overlap with the isoprene OA and other oxidized complex organic matter in

116

ambient samples. High-MW standards with high O/C and high chemical functionality were not available, which limited the mass range of our study.

Figure 5.1 shows that the ion intensities of the standard compounds are proportional to their spiked concentrations in the complex OA mixture. The dependence is almost linear ($R^2 >$ 0.9) with respect to standard concentration. Negative signs of the intercepts suggest that analyte compounds are not detected below a certain threshold, and different values of the intercepts suggest that the threshold is dependent on the nature of the analyte. In general, ESI sensitivity is a measure of ion signal response to concentration; thus, we define the effective sensitivity (α) as the linear slope of the ion signal (I_i) vs. mass concentration of the analyte ($[A]_i$). The effective limit of detection (LOD) is defined as the analyte concentration at which the signal intensity drops below the noise level ($I = 0$).

$$I_i = \alpha \,[A]_i + \beta \quad (E\ 5.1)$$

$$LOD = -\,\beta/\alpha \quad (E\ 5.2)$$

The effective sensitivity reported in this work measures the detected ion abundance of the analyte of interest in parallel to other compounds in a complex matrix. We note that ionization efficiencies studied in previous works are measures of the ability of a compound to form gas-phase ions from a single- or two-component solution. Most molecules in our HR-ESI-MS studies were ionized through a selective mechanism resulting in formation of either protonated or sodiated species, but some molecules like pinonic acid were detected as both sodiated and protonated species. The effective sensitivities for such analytes were obtained by summing up the observed intensities of the $[M+H]^+$ and $[M+Na]^+$ ions. In studies considering only protonation, the total ionization efficiencies for compounds like pinonic acid may be underestimated if there is a sufficient concentration of sodium ions.
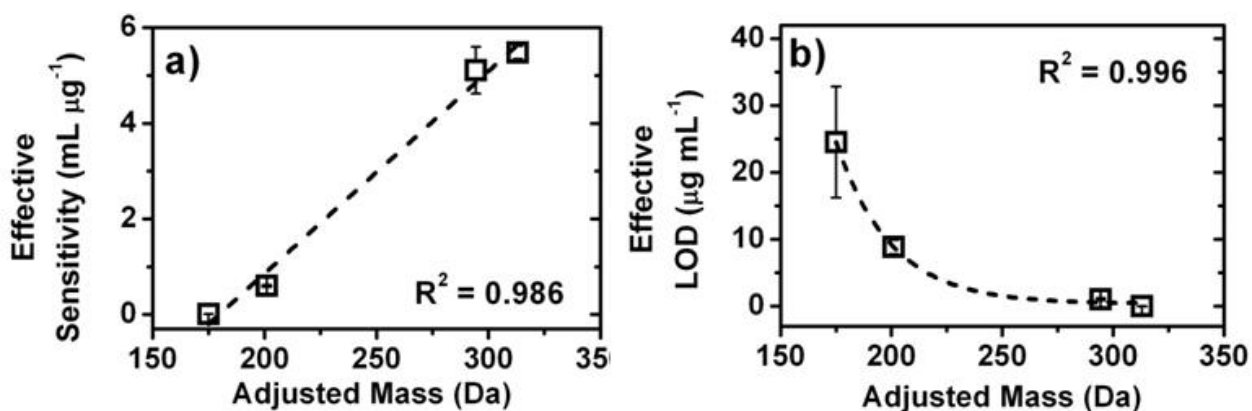
Figure 5.2: Sensitivity and LOD as a function of adjusted mass [AM=(neutral mass) x (H/C ratio)]. Justifications for correlating the effective sensitivity with AM are provided in the text.

Figure 5.2a shows that the effective ESI sensitivities for each standard, α_i, correlate well with the product of neutral molecular mass and H/C ratio (proxy for degree of unsaturation), which we term *adjusted mass* (AM, units of Da).

$$AM = (H/C) \text{ x (molecular mass)} \quad (E\ 5.3)$$

H/C is commonly used to characterize structure of OA compounds [82, 203] but has not been considered as a factor relevant to the ESI ion intensity. The ESI sensitivity for the four standards increase linearly with AM ($R^2 = 0.986$), suggesting AM is a good parameter to use for calibration. The correlation to AM reflects an expected dependence of ionization efficiency on mass and the structure of the standard compounds.

The ESI sensitivity and LOD may not be necessarily a linear function of AM for every sample matrix. However, we suggest that they will strongly correlate to AM in one or another functional form. Nonlinear functions may also be appropriate for parameterizing sensitivities vs. AM, for example, an exponential rise to a maximum, $y[x] = y_0 + A \cdot \exp[-R_0 \cdot AM]$ can be fit to data in Fig. 5.2a with $R^2 = 0.973$ (not shown). The exponential function is more appropriate for high MW compounds because effective sensitivities and LOD (Fig. 5.2b) exhibit asymptotic

118

behavior at higher AM. The higher AM values correlate to lower unsaturation (π-electron density) but higher average polarizability, which may have opposite effects on ionization in each homologous series. Similar saturation behavior in properties like GB at higher AM are observed, which is discussed later in the paper.

The ESI sensitivity correlates poorly with molecular mass ($R^2 = 0.559$) and H/C ratio ($R^2 = 0.489$) individually. The correlation of ESI sensitivity to O/C is similarly poor ($R^2 = 0.299$) and furthermore, O/C cannot be used as a calibration parameter for unoxidized molecules. The fitting parameters for standard compounds are summarized in Table 5.1. It is remarkable that AM is a better dependent variable for our experimental calibration than molecular mass or H/C individually. We propose that the correlation between the effective sensitivity and AM is neither unique to our experiments nor to the specific set of carboxylic acids used as standard compounds. The observed dependence of sensitivity on AM provides the basis for the calibration procedure reported in this study.

LOD is also a function of AM, and increases sharply at low AM (Fig. 5.2b). This observation exemplifies the strong bias of ESI against small molecules when a significant concentration of competing analytes is present. For example, approximately 10 μg mL^{-1} of malic acid (M+Na$^+$ ion m/z 157) in the OA mixture is needed to overcome the effective LOD, compared to ≤ 0.03 μg mL^{-1} needed for 5-oxoazelaic acid (M+Na$^+$ ion m/z 225). In addition to the matrix effects, the high value of LOD for small compounds may also be a reflection of specific experimental conditions used in this work, such as relatively high tube lens voltage (150 V) that reduced the transmission of the low-mass ions into the LTQ. The calibration described in this study must be carried out for specific ESI-MS conditions and can then be applied to all experiments performed under those conditions. However, the variability in the LOD values

indicates that the calibration for analytes of interest needs to be performed *in a realistic matrix*, as opposed to pure solvent.

5.4.2. Application of sensitivity calibration to a complex mass spectrum.

The suggested calibration procedure is applied to an HR-ESI-MS mass spectrum after peak extraction and formula assignment, which makes it possible to calculate AM values for each compound in the mixture from the assigned formulas. We use neutral molecular formulas to calculate AM. The peak intensities are calculated as the sum of intensities of both sodiated and protonated ions. Suitable parameterizations of $\alpha_i(AM)$ (Fig. 5.2a), and LOD*(AM)* (Fig. 5.2b) functions are then used to convert peak intensities into concentrations of individual species:

$$[A]_i = I_i/\alpha(AM) + LOD(AM) \qquad \text{(E 5.4)}$$

Eq. (5.4) can be used as an estimate of the concentration of the analyte. An additional constraint on the total mass concentration of analytes (in is work 200 µg mL^{-1}) in Eq. (5.5) can optionally be used to further re-normalize the $[A]_i$ values calculated from Eq. (5.4) so that

$$\sum_0^n [A]_i = \text{total concentration} = 200 \ \mu\text{g mL}^{-1} \qquad \text{(E 5.5)}$$

Because Equation (5) readjusts the predicted $[A]_i$ values, the calibration is the most sensitive to the *relative* AM-dependent ionization efficiencies of analytes. This effectively reduces errors of the predicted analyte concentrations. Without the normalization, the sum of predicted $[A]_i$ for several OA samples of varying composition were a factor of $2 - 6$ higher than the estimated total organic concentration. As a comparison, the quantitative analyses of peptides in ESI-MS is achieved within a factor of $3 - 5$ of the true value when calibrating with respect to several observable parameters [287].

Figure 5.3 shows the result of applying the calibration to an experimental mass spectrum of isoprene photooxidation OA in water. The ratio of $[A]_i/ I_i$ is a measure of change in ion

abundance relative to the experimentally observed spectrum. A constant value of $[A]_i/I_i$ throughout the mass spectrum indicates identical sensitivities of analytes in the matrix. The lower mass range has higher $[A]_i/I_i$ ratios relative to the higher mass range after applying the calibration because of the lower ionization efficiency of low MW analytes in ESI and bias in ion transmission resulting from potentials used in this study.
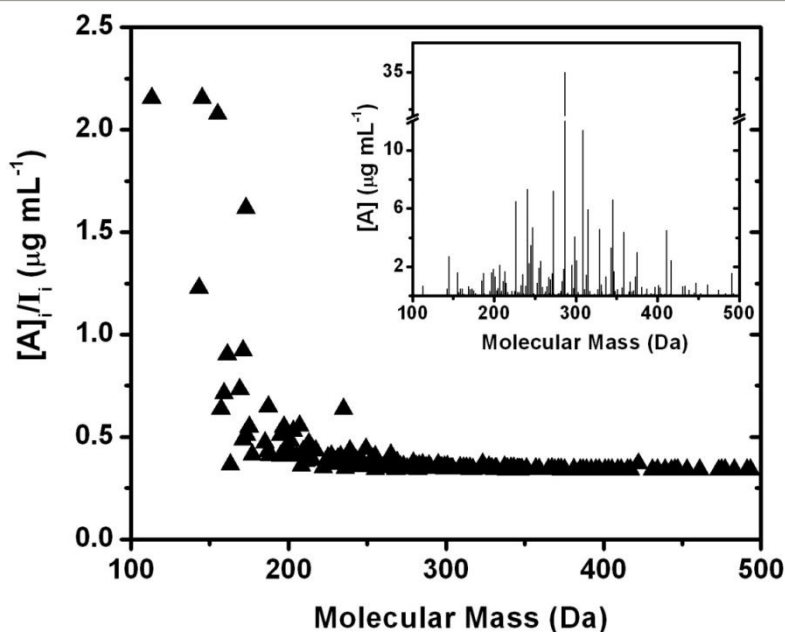
Figure 5.3: An application of the sensitivity-AM correlation to a mass spectrum of isoprene OA dissolved in water. The main graph shows the ratio between the estimated mass concentration and the corresponding peak intensity in the raw mass spectrum. The largest variation occurs at low m/z region where the calibration with standards doped in OA matrices enhanced the signal contribution from low-MW analytes. The inset shows the resulting calibrated mass spectrum.

Higher molecular mass analytes in the range 300 – 600 Da were generally treated as having similar ionization efficiencies due to the asymptotic behavior of the calibration curve of both sensitivity and LOD toward higher AM. This is reflected in the similar $[A]_i/I_i$ ratios of analytes with masses > 300 Da. The main source of variance from the $[A]_i/I_i$ trend is due to the different H/C of OA compounds. For this particular sample, the range over which H/C varies is

relatively small because isoprene OA contains mostly aliphatic molecules (<H/C> = 1.55 ± 0.14). The insert in Figure 5.3 shows the calibrated [A]$_i$ values for each detected compound. The shape of the mass spectrum is generally preserved after applying the calibration but the low masses are enhanced relative to the raw mass spectrum.

The approach to assign mass concentrations by application of Eq. (5.4) and (5.5) in series makes an important simplifying assumption that HR-ESI-MS detects the majority of organic molecules present in the sample. The accuracy of this assumption depends on the sample. The majority of organic molecules ionize well as either protonated or sodiated species in the positive ion mode ESI, but some samples may contain compounds (e.g. small organosulfates, saturated hydrocarbons, etc.) that are poorly-ionizable in the positive ion mode. The appropriate choice of standards becomes increasingly important in these cases.

5.4.3. The adjusted mass axis.

The dependence of the ESI sensitivity on AM is consistent with other accounts in which both molecular size and degree of unsaturation of organic compounds affects experimental ESI response [305, 306]. This association of ESI sensitivity with AM may be rationalized in terms of the effects of the molecular size and structure on the key physico-chemical properties that affect protonation and/or sodiation of organics. These properties [104, 291, 295, 307, 308] include a) the ability of the analyte to form cations in the gas phase, which is controlled by GB and sodium affinity and b) the ability of the analyte ion to stabilize charge, which is controlled by molecular size (mass and volume), degree of conjugation, and average polarizability. However, any particular parameter may have different levels of influence on the ionization efficiencies of different homologous series [290]. We focus on GB and polarizability as representative

122

properties as large compilations of data are available in the literature for many compound classes.
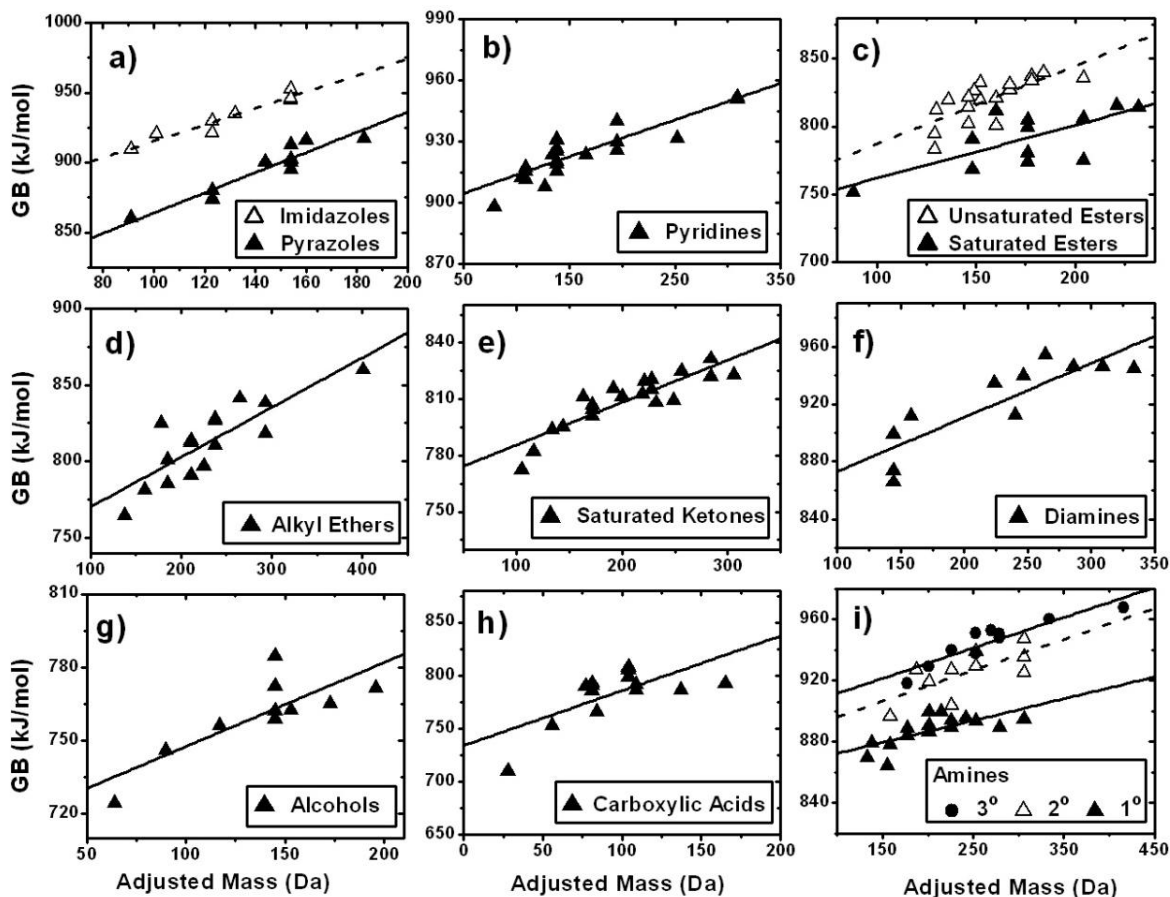
Figure 5.4: Gas-phase basicity (GB) as a function of adjusted mass for 13 classes of molecules (Ref. [37]). Linear least-squares fits have been applied and correlation coefficients are reported in Table 2. Identities of compounds used for analysis are reported in Table B1 of Appendix B.

Figure 5.4 shows that GB correlates well with AM for 13 classes of compounds. Each class of compounds includes 8 – 23 molecules, depending on the availability of data taken from Ref. [309] and references therein. The identities of the compounds used for statistical analysis and their PA, GB, and volume (calculated from atomic radii) values are listed in Table B1 of Appendix B. PA and volume show similar trends with AM as GB (not shown). Linear fits of GB

123

Table 5.2: R^2 values for linear least-squares fit for GB (kJ/mol) as a function of adjusted mass (AM) for 13 classes of molecules. Residual sum of squares (RSS) ratios (please see text for definition) for correlations of AM vs. molecular mass and H/C provides an effective metric for an *improvement in fit.*

Compound Class	# points	Lin. R^2 (AM)	RSS Ratios (mass)	(H/C)
Imidazoles	8	0.921	11	10
Pyrazoles	13	0.886	5.7	8.8
Pyridines	23	0.867	1.9	1.1
Saturated esters	15	0.533	0.7	1.8
Unsaturated esters	15	0.571	1.1	2.0
Alkyl ethers	16	0.687	0.7	2.2
Saturated ketones	20	0.882	1.4	4.1
Diamines	11	0.862	3.9	2.4
Primary amines	16	0.484	1.1	1.5
Secondary amines	11	0.505	0.8	0.9
Tertiary amines	11	0.835	0.8	1.3
Alcohols	10	0.652	1.3	1.1
Carboxylic acids	12	0.465	0.6	0.9
Average values		0.700	2.4	2.9

with respect to AM are shown in Figure 5.4 for each compound class. There is no particular reason to expect a linear, exponential or other type of dependence of GB on AM; however, we use correlation coefficients of linear fits as a semi-quantitative comparison for using AM vs. molecular mass or H/C as a calibration parameter. We note that for many types of compounds, there appears to be a saturation effect for GB at higher AM, consistent with our previous suggestion that calibration is more important for lower masses.

Table 5.2 reports correlation coefficients (R^2), and the ratios of residual sum of squares (RSS) from correlations of GB to AM compared to correlations of GB to molecular mass or H/C for each compound class. RSS ratios provide a convenient metric for comparing the appropriateness of using these parameters for calibration. As low values for RSS indicate better correlation, values of ($RSS_{H/C}/RSS_{AM}$) or (RSS_{mass}/RSS_{AM}) greater than unity imply that AM is a

better parameter for the correlation than either molecular mass or H/C. For the linear correlations reported in Table 5.2, AM is either as good of a parameter to use for calibration (RSS ratio = 1) or better (RSS ratio > 1), based on GB, when comparing to molecular mass and H/C ratio. On average, the correlation of GB with AM is a factor of 2-3 better.
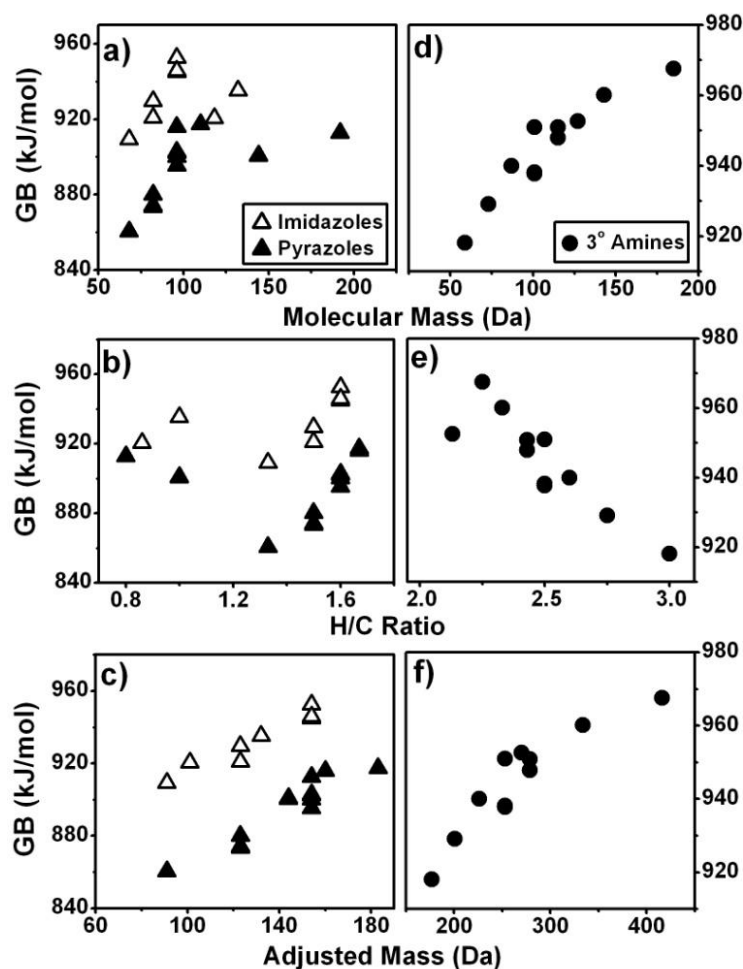
Figure 5.5: GB as a function of molecular mass, H/C ratios and AM for (a-c) imidazoles and pyrazoles and (d-f) tertiary amines.

Examples of the significant improvements in fit with the AM axis are illustrated in Figure 5.5(a-c) for imidazoles and pyrazoles, for which the GB exhibits poor correlation with molecular mass and H/C ratios. GB of alcohols, amines, and alkyl ethers are negatively correlated with H/C

for reasons previously discussed (Section 5.4.1); the correlation is positive for nearly all other families of compounds. This observation is consistent with other experimental and theoretical accounts where alcohols, amines and aliphatic ethers deviate in ionization behavior from other compound classes [104]. Despite varying effects of degree of unsaturation on GB, the correlation of GB on AM is always positive. Figures 5.5d-f illustrate this point for tertiary amines, the GB of which decrease with H/C but increase with molecular mass and with AM. Therefore, even though molecular mass and H/C can provide good correlations with GB for some compound classes, these parameters taken individually do not represent ionization as well as their product does.
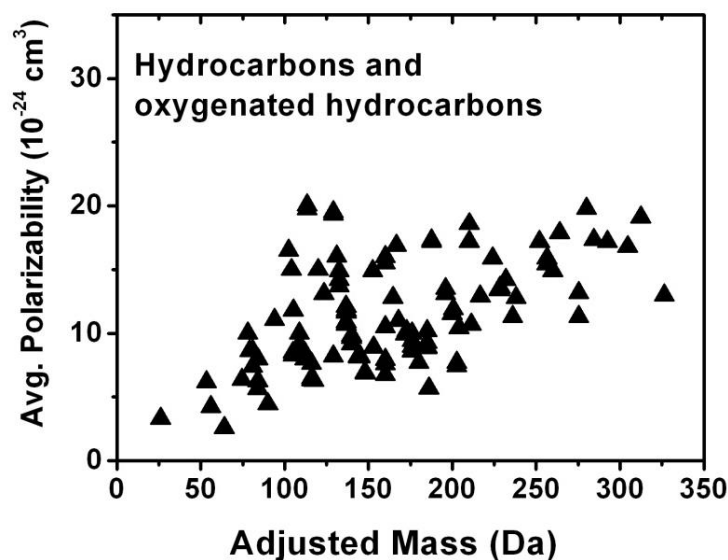
Figure 5.6: Dependence of average polarizability on adjusted mass for hydrocarbons and oxygenated hydrocarbons listed in Table B2 of Appendix B.

Figure 5.6 shows that the average polarizability (cm^3), which determines the strength of the electrostatic interaction between a positive charge and the analyte, is also well-correlated with AM for a large class of hydrocarbons and oxygenated hydrocarbons [310] listed in Table B2 of Appendix B. This increase in average polarizability with respect to AM is expected

126

because polarizability increases with larger molecular size and greater *s* character of the bonds in the molecule [311], both of which result in higher AM values. Similarly to GB, there is a polarizability saturation effect with size as the change in size becomes increasingly smaller in relation to the total size of the molecule. Polarizability affects sodium affinity and GB to a large extent [312-314] and it is reasonable to assume that both the strength of sodium binding and protonation will increase with AM. It is important to emphasize that even though individual physico-chemical properties considered in this study are correlated with AM, positive ion mode ionization will depend on the combination of many factors. Therefore, experimental calibration of the type performed in this work is essential.

Chapter 6: Direct Aqueous Photolysis of Isoprene High-NOx SOA

6.1. Abstract

SOA generated from the high-NOx photooxidation of isoprene was dissolved in water and irradiated with $\lambda > 290$ nm light to simulate direct photolytic processing of organics in atmospheric water droplets. High-resolution mass spectrometry was used to characterize the composition at four time intervals (0, 1, 2, and 4 h). Photolysis resulted in the decomposition of high molecular weight (MW) oligomers, reducing the average length of organics by 2 carbon units. Approximately 65% by count of SOA molecules decomposed during photolysis, accompanied by the formation of new products. An average of 30 % of the organic mass was modified after 4 h of direct photolysis. In contrast, only a small fraction of the mass (< 2 %), belonging primarily to organic nitrates, decomposed in the absence of irradiation by hydrolysis. We observed a statistically-significant increase in average O/C, decrease in H/C, and increase in N/C ratios resulting from photolysis. Furthermore, the concentration of aromatic compounds increased significantly during photolysis. Approximately 10 % of photodegraded compounds and 50 % of the photoproducts contain nitrogen. Organic nitrates and multifunctional oligomers were identified as compounds degraded by photolysis. Low-MW 0N (compounds with 0 nitrogen atoms in their structure) and 2N compounds were the dominant photoproducts. Fragmentation experiments using tandem mass spectrometry (MS^n, n = 2-3) indicate that the 2N products are likely heterocyclic/aromatic and are tentatively identified as furoxans. Although the exact mechanism is unclear, these 2N heterocyclic compounds are produced by reactions between photochemically-formed aqueous NOx species and SOA organics.

6.2. Introduction

Atmospheric fog and cloud droplets are effective scavengers of water-soluble secondary organic aerosols (SOA) and volatile organic compounds (VOC) [315-319]. The aqueous-phase processing in these systems is starting to be recognized as a key aging mechanism for atmospheric organic material (OM), with the most important abiotic processes initiated by sunlight. Photo-induced processing pathways for OM in cloud/fog water include *direct photolysis* where the organic compounds absorb radiation and undergo aqueous-phase chemical transformations, and *indirect photolysis* where solar radiation initiates chemistry through the production of non-selective oxidants like hydroxyl radical (OH) or through photosensitized energy transfers [320, 321]. The non-photolytic fates of OM in cloud/fog droplets include hydrolysis [76, 322] and evaporative processing with inorganic ions [96, 318, 323-325].

Aqueous photoprocessing in general, including both direct and indirect photolysis dramatically modifies the OM composition [326, 327], which alters the optical [65, 328] and physical [329] properties of the OM. Direct and indirect photolysis occur simultaneously and their relative importance is highly dependent on atmospheric conditions (OM concentration, pH, inorganic ion concentration, radiation flux, and temperature) and the physico-chemical properties of the individual organic compounds (absorption cross section, photolysis quantum yield, and reactivity towards OH). For example, at pH > 4, the measured rates of direct and indirect photolysis of dinitrophenols in water are comparable, but indirect photolysis becomes more important at lower pH values [330].

Much attention has been paid to the indirect aqueous photolysis of OM with the OH radical. The bulk of the research was focused on common water-soluble organic compounds including glyoxal and pyruvic acid, which produce high molecular weight (MW) oligomers

when irradiated in the presence of H_2O_2 as an OH source [65, 131, 163, 176, 254, 326, 327, 331-335]. Fewer articles focused on the photochemistry of complex mixtures [329, 336], such as irradiation of SOA extracts mixed with H_2O_2 generating highly-oxidized compounds. As aqueous photochemistry is highly matrix-dependent, studying complex aqueous mixtures such as dissolved SOA is more representative of atmospheric cloud and fog chemistry, although it will lead to dramatically greater complexity in the product distribution. However chemical analysis of such mixtures is possible using advanced separation and/or high resolution mass spectrometry techniques (HR-MS) [82, 91].

In cloud and fog water, the overall concentration of multicomponent dissolved OM is considerably higher than the concentrations of individual organic compounds, which are typically in the $10^{-12} - 10^{-6}$ M range. Measured OM concentrations approach 200 µg/mL in some locations (or up to 10^{-3} M assuming a molecular weight of 200 g/mol for a typical OM compound) [304, 337-344]. In smaller aqueous droplets or in polluted areas, $[OM]_{dissolved}$ can be high and the oxidative capacity of OH may be too low to oxidize all dissolved organics during the droplet lifetime. Furthermore, higher OM concentrations have also been shown to suppress photochemical OH production [345], sometimes diminishing the importance of OH-initiated chemistry almost entirely without significantly perturbing the efficiency of direct photolysis for photolabile compounds [346].

Sparse literature is available on direct aqueous photolysis of atmospherically-relevant OM even though many abundant water-soluble OM compounds, e.g., organic nitrates and carbonyls, are readily affected by direct photolysis due to their significant absorption cross sections in the actinic wavelengths [347-356]. Furthermore, organic nitrates with a neighboring carbonyl group, which are relevant to SOA, have enhanced absorption cross sections in the near

UV wavelengths [348, 349]. Previously, the effect of direct aqueous irradiation on OM composition has been studied only for pyruvic acid [335], phenols [357], and extracts of limonene/ozone SOA [358]. These direct photolysis studies can result in either a net gain or loss in high-MW species, depending if the experiments focused on single compounds or SOA mixtures, again underscoring the dramatic matrix effects.

Direct photolysis rates can be estimated for carbonyls in aqueous extracts of biogenic SOA ($J \sim 2 \times 10^{-6}$ s^{-1}) [358], aqueous solutions of organic peroxides ($J \sim 4 \times 10^{-5}$ s^{-1}) [359], organic nitrates ($J \sim 1 \times 10^{-6} - 4 \times 10^{-5}$ s^{-1}) [348] under clear-sky conditions. Likewise, assuming a near diffusion-limited rate for aqueous OH reaction ($k \sim 1 \times 10^{9}$ M^{-1} s^{-1}) [360] and using the measured [OH] observed in California's Central Valley fog droplets ([OH] $\sim (2 \times 10^{-16} - 4 \times 10^{-15}$ M) [361], a first-order rate constant range of $k_{eff} \sim (2 \times 10^{-7} - 4 \times 10^{-6})$ s^{-1} can be estimated for the non-selective aqueous OH reaction, which is comparable with expected J values for direct photolytic processes. Much higher [OH] values have been modeled in clouds ($\sim 10^{-13}$ M) [362, 363], which would significantly increase k_{eff} relative to J. Although the importance of direct photolysis is dependent on specific atmospheric conditions and chemical system, it is expected to be the dominant photoprocessing mechanism of OM under many atmospherically-relevant scenarios.

This work focuses on the characterization of molecules produced and decomposed in the direct photolysis of aqueous extracts of SOA generated from the high-NOx photooxidation of isoprene (C_5H_8), the most abundant non-methane hydrocarbon in the atmosphere [364, 365]. We also report the effects of hydrolysis in the dark for the same SOA mixture, as this process cannot be completely decoupled from aqueous photolysis. The gas-phase photooxidation of isoprene under high-NOx conditions produces water-soluble compounds such as organic acids, carbonyls

and alcohols in the aerosol phase [30, 36, 37, 39, 41, 191]. In particular, the substantial fraction

of organic nitrates in the SOA (18 – 30 % by count) [38] is expected to be photolabile, and this

work is the first account of the aqueous photolysis of organic nitrates in the presence of other

dissolved organic compounds. A dramatic change in the composition of aqueous isoprene SOA

extracts is observed, compared to the minor change induced by hydrolysis of the same sample in

the dark. The most significant change in composition is due to nitrogen-containing organic

compounds (NOC), reflected by the large increase of heterocyclic compounds containing 2

nitrogen atoms.

6.3. Experimental

6.3.1. Secondary organic aerosol generation
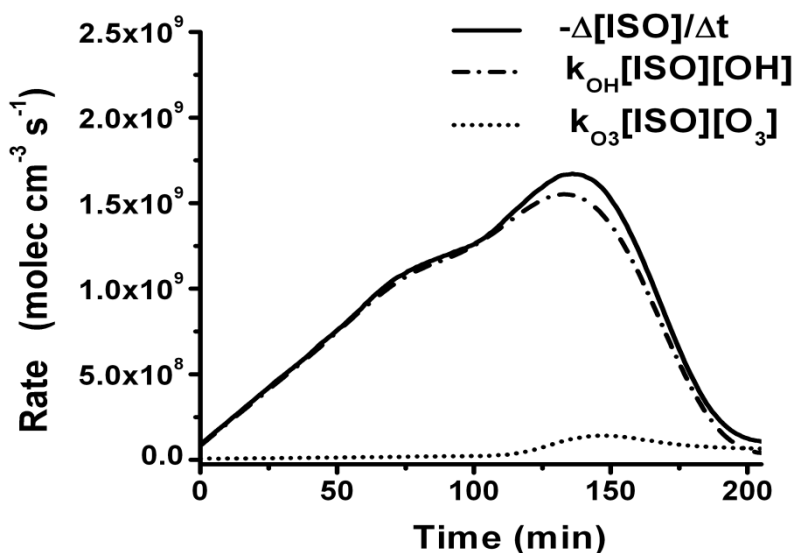
Figure 6.1: Relative contribution of OH and O_3 chemistry to the high-NOx photooxidation of isoprene. The rate of the O_3 + isoprene reaction, $R_{O3} = k_{O3}[O_3][ISO]$ was calculated from the measured concentrations of O_3 (ozone photometer) and isoprene (PTR-ToF-MS). The rate of the OH + isoprene reaction could then be calculated as the difference, $R_{OH} = -d[ISO]/dt - R_{O3}$. The results show that ozone did not make a significant contribution to isoprene oxidation under present conditions.

SOA were generated from the photooxidation of isoprene in the UCI Chamber as described in Section 1.3.1. No inorganic seed aerosols were used. The reaction was carried out at 22°C in the relative humidity (RH) range of 60-70%. Initial mixing ratios of isoprene, NO, NO_2, and O_3 in the chamber were 500 ppb, 700 ppb, 100 ppb and < 5 ppb, respectively. No additional precursors for OH radicals were added. The photooxidation time was approximately 5 h. The majority of isoprene and first-generation products reacted with OH; the estimated contribution of O_3-oxidation to product formation was < 10% (Fig. 6.1). Particle mass accumulated quickly after 2 h of irradiation and SOA mass concentration reached 100 μg m^{-3} at the time of collection (Fig. 6.2a). The time-dependent mixing ratios of NO, NO_y-NO, and O_3 and relevant volatile organic compounds are shown in Fig. 6.2a and 6.2b, respectively, for a typical experiment. The SOA was collected through an activated charcoal denuder onto Teflon filters (Millipore 0.2 μm pore), which were immediately vacuum sealed and deep-frozen for offline photolysis experiments and HR-MS analysis.
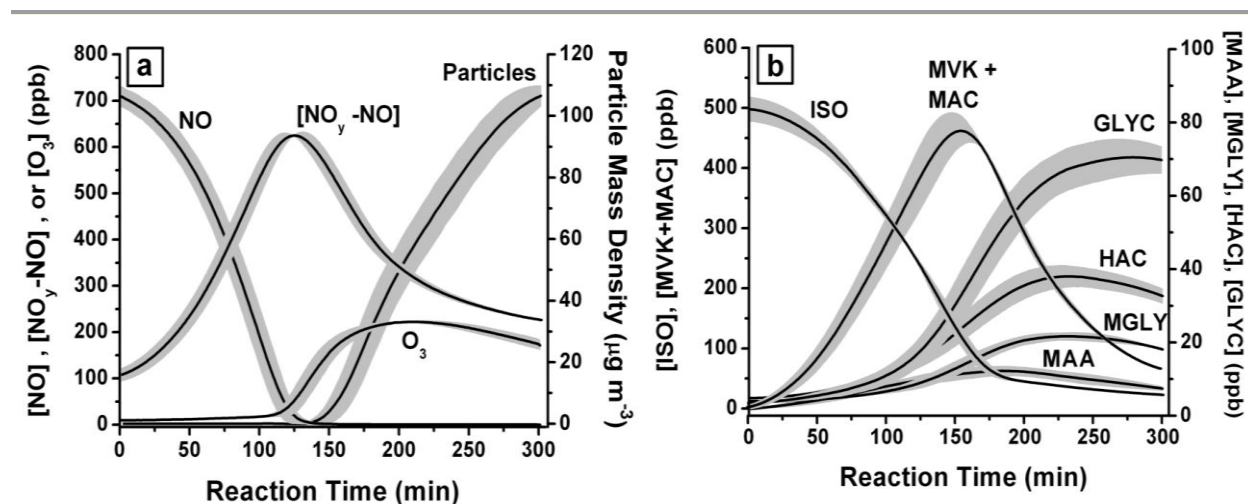
Figure 6.2: Time evolution of (a) oxidants and particles and (b) select VOC in the high-NOx photooxidation reaction including: isoprene (ISO), the sum of isobaric methylvinylketone and methacrolein (MVK+MAC), methacrylic acid (MAA), glycolaldehyde (GLYCOL), hydroxyacetone (HAC), and methylglyoxal (MGLY). Gray shading represents the error between repeated experiments.

134

6.3.2. Aqueous photolysis and control experiments

Filter SOA samples were extracted in $1.5 - 2$ mL water (Fluka, HPLC grade) with 10 min sonication, used to obtain a total aqueous concentration of approximately 200 μg mL^{-1}, comparable to the high OM ratios detected in fog water. [304] Two photolysis experiments and one dark (no irradiation) control experiment were performed with the aqueous SOA extracts in otherwise identical fashion.
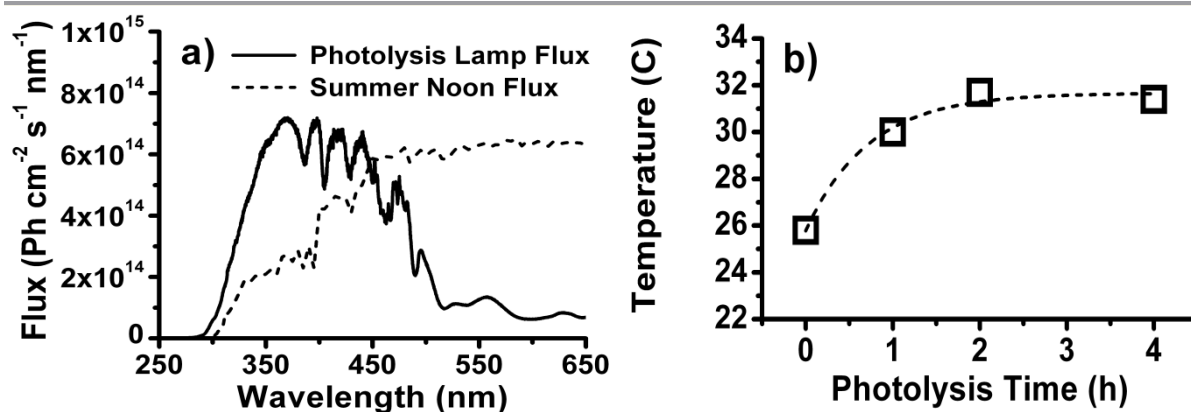
Figure 6.3: Characterization of (a) the flux from the photolysis lamp compared modeled solar flux under summer clear-sky conditions and (b) the temperature change of an aqueous sample under the lamp for the $0 - 4$ h photolysis time period used in this work. The solar flux was calculated using the "Quick TUV" calculator, available at the UCAR website http://cprm.acd.ucar.edu, using the following parameters: SZA = 0, 300 Dobson overhead ozone, surface albedo of 0.1, ground elevation and altitude = 0 km.

The light source used for photolysis experiments was a Xe arc lamp (Newport Optics model 66905 lamp housing and model 69911 power supply). A 90-degree dichroic mirror ($280 - 500$ nm) was used to reduce the visible and IR radiation, and a glass filter was used to remove UV radiation with $\lambda < 290$ nm. The wavelength dependence of the photon flux was measured by a fiber-optic spectrometer (Ocean Optics, USB4000) and the integrated light intensity was measured by a laser power meter (Coherent FieldMate). The wavelength-dependent photon flux is shown in Figure 6.3a, where it is compared with a modeled ground-level solar flux [366]

assuming zenith angle = 0°. The main difference between the experimental flux and solar flux exists in the more-energetic λ < 350 nm region. Based on the total integrated flux for λ < 350 nm, we estimate that 1 h photolysis under our lamp equates up to 3 h photolysis under the overhead sun. The exposure durations reported in this work have not been converted to the equivalent atmospheric values.

The temperature of a blank aqueous sample was monitored under actual photolysis conditions with a K-type thermocouple to gauge the contribution of thermal decomposition of the sample on the time scale of the experiment. Figure 6.3b shows that temperature in an aqueous sample increased by approximately 5 °C after 2 h and stabilized at 31°C from 2 h to 4 h. We observe a constant rate of the production of photoproducts throughout photolysis, which serves as an indirect indication that temperature effects were minimal. As the samples were open to air during photolysis dissolved oxygen was present in the solution, likely at the near-equilibrium solubility level.

During photolysis experiments, 50 µL aliquots of the aqueous SOA sample were removed with a gas-tight syringe (Hamilton, 250 µL), without interruption of photolysis, at 0, 1, 2, and 4 h intervals for high-resolution electrospray ionization (ESI) mass spectrometry analysis. Control samples kept in dark were analyzed similarly.

6.3.3. High resolution electrospray ionization mass spectrometry (HR ESI-MS)

ESI-MS experiments were performed with LTQ-Orbitrap in the positive ion mode with a mass range of m/z 100 – 2000. Aqueous extracts of photolyzed SOA were directly sprayed into the mass spectrometer at a flow rate of 0.5 – 1 µL min^{-1} and ionized with an operating voltage of 4 kV. No other solvents were added in order to characterize only the water-soluble fraction. Analyte compounds were detected as sodiated [M+Na]$^{+}$ and/or protonated [M+H]$^{+}$ species.

Table 6.1: Positive ion mode ESI characterization of organic mono- and di-acid standards in aqueous isoprene SOA sample matrix. Collision induced dissociation (CID) energy is the threshold energy when accompanying loss fragments are produced. Loss fragments are neutral compounds ejected from the CID of the monomer standard or its dimer.

Standard	Structure	CID Energy	Loss Fragments
malic acid $(C_4H_6O_5)$ Detected as Na^+ ion	 134.022 Da	Monomer (23 units) Dimer (0-8 units)	Monomer (CO) Dimer (H_2O, CH_2O_3, C_4H_6O)
tartaric acid $(C_4H_6O_6)$ Detected as H^+ ion	 150.016 Da	Monomer (18 units) Dimer (0 units)	Monomer (C_2H_2O, H_2O) Dimer (CH_2O_3, $C_4H_6O_6$)
3,5-dihydroxy benzoic acid $(C_7H_6O_4)$ Detected as H^+ ion	 154.027 Da	Monomer (16 units) Dimer (N/A)	Monomer (CO_2, H_2O) Dimer (N/A)
pinonic acid $(C_{10}H_{16}O_3)$ Detected as both Na^+ and H^+ ions	 184.110 Da	Monomer (25 units) Dimer (10 units)	Monomer (N/A) Dimer (H_2O, C_4H_6O)
5-oxoazelaic acid $(C_9H_{14}O_4)$ Detected as Na^+ ion	 186.089 Da	Monomer (28 units) Dimer (0 units)	Monomer (H_2O) Dimer ($C_9H_{14}O_4$)
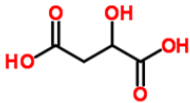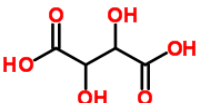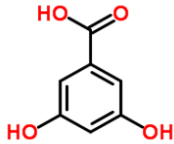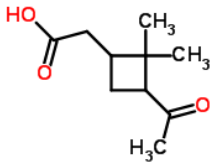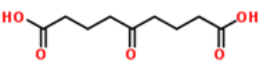
Additional details about the ESI analysis can be found in Section 1.3.3. Data analysis was performed as described in Section 1.3.4. Similarly to our previous works [38, 39, 79]. Background signals obtained from analyses of blank filters sonicated in water were deleted from

sample mass spectra. Peaks in the samples that could not be unambiguously assigned to protonated or sodiated molecules with the atomic restrictions used in this work ($C_cH_hO_oN_{0-2}Na_{0-1}^+$ ions) were insignificant and accounted for *ca.* 2% of the total signal. Mass spectra shown henceforth present only assigned peaks, with the *m/z* values converted into the molecular weights of the corresponding neutral precursors.

The signal intensities of the detected molecules were converted to approximate mass concentration using an ESI sensitivity calibration approach described in Chapter 5. The calibration was performed with multifunctional carboxylic acid standards, followed by scaling the summed signal by the total organic mass concentration ($\sim$ 200 µg mL^{-1}). It is important to emphasize that due to the simplifying assumptions made in the sensitivity calibration, the analyte concentrations should be treated as an approximation and any errors are reported as a measure of precision (one standard deviation of duplicate trials) not as estimates of accuracy. The raw intensity distributions for SOA mass spectra are not drastically altered by the intensity-to-mass conversion. Data in the text will be henceforth presented in terms of mass concentration in units of µg mL^{-1}.

6.3.4. Multistage tandem mass spectrometry (MS^n)

Multistage tandem mass spectrometry (MS^n , n = 2, 3) experiments were performed for ions of interest by mass isolation followed by collision induced dissociation (CID) in the linear ion trap. The MS^n techniques are described in more detail in Chapter 3. This analysis was repeated at the MS^3 level for product ions obtained in the MS^2 stage if there was sufficient signal. Ions subjected to CID eliminate neutral fragments, which in some cases can be used to characterize the structure of the molecules. The collision energy was adjusted so that the precursor ion peak was retained in the MS^n spectra at relative intensities > 10%. The product

ions were analyzed in the high-resolution Orbitrap mass analyzer where they could be unambiguously identified. MS^n analyses were performed for product or degraded peaks of interest in photolyzed SOA samples (preliminary experiments were done to obtain m/z positions of product and degraded peaks). MS^n also confirmed that compounds examined in this work are covalently bonded (determined by threshold CID energy needed to fragment covalent ions vs. dimers and complexes of standard compounds listed in Table 6.1.)

6.3.5. Ion chromatography

Ion chromatography (IC, Metrohm Inc.) analyses were performed using a thermal conductivity detector on the control and photolyzed samples in both the positive and negative ion modes to quantify the amounts of nitrates, nitrites, and other inorganic ion impurities. In the positive ion mode, calibration was performed in the $0.25 - 10$ ppm range for the following ions: Li^+, Na^+, NH_4^+, K^+, Ca^{2+} and Mg^{2+} on a commercial cation column (Metrosep C4 - 250/4.0). Positive ion mode measurements did not determine significant concentrations of cations. In the negative ion mode, calibration was performed in the $0.33 - 10$ ppm range for the following ions: F^-, Cl^-, NO_2^-, Br^-, NO_3^-, PO_4^{3-} and SO_4^{2-} on a commercial anion column with chemical suppression (Metrosep A Supp 5 150/4mm). Ionic peaks were not observed in pure water blanks. Peaks were well-resolved and calibration fits were linear for all ions with R^2 values > 0.999. Appendix C describes measurements of aqueous precursors for the OH radical in further detail, including NO_2^- and NO_3^- that are measured by IC, and ROOH that is measured by a colorimetric test [367]. We estimate based on known radical yields that less than 1% of the changes in composition are due to OH chemistry competing with direct photolysis.

6.4. Results and discussion

6.4.1. Photolysis induced changes in composition
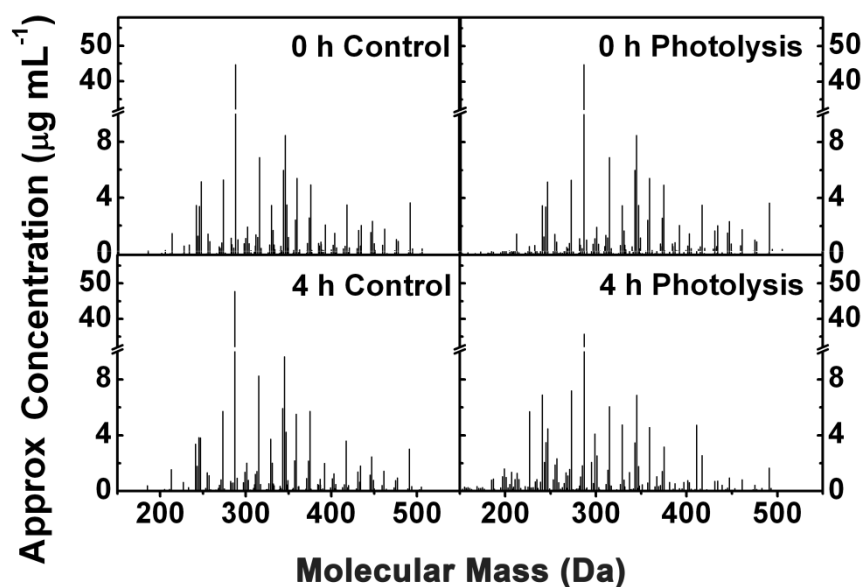
Figure 6.4: Mass spectra of the aqueous SOA extract detected in ESI positive ion mode and converted to neutral molecular formulas for the dark control (panels on the left) and photolysis (panels on the right) experiments for 0 h and 4 h time intervals. Peaks are normalized with respect to the total mass concentration (200 μg mL^{-1}) in the sample. The most abundantly observed compound is sodiated $C_{10}H_{16}O_8$. Mass spectra are also plotted with respect to normalized signal-to-noise in the supporting information (Fig. S4). Note the breaks in the vertical axis.

Figure 6.4 shows representative mass spectra of SOA samples during photolysis and control experiments for the 0 h and 4 h reaction time (1 h and 2 h mass spectra are omitted from Fig. 6.4). The mass spectra change dramatically upon photolytic processing. Notably, the higher-MW (400 – 500 Da) compounds are efficiently converted to lower-MW compounds (150 – 250 Da) with an accompanying shift in the distribution of mass concentrations. In contrast, hydrolysis does not significantly change the mass spectra. For example, the concentration of the most abundant compound in aqueous isoprene SOA, $C_{10}H_{16}O_8$, detected as a sodiated peak at m/z 287.0738, remains constant within 4 h in the dark (47± 2 μg mL^{-1}) but decreases to ~ 36 μg mL^{-1}

after 4 h of photolysis. The MS^n analysis of $C_{10}H_{16}O_8$ suggests that this molecule is formed by condensation of two 2-methylglyceric acid (2MGA, $C_4H_8O_4$) units with $C_2H_4O_2$.

We estimate that no more than 35%, by count, of the peaks in the initial SOA mass spectrum are retained following 4 h photolysis, and 65% of the initially-observed peaks are replaced by photoproduct peaks. It is not straightforward to discern if the initially present peaks that remain in the mass spectra are inert with respect to photolysis because the corresponding compounds may be both formed and decomposed by photolysis. Furthermore, some peaks may represent multiple isomeric compounds, some of which are photolabile while the others are not. The majority of the peaks that remain also change in concentration, e.g., 30% of peaks retained in the 4 h sample have increased or decreased in concentration by more than a factor of 2. In comparison, 73% of the total number of peaks were conserved in the control spectra after 4 hours in the dark.

The control experiments demonstrate that a non-negligible number of compounds in isoprene SOA photooxidation may hydrolyze to some extent at room temperature. We discuss photolysis-induced changes henceforth in this work with respect to changes induced by hydrolysis, which we would refer as "control samples" in figures and discussion. Changes in mass concentration (ρ, μg mL^{-1}) were calculated using Equation (6.1) separately for photoproducts and photodegraded compounds in the 4 h compared to the 0 h samples for the control and photolysis experiments. (In this work, we define "photoproduct" and "photodegraded" compounds as those with ion abundances that *steadily* increase ($\Delta\rho/\Delta t > 0$) or decrease ($\Delta\rho/\Delta t < 0$), respectively, during the *entire* reaction timescale.)

$$\text{Change} = 100\% \ [\Sigma\rho_{4h} - \Sigma\rho_{0h}]_{\text{produced or degraded}} / 200 \ \mu g \ mL^{-1} \qquad \text{(E 6.1)}$$

The changes in mass concentration induced by hydrolysis are significantly smaller ($\pm\ 1 - 2$ %) compared to photolysis ($\sim \pm\ 29 - 32\%$) within a 4 h time period.

Information about the average elemental ratios (H/C, O/C, and N/C), average molecular size (parameterized by the number of C atoms per molecule), and number of N atoms in the molecule, and aromaticity index (AI) [1] are extracted from the assigned molecular formulas. For brevity, we denote compounds $C_cH_hO_oN_n$ where n = (0, 1, 2) as 0N, 1N, and 2N compounds, respectively. These averaged quantities can be used to evaluate the overall change in the SOA composition. All averaged quantities are calculated with respect to ρ for *all* observed compounds as shown below (note: calculations weighted by raw intensities yielded similar results):

$$\langle X/C \rangle = \Sigma\ (X \cdot \rho)\ /\ \Sigma\ (C \cdot \rho) \quad (X = O, H, N) \qquad \text{(E 6.2)}$$

$$\langle C \rangle = \Sigma C \cdot \rho /\ \Sigma \rho \qquad \text{(E 6.3)}$$

$$\%\ nN\ \text{compounds} = 100\%\ (\Sigma \rho_{nN}\ /\ \Sigma \rho) \quad (n = 0, 1, 2) \qquad \text{(E 6.4)}$$

$$AI = (1 + c - o - 0.5h)\ /\ (c - o - n) \qquad \text{(E 6.5)}$$

$$\%\ \text{Aromaticity} = 100\%\ (\Sigma \rho_{AI>0.67}/\ \Sigma \rho) \qquad \text{(E 6.6)}$$

For $C_cH_hO_oN_n$ compounds, Equation (5) defines AI as the total number of double bonds that are not attached to heteroatoms. Therefore, AI > 0 correlates to a positive number of carbon-carbon double bonds and AI > 0.67 (E6) suggests condensed aromatic structures in a molecule [1]. The results from the statistical analyses of photolysis and control samples are compiled in Table 6.2 for each reaction time interval. Figure 6.5 shows the time-dependent changes in the averaged number of carbon atoms $\langle C \rangle$ of all the SOA compounds, and ratios of $\langle O/C \rangle$, $\langle H/C \rangle$, $\langle N/C \rangle$. Figure 6.6 shows the mass % of 0N, 1N and 2N compounds, and % of aromatic compounds in the photolysis and dark control samples. Negligible changes in average quantities were observed in the control samples, with the exception of 1N compounds that decreased slowly in the dark.
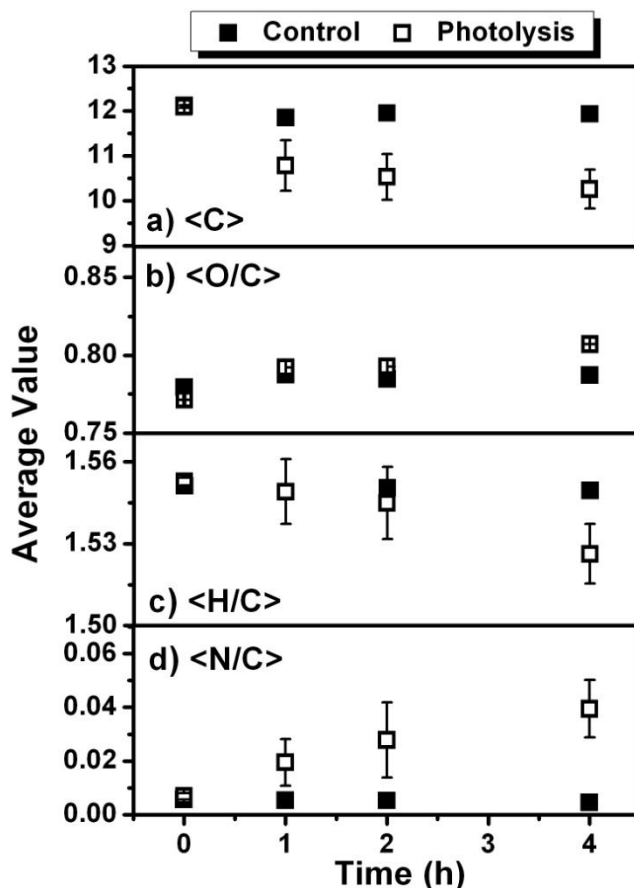
Figure 6.5: Changes in the average (a) number of carbon atoms and (b-d) elemental ratios of compounds in the photolysis and dark control samples with respect to time of photolysis (open markers) or hydrolysis (closed markers). Errors represent 1σ between repeated experiments.

Figure 6.5a shows that initially the SOA compounds have an average of 12 carbons in their molecular structure. After 4 h of photolysis, <C> is reduced to approximately 10 carbons. The trend in <C> mirrors the observation that high-MW oligomers are degraded, as reflected in the evolution of the mass spectra shown in Figure 6.4. Degradation of oligomer peaks was also an important result in the aqueous direct photolysis of low-NOx limonene ozonolysis SOA [358]. In contrast, indirect photolysis studies of model organic compounds typically form high-MW compounds instead of degrading them [327].

Table 6.2: Average mass-weighted number of carbon atoms, elemental ratios, and percent abundance of molecules with high aromaticity index (AI > 0.67), 0N ($C_cH_hO_o$), 1N ($C_cH_hO_oN$), and 2N ($C_cH_hO_oN_2$) compounds at various photolysis and dark reaction times. Errors are reported as 1σ spread between experiments, where applicable.

Photolysis	\<C\>	\<O/C\>	\<H/C\>	\<N/C\>	% Arom.	% 0 N	% 1 N	% 2 N
0 h	12.1	0.771	1.553	0.007	3.7	92.8	6.2	1.1
	(0.0)	(0.008	(0.001	(0.001)	(0.9)	(0.6)	(0.4)	(0.9)
1 h	10.8	0.792	1.549	0.020	10.1	88.4	2.6	9.0
	(0.6)	(0.001	(0.012	(0.009)	(3.7)	(4.1)	(0.2)	(4.3)
2 h	10.5	0.793	1.545	0.028	13.7	84.1	3.3	12.6
	(0.5)	(0.000	(0.013	(0.014)	(5.9)	(7.1)	(0.9)	(6.2)
4 h	10.3	0.807	1.526	0.039	19.4	78.8	2.3	18.9
	(0.4)	(0.000	(0.010	(0.011)	(4.2)	(4.9)	(0.4)	(4.4)
Control	\<C\>	\<O/C\>	\<H/C\>	\<N/C\>	% Arom.	% 0 N	% 1 N	% 2 N
0 h	12.1	0.779	1.551	0.006	2.6	93.3	6.6	0.1
1 h	11.9	0.788	1.549	0.005	2.7	93.8	6.1	0.1
2 h	12.0	0.785	1.551	0.005	2.9	94.0	5.8	0.1
4 h	11.9	0.787	1.550	0.005	2.5	94.7	5.2	0.1

The \<O/C\> traditionally describes the degree of oxidation of a compound. In isoprene SOA, \<O/C\> for the water-soluble fraction is ~ 0.77 and increases slightly to ~ 0.81 following 4 h of photolysis (Fig. 6.5b). The results from our work are in good agreement with the observations by *Bateman et al.* [2011]. The net increase in \<O/C\> may be due to the production of high-O/C molecules as a result of photodegradation of low-O/C molecules in water, as proposed by *Bateman et al.* [2011]. This explanation is qualitatively consistent with aqueous photolysis studies of natural organic matter [368, 369]. In our experiments, the increase in the \<O/C\> in photolyzed SOA samples cannot be attributed to aqueous OH-oxidation chemistry because OH formation is not expected to be significant (Appendix C).

The <H/C> is a good indicator of the degree of unsaturation in SOA molecules. Our data show that <H/C> is decreasing (-ΔH/C ~ 0.03 in 4 h) with respect to photolysis time (Fig. 6.5c). The decrease in H/C in the SOA compounds for our samples can be attributed to the photoformation of molecules with double bonds or rings. Our observations are different from those of *Bateman et al.* [2011], who reported the opposite trend for the low-NOx limonene/O_3 SOA system. The low-NOx ozonolysis system may behave differently than the high-NOx photooxidation SOA studied in this work. The high concentration (10^{-5} M) peroxide quantified in the work of *Bateman et al.* [2011] may produce OH radicals upon photolysis to destroy intact C=C bonds left over from the incomplete oxidation of limonene. In our experiments, we expect a relatively complete oxidation of double bonds from of isoprene and its first-generation products (Fig. 6.2) prior to SOA collection and we quantified the concentrations of OH precursors (Appendix C) in this work to be negligible.

The <N/C> has been quantified in lab-generated [79] and ambient [202] biogenic OA samples in the range of 0.02 – 0.03. Urban OA may have <N/C> in the range of 0.01 – 0.09 [203, 370-372]. This work determines <N/C> of the purely water-soluble fraction of isoprene photooxidation SOA to be ~ 0.01, a value that increases to ~0.04 after 4 h of photolysis (Fig. 6.5c). The increase in N/C ratio suggests that the nitrogen mass is not conserved and we speculate that the poorly-ionizable organic nitrates present only in the background may be transformed into more highly-ionizable nitrogen products. Considering the small initial <N/C> observed in aerosol samples, the fourfold increase in <N/C> during 4 h photolysis is substantial.

Effect of photolysis on the distribution of N atoms in the molecules is similarly dramatic. The mass fraction of water-soluble 0N compounds is dominant (93%) initially in the high-NOx isoprene SOA. This fraction increases slightly (to 95%) after 4 h in the dark as organic nitrates
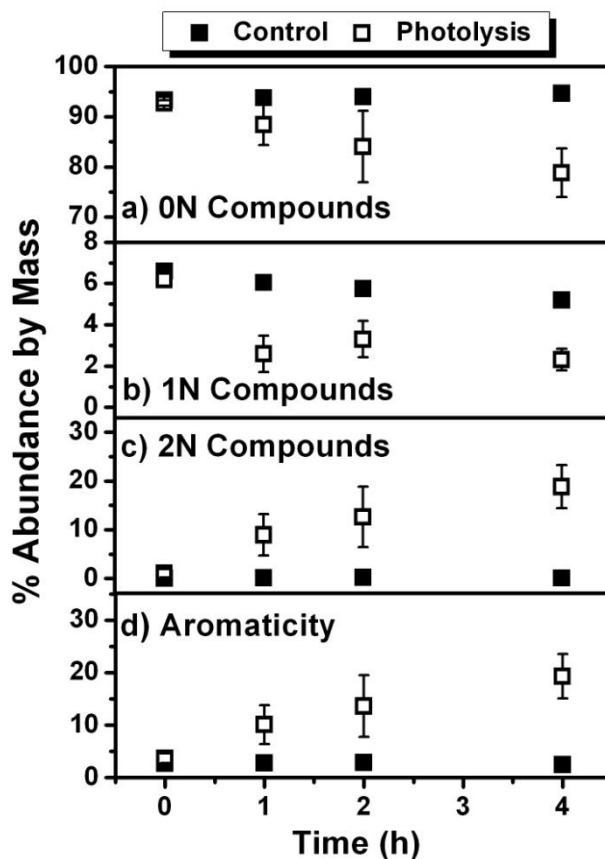
Figure 6.6: Changes in mass abundance of compounds with (a) 0N ($C_xH_yO_z$), (b) 1N ($C_xH_yO_zN$), (c) 2N ($C_xH_yO_zN_2$) and (d) compounds with high aromaticity index (AI > 0.67) in the photolysis (open markers) and dark control (closed markers) samples with respect to time. Errors represent 1σ between repeated experiments.

are hydrolyzed to alcohols [322, 373]. However, photolysis degrades 0N compounds (Fig. 6.6a) and reduces the 0N fraction to an average of 79% after 4 h. This net loss in 0N compounds occurs despite simultaneous production of different 0N compounds in the photoproduct pool (Section 6.4.3). A net loss is also observed for 1N compounds, which are known to be organic nitrates [30, 36, 38, 40] and further verified by MS^n in this work. The 1N compounds are present at ~ 6% initial fraction and are reduced to ~ 5% from 4 h hydrolysis in the dark. The effect of hydrolysis on 1N compounds is clear from the slow linear decline in the concentration of 1N compounds (Fig. 6.6c). However, photolysis is a faster loss mechanism for these organic nitrates.

After 4 h photolysis the fraction of 1N compounds is reduced to ~ 2%, a four-fold enhancement in the loss rate compared to hydrolysis. We note that nitrates may be underrepresented in our work due to their low ionization efficiencies in the positive ion mode, so the effect of photolysis may in fact be greater.

A large increase in 2N compounds is observed after 4 h photolysis (Fig. 6.6c), which increases the N/C of the sample mixture despite photolysis of organic nitrates. Before irradiation, 2N compounds, most likely dinitrates [30], comprise less than 1% of the SOA molecular pool, a result consistent with our earlier work [38]. The fraction of 2N compounds increases up to 19% after 4 h photolysis. This large increase in 2N compounds is unexpected as such a substantial change in the distribution of NOC during photolysis of dissolved organic material has not been previously observed.

The differences in the mass fractions do not appear to add up: 1N fraction is reduced from 6% to 2% whereas 2N fraction is increased from 1% to 19%. We partially attribute this inconsistency to a change in the ionization efficiencies between the 1N precursors and 2N photoproducts. Additionally a portion of the 2N products may be produced from the inorganic nitrogen initially present (presumably from nitric acid and HONO in the chamber). The already poor ionization efficiencies for these organic nitrates (the majority of the 1N compounds) are further reduced if they have low-MW and if the ionization happens in water. It's possible that the photolysis of non-ionizable 1N compounds (that are undetected) serves as a partial source of nitrogen to produce larger and more easily ionizable 2N compounds. Furthermore, our results from MS^n (Section 6.4.4) show that the fragmentation signatures of these 2N compounds are not consistent with organic dinitrates. Instead, the 2N photoproducts may be the type of nitrogen

compounds that have high efficiency in ESI, e.g. heterocyclic nitrogen. Therefore, the mass fraction of 1N and 2N compounds should be considered lower and upper limits, respectively.

The increase in the degree of unsaturation, <N/C> and % of 2N compounds is reflected in the increase in abundance of possibly-aromatic molecules (those with AI > 0.67) (Fig. 6.6d). The fraction of possibly aromatic SOA compounds is ~ 4 % initially and increases to ~20 % after 4 h of photolysis. The large increase in AI is consistent with both the photoproduction of alkenyl moieties from Norrish II photochemistry of larger (> C_4) carbonyls [60, 61] and the production of aromatic 2N species. Table 6.2 shows that the mass percent of 2N compounds and those with AI > 0.67 are roughly equivalent throughout the photolysis experiment, suggesting that the 2N products or their precursors are aromatic species.

6.4.2. Specific photodegraded compounds

The main advantage of HR-MS is its ability to simultaneously detect a large number of individual compounds.   There were approximately 50 specific compounds (out of *ca.* 300 observed) in each sample whose mass concentration decreased consistently over photolysis period. The identities and mass concentrations of the photodegraded compounds reproducibly observed between duplicate trials are shown in Table 6.3, and the entire list of compounds whose concentration steadily decreased due to photolysis or dark hydrolysis (control) is shown in Table D1 a,b of Appendix D. The photodegraded compounds can be quite large, up to 18 carbons in length. Table 6.3 shows that 0N and 1N compounds are predominantly photodegraded, consistent with the expectation that carbonyls and nitrates in isoprene SOA are readily photolyzed. The structures of NOCs shown in Table 6.2 corresponding to ester oligomers of 2MGA and its nitrate derivatives (2MGAN, $C_4H_7O_6N$). These nitrate esters of 2MGA have been

Table 6.3: List of compounds reproducibly degraded from irradiation of aqueous isoprene high-NOx SOA samples. The rates of degradation are derived from linear fits of concentration vs. time profiles. Errors in the initial concentration of a compound in the SOA extract are reported as 1σ spread between experiments, and errors in the rate of decrease due to photolysis are reported as deviations in the slope. Compounds are sorted by increasing number of carbon atoms.

Molecular Formula	Concentration in SOA ($\mu g\ mL^{-1}$)	Rate of Change ($\mu g\ mL^{-1}\ h^{-1}$)
$C_8H_{13}O_9N$ [a-c]	0.88 (±0.11)	-0.17 (±0.06)
$C_{12}H_{19}O_{12}N$ [a-c]	1.70 (±0.35)	-0.35 (±0.17)
$C_{12}H_{20}O_{10}$	2.65 (±0.82)	-0.38 (±0.15)
$C_{13}H_{19}O_{11}N$	0.26 (±0.02)	-0.06 (±0.03)
$C_{13}H_{22}O_9$	0.11 (±0.01)	-0.03 (±0.01)
$C_{14}H_{20}O_9$	0.27 (±0.05)	-0.05 (±0.01)
$C_{14}H_{21}O_{13}N$ [a]	2.20 (±0.19)	-0.39 (±0.21)
$C_{14}H_{22}O_{10}$	2.93 (±0.38)	-0.46 (±0.19)
$C_{14}H_{22}O_{11}$	23.33 (±1.66)	-3.23 (±1.60)
$C_{14}H_{24}O_8$	0.28 (±0.15)	-0.05 (±0.02)
$C_{15}H_{22}O_{12}$	3.33 (±0.16)	-0.43(±0.29)
$C_{15}H_{24}O_9$	0.53 (±0.08)	-0.12 (±0.05)
$C_{16}H_{24}O_{11}$	0.50 (±0.02)	-0.08 (±0.04)
$C_{16}H_{24}O_{12}$	1.83 (±0.17)	-0.30 (±0.12)
$C_{17}H_{26}O_{11}$	0.32 (±0.02)	-0.07 (±0.03)
$C_{17}H_{26}O_{13}$	1.84 (±0.10)	-0.32 (±0.14)
$C_{18}H_{28}O_{14}$	3.48 (±0.16)	-0.66 (±0.45)

Structures previously reported by: a. Ref:[38]   b. Ref:[36]   c. Ref:[40]

previously characterized in isoprene SOA by us [79] and other groups [36, 40]. For example, it has been demonstrated that $C_8H_{13}O_9N$ is formed through condensation of 2MGA and 2MGAN, and $C_{12}H_{19}O_{12}N$ is a product of condensation of two 2MGA units and one 2MGAN unit.

Table 6.4a shows average characteristics for compounds degraded by photolysis. For example, photodegraded molecules are larger than the average SOA compound, e.g. <C> = 14 for the photodegraded compounds compared to a smaller value of <C> = 12 for the entire SOA

Table 6.4: Average number of carbon atoms and elemental ratios for all formed and degraded peaks, segregated into NOC (1N and 2N) and non-NOC (0N) fractions.

a. Degraded Compounds	\<C\>	\<H/C\>	\<O/C\>	\<N/C\>
Total	14	1.54	0.79	0.01
Non-NOC Fraction	14	1.54	0.77	0.00
NOC Fraction	13	1.67	0.93	0.05
b. Product Compounds	**\<C\>**	**\<H/C\>**	**\<O/C\>**	**\<N/C\>**
Total	9	1.45	0.88	0.10
Non- NOC Fraction	10	1.54	0.68	0.00
NOC Fraction	8	1.32	1.17	0.25

sample. In general the elemental ratios for the degraded compounds are similar to that for the SOA. Separating the degraded compounds into NOC and non-NOC fractions can be instructive. The NOC fraction has a much higher \<O/C\>, again consistent with NOC being oxygen-rich organic nitrates bearing three O atoms in nitrate groups. The \<H/C\> is also higher in the NOC fraction because the formation of organic nitrates does not involve H abstraction by molecular oxygen like in the formation of carbonyls from alkoxy radicals.

The time-dependent concentrations of two select 1N and two select 0N compounds are shown in Figures 6.7a-b and 6.7c-d, respectively. The mass concentration changes significantly due to photolysis for these molecules; for example, the aforementioned 2MGA – 2MGAN dimer ($C_8H_{13}O_9N$) remains at roughly 1 µg mL^{-1} in solution if kept in the dark but is almost completely degraded at the end of the 4 h photolysis experiment. Figure 6.6b suggests that some 1N compounds may hydrolyze more quickly than $C_8H_{13}O_9N$ and Table D1b lists several examples of 1N compounds susceptible to hydrolysis. NOC that are able to hydrolyze may be tertiary nitrates [322]. Our data indicate that the non-hydrolyzable organic nitrates are the major fraction
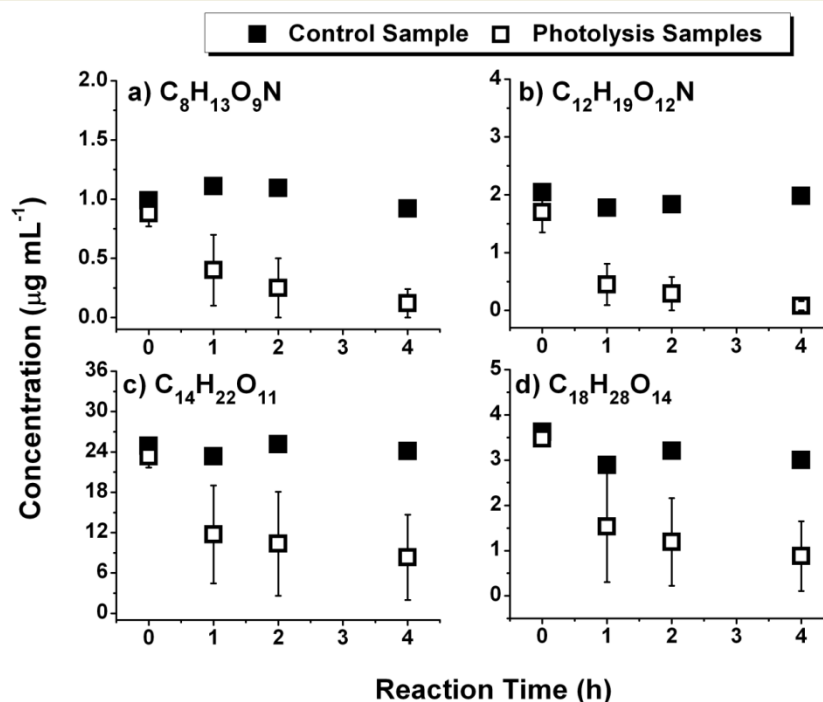
Figure 6.7: Time-dependent abundance for select peaks degraded in the photolysis samples. The same peaks do not decrease in abundance with the same rate in the control samples. Errors represent 1σ between repeated experiments.

of NOC in isoprene SOA, and that photolysis is a faster route to the decomposition of all NOC present in isoprene SOA compared to hydrolysis, regardless of their specific structure.

6.4.3. Specific photoproducts

There were approximately 40 specific compounds in each sample whose mass concentration increased consistently over the photolysis period. In comparison, there were only 5 compounds in the dark control sample that increased in concentration and they are likely hydrolysis products. The photoproducts that were reproducibly observed between photolysis trials are reported in Table 6.5. The full list of photoproducts and hydrolysis products is available in Table D2a-b in Appendix D. The photoproducts shown in Table 6.5 are comprised of 0N and 2N compounds with generally zero or small initial concentrations. There are some exceptions of

Table 6.5: List of compounds reproducibly formed by irradiation of aqueous isoprene high-NOx SOA samples. The rates of formation are derived from linear fits of concentration vs. time profiles. Errors in the initial concentration of a compound in the SOA extract are reported as 1σ between trials and errors in the rate of increase due to photolysis are reported as deviations from a linear slope. Compounds are sorted by increasing number of carbon atoms.

Molecular Formula	Concentration in SOA ($\mu g\ mL^{-1}$)	Rate of Change ($\mu g\ mL^{-1}\ h^{-1}$)
$C_5H_6O_7N_2$	0.35 ($\pm$0.35)	0.35 ($\pm$0.12)
$C_5H_{12}O_4$	0.00 ($\pm$0.00)	0.07 ($\pm$0.01)
$C_6H_6O_8N_2$	0.17 ($\pm$0.17)	0.29 ($\pm$0.06)
$C_7H_8O_9N_2$	0.09 ($\pm$0.09)	0.26 ($\pm$0.06)
$C_7H_{10}O_9N_2$	0.30 ($\pm$0.30)	1.24 ($\pm$ 0.20)
$C_7H_{12}O_5$	0.00 ($\pm$0.00)	0.51 ($\pm$0.03)
$C_7H_{12}O_6$	0.00 ($\pm$0.00)	0.13 ($\pm$0.02)
$C_8H_{10}O_8N_2$	0.16 ($\pm$0.16)	0.32 ($\pm$0.13)
$C_8H_{10}O_{10}N_2$	0.42 ($\pm$0.11)	1.29 ($\pm$0.24)
$C_8H_{12}O_4$	0.00 ($\pm$0.00)	0.06 ($\pm$0.01)
$C_8H_{12}O_6$	0.60 ($\pm$0.07)	0.99 ($\pm$0.09)
$C_9H_{12}O_{10}N_2$	0.39 ($\pm$0.26)	2.78 ($\pm$0.46)
$C_{10}H_{16}O_5$	0.24 ($\pm$0.18)	0.18 ($\pm$0.03)
$C_{11}H_{16}O_6$	0.16 ($\pm$0.11)	0.10 ($\pm$0.03)
$C_{11}H_{16}O_8$	1.23 ($\pm$0.15)	1.07 ($\pm$0.06)

compounds, such as $C_{11}H_{16}O_8$ and $C_8H_{12}O_6$, which are already present at substantial initial concentrations in the SOA. It is likely that the photolysis of higher-MW oligomer species generates monomeric compounds that are already present in the original SOA extract.

Figure 6.8 shows the changes in mass concentration with respect to photolysis time for select 2N (Fig. 6.8 a-b) and 0N (Fig. 6.8 c-d) products. These compounds are not produced in the absence of irradiation. Many of the photoproducts increase with time linearly during 4 h of photolysis interval. However, some species show a saturation behavior that may be attributed to the complete consumption of precursor molecule(s) or their own photodegradation. The apparent

concentrations of some NOC products are high (> 10 µg mL^{-1} out of 200 µg mL^{-1} total organics) at the end of 4 h. However, as previously discussed, these nitrogen compounds may be overrepresented in ESI techniques, and the mass concentration of photoproduct NOC should be treated as an upper limit.
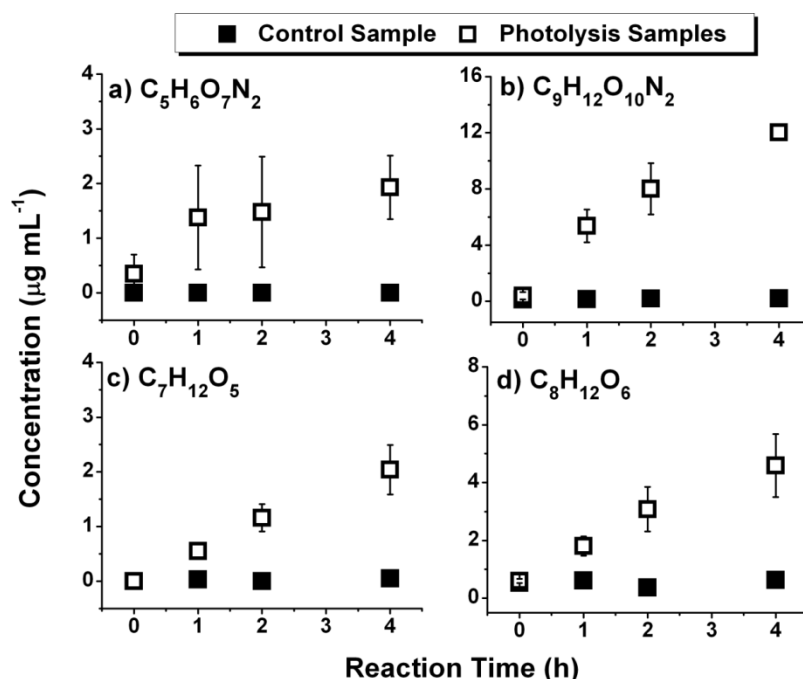
Figure 6.8: Time-dependent abundance for select peaks produced in the photolysis samples. The same peaks do not increase in abundance in the control samples. Errors represent 1σ between repeated experiments.

The steady growth of 2N photoproducts is an important, and non-obvious, result. As studies of direct photolysis of complex mixtures comprising organic nitrates and oxygenated compounds are not available in the literature, the observations in this work cannot be compared to others. The particular 2N products shown in Table 6.5 are generally small (<C$_8$) and highly oxidized. Table 6.4b shows average characteristics for only photoproducts, which are smaller (<C> = 9) than non-photolyzed SOA compounds (<C> = 12). The <O/C> and <N/C> for photoproducts are higher than the average for the SOA, and the H/C ratio is lower, which are

expected results based on Figure 6.5b. Again, we can separate the photoproducts into NOC and non-NOC fractions. The non-NOC fraction is larger by 1 carbon and has a lower <O/C> (0.68) and higher <H/C> (1.54) than the corresponding values for all the photoproducts. We can speculate that the lower <O/C> of the non-NOC compounds may be due to some extent to decarboxylation of the precursor 0N compounds (loss of CO_2).

Conversely, the NOC products, i.e., 2N compounds, are generally 1 carbon smaller, have smaller <H/C> (1.32) and higher <O/C> (1.17) compared to all photoproducts. The <H/C> of the 2N photoproducts are characteristic of aromatic molecules. For example, unsaturated molecules that are aromatic, e.g., benzene (C_6H_6, H/C = 1.0) or trimethylbenzene (C_9H_{12}, H/C = 1.33), have much lower H/C than unsaturated molecules that are aliphatic, e.g., limonene ($C_{10}H_{16}$, H/C =1.6) or squalene ($C_{30}H_{50}$, H/C =1.7). Furthermore, H/C show little variability for aliphatic molecules initially present in aqueous isoprene SOA. For example, the spread in <H/C> for all observed molecular formulas is small (1.55 ± 0.14). This places the H/C value for NOC products outside the expected range (note the quoted error value is the standard deviation in all observed <H/C> in one data set and is different from the standard deviation between trials presented in Table 6.2) and further suggests that the 2N photoproducts are heterocyclic and/or aromatic. MS^n experiments can differentiate between nitrate and other types of nitrogen functional group and indeed results from Section 6.4.4 support the suggestion that 2N compounds are heterocyclic and/or aromatic. The <O/C> is also unexpectedly high for the 2N photoproducts, indicating that oxidized nitrogen species are present in the formation steps of 2N products.

6.4.4. MS^n characterization of degraded compounds and photoproducts

MS^n studies provide valuable insight into the chemical structure of organic molecules. Neutral loss fragments resulting from CID can be used to characterize certain classes of

compounds. For example, past work on isoprene SOA determined that organic nitrates tend to lose neutral molecules of the type RNOx (e.g., HNO_3, CH_3NO_3, HNO_2, etc.) Furthermore the characteristic neutral loss of $C_4H_6O_3$ for 2MGA oligomers was determined using fragmentation studies [36, 38] and the ester functionality was confirmed by chromatography techniques [37]. In order to better understand fragmentation patterns for the instrument conditions used in our work we first performed MS^n experiments for several organic acids listed in Table 6.1. The resulting neutral loss patterns of standards are compiled in the same table. Losses of CO, H_2O, and C_2H_2O were observed for aliphatic acids, and CO_2 loss was observed for the singular aromatic acid used in the study. None of the standard acid monomers or dimers lost $C_4H_6O_3$, confirming that loss of $C_4H_6O_3$ is characteristic of 2MGA oligomers when considering isoprene SOA and similar compounds.
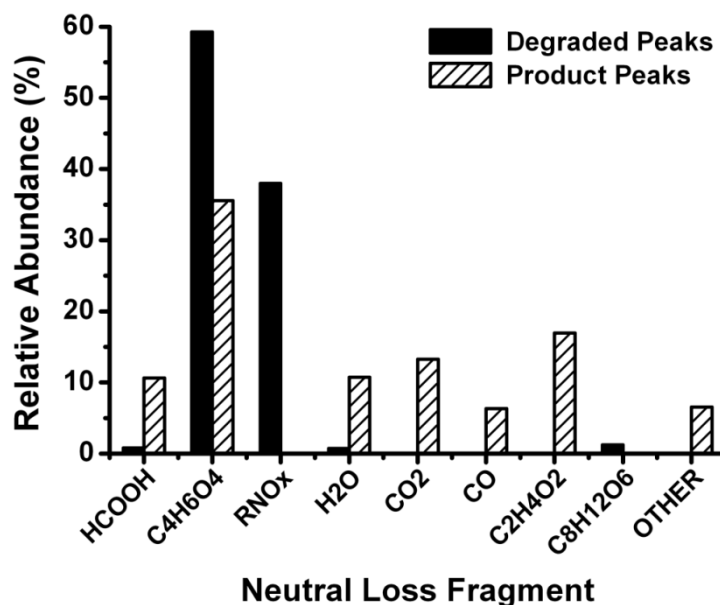
Figure 6.9: Most abundant neutral losses in MS^n experiments of photodegraded and photoproduct peaks. RNOx fragments (where R can be H and x = 1, 2, 3) correspond to the sum of neutral losses from alkyl nitrates because all N-containing neutral losses from organic nitrates conserve the N-O bond. The category of "other" losses corresponds to infrequently-observed carbon fragments like $C_4H_6O_3$.

Figure 6.9 shows combined fragmentation results of MS^n characterization of photodegraded compounds and photoproducts observed with sufficient signal and in the absence of interfering peaks. Fragmentation was performed on more than 10 peaks in each case and the results from MS^2 and MS^3 are combined for a particular peak in order to make general comments about the chemical nature of photodegraded and photoproduct compounds. The photodegraded NOC lost neutral RNOx fragments, in good agreement with previous reports. The photodegraded 0N compounds lost primarily $C_4H_6O_3$. A signature fragmentation pattern emerged for photolyzed 0N compounds in that the major loss is $C_4H_6O_3$ (normalized to 100%), followed by $C_8H_{12}O_6$ (4-6%), HCOOH (3-4%) and H_2O (1-3%). These results suggest that degraded compounds are chemically homogeneous. Similar to our previous work [38], the loss of $C_4H_6O_3$ here suggests that the compounds undergoing CID are esters of 2MGA, and the loss of HCOOH suggests that there are hydroxyl groups in alpha positions relative to carboxylic acid groups. The ester group is not known to be photolabile and is unlikely to be the part of the 2MGA oligomer that absorbs light and decomposes. Rather, these are likely carbonyl groups in the multifunctional oligomers that were photodegraded [60, 61]. Furthermore, the MS^n experiments indicate that the ester functionality is still present in the degraded molecules.

A common fragmentation pattern was not observed for photoproducts. The various losses shown in Figure 6.9 indicate that photoproducts are a diverse set of molecules, suggesting that photolysis introduces more heterogeneity in the dissolved organic composition. For example, the primary neutral loss for two photoproducts, $C_8H_{12}O_6$ and $C_{11}H_{16}O_8$ (Table 6.5), was HCOOH and $C_4H_6O_3$, respectively. The category of "other" losses shown in Figure 6.9 includes a compilation of $C_1 - C_4$ carbon fragments, e.g., $C_3H_4O_3$ (pyruvic acid), which was observed only

156

once. Losses of $C_2H_4O_2$, $C_4H_6O_3$, H_2O and CO observed for 0N photoproducts indicate that, as expected, photolysis results in formation of multifunctional acids, carbonyls or alcohols.
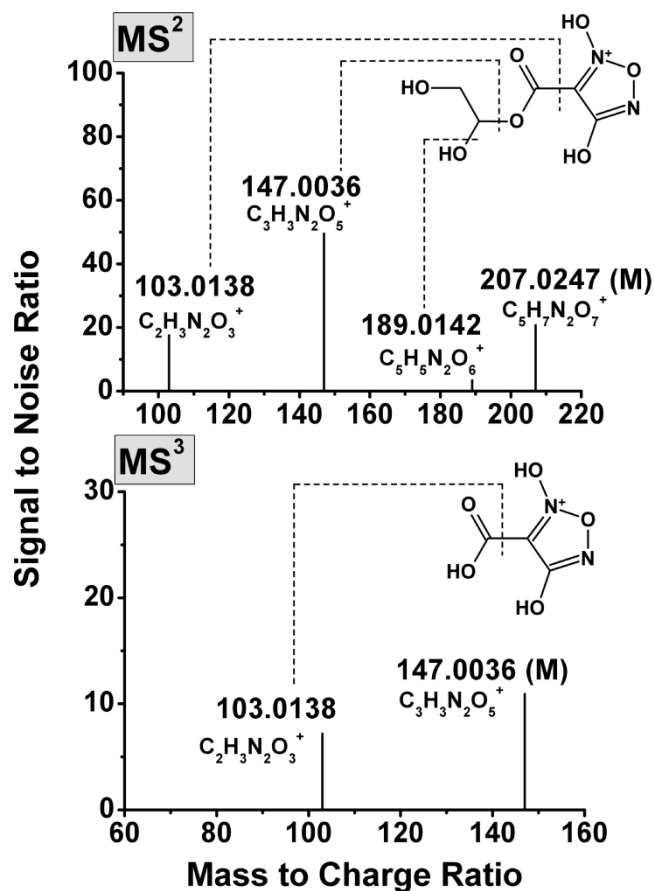
Figure 6.10: MS^{2-3} spectra for protonated $C_5H_6O_7N_2$, with possible fragmentation routes leading to product ions illustrated as dashed lines at the cleavage sites (generally accompanied by H transfer). Structural characterization of the protonated photoproduct is consistent with a heterocyclic structure.

Unlike photodegraded compounds, 2N photoproducts do not lose RNOx fragments. Figure 6.10 shows MS^n data for a representative 2N product, $C_5H_6O_7N_2$, where the neutral losses are not consistent with nitrate (-RNOx), amine (-RNH$_2$), or imine (-RNH) functional groups. Instead the smallest product ion, e.g. m/z 103.0138 or $C_2H_3N_2O_3^+$, still contains two nitrogen atoms. The presence of two nitrogen atoms in the most stable part of the molecule indicates that

the 2N compounds are cyclic or aromatic. Certain types of heterocyclic 2N compounds with reduced nitrogen atoms, e.g., imidazoles, pyrazole, pyrazines, etc.[77], have been previously associated with SOA. However, this particular product has very high oxygen content, which does not correlate with reduced 2N heterocyclic core structures. Rather, the most reasonable interpretation for the product ion $C_2H_3N_2O_3^+$ is a hydroxylated furoxan structure as shown in Figure 6.10. Furoxans are the N-oxide of furazan and are important biological moieties [374]. Alternatively, $C_2H_3N_2O_3^+$ may be visualized as having an N=N bond instead of two C=N bonds, and there is not sufficient information to discriminate between these different structures. The formation of furoxan-like derivatives is consistent with all of the observations derived from HR-MS and HR-MS^n. Specifically, they have sufficiently high O/C, high N/C, low H/C and are not likely to produce RNOx neutral losses in CID. We emphasize that the probability of incorrect assignment or interference for a low-MW ion at *m/z* 103.0138 is very small.

Additionally, CO_2 neutral loses were prominent in the fragmentation of some 2N products. CO_2 loss is not common in the positive ion mode [207, 375]. However, we observe this loss as the dominant fragmentation channel for dihydroxybenzoic acid, the only aromatic acid standard in our fragmentation study. In light of other evidence, namely low H/C of photoproducts and MS^n signatures, the CO_2 loss from our limited fragmentation experiments is consistent with aromatics being formed during photolysis. Therefore, we hypothesize that cyclization reactions of organic nitrogen oxides may be induced by photolysis to form stable 2N heterocyclic molecules and we discuss possible routes to their formation in the following section.

6.4.5. Mechanism of formation for NOC

The aqueous photolytic processing of the complex SOA involves a vast number of radical combination reactions resulting in formation of photostable products. The majority of

photoproducts observed in this work do not contain nitrogen and it is currently not possible to speciate the entire fraction of 0N compounds. However, the distinct CID signatures of aliphatic and heterocyclic NOC observed in this work enable more in-depth discussion about the formation of NOC products. Therefore, we focus on the possible formation pathways leading to the unexpected heterocyclic 2N products that accumulate during photolysis. As the concentrations of organic nitrates decrease from photolysis, and those for NO_3^- and NO_2^- do not, the source of 2N photoproducts in the irradiated SOA samples must be due primarily to the photolysis of organic nitrates, which are present at initially a factor of $100 - 1000$ greater molar concentration than inorganic nitrogen ions.

Organic nitrates are known to photolyze mainly via three primary processes [356, 376, 377], with the predominant pathway being the cleavage of the $RO–NO_2$ bond:

$$RONO_2 + hv \rightarrow RO + NO_2 \qquad\qquad (R\ 6.1)$$

The NO_2 produced from photolysis may have the following photolytic fates in water:

$$NO_2 + hv\ (\lambda < 400\ nm) \rightarrow NO + O \qquad\qquad (R\ 6.2)$$

$$NO_2 + hv\ (\lambda > 400\ nm) \rightarrow NO_2^* \qquad\qquad (R\ 6.3)$$

Both Reactions (2) and (3) are expected to be important, with a calculated $J_{NO2} = 0.03\ s^{-1}$ and $0.02\ s^{-1}$, respectively, using gas-phase absorption cross sections [378, 379], quantum yields [380], and the measured radiation flux from our lamps.

In water, the NO_2 radical may exist in equilibrium with its dimer N_2O_4. The dimer may disproportionate quickly in water to yield NO_3^- and NO_2^- ions [381]. At moderate NO_2 pressures ($p_{NO2} = 1\ x\ 10^{-5}$ atm) the $[N_2O_4]/[NO_2]$ ratio is less than 0.02 [382], in good agreement with our IC analysis (Section 6.3.5) which shows that NO_3^- and NO_2^- ions are negligibly enhanced in the

photolysis sample. The NO radical formed in Reaction (2) can participate in autooxidation reactions in the presence of oxygen to form NO_2, N_2O_3, or NO_2^- [383]. HONO can also be introduced into solution in several ways: aqueous uptake onto aerosol water from the chamber experiments, NO_2^- equilibrium in solution, NO oxidation by OH, or NO reaction with H_3O^+. If HONO is present, then the reactive NO^+ species is available for nitrosation reaction [384, 385].

The product of Reaction (7.3), NO_2^* (the electronically-excited NO_2), is quickly quenched in solution. However, if NO_2^* is formed in the immediate vicinity of an SOA molecule, it may react much faster than NO_2 with organics by H atom abstraction, addition, or electron transfer mechanisms to produce aldehydes, nitro (RNO_2) compounds, dinitro compounds, HONO, and other products [377, 381, 386, 387], although no evidence of heterocyclic N products have been reported from these reactions.

The 1,2-addition of oxidized nitrogen groups to alkenes may produce intermediates to furoxan-like molecules. We do not expect alkenes to be abundant in the initial composition due to the relatively complete oxidation of isoprene. Furthermore, the mass fraction of SOA compounds with positive AI, correlating to a non-zero number of C=C bonds, is $3 - 4$ % before photolysis. However the photochemical production of unsaturated hydrocarbons through Norrish II photochemistry (Section 6.4.1) may provide suitable alkenyl precursors for the formation of N-heterocyclic products. For example, the photolysis of one C_4 (or higher) carbonyl generates up to two alkenes with the Norrish II mechanism. As isoprene SOA compounds are initially large ($<C> \sim 12$, Fig. 6.4a), the likelihood of Norrish II photochemistry should be high.

The aforementioned oxidized nitrogen species, stemming from the reaction of NO_2 and NO, in water that may participate in nitrosation of organics in the photolysis sample include N_2O_4, N_2O_3, and NO^+ [384]. NO^+ will directly lead to nitrosation of alkenes; although the

stepwise reaction may render the formation of vicinal dinitrogen groups uncompetitive. N_2O_4 and N_2O_3 (introduced into the solution by NO/O_2 system or NO_2^-/H_3O^+ system, respectively) will both react with alkenes in polar solvents to produce vicinal nitro-nitroso (R_1-C(NO_2)-C(NO)R_2) compounds [388-391] that ultimately lead to furoxans if there is sufficient acidity (pH ~ 4) or oxidative conditions available for ring closure. However, the reaction is slow at room temperature (spanning several hours). Heat (*ca.* 100 °C) can also be used for the cyclization of vicinal dinitrogen compounds to form stable furoxans. However, these ring-closure conditions are not relevant to our experiments (Fig. 6.3b). No available literature sources describe photochemical routes to the furoxan, from nitro-nitroso compounds or otherwise. We speculate this route has not been well-studied due to the relatively convenient alternative preparative routes to generate furoxans. It is possible that UV-visible radiation may accelerate the production of furoxans by generating more reactive intermediates, but this suggestion remains to be verified. Other types of compounds, e.g., substituted ketones, may also be subject to nitrosation by N_2O_3 followed by *inter*molecular C-C coupling (at the nitro site) and subsequent ring closure to form furoxans [392].

We note that the aforementioned reactions were studied under conditions not readily extrapolated to our experiments, e.g., high nitrite concentrations or low pH. Furthermore, data are not available on the relative importance of each step and whether the rates of reaction can be enhanced through UV-visible irradiation. However, these nitrosation-promoting conditions and 2N heterocyclic formation should be more common in atmospheric droplets. Photoinduced nitrosation reactions in the atmosphere have been documented in the case of aromatic molecules [393]. The mechanism is not completely understood but the involvement of photo-produced NO_2 and NO is well-established. In this work, the role of photochemistry in the production of 2N

heterocyclics is proposed, but future work is needed to obtain better understanding of the underlying mechanisms. Photochemically generated NOx species from RONO$_2$ must play a role in product formation; however, there seems to be a missing mechanism for ring closure. A possibility is that photochemical ring closure of dinitrogen intermediates traps the N compounds as a heterocycle; although relatively little is known about the aqueous photochemistry of organic nitrogen at this point to comment on the likelihood of this process. The hypothesis, however, is qualitatively consistent with the stable formation trends for 2N products during the continuous irradiation.

The exceptional stability of these furoxan-like heterocycles with respect to hydrolysis and UV irradiation [394] elevates their importance in atmospheric chemistry because they may ultimately be nitrogen sinks in the atmosphere. For example, photolysis of benzofuroxan (λ= 366 nm) [395, 396] and 3,4-dimethylfuroxan (λ= 254 nm) [397] produces the short-lived dinitroso intermediate that both thermally and photochemically regenerates the heterocycle. Comparatively, other photoproducts like carbonyls and nitro compounds are much more photolabile. Even if the formation of 2N heterocycles represents minor pathways compared to other organics, they may accumulate in substantial quantities in solution within the timescale of the photolysis experiments due to the stability of the aromatic 5-member ring. The sources for these long-lived pollutants in the atmosphere warrants further study as they may be formed under mildly photolytic conditions whenever the photoproduction of aqueous NOx occurs in the presence of dissolved organics.

6.5. Conclusion and Atmospheric Significance

This work demonstrated that the composition of dissolved SOA may be significantly modified by solar radiation (~ 30 % by mass after 4 h) and the effect of direct photolysis should

not be ignored in studies of aqueous photochemistry. Furthermore, hydrolysis contributed a small but non-negligible loss pathway for some types of molecules, e.g., organic nitrates. The composition changes are observed within 1 h photolysis (up to 3 h in the atmosphere), which is on the order of the lifetime of clouds, water films on environmental surfaces, and hydrated SOA. The presence of a large amount of ultrafine aerosols can further promote the formation of photoproducts in clouds due to both increasing the lifetime of clouds [8] and increase the concentration of dissolved OM.

The tentative identification of furoxan-like compounds in our work is the first association of these types of molecules with organic aerosols and the first report of the photochemical production of N heterocycles in cloud processing of SOA. Furoxans are typically researched as potential drugs as they are nitrogen oxide donors [394]. As such, the presence of the bound N=O moiety in SOA material may have a large potential for bioactivity. N-heterocycles based on the 5-member imidazole or the 6-member pyridine and their derivatives have only recently been recognized as important components in atmospheric OM from their association with brown carbon [63, 93] and biomass burning OA [77]. The detection of abundant signal from molecules with C-N bonds in ambient aerosols from urban atmospheres, which are not associated with oxidation chemistry [78], lend further support that reactions producing N-heterocycles may be more prevalent in nature than currently realized.

Our study discussed possible aqueous pathways to the formation of N-heterocycles from compounds commonly found in SOA. The 19% yield of 2N photoproducts in this work is unexpectedly large and it is reasonable to conclude that a photochemical mechanism for 2N heterocyclics is still undiscovered. However, the known conditions that may promote heterocyclic furoxan production are vastly more common in the atmosphere than in our

experiments, as high concentrations of NO_2^-, NO_3^-, acidity, oxidants and dissolved organic compounds can be found in cloud/fog droplets and wet aerosol. Therefore atmospheric water samples should be closely examined with HR-MS techniques for heterocyclic nitrogen. The conversion of aliphatic organic nitrates to photostable 2N heterocyclics has important implications for the nitrogen budget in the atmosphere. There are still large gaps in the collective knowledge of atmospheric aqueous photochemistry, but it is clear that direct photolysis can be important for many classes of compounds and ambient conditions.

Chapter 7: Brown Carbon Formation in Aged Limonene Ozonolysis SOA

Part I - Acceleration of Formation Rates due to Simulated Cloud and Fog

Processing

7.1. Abstract

This chapter is the first of two chapters describing brown carbon formation from limonene ozonolysis SOA. Aqueous extracts of SOA were subjected to dissolution, evaporation, and re-dissolution in the presence and absence of ammonium sulfate (AS). Evaporation with AS at pH 4-9 produced chromophores that were stable with respect to hydrolysis and had a distinctive absorption band at 500 nm. Evaporation accelerated the rate of chromophore formation by at least three orders of magnitude compared to the reaction in aqueous solution, which produced similar compounds. Absorption spectroscopy and high-resolution nanospray desorption electrospray ionization (nano-DESI) mass spectrometry experiments suggested that the molar fraction of the chromophores was small ($< 2\%$), and that they contained nitrogen atoms. Although the colored products represented only a small fraction of SOA, their large extinction coefficients ($>10^5$ L mol^{-1} cm^{-1} at 500 nm) increased the effective mass absorption coefficient of the residual organics in excess of 10^3 cm^2 g^{-1} - a dramatic effect on the optical properties from minor constituents. Evaporation of SOA extracts in the absence of AS resulted in the production of colored compounds only when the SOA extract was acidified to pH $\sim$ 2 with sulfuric acid. These chromophores were produced by acid-catalyzed aldol condensation, followed by a conversion into organosulfates. The presence of organosulfates was confirmed by high resolution mass spectrometry experiments. Results of this study suggest that evaporation of cloud or fog droplets containing dissolved organics leads to significant modification of the molecular composition and serves as a potentially important source of light-absorbing compounds.

7.2. Introduction

Monoterpenes ($C_{10}H_{16}$) comprise a significant fraction of biogenic emissions [45]. Numerous laboratory, field, and modeling studies have demonstrated that atmospheric oxidation of monoterpenes by O_3 and OH is a globally important source of secondary organic aerosols (SOA) [9, 398]. Laboratory measurements have shown that monoterpene SOA efficiently activate cloud and fog droplets due to the high water solubility of the SOA material [399-401]. Likewise, atmospheric modeling studies show that the composition of the aerosol can significantly affect cloud droplet properties [402, 403].

The nuclei of clouds and fogs commonly represent mixtures of organic material and inorganic compounds such as ammonium sulfate, $(NH_4)_2SO_4$ (AS). Once formed, the droplets continue to build up dissolved organic and inorganic material [404] by wet deposition of water-soluble compounds, including polar organics [405, 406]; aqueous oxidation of SO_2 to H_2SO_4 [171]; cloud-processing of volatile organics [132, 407, 408]; scavenging additional particles; droplet coalescence; and a number of other processes [404, 409]. The total dissolved organic carbon (DOC) content, inorganic ion content, and acidity are greatly enhanced in smaller atmospheric droplets, which alters the chemistry of the droplet [410-412]. For example, fog water can have a wide pH range of 2.1-7.6 [413-415], DOC of up to 0.2 g/L [342, 414, 416], and sulfate (SO_4^{2-}) and ammonium (NH_4^+) concentrations in excess of 0.15 g/L [342, 344, 417]. The changes in DOC concentration with droplet size may be induced by, amongst other things, evaporation in cloud and fog droplets.

When the relative humidity drops and the droplets evaporate, the residual particles contain a mixture of organic and inorganic compounds from the initial droplet nuclei and from the gases and inorganic compounds the droplets picked up during their lifecycle. The processes

167

involving dissolution of particles followed by evaporation of the resulting droplets (cloud cycling) are quite common in the lower atmosphere [418, 419]. Furthermore, any given cloud droplet exists on average only a few minutes [409]. The clouds themselves last longer but most of them also dissipate via evaporation on a time scale of hours. "Attempted rains", where droplets scavenge particles and gases during their descent and evaporate without ever hitting the ground, are also quite common [420, 421]. Finally, nighttime fogs tend to scavenge soluble material during the night and evaporate in the morning.

The increased concentration and acidity of DOC resulting from evaporation may promote various chemical reactions such as acid-catalyzed processes and condensation reactions that generate water as a reaction product. Chemical processes occurring during evaporation have received little attention from atmospheric chemists despite the fact that aerosols undergo a number of dissolution/evaporation cycles during their lifetime. Previous work focused on evaporation of single-component solutions of glyoxal and methylglyoxal, which was shown to result in formation of involatile oligomeric residues [162, 422]. So far, there have been no studies of evaporation of solutions containing SOA material or SOA mixed with typical inorganic constituents of clouds and fogs.

Evaporation processes that can produce light-absorbing compounds from the initially colorless SOA organics are of particular interest. Our recent work [91, 423] demonstrated that biogenic SOA produced by ozone-initiated oxidation of d-limonene undergoes browning as a result of chemical reactions between the carbonyl species in SOA and ammonia. The chromophores formed in these reactions are conjugated nitrogen-containing organic compounds (NOC). These reactions are similar in mechanism to the well-known Maillard browning reaction [424] between amino acids and reducing sugars. Formation of light-absorbing NOC species has

also been observed in the reaction of 1,2-dicarbonyls (glyoxal, methylglyoxal) with hydrated AS aerosols [425], with aqueous solutions of amino acids [426] and with aqueous solutions of AS [94, 95, 427, 428]. Reactions of photo-oxidized solutions of pyruvic acid mixed with AS also produced colored compounds [65, 429]. Light-absorbing species can also be produced by mechanisms that do not involve chemistry of reduced nitrogen. For example, photo-oxidation of aromatics under high-NOx conditions produces aerosol that has intense brown color because of the presence of nitro-aromatics [430]. Aldol condensation of volatile carbonyls under highly-acidic conditions results in formation of larger, light-absorbing, unsaturated carbonyls [258, 431-436]. Oxidation of hydroxybenzoic acid by Fenton mechanism was shown to produce light-absorbing aromatic compounds [437]. As these processes involve condensation reactions, they should be promoted by evaporation, and more generally by low relative humidity conditions. Our previous work demonstrated that condensation oligomers are significantly enhanced in isoprene photooxidation SOA under low relative humidity conditions [39]. The goal of this work is to examine the possibility of formation of light-absorbing "brown carbon" compounds and other major products during evaporation of aqueous solutions of model biogenic SOA in the presence and absence of AS.

7.3. Experimental

7.3.1. SOA Generation

For the majority of experiments, model SOA was produced as previously described [423] from the reaction of d-limonene, one of the most common atmospheric monoterpenes [45], with ozone in a 17 L glass flow tube at ambient atmospheric pressure (750 ± 10 Torr), low relative humidity (<2%) and ambient temperature (295 ± 2 K). Throughout this work, the SOA produced

from ozonolysis of d-limonene will be referred to as simply "SOA." d-limonene (Sigma-Aldrich, 97%) was introduced into a flow of zero air and ozone via a syringe pump (Fisher, KDS100) at a rate of 25 μL/hr. The injector was located at the flow cell entrance. Purified air was supplied by a purge gas generator (Parker75- 62), while ozone was produced by flowing oxygen gas (99.994% purity) through a commercial ozone generator. The overall flow through the tube was 3 SLM (standard liters per minute) resulting in a 5-6 min residence time. The estimated steady-state limonene mixing ratio in the absence of ozone was 20 ppm, and the measured ozone mixing ratio was around 100 ppm. The 5:1 O_3:limonene ratio was selected to ensure full oxidation of both exo- and endo-cyclic double bonds in limonene [438]. After the flow tube, the resulting mixture was sent through a denuder filled with activated charcoal where excess ozone and volatile organic compounds were removed. The SOA was collected on a pre-weighed filter (Millipore Fluoropore membrane filter, 0.2 μm pore size) at 25 SLM (3 SLM from the cell + 22 SLM of makeup clean air). The filter loading was typically 2-3 mg of SOA material (weighed with Sartorius ME5-F filter balance; ±0.001 mg precision) after operating the reactor for approximately 1 hour. Additional SOA samples were prepared using lower limonene mixing ratios (300ppb - 5 ppm), while keeping the O_3:limonene ratio at 5:1, to investigate the effect of the concentrations on the evaporative browning. Finally, some of the samples were also prepared in a 5 m^3 chamber as described by *Bateman et al.* [2011] using limonene mixing ratios below 1 ppm. The chamber-generated SOA had the same properties as the flow-tube SOA produced at the same limonene and O_3 mixing ratios.

7.3.2. Dissolution, evaporation, and redissolution experiments

We performed experiments on evaporation of aqueous SOA extracts in the presence and absence of ammonium sulfate (AS) at various pH values. The freshly-prepared SOA samples were extracted into ultra-purified water (R ≈18 MΩ-cm, Thermo Barnstead Nanopure) using 15 min sonication to obtain a stock solution with a mass concentration of 0.3 g/L for the dissolved SOA material. We verified the completeness of the filter extraction by performing a secondary extraction of the same filter in water or methanol, which did not dissolve additional organic material, as demonstrated by negligible optical absorption around 200-300 nm (where most organic compounds absorb) of the secondary extract compared to the primary one. A fresh stock solution was prepared for each evaporation experiment and used immediately. A 2 mL aliquot of SOA extract was placed in a 10 mL glass vial. The pH was measured with a digital pH-meter (Mettler Toledo S20) against a calibrated Ag/AgCl reference electrode. The pH of the initial SOA solution at 0.3 g/L was typically 4.5 ± 0.3 reflecting a significant amount of carboxylic acid functionality in SOA. In experiments with AS, a pre-mixed solution of AS was added to the vial to achieve a mass concentration ranging from 0.0003 to 3 g/L (either well below or in excess of the SOA mass concentration of 0.3 g/L). The addition of AS increased the solution pH somewhat (ΔpH <0.5), depending on the amount added. The pH of the extract was further adjusted to pH=2-9 by addition of pre-mixed solutions of H_2SO_4 or NaOH. The AS addition, as well as pH adjustments, typically increased the volume of the SOA extracts in the vial by 5-200 μL.

The content of the vial was transferred to a standard 1 cm quartz cuvette, and a UV/Vis absorption spectrum was recorded in a dual-beam spectrophotometer (Shimadzu UV-2450) using ultra-purified water as the reference. The solution was then evaporated to dryness using a rotary evaporator (Buchi R-210) at a bath temperature of T = 50 °C. Because 50 °C is higher than the

temperature at which atmospheric cloud and fog droplets normally evaporate, we first investigated the effect of the temperature on the extent of browning. Figure 7.1 shows that the chromophore concentration increased by about 30% when the temperature was reduced from 50°C to 25°C in our evaporation experiments. Despite this temperature effect, T=50°C bath temperature was chosen to reduce the evaporation time of relatively large sample volumes (2-3 mL). For example, it takes <10 min to evaporate 2 mL from the vial at T=50°C as opposed to >60 minutes at 25°C. As water was always present in the parts of the evaporator that were at room temperature and the pumping rate was relatively low, the pressure in the evaporator was around 15-20 Torr during the evaporation experiments, and it was dominated by the water vapor. This corresponds to about 16-22% relative humidity in the vial at the end of the evaporation (equilibrium water vapor pressure at 50°C is 93 Torr). We will come back to this point when we discuss the atmospheric implications of this work.
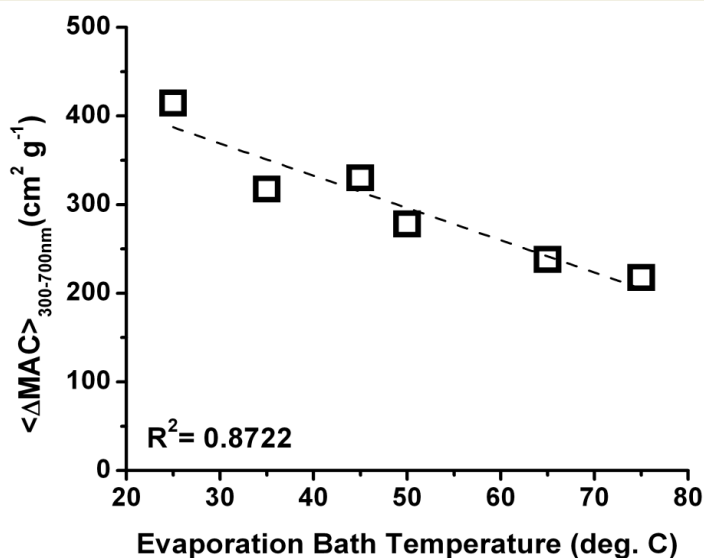
Figure 7.1: Average ΔMAC values observed after evaporation/redissolution of SOA+AS solutions at different rotary evaporator bath temperatures. Experiments were conducted at 50°C in order to accelerate the evaporation process. We expect that evaporation of samples at 25 °C would result in ~30% higher MAC relative to the values reported in the text.

After evaporation, the residue was redissolved in ultra-purified water to achieve the original SOA concentration of 0.3 g/L, and the UV/Vis absorption spectrum of the resulting solution was recorded, thus completing the dissolution/evaporation/redissolution cycle. The redissolution step was necessary in our experiments in order to quantitatively compare optical properties of the water-soluble organics before and after evaporation, and investigate the stability of the chromophores with respect to hydrolysis. For each set of pH and AS concentrations, the experiment was repeated 2-4 times using different SOA batches in order to assess the degree of variability in the results. Uncertainties are reported within one standard deviation.

We quantify the degree of browning in terms of the effective average mass absorption coefficient (MAC, measured in the units of $cm^2\,g^{-1}$) of the organic material, which can be directly calculated [3] from the base-10 absorbance A_{10} of an SOA extract with the solution mass concentration C_{mass} ($g\,cm^{-3}$) measured over pathlength b (cm):

$$MAC\,\lambda\ = \frac{A_{10}^{solution}\ \lambda\ \times \ln(10)}{b \times C_{mass}} \qquad (E\ 7.1)$$

It is also convenient to define $\langle MAC \rangle$ averaged over the desired wavelength range, typically from 300 to 700 nm:

$$\langle MAC \rangle_{\lambda_1 - \lambda_2} = \frac{1}{\lambda_2 - \lambda_1} \times \int_{\lambda_1}^{\lambda_2} MAC\,\lambda\ d\lambda \qquad (E\ 7.2)$$

For the sake of consistency, we only included the mass concentration of the organic material in Eqs. (7.1) and (7.2), and excluded the mass concentration of the inorganic additives (AS, H_2SO_4, and NaOH).

We found that the calculated $\langle MAC \rangle$ depended weakly on the initial limonene mixing ratio used in SOA preparation for SOA extracts examined at 0.3 g/L mass concentration. For

example, $\langle MAC \rangle$ for evaporated samples with AS ("brown samples") increased by about 30% between the experiments using the lowest (300 ppb) and the highest (20 ppm) limonene mixing ratios. We have not corrected the measured values for these concentration effects. In view of the observed SOA precursor concentration dependence, the MAC values reported here should be treated as an upper limit to the MAC expected for atmospherically relevant limonene concentrations.

7.3.3. High resolution mass spectrometry analysis

The solutions were analyzed before and after evaporation using a high-resolution LTQ-Orbitrap™ mass spectrometer with an electrospray ionization (ESI) source. Acetonitrile (ACN) was added to the solutions to improve the stability of the ESI. The dry residue formed in the evaporation was also analyzed using a home-built nano-DESI source described in Section 1.3.3. For nano-DESI experiments, a droplet of the solution was placed on the surface of a microscope slide and evaporated to dryness with gentle heating. Blank mass spectra were obtained from the unexposed microscope slide surface, which were not significantly different from the mass spectra of the working solvent itself. A solvent flow rate of $0.5-1.0\mu L \ min^{-1}$ and a spray voltage of about 4.0 kV were used. The system was operated in both positive and negative ion modes with a mass range of m/z 100–2000. Data analysis was similar to that described in Section 1.3.4. Peaks in the positive ion mode spectra (for the samples evaporated with AS) were assigned to formulas $C_cH_hO_oN_{0-2}S_{0-2}Na_{0-1}^+$ while peaks in the negative ion mode spectra (for the samples evaporated with H_2SO_4) were assigned to $C_cH_hO_oN_{0-2}S_{0-2}^-$. The formula assignment procedure did not allow ions to have both N and Na atoms (under the assumption that molecules contacting reduced nitrogen should have high proton affinities). The H/C and O/C ratios were limited to

0.8-2.1 and 0.1-1.5, respectively. Ambiguous assignments were evaluated by checking mass defects, parities, atomic ratios, and double bond equivalents (DBE) [82].

7.4. Results and discussion

7.4.1. Evaporation of limonene SOA in the presence of AS

Evaporation of limonene SOA solutions in the presence of AS reproducibly generated a brown residue in the evaporation vial. The solution remained colorless during the initial stages of evaporation, with the color change occurring over a short period of time, usually in less than a minute, as the residual water was removed from the sample. The residue was fully soluble in water and the resulting solution maintained its brown color for more than 12 hours, indicating that the chromophores were stable with respect to hydrolysis.
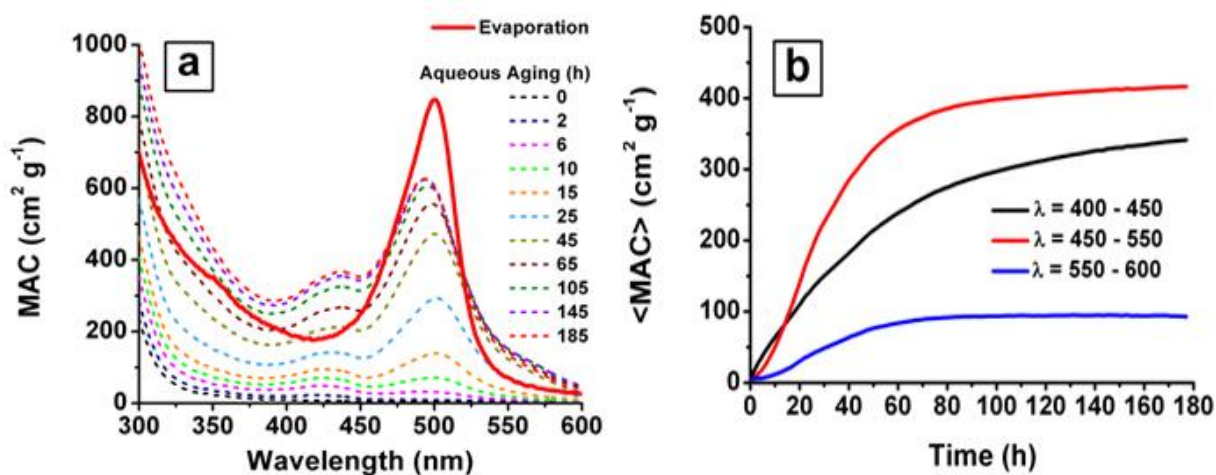
Figure 7.2. Comparison of the absorption spectra of a solution containing 0.3 g/L of SOA and 0.3 g/L of AS at different reaction times (dashed lines) with the absorption spectrum of the evaporated/redissolved sample obtained after subtraction of the pre-evaporated spectrum (solid red line) with the same initial concentrations. Panel (b) shows the time dependence of the average MAC values corresponding to the 400-450, 450-550, and 550-600 nm windows.

The solid red trace in Figure 7.2a shows a typical UV/Vis absorption spectrum obtained by subtracting the pre-evaporation spectrum of an SOA+AS extract (pH= 4.5) from the post-

evaporation/redissolution spectrum. Because the initial SOA+AS solutions do not absorb significantly above 300 nm, the difference spectra in the 300-700 nm range are entirely due to the chromophores generated during the evaporation. All of the absorption spectra presented henceforth correspond to the difference spectra converted into *MAC* units using Eq. (1).
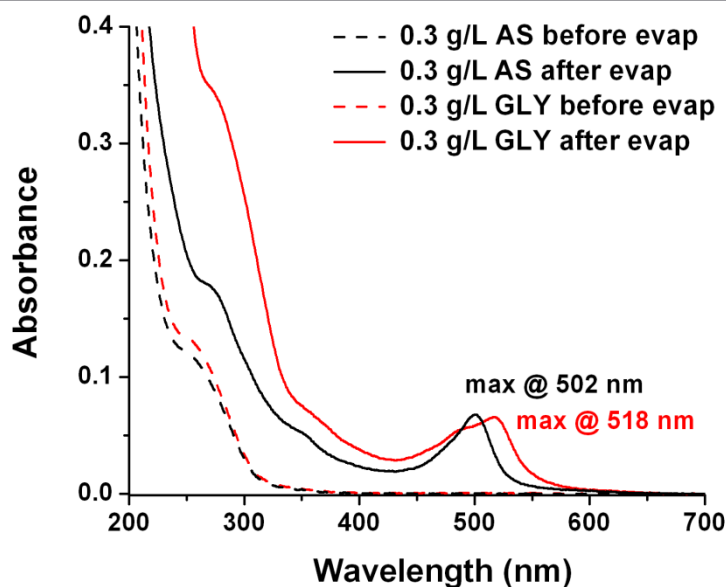
Figure 7.3: Absorption spectra of the SOA extract before and after evaporation in the presence of ammonium sulfate and the simplest amino acid glycine. The shift in the position of the 500 nm band provides indirect evidence of incorporation of nitrogen in the chromophores' structures.

The evaporated/redissolved SOA+AS extracts have a distinctive absorption band at around 500 nm superimposed on a broad absorption that smoothly increases towards UV. Similar absorption spectra were obtained at other pH values, as discussed below. A similar 500 nm absorption band appeared in the slow SOA+AS chemistry occurring in the bulk aqueous phase on a timescale of hours to days [423]. This band was also observed when limonene SOA collected on a substrate was exposed to humid air containing ammonia (NH_3) [91]. Comparison of the absorption spectra suggests that the general features of the browning mechanism are similar for the SOA+AS (solution), SOA+AS (evaporated solution), and SOA+NH_3 (gas -

particle) cases. *Bones et al.* [2010] also studied the reaction between amino acids and SOA in the aqueous phase. From the amino acid dependent shifts in the position of the 500 nm absorption band, it was concluded that the chromophores were likely nitrogen-containing organic compounds (NOC). Evaporation experiments in which AS was replaced by glycine also resulted in a significant red shift in the position of the 500 nm band (Figure 7.3), confirming that the 500 nm chromophores formed during the evaporation also correspond to NOC.

However, there are also reproducible differences in the chemistry between the aqueous and evaporation aging experiments. The dashed traces in Figure 7.2a correspond to the UV/Vis absorption spectra for the aqueous mixture containing 0.3 g/L SOA and 0.3 g/L AS, obtained as a function of reaction time in bulk solution. When compared with the spectrum obtained by evaporation and redissolution of the same mixture (solid red line), it is obvious that the evaporation chemistry produces chromophores absorbing in the 500 nm region on an accelerated timescale. In aqueous solutions of limonene SOA aged with AS, the 500 nm absorption band and another absorption band at 430 nm slowly form over the course of ~ 180 h. There is an additional shoulder at 570 nm, which becomes discernable after 2 days of reaction. For brevity, chromophores absorbing at $\lambda = X$ nm will be referred to henceforth as C_X.

The spectral position of C_{430} continuously shifts toward the red (from $\lambda_{max} \sim 425$ nm at early times to ~440 nm after 180 hours) and the position of C_{500} continually shifts toward the blue (from $\lambda_{max} \sim 505$ nm at early times to ~490 nm after 180 hours) throughout the experiment, possibly due to additional peaks growing in the same spectral region or/and slow aqueous oxidation of the chromophores. Such slow reactions should not, and does not, affect the chromophores in the evaporated/redissolved samples, which are produced and analyzed on a considerably shorter experimental timescale (minutes). In contrast, C_{430} is not visible in the

177

spectrum of the evaporated sample (this band does appear in the evaporated solutions at considerably lower AS concentrations, see below). The shape of C_{500} is considerably narrower in the evaporated sample, and there is no evidence of the C_{570} shoulder band. It appears that the slower SOA + AS aqueous chemistry produces a considerably wider range of chromophoric compounds, and evaporation selectively favors the compounds absorbing at 500 nm.

Bones et al. [2010] compared the UV/Vis spectra of AS + excess SOA and SOA + excess AS in bulk solution after 20 hours of reaction. The absorption of C_{430} was significantly stronger in the AS + excess SOA case, which led to the suggestion that C_{430} are either imine-based intermediates in the formation of C_{500} or formed in an NH_4^+-catalyzed reaction. In this work, the kinetics of C_{430} and C_{500} were followed over a significantly longer time scale (Fig. 7.2b), and the results are more consistent with NH_4^+ catalysis to form C_{430} and N-incorporation to form C_{500}. In order to account for the slow shift in the peak positions, the time dependence data presented in Figure 7.3b were averaged over the 400-450 nm range for C_{430}, the 450-550 nm range for C_{500}, and the 550-600 nm for C_{570}. The growth of C_{500} and C_{570} follows sigmoidal time dependence, which is consistent with the sequential "SOA compound $\rightarrow$ intermediate $\rightarrow$ chromophore" mechanism. The kinetics of C_{500} could be fitted with the effective first order rate constants of 0.044 and 0.090 hr^{-1} for the two sequential steps. The observed growth of C_{430} could be well described with a single effective rate constant of 0.019 hr^{-1}. Because of its slower rate of formation, C_{430} continues to grow after 180 hours when C_{500} and C_{570} are close to saturation. The difference in the rate constants indicates that C_{430} is not an intermediate in the formation of C_{500} or C_{570}; they are formed by independent mechanisms.

The dependence of the chromophore production on the AS concentration in the evaporation/redissolution experiments was examined by varying the initial mass concentration of

AS (= $[AS]_{mass}$) relative to that of SOA by several orders of magnitude from $[AS]_{mass}$:$[SOA]_{mass}$ = 1:1000 to 10:1. The $[SOA]_{mass}$ remained fixed at 0.3 g/L in these experiments. Although the addition of AS increased the solution pH to $4.5 - 5.0$, we have not compensated for this because the browning chemistry does not change significantly over this pH range (see below).
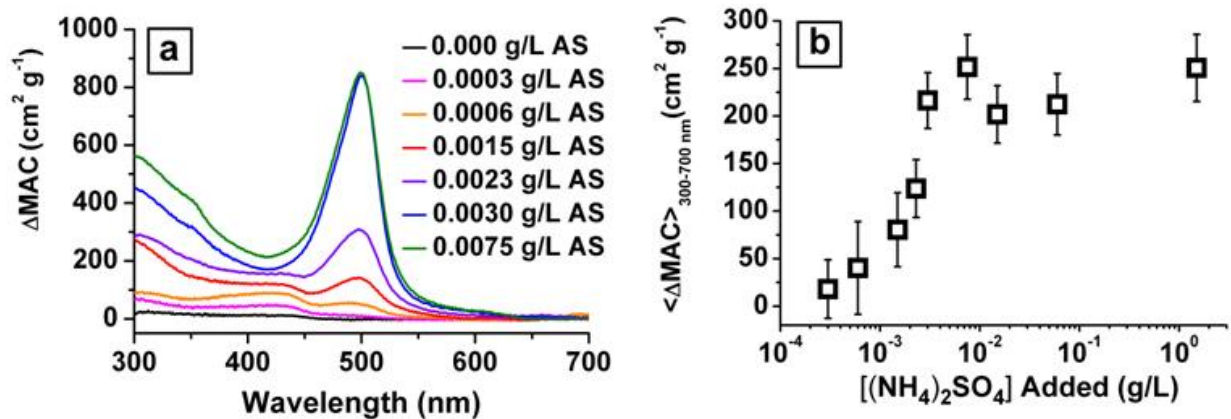
Figure 7.4. The effect of the initial AS mass concentration on (a) the absorption spectra and (b) the $\langle \Delta MAC \rangle_{300\text{-}700nm}$ values of the evaporated/redissolved SOA + AS solutions. The SOA mass concentration is 0.3 g/L in all cases. The absorbance saturates above the relative AS:SOA mass ratio of 1:100. The C_{430} chromophore is favored at low AS concentrations, but the C_{500} chromophore becomes dominant above this saturation ratio.

Figure 7.4a shows the dependence of the absorption spectrum of the evaporated/ redissolved SOA+AS solution on the initial $[AS]_{mass}$. There is a distinction between absorption spectra in the low $[AS]_{mass}$ and higher $[AS]_{mass}$ range: small concentrations of AS lead to an exclusive formation of C_{430}, whereas higher concentrations of AS suppress C_{430} in favor of C_{500}. Figure 7.4b shows the $\langle MAC \rangle_{300\text{-}700nm}$ of the evaporated/redissolved sample as a function of the initial $[AS]_{mass}$. At the lower $[AS]_{mass}$, both C_{430} and C_{500} contribute to $\langle MAC \rangle_{300\text{-}700nm}$, with C_{500} absorption becoming dominant at higher $[AS]_{mass}$, in good agreement with the observations of *Bones et al.* [2010] in the aqueous phase.

Remarkably, the $\langle MAC \rangle_{300\text{-}700nm}$ values reach a plateau after the $[AS]_{mass}$:$[SOA]_{mass}$ ratio exceeds 1:100. Assuming an average molecular weight of 300 g/mol for limonene SOA compounds, this translates into an effective molar ratio of AS:SOA of 0.022. Further assuming that each AS molecule may supply two NH_4^+ ions for reaction with SOA compounds to produce C_{500}, we estimate that <2% of SOA compounds are converted into C_{500}. It is of course entirely possible that additional SOA compounds undergo competing reactions with NH_4^+, which do not lead to products absorbing in the visible region, or that C_{500} contains more than one nitrogen atom. Such reactions would lower the estimate of the molar fraction of SOA compounds capable of generating brown products even further. Using the same assumptions, we can also place the lower limit for the molar extinction coefficient of the chromophores as $>10^5$ L mol^{-1} cm^{-1} at 500 nm. We conclude that the *MAC* of the browned SOA mixture is dominated by a very small number (<2%) of very strong absorbers, with the rest of the SOA compounds absorbing little or no visible light. We will come back to this important point during the discussion of the atmospheric relevance of these results.

The dependence of C_{430} and C_{500} formation on $[AS]_{mass}$ further supports the hypothesis that they are produced by different mechanisms. Our observations are qualitatively consistent with an AS-catalyzed formation of C_{430}, and with a two-stage mechanism of C_{500} production, which must involve a reaction with AS in one of these steps to produce an NOC with at least one nitrogen atom:

$$SOA_1 \; (+AS)_{catalyzed} \rightarrow C_{430} \qquad\qquad (R\ 7.1)$$

$$SOA_2 \; (+AS)_{catalyzed} \rightarrow Intermediate \qquad\qquad (R\ 7.2a)$$

$$Intermediate + AS_{.} \rightarrow C_{500} \qquad\qquad (R\ 7.2b)$$

Catalysis by NH_4^+ has been documented in certain reactions involving carbonyls such as aldol condensation [439, 440] leading to the formation of oligomeric and fulvic-like compounds [441]. Based on experiments conducted in this study, it is likely C_{430} is nitrogen-free (although we do not have enough evidence to completely rule out direct reaction with NH_4^+). At higher AS concentrations, production of the NOC chromophore C_{500} becomes more favorable because the exponential dependence of C_{500} formation on [AS] is amplified at higher $[AS]_{mass}$, resulting in the almost exclusive formation of the 500 nm chromophore.
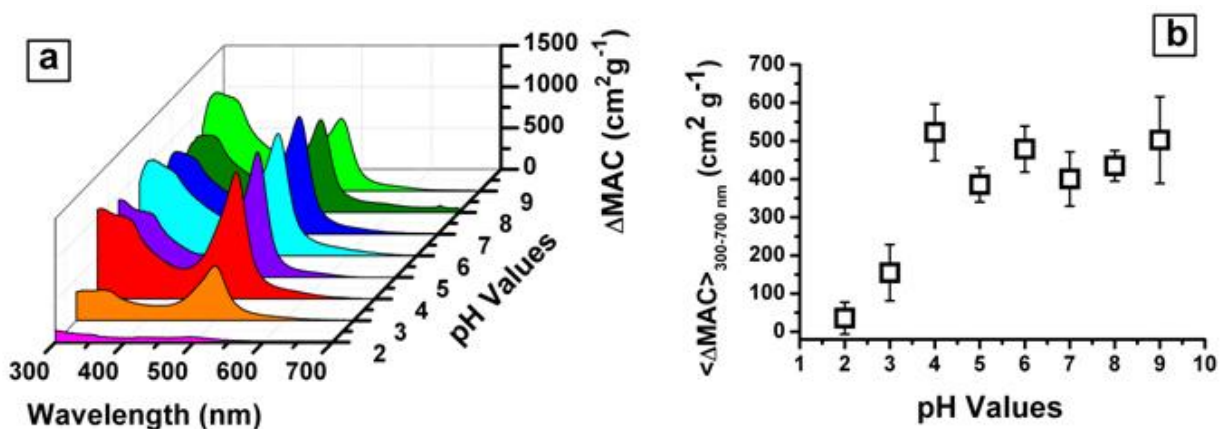
Figure 7.5. Absorption spectra observed after evaporation/redissolution of SOA + AS solutions at different initial pH. The absorbance was converted into MAC units using Eq. (1). $\langle \Delta MAC \rangle_{300-700nm}$ shown in panel (b) were calculated from Eq. (2). The reaction between SOA and AS appears to be suppressed under acidic conditions.

Regardless of the formation mechanism for the light-absorbing products, it is clear that evaporation significantly accelerates the formation of chromophores, mainly C_{500}, with respect to the aqueous phase. It takes >150 hours for the bulk aqueous chemistry to reach *MAC* values in the 500 nm region comparable to what can be achieved in a 10 min evaporation/redissolution experiment. The reaction is effectively accelerated by approximately 3 orders of magnitude. Because the color change takes place in less than one minute during the last stages of the

evaporation, the actual rate enhancement is even greater. Considering the widespread nature of droplet evaporation events in the atmospheric environment, this kind of evaporation-driven chemistry has a real potential to irreversibly modify light absorbing properties and chemical composition of the dissolved organic material.

The evaporation/redissolution experiments were performed at different initial pH values to confirm that the evaporation-induced browning occurs under atmospherically relevant conditions. Figure 7.5a shows absorption spectra and Figure 7.5b shows $\langle MAC \rangle_{300\text{-}700nm}$ values for the evaporated/redissolved SOA+AS sample as a function of the initial solution pH. The average MAC values are of the order 500 cm^2 g^{-1}, and the peak values (at 500 nm) are in excess of 10^3 cm^2 g^{-1}. At pH values below 4, the browning is inhibited. The suppression of the NH_4^+ - induced chromophore formation under acidic conditions was also observed in the bulk solutions of carbonyls + AS [95, 441] and limonene SOA + AS reaction [423]. It is notable that in the absence of AS, SOA extracts acidified by H_2SO_4 at pH =2 do produce light-absorbing compounds upon evaporation (see Section 7.4.3). However, the AS+H_2SO_4+SOA solutions at pH =2 do not show significant browning during evaporation. Mixtures of H_2SO_4 and AS have complex phase diagrams [442, 443] and may form solid phases corresponding to $(NH_4)_zH_{[2\text{-}z]}SO_4$ (z=2 for ammonium sulfate, 1 for ammonium bisulfate, 1.5 for letovicite) upon removal of water. Formation of these solid phases in the evaporated AS+H_2SO_4+SOA system may bind the H^+ and NH_4^+ ions and make them unavailable for participation in the browning reactions that occur in the evaporated H_2SO_4+SOA system at pH=2 and in the AS+SOA system at pH≥4. The shape of the absorption spectrum does not significantly change in the range of pH=4-9 (Fig. 7.5a), suggesting that the addition of NaOH to increase the pH does not significantly alter the chemistry.

7.4.2. Composition of evaporated SOA extracts in the presence of AS studied with high-resolution mass spectrometry

Evaporation of solutions of methylglyoxal in the presence of amino acids was found to form oligomers of NOC, which were strongly light-absorbing [426]. Aqueous solutions of AS mixed with glyoxal or methylglyoxal [94, 95, 427, 428], and AS mixed with pyruvic acid [65, 429] were also shown to undergo browning and form complex NOC simultaneously. Our previous experiments on aqueous reactions of limonene SOA with amino acids and AS demonstrated that C_{500} is a light-absorbing NOC based on evaporated (Fig. 7.3) and aqueous [423] experiments. Because chromophores produced during evaporation of limonene SOA + AS solutions and in the bulk aqueous phase have similar absorption spectra, we expected to observe a significant fraction of NOC in the mass spectra of the dry residues.
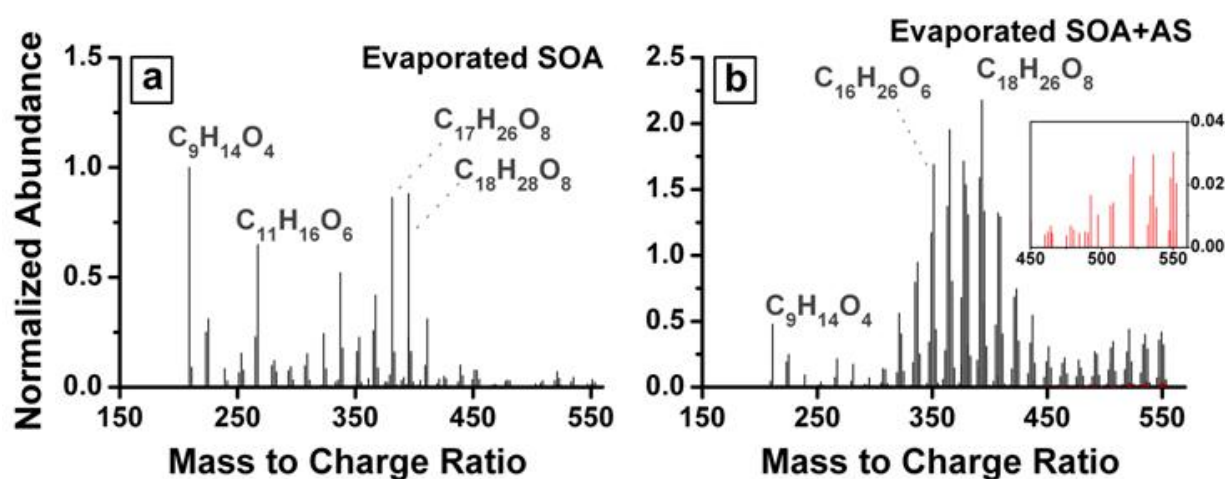
Figure 7.7. Positive ion mode nano-DESI mass spectra of evaporated SOA residues obtained (a) without AS and (b) with AS. Red peaks correspond to formulas containing nitrogen (magnified in the insert). Selected peaks are labeled with the formulas of the corresponding neutral molecules. Peak intensities of both spectra were normalized to the intensity of the sodiated $C_9H_{14}O_4$ (*m/z 209.0784*) found in the evaporated SOA spectrum.

Figure 7.6 shows the nano-DESI mass spectra of the evaporated SOA residues produced in the absence (a) and presence (b) of AS. The spectra include only compounds for which the

elemental composition could be unambiguously assigned. Selected high-abundance peaks are labeled with the formula of the corresponding SOA compound. Peak intensities were normalized with respect to a known major limonene/O_3 oxidation product, sodiated keto-limononic acid [53, 54] ($C_9H_{14}O_4Na^+$, *m/z 209.079*). The same normalization was applied to the evaporated AS+SOA spectrum (although the intensities are not easily comparable between nano-DESI spectra of different samples). The spectra are not dramatically different between the samples evaporated with and without AS. However, the fraction of higher-MW compounds is larger in the former. Although the contribution of NOC compounds increased from 2% to 11% by count (Table E1 in Appendix E) when evaporation was done with AS, the contribution of NOC to the total ion current (TIC) was <1%. A negligible fraction (<1% by count) of compounds in the evaporated AS+SOA sample could be assigned to sulfur-containing organic compounds (SOC). No SOC appeared in the evaporated SOA sample without AS, as expected.

The fraction of NOC in the evaporated SOA+AS residues appears to be surprisingly small. *Bones et al.* [2010] also found little change in the ESI mass spectra and no evidence of extensive production of NOC in the SOA+AS solutions after they browned. These observations are consistent with the "titration" experiment shown in Figure 7.4, which suggested that less than ~ 2% of the SOA compounds participate in the production of chromophores in reactions with AS. It is remarkable that the optical characteristics of SOA material can change so drastically without an accompanying change in the overall molecular composition.

The low NOC fraction observed in the AS+SOA case should be contrasted to the previous DESI and ESI MS study, which detected a significantly higher fraction of NOC in the mass spectra of limonene SOA immobilized on a substrate and exposed to humid NH_3 vapor [91]. It appears that gaseous ammonia is more efficient at producing NOC than AS. Indirect

support for this hypothesis comes from our measurements of *MAC* for different types of organic aerosols aged with humid NH_3 vapor. That study showed that $\langle MAC \rangle_{300\text{-}700nm}$ values of limonene SOA exposed to humid NH_3 vapor exceed *MAC* for the dissolved/evaporated SOA+AS sample by a factor of ~ 2, with an array of NOC compounds detectable by nano-DESI. In order to keep this paper focused on evaporation, the results of the SOA + humid NH_3 vapor study will be presented elsewhere.

7.4.3. Evaporation of limonene SOA acidified by H_2SO_4

Evaporation and redissolution experiments for SOA + H_2SO_4 (or NaOH) mixtures were performed over a range of initial pH values. The evaporation of SOA solutions in the pH range of 3-9 did not produce light-absorbing species. However, SOA solutions acidified with H_2SO_4 to pH=2 produced oily red-brown residues after evaporation. Unlike the SOA+AS case, the residue
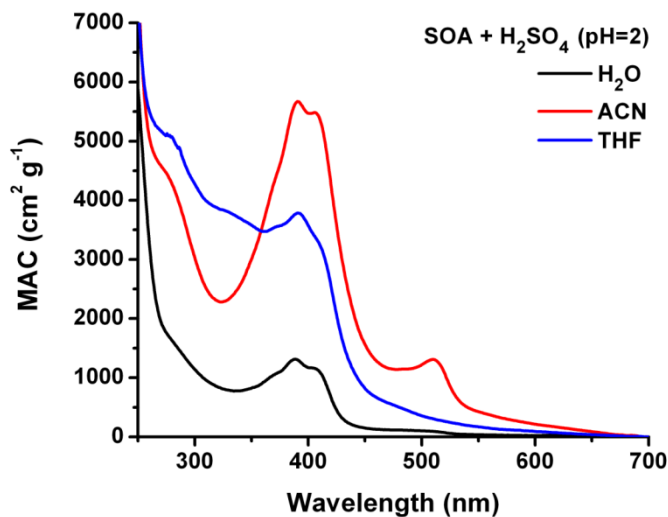
Figure 7.7. UV/Vis spectra of samples obtained by evaporations of SOA + H_2SO_4 solution with the initial pH =2 and redissolving the red-brown residue in either water (H_2O), acetonitrile (ACN), or tetrahydrofuran (THF). The residue could not be completely redissolved in water, and this is reflected in the smaller MAC of the reconstituted H_2O solution. This behavior can be contrasted with the SOA+AS case, where the residue could be fully redissolved in water.

was only partially soluble in water (Figure 7.7 shows that water extracted a smaller fraction of light-absorbing organics from the residue compared to acetonitrile and tetrahydrofuran). Similar to the SOA+AS case, the water-soluble chromophores formed in the SOA+H_2SO_4 reaction were stable with respect to hydrolysis on a time scale of at least a day. In this study we examined the water soluble fraction by UV/Vis spectroscopy, and the water/acetonitrile soluble fraction with high resolution ESI mass spectrometry.
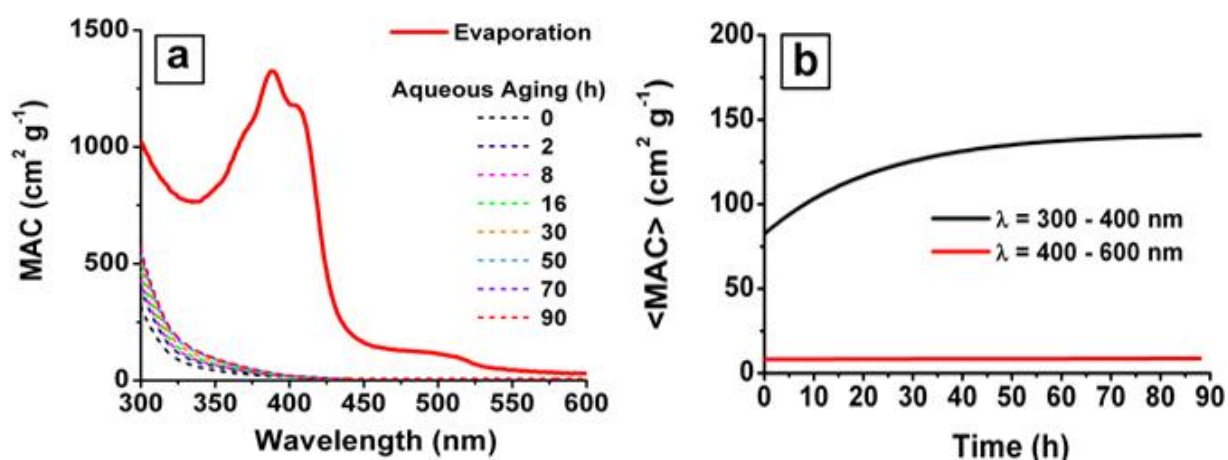
Figure 7.8. Comparison of the evolution of absorption spectra over time of a solution containing 0.3 g/L of SOA, acidified to pH = 2 with H_2SO_4, with the absorption spectrum of the evaporated/redissolved sample with the same initial concentrations. The evaporation chemistry is distinctly different from the aqueous chemistry, where no visible light-absorbing compounds are produced. Panel (b) shows the time dependence of the average MAC values corresponding to the 300 - 400 nm and 400 - 600 nm windows.

In the absence of AS, evaporation of acidic aqueous solutions promotes the production of light-absorbing compounds that would not be produced otherwise in the aqueous phase chemistry. Figure 7.8 compares the evolution of the absorption spectrum during slow aqueous-phase chemistry of pH=2 SOA extracts with the spectrum obtained after evaporation/redissolution. In the SOA+AS system, the aqueous-phase chemistry slowly produced absorption spectra that were qualitatively similar to the spectra resulting from

186

evaporation (Figure 7.2). In contrast, the aqueous-phase reactions in SOA + H_2SO_4 (pH=2) system do not produce light-absorbing compounds without evaporation, except for small changes occurring in the near-UV region.
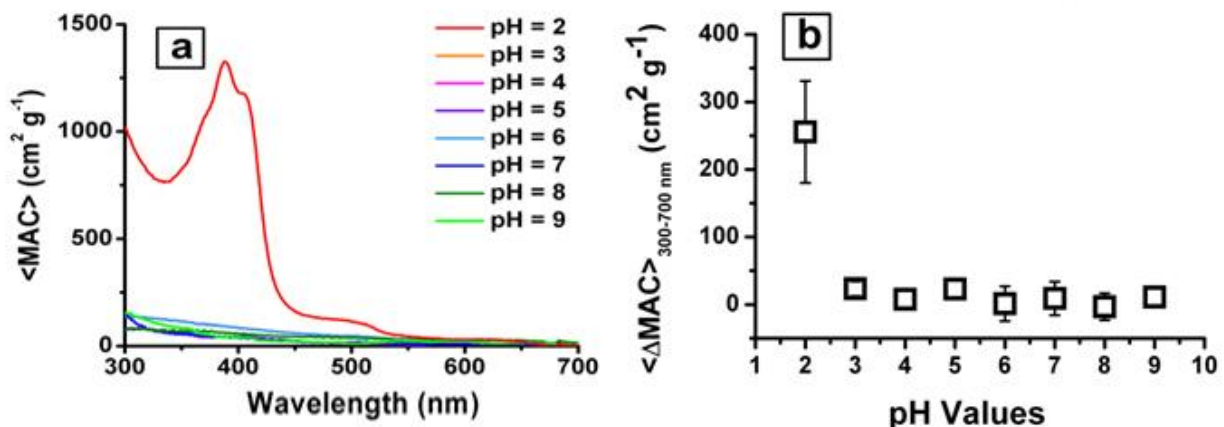
Figure 7.9. Absorption spectra observed after evaporation/redissolution of SOA + H_2SO_4 solutions at different initial pH values. The absorbance was converted into MAC units using Eq. (1). $\langle\Delta MAC\rangle_{300\text{-}700nm}$, shown in panel (b), was calculated from Eq. (7.2). Unlike the AS+SOA evaporation case, browning is more efficient under acidic conditions.

Figure 7.9a shows absorption spectra of the evaporated SOA as a function of pH (H_2SO_4 and NaOH were used for pH adjustment). Chromophoric compounds are produced at pH = 2, as evidenced by overlapping absorption peaks at 390 nm and 410 nm. There is also a small peak at 510 nm. Figure 7.10b demonstrates that the $\langle MAC\rangle_{300\text{-}700nm}$ values decrease sharply at pH >2 from approximately 250 cm^2 g^{-1} to <50cm^2 g^{-1}. Based on the comparison of the UV/Vis spectra in Fig. 7.5 and Fig. 7.9, and on the observed pH dependence, it is clear that the chemistry governing the production of chromophores in the experiments with H_2SO_4 is starkly different from that occurring in the experiments with AS. Both the 430 nm and 500 nm bands found in SOA+AS evaporated residues are absent in the SOA+H_2SO_4 spectra in Figure 7.9a. Lower pH suppresses browning in the SOA+AS case and enhances it in the SOA+H_2SO_4 case.

187

The mechanism of chromophore production from the evaporation of SOA extracts with H_2SO_4 may be similar to the acid-catalyzed aldol condensation reaction of carbonyl compounds in solutions of concentrated H_2SO_4 [431, 434, 436, 444]. The active removal of water during the evaporation and simultaneous increase in the acidity both help shift the equilibrium from reactants towards the aldol condensation products. A large fraction of the compounds in limonene ozonolysis SOA are carbonyls. For example, *Bateman et al.* [2008] previously estimated that at least 40% of the SOA compounds are either ketones or aldehydes. The high concentration of acid coupled to the removal of water may catalyze the production of light-absorbing aldol products in the evaporated samples, similar to the results obtained in the reactions of simple C_2-C_8 carbonyls with concentrated H_2SO_4 solutions [258, 431, 434, 436, 444].
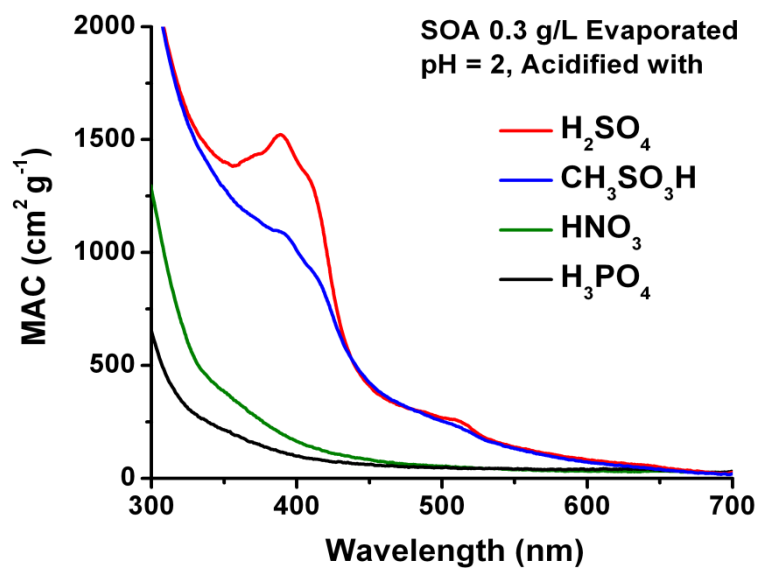
Figure 7.10. Absorption spectra (converted into MAC) observed after evaporation of SOA solutions acidified to pH=2 with various acids, followed by redissolution in water. The change in the positions of the absorption bands for the sulfuric and methanesulfonic acids provides indirect evidence for the incorporation of S atoms in the chromophores.

Although the 390 nm and 410 nm absorption bands observed in this work do not exactly match the bands produced in H_2SO_4-catalyzed reactions of C_2-C_8 carbonyls, the wavelength range over which absorption happens (350-450 nm) is the same. The carbonyls found in limonene SOA are larger ($>C_8$) and multifunctional. The average molecular "formula" for the monomeric limonene/O_3 SOA compounds can be best expressed as $C_{10}H_{16}O_4$, containing 2-4 oxygenated functional groups per molecule [53, 54]. Therefore, the aldol condensation products in the limonene SOA are expected to be highly substituted, with a higher degree of conjugation and different absorption properties as compared to the aldol condensates formed from the simpler carbonyls.

Acidity alone does not fully explain the formation of light-absorbing compounds. We conducted experiments in which H_2SO_4 was replaced by either nitric acid (HNO_3), phosphoric acid (H_3PO_4), or methanesulfonic acid (CH_3SO_3H, MSA). Evaporation of SOA solutions acidified at pH=2 with HNO_3 and H_3PO_4 did not result in visible browning or the production of C_{390}, C_{410} or C_{500} bands observed in evaporation/redissolution of the SOA+H_2SO_4 mixtures (Figure 7.10). More significantly, replacing H_2SO_4 by MSA produced a small wavelength shift in the positions of the C_{390} and C_{410} bands, in both the water soluble fraction (Figure 7.10) and in the fraction that dissolved in acetonitrile, implying that these chromophores are sulfur-containing organic compounds (SOC). We will show in the next section that evaporation of the SOA+H_2SO_4 solutions is accompanied by formation of a number of organosulfates. While the $-OS(O)_2OH$ and $-OS(O)_2CH_3$ groups are not chromophoric by themselves, incorporation of these groups next to the chromophoric core of a molecule may change its optical properties. Based on these observations, we conclude that the chromophores formed during evaporation of the SOA+H_2SO_4 solutions are SOC, and the presence of sulfur affects their optical properties.

7.4.4. Composition of evaporated SOA extracts acidified by H_2SO_4 studied with high-resolution mass spectrometry

The same conditions that favor production of aldol condensates in evaporating SOA + H_2SO_4 solutions are also favorable for production of organosulfates (H_2SO_4 esters). Organosulfates represent an important fraction of atmospheric aerosols. They have been observed in field studies of aerosols [445-450] and in laboratory SOA generated in the presence of acidic seeds [451-454]. They can also be generated by aqueous photolysis of organics in the presence of sulfates [455]. In particular, oxidation of limonene by ozone has been demonstrated to produce organosulfate oligomers on acidified seeds [454]. However, no accompanying color change was reported in these experiments.

Direct esterification of alcohols is one possible route to organosulfates but it is believed to be too slow under most atmospherically relevant conditions [456-458]:

$$R\text{-OH} + H_2SO_4 \rightarrow R\text{-OS(O)}_2OH + H_2O \qquad (R\ 7.3)$$

It should be noted that enolic forms of carbonyls may contribute to R-OH in reaction (R3) and in the case of deliquesced particles, the keto-enol tautomerism equilibrium may be shifted toward the enol, enhancing direct esterification [459]. Additionally, organosulfates may be formed in the more kinetically favorable ring-opening reaction of epoxides by H_2SO_4, as proposed in a number of previous studies, e.g., see [456, 457] and references therein.

$$(R\ 7.4)$$
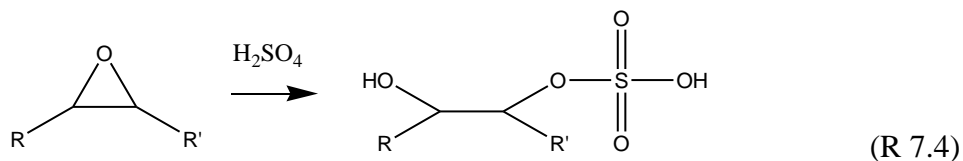
Both reactions (R3) and (R4) are acid-catalyzed and therefore should be accelerated by evaporation in the presence of acids. Reaction (R3) is a condensation process and should additionally benefit from the active removal of water during evaporation.
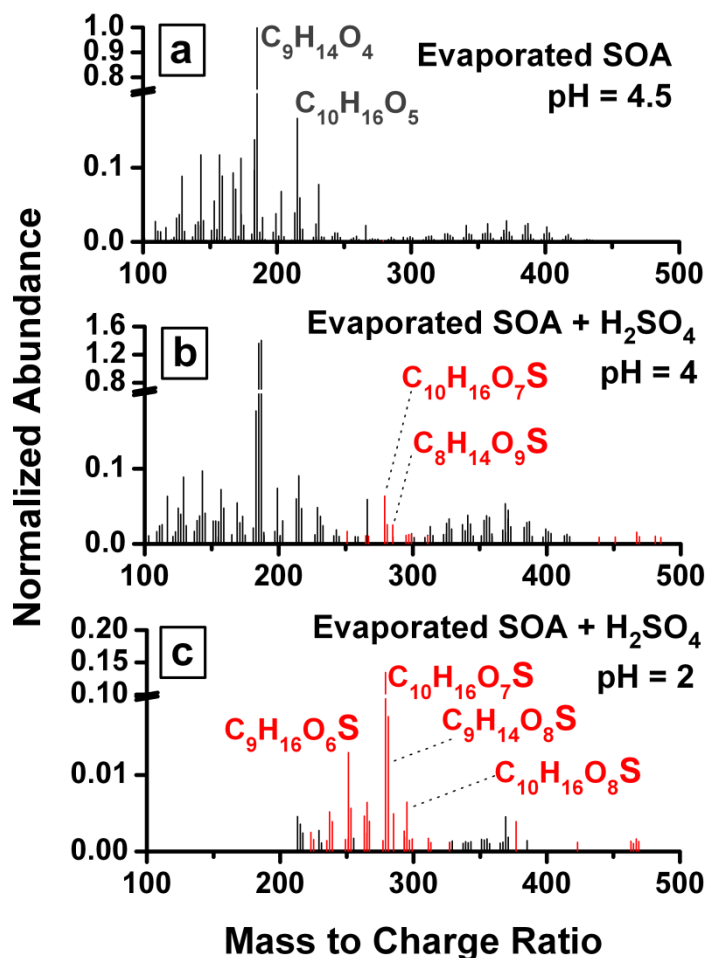
Figure 7.12. Negative ion mode ESI mass spectra of evaporated/redissolved solutions of: (a) SOA; (b) SOA+ H_2SO_4 at pH=4; and (c) SOA+ H_2SO_4 at pH=2. Red peaks correspond to formulas containing sulfur. Assignments of neutral precursors corresponding to selected peaks are shown next to the peaks. All mass spectra were normalized to the intensity of the $C_9H_{13}O_4^-$ peak at *m/z* 185.0819 in the evaporated SOA spectrum. Note the different abundance ranges and breaks in the vertical axis.

We examined the composition of the redissolved evaporation residues with high-resolution mass spectrometry using negative ion mode ESI. Figure 7.11 shows assigned peaks in the mass spectra of evaporated/redissolved limonene SOA (Fig. 7.11a), limonene SOA + H_2SO_4 at pH = 4 (Fig. 7.12b) and limonene SOA + H_2SO_4 at pH=2 (Fig. 7.11c). All three spectra were taken under identical instrumental conditions. The intensities in Fig. 7.11a were normalized to

the peak corresponding to deprotonated keto-limononic acid ($C_9H_{13}O_4^-$, *m/z 185.0819*), and the same normalization was applied to spectra in Fig. 7.11b and 7.11c. We intentionally excluded the peak at *m/z* 96.960 corresponding to the HSO_4^- ion, which would have overwhelmed the mass spectrum otherwise, by setting the lower limit for the mass range to *m/z* =100 during data acquisition. A considerable number of SOC peaks were detected by negative ion mode ESI-MS (Table E2 in Appendix E). Tandem mass spectrometry (MS^n) was performed on prominent SOC peaks to confirm that they represent genuine deprotonated molecular ions, and not weakly-bound complexes of the type $M\text{—}HSO_4^-$. The collision energies required to break these ions were characteristic of covalent bonding, and although the collision induced dissociation was dominated by the loss of HSO_4^-, losses of neutral fragments leaving behind ions that retained S-atoms were also observed.

HR-MS data can potentially distinguish between reactions (R 7.3) and (R 7.4) because these reactions add an equivalent of SO_3 (79.9568 Da) and H_2SO_4 (97.9674 Da), respectively, to the original molecular formula of the SOC precursor. We examined all SOC compounds observed in the mass spectra, and in most cases each SOC could be matched to either one or both corresponding precursor compounds ($C_cH_hO_oS_s - SO_3$ or $C_cH_hO_oS_s - H_2SO_4$) in the pre-evaporated sample. The results showed no clear pattern that would make it possible to rule out either reaction (R 7.3) or (R 7.4) as possibilities.

The mass spectrum of the evaporated/redissolved SOA solution (Fig. 7.11a) is quite similar to the published ESI mass spectra of limonene SOA extracted in acetonitrile [53] or water [460]. The characteristic envelopes corresponding to the monomeric (centered at *m/z* 180) and dimeric (centered at *m/z* 370) compounds are clearly visible in the spectrum. Evaporation/redissolution of SOA + H_2SO_4 at pH=4 produced a colorless solution and preserved

Table 7.1: High-resolution mass spectrometry results from the molecular composition analysis of aqueous extracts of SOA and of SOA acidified with H_2SO_4 before and after evaporation/redissolution at different initial pH values. The number of assigned peaks below *m/z* 500 is given in the third column. % count and % TIC refer to the percentage of the peaks and percentage of the total ion current, respectively, assigned to sulfur-containing organic compounds (SOC). The average O/C ratio is calculated as the intensity-weighted average for all assigned peaks.

Sample	Evaporation	Total Peaks	SOC (%count)	SOC (% TIC)	$\langle O/C\rangle$
SOA, nothing added	Before	203	0	0	0.50
SOA, nothing added	After	218	0	0	0.48
SOA + H$_2$SO$_4$ (pH=4)	Before	147	7	2	0.51
SOA + H$_2$SO$_4$ (pH=4)	After	138	12	3	0.54
SOA + H$_2$SO$_4$ (pH=2)	Before	95	30	27	0.58
SOA + H$_2$SO$_4$ (pH=2)	After	54	57	85	0.69

most of the peaks in the original SOA spectrum, including their relative intensity distribution. Several new peaks observed for this system correspond to SOC (Fig. 7.11b). Evaporation/redissolution at pH~2, produced a brown solution, and led to a dramatic change in the appearance of the mass spectrum (Fig. 7.11c). The majority of peaks pertaining to the original SOA material disappeared, and the peaks that remained were dominated by SOC.

Table 7.1 shows the number of assigned peaks, the fraction of peaks corresponding to SOC, the fractional ion current of SOC, and the intensity-weighted average O/C ratios ($\langle O/C\rangle$ = $\Sigma[o_i\times intensity_i]/\Sigma[c_i\times intensity_i]$) for six types of samples: the pre-evaporated and evaporated/redissolved solutions for each of non-acidified SOA, SOA acidified to pH=4 and SOA acidified to pH=2. Evaporation/redissolution of the SOA material without addition of H_2SO_4 did not produce a color change. Furthermore, the average composition of the SOA was not significantly different: 92% of the peaks from the pre-evaporated samples were retained, and the overall number of peaks did not decrease. A small fraction (13% by count) of additional

compounds were observed in the non-acidified evaporated SOA sample, suggesting that subtle chemical changes occurred in the evaporation process even without acids present. The new compounds found uniquely in the evaporated sample had an average double bond equivalency $(DBE = 1 - h/2 + c)$ of $\langle DBE \rangle \sim 5$ and $\langle O/C \rangle = 0.38$, compared to an average $\langle DBE \rangle \sim 4$ and $\langle O/C \rangle = 0.51$ for all the compounds observed in the pre-evaporated sample. This implied that the new compounds formed by the evaporation process on average gained one double bond and lost one oxygen atom. This increase in $\langle DBE \rangle$ and concurrent decrease in $\langle O/C \rangle$ is consistent with the production of (colorless) aldol condensation products during evaporation, in which one double bond is added to the molecular structure and one oxygen is removed for each condensation reaction that is accompanied by a loss a water molecule.

In acidified samples, we observe a general trend that the total number of detected peaks decreases, the number of SOC increases, and the $\langle O/C \rangle$ ratio increases with increasing acidity. Evaporation of the acidified samples further amplifies the trend. The increase in SOC and $\langle O/C \rangle$ is expected, as reactions (R 7.3) and (R 7.4) produce SOC from H_2SO_4 and enrich the oxygen content of the molecule. The decrease in the total number of peaks is due to the ionization suppression by much more abundant ions HSO_4^- and $H_2SO_4\text{-}HSO_4^-$ present in the electrospray. Indeed, the $H_2SO_4\text{-}HSO_4^-$ peak would dominate the spectrum in Fig. 7.11c if this peak was not removed as part of the background correction process. At pH=4, the small amount of added H_2SO_4 resulted in production of 7% assignable peaks corresponding to SOC. Compared to the non-acidified SOA case, the total number of observed peaks decreased from ~200 to ~150.

Evaporation/redissolution of the pH=4 sample increased the $\langle O/C \rangle$ ratio from 0.51 to 0.54, and increased the fraction of detected SOC, from 7% to 12% by number. At pH=2, the number of observed peaks in the pre-evaporated sample further decreased to ~100. The fraction

of SOC compounds increased from 7% to 30% and the $\langle O/C \rangle$ increased from 0.51 to 0.58. Evaporation/redissolution of the pH=2 sample further increased $\langle O/C \rangle$ to 0.69, reduced the total number of observed compounds, and dramatically increased the faction of SOC in the sample (~60% by number). We note that the relative fractions of SOC quoted above should be considered an upper limit because of the high ionization efficiency of SOC in negative ion mode ESI.

In summary, we observed a dramatic change in composition of the acidified and evaporated SOA extracts, which paralleled similarly dramatic changes in the optical and physical (solubility in water) properties of the dissolved organics.

7.5. Atmospheric implications

Cloud and fog processing of atmospheric gases and particles is an important driver of atmospheric chemistry. A number of key atmospheric processes occur in water, with the classic example being oxidation of SO_2 to sulfuric acid [171]. Organic compounds dissolved in cloud and fog droplets can undergo photooxidation by dissolved OH [132], direct photolysis [358], hydrolysis, and other chemical transformations on atmospherically relevant time scales. However, a number of aqueous phase reactions are too slow under atmospherically relevant conditions because of insufficient reactant concentrations, insufficient time spent by the molecules in droplets, unfavorable equilibria, solubility limitations, etc. Relevant examples include acid-catalyzed aldol condensation of aliphatic carbonyls in aqueous H_2SO_4 [258, 431], formation of organosulfates by esterification of alcohols with H_2SO_4 in aqueous solutions [458], and formation of light-absorbing nitrogen containing compounds in aqueous reactions between SOA compounds and ammonium sulfate (AS) [423]. In this work, we demonstrate that evaporation of water droplets, a very common process in the atmosphere, can greatly accelerate

195

some otherwise slow processes, and lead to dramatic changes in the composition or/and optical properties of the dissolved organics. The main driving forces behind this acceleration are increased reactant concentrations and increased acidity produced by evaporation, and in the case of condensation reactions, shifting equilibria towards the products by actively removing water from the system.

More specifically, we have shown that evaporation of solutions containing dissolved SOA material mixed with dissolved AS can produce nitrogen-containing chromophoric compounds. Such compounds represent a minor fraction of the overall composition, and they would not be readily detectable by on-line aerosol mass spectrometry methods [83, 461-463]. This irreversible process occurs readily over the pH range of 4-9 and requires small amounts of dissolved AS (<< 1 mg/L), conditions commonly found in cloud and fog droplets [344, 464]. Given the widespread occurrence of SOA and AS in the environment, this evaporation-driven process and similar reactions occurring during evaporation of water from droplets and wet aerosols may be an important pathway to brown carbon. The mass absorption coefficient (MAC) for the material produced by evaporations is around 0.1 m^2 g^{-1} at 500 nm, which is comparable to the measured MAC values for the brown carbon obtained by burning wood (< 0.5 m^2 g^{-1} at 500 nm) [3].

In addition, we have shown that evaporation of SOA solutions in the presence of H_2SO_4 produces organosulfates and aldol products. Under sufficiently acidic conditions, at the initial solution pH=2, evaporation in the presence of H_2SO_4 irreversibly produces light-absorbing products with maximum absorption peaks around 400 nm. High resolution mass spectrometry of the products suggests that this kind of "evaporative processing" results in a dramatic change in the composition of the organics, with a number of the initial compounds being converted into

organosulfates and other products. The solubility of the organic material in water is also reduced by this process. Although the acidity of pH=2 required for these transformations in the composition, solubility, and optical properties is outside the range of relevance for cloud droplets, it can be easily achieved in smaller fog droplets and in hydrated aerosols.

In our experiments, drying the solutions from an equivalent of saturation (RH ~100 %) to an equivalent of RH~20 % triggered a sudden change in the composition and color of the dissolved solutes. Can we expect the conditions in which the RH in the air surrounding droplets or wet aerosols can change from saturated to dry on reasonably fast time scales? Although individual droplets within clouds and fogs appear and evaporate on a time scale of minutes, the interstitial RH remains close to 100% [409] making the evaporation-driven chemistry unlikely. A more likely scenario is evaporation of falling rain droplets before they hit the ground, which is very common in semiarid continental regions and in deserts [420]. In these regions falling droplets become exposed to very dry air on their way down, and dry completely, leaving a processed particle behind. Heat-driven dissipation of fogs, which occurs on the time scales of hours, represents another scenario in which evaporation is likely to be important. Transitions between high and low RH conditions should be even more common for aerosols. Although the concentration regime investigated in this work is more relevant for cloud and fog chemistry, especially in polluted urban regions, it is reasonable to assume that the same processes will also occur when internally mixed organic/inorganic aerosols lose adsorbed water by drying. In fact, these evaporation-driven reactions may be even more efficient because of the higher concentrations and, for acid-catalyzed reactions, lower pH values found in wet aerosols.

This work demonstrates that chemical and physical changes may occur in SOA compounds due to atmospheric dynamics. The physical motion of air masses or rain droplets is

ultimately responsible for the change in the relative humidity, which then triggers evaporation and the associated chemistry. Therefore, future modeling of the atmospheric significance of these processes, as well as assessing their role in the brown carbon production, will require explicit inclusion of atmospheric dynamics and chromophore formation chemistry in the models.

Chapter 8: Brown Carbon Formation in Aged Limonene Ozonolysis SOA

Part II - Precursor Structure, Chromophore Structure and Kinetics

8.1. Abstract

This chapter is the second of two chapters describing brown carbon formation from limonene ozonolysis SOA. Brown carbon is believed to make a significant contribution to light absorption by aerosols but its sources are poorly understood. This work identifies, for the first time, brown carbon precursors in limonene ozonolysis SOA as the reactive compound ketolimononaldehyde (KLA). KLA is the most abundant compound in the aerosol phase of limonene ozonolysis SOA and is likely the dominant precursor to brown carbon through its reaction with ammonium sulfate (AS) and amino acids. Synthesized and purified KLA was demonstrated to produce identical chromophores to limonene SOA when reacted with AS and glycine, the simplest amino acid. Limononaldehyde (LA), a first-generation ketoaldehyde product in limonene oxidation, was also synthesized and used as a control to demonstrate that the unique structure of KLA is necessary to produce brown carbon. UV-Vis, FT-IR and NMR spectroscopy and high-resolution mass spectrometry (HR-MS) were used to characterize the chemical structures of the chromophores after separation with reverse-phase LC-UV. The kinetics of reaction were also quantified in both aqueous and evaporative reactions. This work proposes a nitrogen-containing structure and a mechanism of formation for the chromophores based on analytical clues. Results of this study provide important insights on the secondary source of brown carbon from compounds relevant to secondary organic aerosols.

8.2. Introduction

The previous chapter described brown carbon formation from the ammonium- (NH_4^+) and amino acid-mediated reactions in limonene ozonolysis SOA and established the importance of secondary brown carbon formation on the radiative forcing of SOA. Briefly it was found that a small fraction of brown carbon chromophores dominate the optical properties of SOA due to its high extinction coefficient. Previous work in our group and other groups [63, 64, 93, 94, 427] implicated the importance of nitrogen-containing organic compounds (NOC) in the formation of brown carbon. Specifically the C=N moiety from imines, imidazoles, pyridines and NOC oligomers have been suggested by mass spectrometry as an important characteristic of the chromophore structure [77, 93]. These reduced nitrogen compounds may be formed from the reaction of 1,2–dicarbonyls like glyoxal with NH_4^+ and amino acids via the Debus mechanism (Scheme 8.1) [465]. The reaction of carbonyls with amino acids leads to the formation of a Schiff base (R-C=NR$_1$, R$_1$≠H), whose protonated salt form can be highly absorbing provided that there is sufficient conjugation in the chromophore structure [466]. Similarly, the imidazole-like compounds from the Debus mechanism do not absorb light in the visible region unless coupled to extensively conjugated side structure.
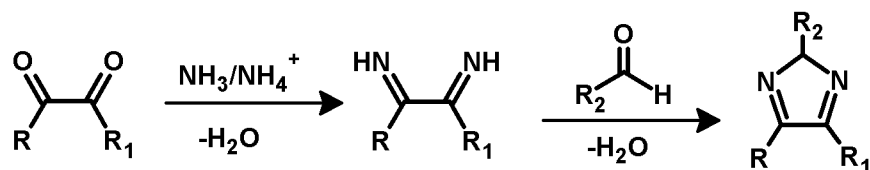
Scheme 8.1. The Debus mechanism of 1,2–dicarbonyls and ammonia or ammonium. A di-imine is formed and further reaction with a carbonyl compound affords a substituted imidazole.

From previous work we know that the reaction with NH_4^+ proceeds under slightly acidic (pH ~ 4) to neutral conditions and is accelerated by the removal of water. Also, we know that at

least two chromophores are formed in the NH_4^+-mediated reaction in water: one that absorbs light at 430 nm and one at 500 nm. For brevity we refer to chromophores absorbing at $\lambda = X$ nm as C_X. The production of C_{500} is independent of C_{430}, and is favored in the evaporative reaction. However, despite the extensive investigations carried out in the last few years, the understanding of chromophore formation from limonene/O_3 SOA compounds is still in its infancy. Several important questions remain to be answered:

(1) **What is the structure of the precursor?** Limonene ozonolysis produces tens of primary and secondary products (Figure 1.2) and hundreds of oligomers [53]. However, the ozonolysis mechanism cannot directly generate 1,2–dicarbonyls from the structure of limonene. Therefore the precursor(s) for light-absorbing species in limonene/O_3 SOA is (are) currently unidentified.

(2) ***How many individual precursors and chromophore structures exist?*** In other words, is the formation of brown carbon in limonene ozonolysis SOA driven by one specific compound, by a family of structurally related compounds, or by compounds with very different types of structures? If only one precursor exists, are there multiple types of chromophores it can form?

(3) **What are the kinetics (orders and rates) of the reaction?** Is the reaction going to be relevant under typical atmospheric conditions in aerosols, clouds, fogs, or on environmental surfaces?

(4) ***What are the chemical functionalities responsible for light absorption?***

(5) ***What is the mechanism of brown carbon formation for compounds relevant to limonene/O_3 SOA?***

There are significant analytical challenges in addressing these questions. In particular, without knowing detailed information about precursors, kinetics and mechanism are impossible to study. Also, structure elucidation proved difficult in the past as the chromophores are minor species.

However, through modifying experimental design by placing an emphasis on isolating pure precursor candidates, the subsequent analyses may become less daunting.
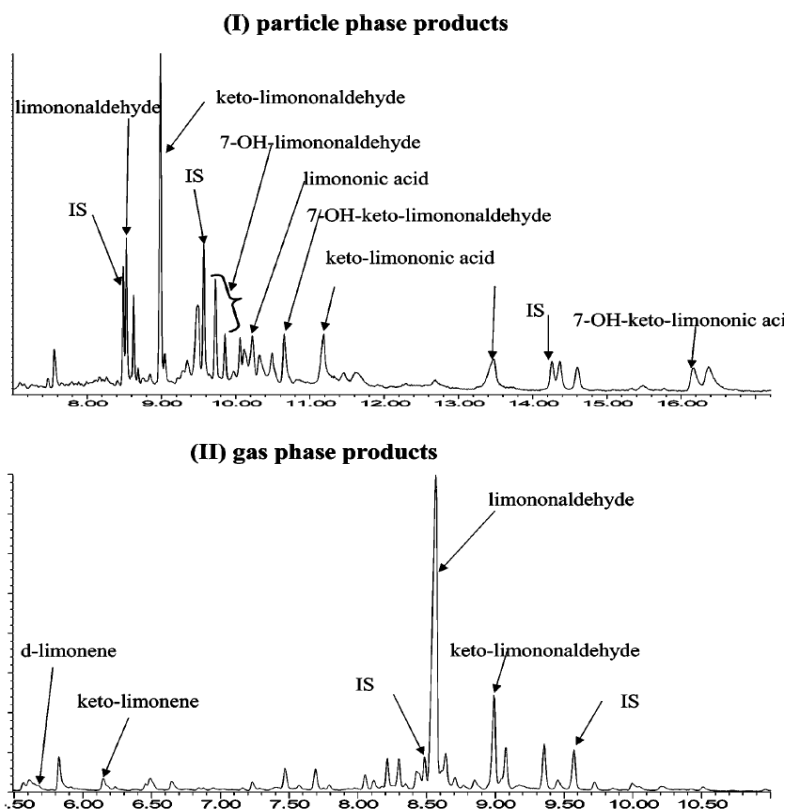
Figure 8.1. Gas chromatogram of limonene ozonolysis (a) particle-phase and (b) gas-phase products. Figure reproduced with permission from Leungsakul et al., *Environ. Sci. Technol.* 2005 © American Chemical Society.

This chapter presents unpublished work in the attempt to answer questions $(1 - 5)$. The approach taken in this work is to select two most probable precursors from the list of monomeric products stemming from limonene ozonolysis (Figure 1.2). The work of *Leungsakul et al (2005)* determined that up to 60% of the SOA mass from limonene are comprised of monomers because the limonene structure produces condensable products even with first-generation oxidation chemistry [50]. Figure 8.1 reproduces the chromatography data from that work, which shows that in the aerosol phase, keto-limononaldehyde (KLA) is the most abundant compound, followed by

limononaldehyde (LA). These results are consistent with the high-resolution mass spectrometry (HR-MS) results of *Walser et al (2008)* who reported that KLA and LA are 2 of the top 5 detected compounds [53].

This work hypothesizes that KLA and/or LA may be the brown carbon precursors as they are the most reactive species from the product pool. KLA and LA were synthesized and purified in order to study their reaction with NH_4^+ and the simplest amino acid, glycine (GLY, HOOC-CH_2-NH_2). The following sections demonstrate that KLA, but remarkably not LA, reproduces the browning phenomenon observed with the limonene/O_3 SOA mixture on its own. This work represents the first evidence of KLA as a precursor to secondary brown carbon. The thorough investigations of the KLA browning reactions outlined in this chapter provide missing data on the nature of the brown carbon structure, reactions, and rates.

8.3. Experimental

8.3.1. Synthesis and purification of LA and KLA
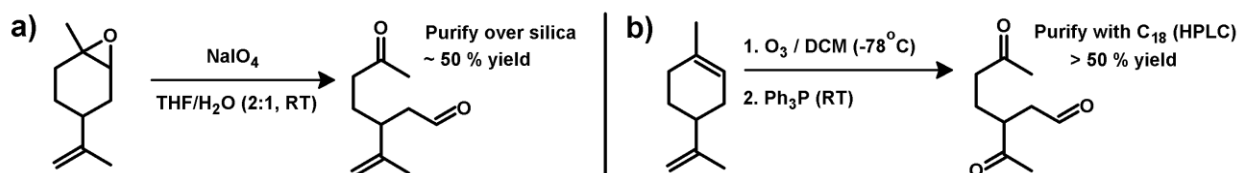
Scheme 8.2. Syntheses of (a) limononaldehyde (LA) from the oxidative ring opening of limonene oxide by sodium metaperiodate and (b) keto-limononaldehyde (KLA) from the cold ozonolysis of limonene and subsequent reduction with triphenylphosphene.

Scheme 8.2 shows the synthetic routes to pure limononaldehyde (LA, $C_{10}H_{16}O_2$) and keto-limononaldehyde (KLA, $C_9H_{14}O_3$). LA was synthesized from the one-pot oxidative ring opening of the 1,2–epoxide of limonene, according to the procedure reported by *Binder et al*
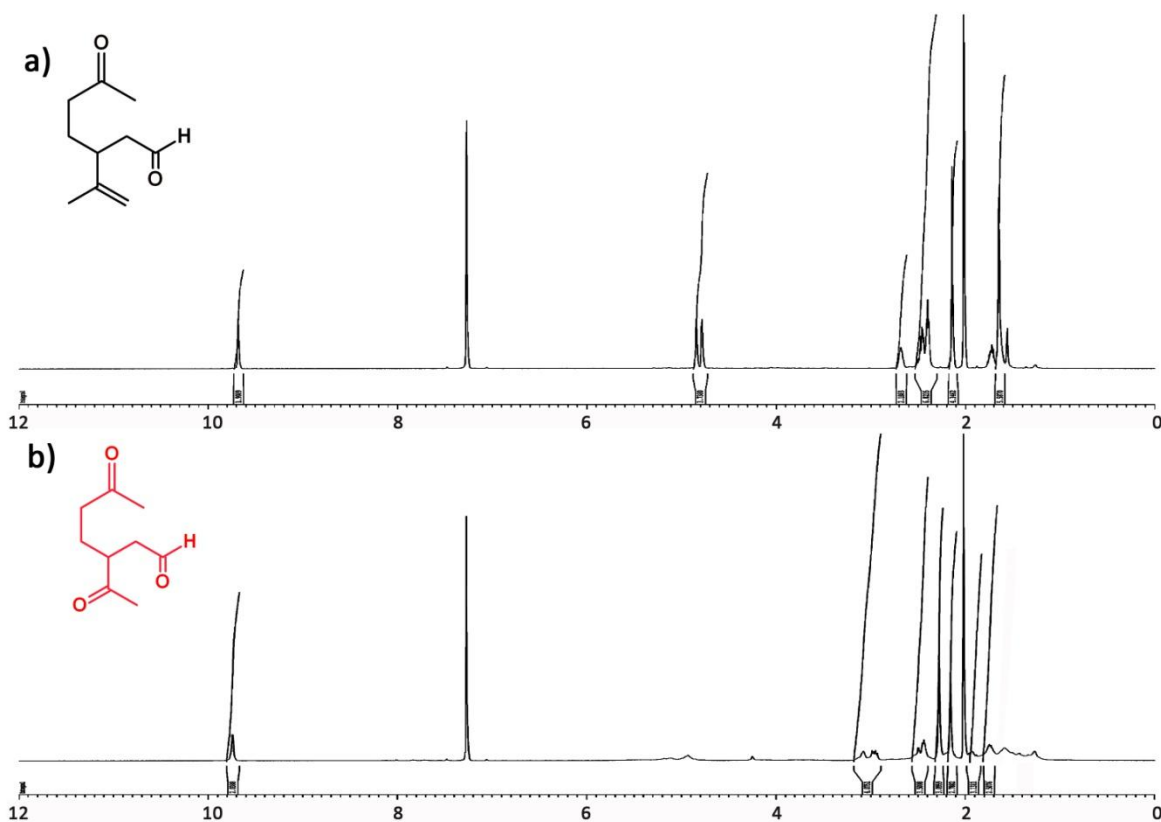
Figure 8.2. ^{1}H NMR spectra in CDCl$_3$ (a) limononaldehyde (LA) and (b) keto-limononaldehyde (KLA). Resonances and integrated peak areas are reported in Table 8.1.

(2008) [467]. The synthesis proceeded as follows: 1 mmol of limonene oxide (Aldrich, 99% purity) was continuously stirred with 2 molar equivalents of sodium metaperiodiate (NaIO$_4$, Alfa Aesar, 99.8% purity) at room temperature in 40 mL of a solvent mixture, comprising of 2:1 tetrahydrofuran (Aldrich, ACS grade) and water (Aldrich, HPLC grade). The reaction was monitored with thin layer chromatography (TLC) and came to completion in approximately 2 hours, when the starting material is no longer observed with TLC and product spots do not change. The solvent system for TLC was a mixture of 3:1 hexanes/ethyl acetate (both Fluka, ACS grade) and the results were visualized with a potassium permanganate (KMnO$_4$) stain. The precipitate was filtered and washed with anhydrous diethyl ether (EMD, ACS grade). The

aqueous phase was extracted twice more with ether and the organic phase combined. Approximately 1.2 g of a semi-viscous crude comprising of two products was collected after concentrating the ether under vacuum. The crude was separated over a silica gel column (60 Å pores, 32-63 μm particles, Sorbent Tech.) with 3:1 hexanes/ethyl acetate. The fractions with LA (TLC retardation factor $r_f \sim 0.2$) were combined and concentrated under vacuum. The ^{1}H nuclear magnetic resonance (NMR) spectrum of LA taken in $CDCl_3$ with a Bruker 500 MHz instrument is shown in Figure 8.2a. The spectra are identical to those reported in the literature [468], and the integrated peak areas (Table 8.1) are consistent with the expected protons in LA.

KLA was synthesized from the ozonolysis of limonene, with a procedure modified from that reported by *Griesbaum et al (1997)* [469]. 1 mmol of limonene (Acros, 97% purity) was dissolved in approximately 2 mL of dichloromethane (Aldrich, ACS grade) and ozonized with a 2 SLM flow of O_3/O_2 with continuous stirring. The limonene starting material contained 0.03% tocopherol as a stabilizing agent. Tocopherol is not reactive with respect to ozone; however, its phenyl component may scavenge free radicals in the solution. The ozonolysis was performed at a temperature of -78°C in an acetone/dry ice bath. The ozonolysis was finished after approximately 20 minutes, when a blue color (liquid O_3) was observed in the chilled reaction mixture. Excess triphenylphosphene (Alfa Aesar, 99% purity) was immediately added and left to stir at room temperature for > 24 hours. The reaction mixture was concentrated under vacuum. The crude was separated with a semi-prep (10 x 250 mm, 100 Å) reverse-phase (C_{18}, Luna, Phenomenex, Inc.) liquid chromatography column with UV-Vis detection (LC-UV) at 2 mL min^{-1} in acetonitrile (ACN, Aldrich HPLC grade). The KLA fraction was concentrated and the ^{1}H NMR spectrum (Figure 8.2b) was recorded in $CDCl_3$. The NMR peak positions and integrated areas (Table 8.1) were consistent with literature data [469, 470]. However, in the KLA ^{1}H spectrum, a

singlet correlating to an ACN impurity can be observed at 2.10 ppm [471]. We do not expect this impurity to interfere with experiments because ACN does not absorb in the visible wavelengths and it has been established that ACN is inert with respect to reaction with carbonyls [87].

Table 8.1. [1]H resonance peak positions, multiplicity (s = singlet, d = doublet, m = multiplet) and integrated peak areas for identification of limononaldehyde (LA) and keto-limononaldehyde (KLA). ^{1}H NMR spectra and structures are shown in Figure 8.1. NMR data of LA matched those reported by Ref. [468] and NMR data for KLA matched those reported by Refs. [470] and [472].

Limononaldehyde			*Keto–limononaldehyde*		
[1]H peak (ppm)	Multi-plicity	Peak Area	[1]H peak (ppm)	Multi-plicity	Peak Area
1.68 – 1.71	m	5.19	1.64 – 1.82	m	2.12
2.14	s	3.00	1.86 – 2.02	m	1.12
2.30 – 2.52	m	4.04	2.16	s	2.92
2.68	s	1.08	2.27	s	2.91
4.78, 4.84	d	2.09	2.38 – 2.60	m	2.10
9.68	s	1.00	2.90 – 3.18	m	1.93
			9.73	s	1.00

8.3.2. UV-Vis absorption spectroscopy

Synthesized and purified KLA and LA were dissolved in water (18 MΩ-cm, Barnstead Nanopure) with gentle heating and sonication for aging experiments. Solutions had the concentration range of 10^{-4} – 10^{-3} M and used within 2 hours. Aging of KLA and LA was performed at room temperature. Small (μL) volumes of stock (20 g/L) ammonium sulfate (AS, $(NH_4)_2SO_4$) and glycine (GLY) solutions were added, in appropriate molar ratios, in order o avoid significantly diluting the ketoaldehyde. "Aqueous aging" refers to a process in which an aqueous solution of KLA or LA with various amounts of AS/GLY added is left to react over the timescale of hours. "Evaporative aging" refers to otherwise identical solutions of KLA or LA with AS/GLY added that has been evaporated to dryness using a rotary evaporator (Buchi R-

210) at a bath temperature of T = 45 °C. The dry residue was then redissolved in water to the original dilution, as described in more detail in Chapter 7.
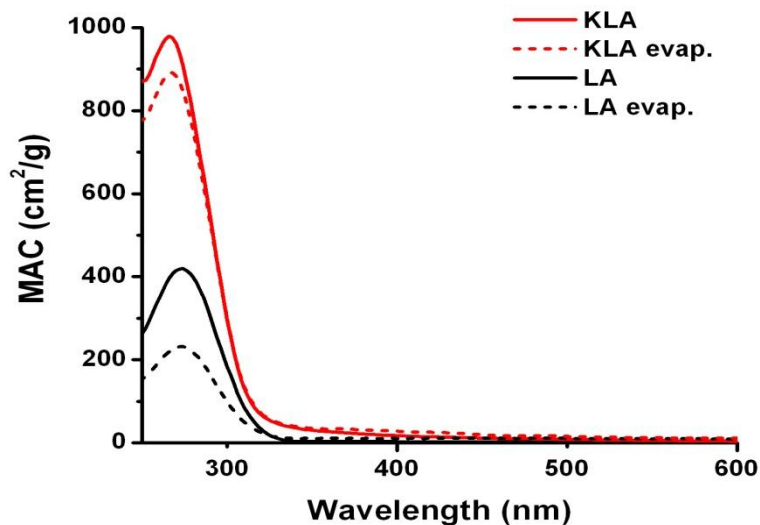
Figure 8.3. UV-Vis absorption spectra of control experiments: evaporation of KLA and LA aqueous solutions do not brown in the absence of additives.

To quantify the degree of visible light absorption, UV-Vis absorbance spectra were monitored using a dual-beam spectrometer (Shimadzu UV-2450) with purified water as the reference. The data were recorded in 1 cm quartz cuvettes in the wavelength range of $200 - 700$ nm. As the brown carbon chromophores are highly absorbing, most aged samples required dilution up to 20-fold in order for the recorded absorbance to stay well within the linearity limit of the spectrometer. All absorbance data were scaled to correspond to the initial undiluted solutions, and reported values are identified as "corrected absorbance" obtained by multiplying the measured absorbance of a diluted solution by the corresponding dilution factor.

Here, the degree of browning is quantified similarly to the method used in Chapter 7, by using the effective mass absorption coefficient (*MAC*, units of $cm^2 \ g^{-1}$) of the organic material.

MAC and ΔMAC are calculated from the base-10 absorbance A_{10} of an SOA extract with the solution mass concentration C_{mass} (g cm^{-3}) measured over pathlength b (cm) [3]:

$$MAC\ \lambda\ = \frac{A_{10}^{solution}\ \lambda\ \times \ln(10)}{b \times C_{mass}} \qquad \text{(E 8.1)}$$

$$\Delta\ MAC\ (\lambda) = (MAC)_{aged} - (MAC)_{control} \qquad \text{(E 8.2)}$$

We also define an average value $\langle MAC \rangle$ over a specific wavelength range:

$$\langle MAC \rangle_{\lambda_1 - \lambda_2} = \frac{1}{\lambda_2 - \lambda_1} \times \int_{\lambda_1}^{\lambda_2} MAC\ \lambda\ d\lambda \qquad \text{(E 8.3)}$$

Reported MAC values correspond only to the mass concentration of the organic material derived from the synthesized compounds and not those of the nitrogen-containing additives (AS, GLY) that do not absorb radiation above $\lambda = 300$ nm.

Both sample and control experiments were analyzed in identical manner. Controls for the aqueous aging experiments refer to KLA or LA "aged" in water for the same time interval, but without additives. Controls for the evaporative aging experiments refer to aqueous KLA or LA solutions evaporated to dryness and redissolved in water without additives. In both cases, no visible browning occurred. The absorbance spectra for the control samples are clearly indicative of carbonyl compounds with peak absorbances around 280 nm (Figure 8.3), and the MAC values for control samples in the 400 – 550 nm region where C$_{430}$ and C$_{500}$ absorption is < 30, more than 2 orders of magnitude smaller than the aged KLA samples.

8.3.3. Liquid chromatography

Aged samples were separated isocratically with reversed-phased LC at 2 mL min^{-1} in (1:1) ACN:H$_2$O using the instrument and C$_{18}$ column described in Section 8.3.1. Chromophores were detected by their UV-Visible (200 – 500 nm) absorption using a diode array detector. The

solvent mixture was degassed under vacuum within 1 h of use. The column was flushed for ~ 2 h with solvent before separation. The run times were typically 15 – 20 minutes and the dead time was 3 – 4 minutes. The desired fractions were collected after their elution in clean scintillation vials. Typically, several fractions were combined and concentrated under vacuum. The dried residues of the separated chromophores were redissolved in solvents suitable for further analysis.

8.3.4. Infrared spectroscopy

Vibrational data were recorded on a single-beam Fourier-transform infrared (FT-IR) spectrometer (Mattson Galaxy 5000) in the spectral range of $700 – 4000$ cm^{-1} with a resolution of 4 cm^{-1}. FT-IR spectra of brown carbon residues were taken with 3 mm thick zinc-selenide (ZnSe) optical windows (Cradley Crystals Corp.) in two sets of experiments: aqueous aging and surface aging. These experiments are designed to be complementary – aqueous aging experiments show the vibrational features of the dissolved chromophore without interference from the parent and surface aging experiments show the changes in chemical functionality as the chromophore is produced from KLA as a function of time:

(a)   *Aqueous aging*: samples aged in the aqueous phase were separated with LC-UV, dried under vacuum, and redissolved in 500 μL deuterium oxide (D$_2$O, Cambridge Isotope Laboratories, Inc. 99.9% purity). The concentrated D$_2$O samples were loaded onto a plastic pipette tip and finely aerosolized with the aid of 30 psi UHP air pressure onto the ZnSe windows. The windows with the brown carbon residues deposited as an even fine mist were dried at room temperature for 3 days and spectra were recorded.

(b)   *Surface aging*: Previous experiments established that limonene/O$_3$ SOA films aged with humid NH$_3$ vapor also produced the C$_{500}$ chromophore observed with evaporative or aqueous aging with NH$_4^+$ [91, 473]. For the surface aging experiments, a film of KLA

was deposited onto ZnSe windows and placed into a small polyethylene dish. The polyethylene dish was allowed to float on top of a solution ~ 0.5 M ammonium nitrate (NH_4NO_3, Fluka ACS grade) in a larger sealed glass Petri dish. The headspace was approximately 40 mL and the window remained separated from both the NH_4NO_3 solution and the top of the Petri dish. Humid NH_3 vapor filled the headspace of the sealed Petri dish and aged the KLA film. The window was removed at time intervals of 0, 12, 36, and 84 h and dried under vacuum in a desiccator over Drierite for several hours to remove condensed water prior to FT-IR analyses.

8.3.5. Nuclear magnetic resonance spectroscopy

Proton (^1H) and carbon (^{13}C) NMR experiments were performed in the UCI NMR Facility. Spectra were taken with the "Cryo500" (Bruker DRX500) instrument equipped with a liquid-nitrogen cooled cryogenic probe, which greatly improves the signal to noise ratio of the sample. The resonance frequency of the instrument with respect to protons is 500 MHz. The experiment names as they appear in the UCI NMR experiment database will be given in parenthesis, e.g., experiment name X (exp: X). Deuterated solvents used for NMR were purchased from Cambridge Isotope Laboratories with purity > 99.8% D. The probes were manually aligned before experiments in both the proton and carbon channels. The ^1H spectra (exp: h1.c) of KLA and LA were taken in $CDCl_3$ and referenced by the residual (deuterated solvent less one deuterium atom) peak at 7.27 ppm.

The ^1H and ^{13}C spectra of the separated/concentrated C_{500} were taken in two water-based solvent systems because C_{500} is poorly soluble in nonpolar organic solvents: (a) D_2O and (b) 90% H_2O with 10% D_2O. The small amount of D_2O added in experiment (b) was used only to obtain an instrumental deuterium lock. These two NMR experiments were designed to showcase

H/D exchange between the solvent and exchangeable protons of organic acids (–COOH), amines (C–NHR), imines (C=NH), and alcohols (C–OH) in the sample. H/D exchange is also possible for amide protons but is expected to be slow. The D_2O experiments were referenced by the residual water peak at 4.79 ppm. The high-H_2O experiments were performed with pulse-field gradient (PFG) water suppression (exp: h1sup.c) to remove the signal of the water protons that would otherwise overwhelm the spectra. An initial scan was performed to obtain the exact frequency of the water proton resonance. This resonance was also used to reference the water-suppressed spectra. Subsequently during the PFG scans, short magnetic pulses defocus the pre-set resonance of water without significantly perturbing the resonant signals of other protons.

The ^{13}C spectra were taken with a 1.5 s relaxation delay (exp: c13d1=1.5.s) using the ^1H spectrum of the same sample taken immediately prior as reference. A 2D proton-proton correlation through bonds experiment (COSY) was also obtained with water suppression (exp: cosynw.c). This experiment determines the multiplicity of proton resonances because off-diagonal resonances indicate coupling between protons 2 – 3 bonds away.

8.3.6. High-resolution mass spectrometry

Four separated C_{500} fractions were analyzed with high-resolution mass spectrometry (HR-MS) at PNNL. Data acquisition was performed with positive ion mode electrospray ionization (ESI) in the LTQ-Orbitrap in the manner described in Section 1.3.3 and data analyses were performed as described in Section 1.3.4. These four samples, as expected, showed similar mass spectra and the mass spectrum from a representative sample is reported. The mass range for acquisition was *m/z* 100 – 2000 and the ESI spray voltage was 4 kV. Similarly to NMR experiments, H/D exchange was probed with HR-MS by analyzing the same sample in both 90% H_2O/10% ACN and 90% D_2O/10% ACN solvent mixtures (ACN was added to improve

electrospray stability by decreasing the surface tension of the resultant ACN/H_2O solvent). During data analysis, the signals from ^{13}C and D were verified by the exact mass differences of these isotopes and the expected abundances. Signals from ^{13}C were removed but those from D in the deuterated samples were conserved.

8.4. Results and discussion

8.4.1. Brown carbon formation from ketolimononaldehyde

The central result of this work is the first identification of KLA as a precursor to brown carbon. Figure 8.4 shows a picture of unaged and aged KLA (top row) and LA aqueous solutions after approximately 15 hours of reaction and reports the molar ratios of nitrogen-to-ketoaldehyde in the caption. AS-aged KLA solutions produce the characteristic yellow-to-brown chromophores and the GLY-aged KLA produce the red/pink chromophores. In the aqueous reaction, the formation of chromophore appears to be proportional to the concentration of added nitrogen (more quantitative description of the concentration dependence will be presented below). Furthermore, the GLY-aged chromophore appear to have a slightly higher molar extinction coefficient than its NH_4^+-aged counterpart for a given time and molar ratio. LA, remarkably, does not participate in browning reactions and remained colorless even after several days of aqueous reaction. Because KLA and LA are both 1,6- ketoaldehydes, the observation that they undergo different reactions with reduced nitrogen, and only those reactions from KLA produce brown carbon, suggests that the additional ketone functional group is an important component. It is possible that the 1,4-ketoaldehyde or the 1,5-diketone structural motif is required for brown carbon formation.

Figure 8.4. KLA aqueous solutions (top row) form visible light-absorbing chromophores from addition of ammonium sulfate (AS) and glycine (GLY) while LA solutions (bottom row) do not. Top row from left to right: KLA (control), AS/KLA (1:1), AS/KLA (3:1), AS/KLA (10:1), GLY/KLA (1:1), GLY/KLA (3:1), GLY/KLA (10:1). Bottom row: same AS and GLY ratios as top row but with LA instead of KLA.

The extent of browning can be quantified with mass absorption coefficient (MAC) values using equations (8.1 – 8.3). The wavelength-dependent differences in MAC ($\Delta MAC = MAC_{aged} - MAC_{control}$) is a convenient meassure of the extent of browning because it corresponds to the absorbance due to the the compounds produced during aging. Figure 8.5 shows the absorbance spectrum converted to ΔMAC of the aqueous reactions of AS and GLY with LA. Although there is an enhancement in absorption in the near UV induced by AS-aging of LA that is not dependent on [AS], there is no change in the visible wavelengths $\lambda > 400$ nm. We speculate the reason for this UV absorption enhancement is that the NH_4^+ may catalyze intramolecular aldol reaction of LA [474]. Aldolization would destroy one carbonyl group out of the two that reacted; however, the remaining carbonyl would be conjugated after condensation and thus the absorption at 280 nm would be enhanced. The reaction of LA with GLY also leads to an enhancement of absorption at $\lambda < 350$ nm, perhaps for similar reasons. This change may not be due to the addition of GLY itself, as this amino acid has an exceedingly small absorbance above 250 nm.

214
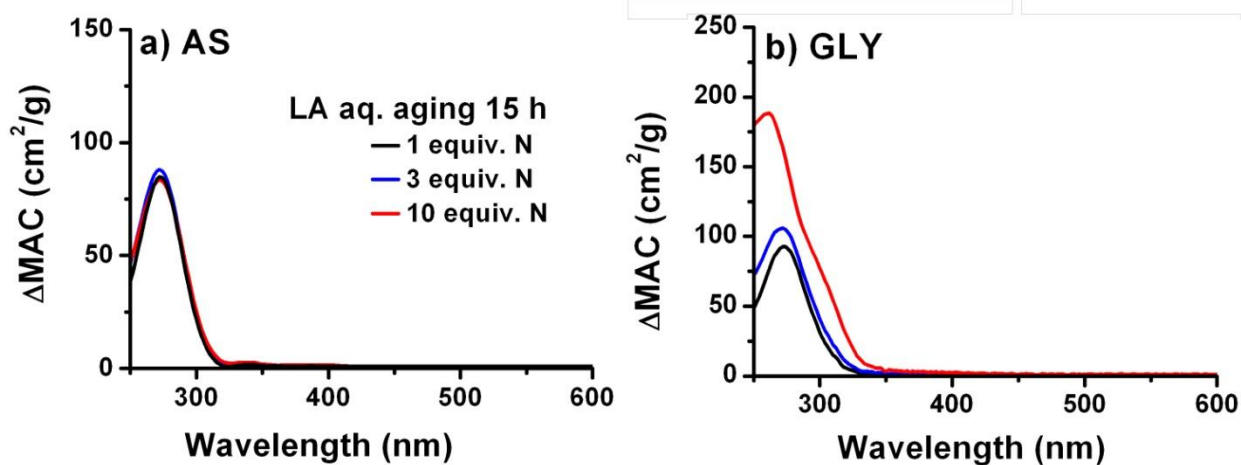
Figure 8.5. Wavelength-dependent ΔMAC (Eq. 8.2) of LA aqueous solutions aged with various molar equivalents of (a) AS and (b) GLY confirm that LA does not produce visible light-absorbing chromophores through aqueous chemical aging with reduced nitrogen.
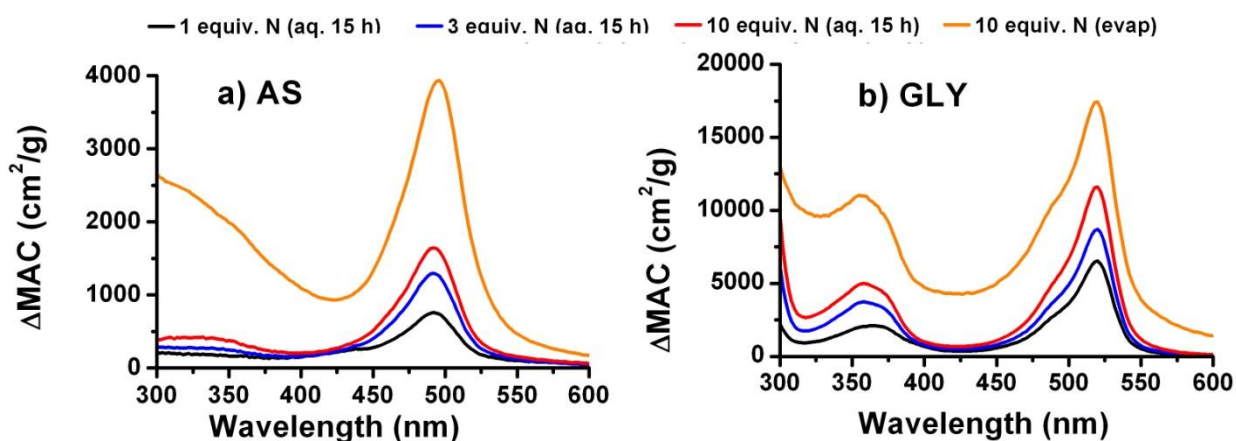
Figure 8.6. Wavelength-dependent ΔMAC of KLA aqueous solutions aged with various molar equivalents of (a) AS and (b) GLY show the net production of visible light-absorbing chromophores trough both aqueous and evaporated aging. The orange traces correspond to evaporated experiments at 10 molar equivalent of nitrogen.

In contrast, Figure 8.6 shows that the ΔMAC values for KLA solutions aged with AS and GLY increased dramatically in the visible wavelengths. For aqueous samples, ΔMAC increases in response to increasing molar concentrations of nitrogen in both AS- and GLY-induced aging. The ΔMAC values reach a maximum when evaporated, indicating complete reaction. This observation is consistent with our previous studies. Compared to aqueous aging for 15 hours, the

instantaneous evaporation of the 10:1 N:KLA mixture increased ΔMAC by a factor of 1.5 – 3. Furthermore, evaporation of the 20:1 N:KLA mixture (not shown) does not improve ΔMAC, suggesting a KLA-limited reaction.
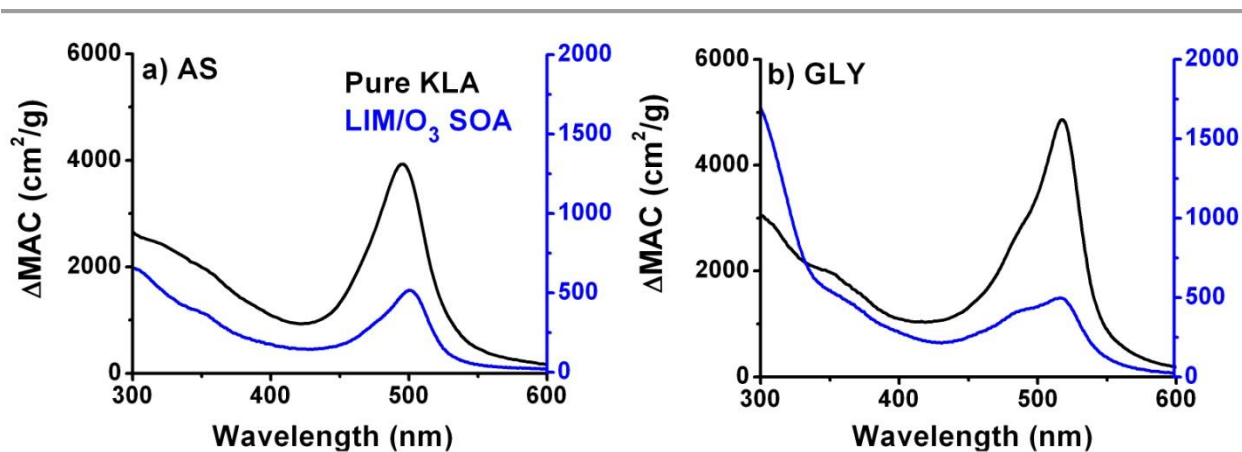
Figure 8.7. The absorption spectra of evaporation-induced aging of (1:1) AS:KLA and (1:3) GLY:KLA are similar to that of limonene/O_3 SOA. The ΔMAC values of the evaporation-produced chromophores are not dependent on the concentration of the nitrogen species and have been normalized to the mass concentration of KLA. Note that the black traces (pure KLA) and blue traces (limonene/O_3 SOA) have separate vertical axes for MAC.

Figure 8.7 shows the absorbance spectra of aged KLA superimposed on those of aged limonene/O_3 SOA (hereinafter, just "SOA" for brevity). Compared to SOA, these features are almost identical. For both the aqueous and evaporative aging, the KLA + AS reaction produces chromophore that absorb at λ ~ 495 nm, compared to 500 nm in SOA. The KLA + GLY reaction produces chromophores that absorb at λ ~ 360 nm and λ ~ 518 nm when evaporated with an excess of GLY and only chromophores absorbing at λ ~ 518 nm in the regime where KLA is in excess. The peak absorbance for the evaporated SOA/GLY mixture is at λ ~ 520 nm. The spectral shape of the aged KLA compares very well with that of the aged SOA, e.g., even the distinctive double feature of the SOA/GLY peak at 520 nm is preserved, a strong suggestion that the choromophores are the same or very similar in structure. As the absorbance maxima for aged

SOA can shift by as much as $\Delta\lambda \sim 15$ nm with respect to aging conditions [96], the small ($\Delta\lambda \leq 5$ nm) discrepancies in the peak maxima can be considered inconsequential (they could, for example, result from the solvent effects).
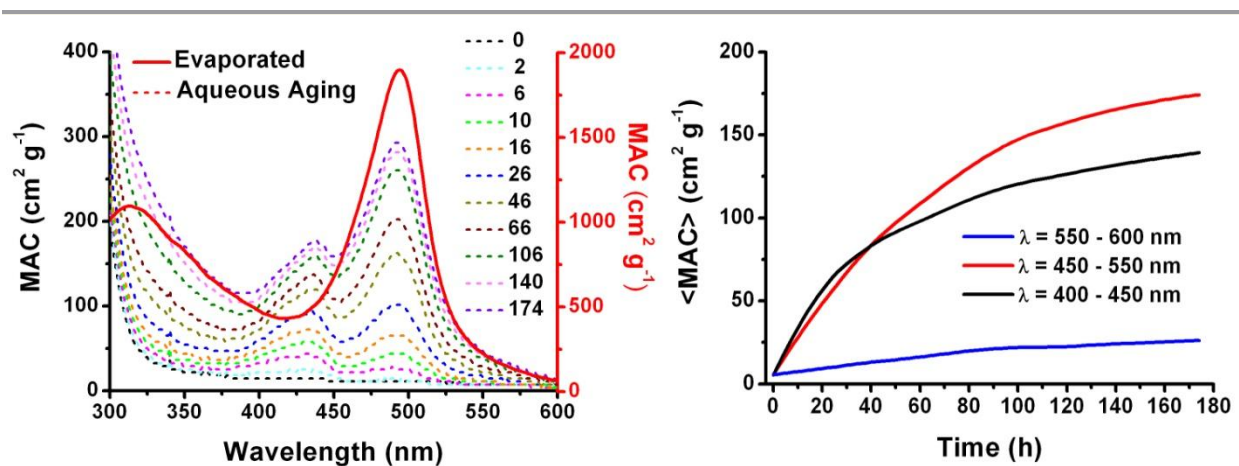
Figure 8.8. KLA aged with 1 molar equivalent AS at different reaction times (dashed lines, and left MAC axis) and after evaporation (solid red line, and right MAC axis). The KLA reaction produces the C_{430} and C_{500} chromophores in the same order as the reaction of limonene/O_3 SOA with AS. The right panel shows the time dependence of the average MAC values corresponding to the 400-450, 450-550, and 550-600 nm windows.

As expected, the ΔMAC values for the KLA reactions with AS and GLY are larger than those of SOA due to the assumption made in Equation (8.1) that all of the SOA contributes to the browning when, in reality, only a fraction of the SOA mass are active reagents. Additionally, any side reactions with AS/GLY in the complex SOA mixture that yield non-absorbing products will lower the effective MAC of SOA. ΔMAC for KLA are $8 - 10$ times larger in the AS ($\text{MAC}_{\text{peak}} \sim$ 4000 cm^2/g) and GLY ($\text{MAC}_{\text{peak}} \sim 5000$ cm^2/g) reactions, respectively, than for SOA (MAC peak ~ 500 cm^2/g). This implies that if KLA were the only precursor it would be present in the SOA at a mass concentration of ***10 − 13%***, a result qualitatively consistent with the chromatogram shown in Figure 8.1 and the fact that KLA is expected to be the dominant species

in the aerosol phase [50]. However, [KLA] has not been quantified in previous studies and direct comparisons are not possible.

Another distinctive characteristic of the SOA+AS reaction is the time evolution of chromophores (Fig. 7.2 in the previous chapter). *Nguyen et al (2012)* followed the aqueous reaction of SOA + AS over the course of 190 h and showed that C_{430} is formed immediately upon addition of AS, followed by the delayed formation of C_{500} and a slow growth of a shoulder band at 570 nm [96]. Figure 8.8 shows the same study performed on KLA/AS (1:1) where the time-dependent behavior of chromophore formation is qualitively similar to aged SOA. Additionally, the shift of C_{500} toward the blue and C_{430} toward the red was also reproduced in KLA, suggesting that the overall reaction is similar. MAC was averaged over three wavelength intervals, e.g., $400 - 450$, $450 - 550$, and $550 - 600$ nm, to account for the slow shift in absorbance maxima.

The time evolution of chromphore bands shown in the right panel of Figure 8.8 is also similar to that of SOA. However, the chromophore features in SOA showed a much stronger saturation effect with time, e.g., <MAC> did not increase much after 80 h in SOA whereas with KLA the <MAC> values continue to grow after 180 h. In addition, the evaporation experiment, which can be viewed as a terminal result, increased MAC by more than a factor of 5 for KLA and by a smaller factor in SOA. Kinetic results in the next section demonstrate that concentration of nitrogen in the aqueous phase affects kinetics and the dissimilarities in kinetic behavior are likely due to the (1:1) molar ratio of NH_4^+ chosen for the KLA experiment instead of the excess NH_4^+ used to aged SOA. However, despite small discrepancies, the bulk kinetics of chromophore formation from KLA mimics SOA quite well.

8.4.2. Reaction order and rates

Kinetics of the aqueous and evaporative aging reactions of KLA were studied using UV-Vis spectroscopy. To obtain the order of reaction with respect to the reduced nitrogen compound, [KLA] was kept constant at 0.0075 M and the molar ratio of ***nitrogen***, e.g. NH_4^+ (not AS) and GLY, was varied at 0.33, 1, and 3. Similarly to obtain the order of reaction with respect to KLA, [nitrogen] was kept fixed at 0.0075 M and the molar concentration of KLA was varied at 0.33, 1, and 3. Dilution tests at 1, 0.1, and 0.01 dilutions of the (1:1) N:KLA solution were performed to assess changes in equilibrium in the aqueous and evaporative aging. Full UV-Vis spectra were recorded at 6 time intervals for the aqueous aging experiments to obtain a linear initial rate of reaction: 0, 2, 6, 12, 26 and 50 h. For evaporative aging experiments, spectra were recorded before and after evaporation. The evaporative aging experiments used the same concentration ratios as the aqueous aging, with the addition of a (1:10) N:KLA solution to more accurately describe the low nitrogen kinetic regime.

Figures 8.9 (I) and (II) show the kinetics experiment results for the KLA/AS and KLA/GLY reaction, respectively. The absorbances of each chromophore (C_{430} and C_{500} for KLA/AS; C_{360} and C_{520} for KLA/GLY) were monitored in lieu of their concentration. Dilutions (10 − 20 fold) were performed to stay within the Beer's Law (Abs = $\epsilon \cdot C \cdot b$) linearity limits, where ϵ is the molar extinction coefficient in M^{-1} cm^{-1}, b is the pathlength in cm, and C is the concentration in M. Therefore, we can make an assumption that the rates using absorbance values are proportional to concentration ($d[C]/dt = (\epsilon \, b)^{-1} \cdot d[Abs]/dt$). The absorbances were corrected to report the undiluted values.

In Figure 8.9 (I a-b), [NH_4^+] was varied and the rates of C_{430} and C_{500} both increased proportionally with respect to the amount of added nitrogen. In 8.9 (I c-d), [KLA] was varied and
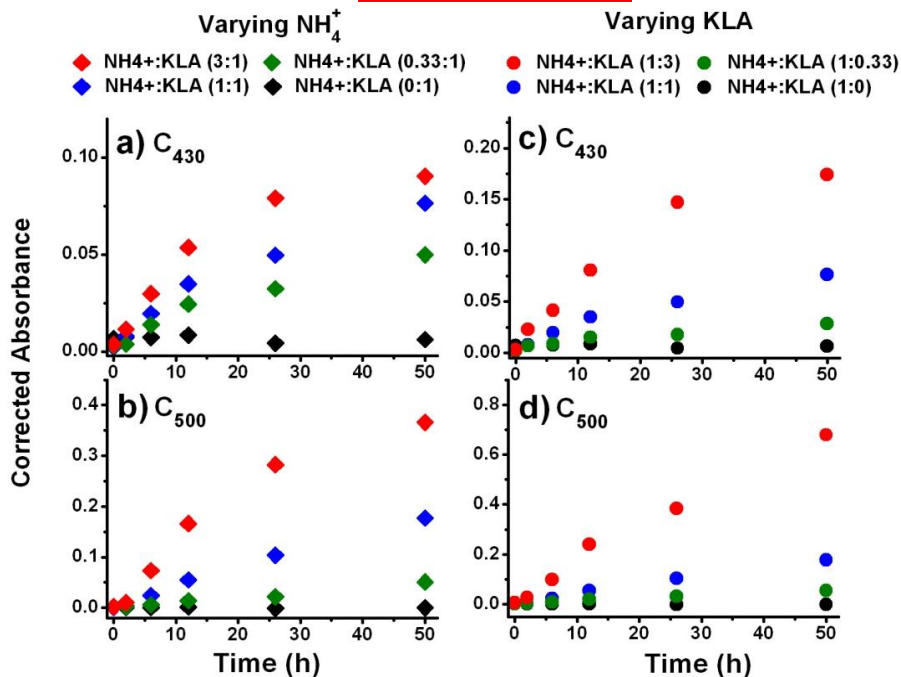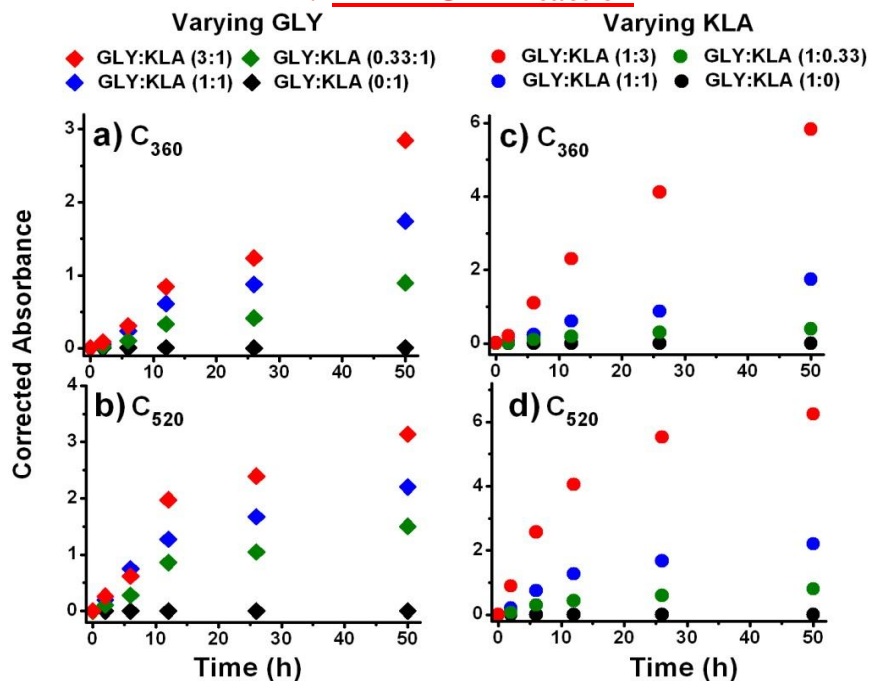
Figure 8.9. Corrected absorbance values of chromophores from the aqueous reactions of (top) KLA + NH_4^+ and (bottom) and KLA + GLY. The left and right panels correspond to experiments that vary the nitrogen and KLA contents, respectively. Linear initial rates of rise in the corrected absorbance are reported in Table 8.2.

a clear concentration dependence is observed. For the GLY reaction in Figure 8.9 (II a-b), there is only a small observed dependence of C_{360} and C_{520} on [GLY]. Even when [GLY] increased three-fold, the rate (red diamonds) increased modestly. In 8.9 (II c-d) the dependence on [KLA] is clearly proportional for both C_{360} and C_{520}.

For the evaporated samples, the corrected absorbance values were plotted with respect to reagent concentration in Figure 8.10 because evaporation happens quickly, and the temporal information is not available. Figures 8.10 (a − c) and 8.10 (d − f) show the concentration dependence of the KLA/AS and KLA/GLY reactions, respectively. In panels (a) and (d) the samples were diluted by three orders of magnitude and evaporated. The results are linear with respect to concentration of [KLA], suggesting that water equilibrium effects are minimal in the evaporation experiments. Similar experiments were performed in the aqueous phase with identical results. In panels (b) and (e), the samples were varied in [KLA] while the nitrogen content was kept constant. The absorbances were linear with respect to [KLA], indicating that [KLA] is the limiting reagent. In panels (c) and (f), [KLA] was kept constant and the molar concentration of nitrogen species varied. In both the AS and GLY reactions, there appears to be no dependence on nitrogen compounds after approximately 10% by mole N. This type of dependence may indicate a catalytic reaction or a KLA-limited reaction, especially if a specific chemical form of KLA is needed for reaction.

With the rate information gained from absorption spectroscopy and the assumption that KLA is the only chromophoric precursor, we can obtain the orders of the AS + KLA and GLY+KLA reactions. Table 8.2 reports the initial (linear) aqueous rates of reaction for the formation of each chromophore at each reagent concentration. A standard law of mass action reaction rate expression was assumed, i.e., $R = k[A]^a[B]^b$, and the relative rates were used to

221

obtain the orders with respect to [KLA], [NH$_4^+$] or [GLY] in the aqueous phase. For the evaporated experiments, an assumption was made that complete reaction occurs. The resulting ΔC, and therefore the reaction rate, is consequently directly proportional to $(\epsilon\ b)^{-1} \cdot \Delta Abs$. The calculated orders of reaction obtained at different concentrations were averaged. As evaporation-driven reactions suppress the formation of the smaller C$_{430}$ and C$_{360}$ chromophores, those species were not included in calculating the reaction order.
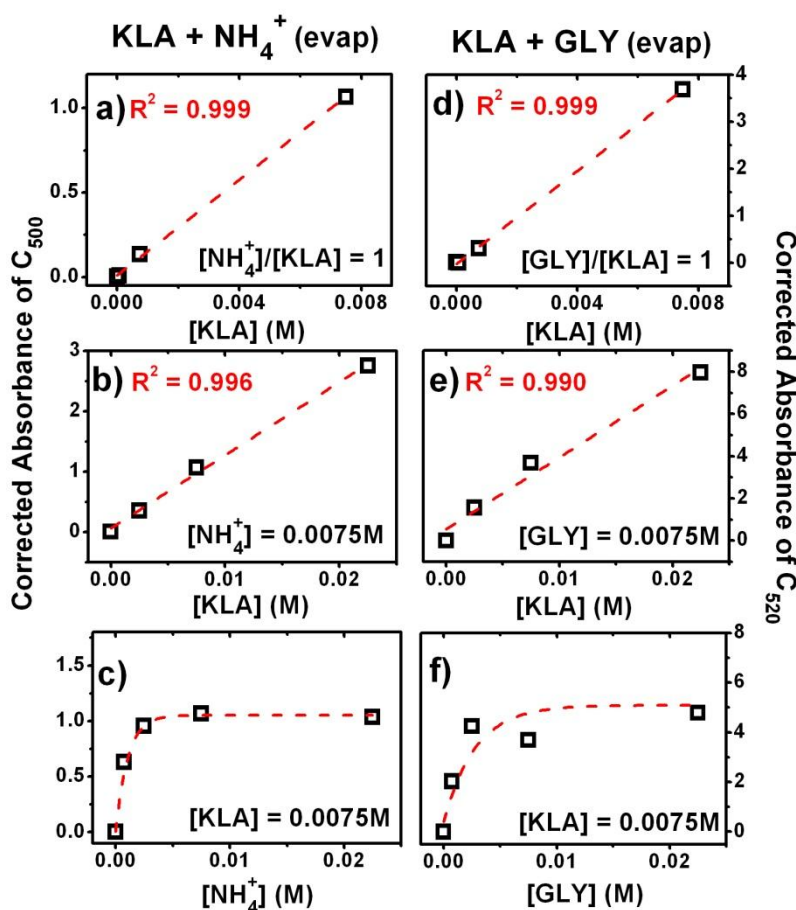
Figure 8.10. Absorbance maxima values of chromophores from the evaporated reaction of KLA aged with (a-c) NH$_4^+$ and (d-f) GLY. Reaction orders are reported in Table 8.2.

Table 8.2 shows that the orders of the chromophore-formation reaction with respect to [KLA] are approximately unity for each experiment, whether aqueous or evaporation. This

expected result confirms that it is the KLA structure that is modified to produce the chromophores. The aqueous reactions can be peformed more precisely because the only errors stem from dilution before measurement. The evaporation reactions have potentially high errors due to the imprecise nature of evaporation in the rotavap. For example, the evaporated formation of C_{520} deviates the most from unity at 0.75; however, given the behavior of the other reactions, we assume that this reaction is not fractional in order with respect to [KLA]. Further work is needed to estimate an uncertainty range following several evaporation trials.

Table 8.2. Linear initial rates (in Abs h^{-1}) of the aqueous KLA reaction with AS and GLY. The varied reactant concentrations are shown in bold text. Reaction orders for aqueous experiments were obtained by assuming that the law of mass action applies, $R = k[A]^a[B]^b$, and using the method of relative rates. Reaction orders for evaporated experiments, were obtained by assuming the reaction goes to completion and calculating the ratio of absorbances only at the peak maxima.

AS-aging reaction					GLY-aging reaction			
[KLA] (M)	[NH$_4^+$] (M)	Rate C_{430}	Rate C_{500}		[KLA] (M)	[GLY] (M)	Rate C_{360}	Rate C_{520}
0.0075	**0.0000**	0.0002	0.0002		0.0075	**0.0000**	0.0001	0.0000
0.0075	**0.0025**	0.0012	0.0010		0.0075	**0.0025**	0.0280	0.0710
0.0075	**0.0075**	0.0018	0.0033		0.0075	**0.0075**	0.0510	0.1080
0.0075	**0.0225**	0.0029	0.0110		0.0075	**0.0225**	0.0710	0.1620
Order – Aqueous		**0.41**	**1.09**		**Order – Aqueous**		**0.43**	**0.38**
Order – Evap.			**-0.02**		**Order – Evap.**			**0.06**
[KLA] (M)	[NH$_4^+$] (M)	Rate C_{430}	Rate C_{500}		[KLA] (M)	[GLY] (M)	Rate C_{360}	Rate C_{520}
0.0000	0.0075	0.0000	0.0000		**0.0000**	0.0075	0.0000	0.0000
0.0025	0.0075	0.0006	0.0012		**0.0025**	0.0075	0.0170	0.0370
0.0075	0.0075	0.0018	0.0033		**0.0075**	0.0075	0.0510	0.1080
0.0225	0.0075	0.0054	0.0140		**0.0225**	0.0075	0.1860	0.3360
Order – Aqueous		**1.03**	**1.10**		**Order – Aqueous**		**1.11**	**1.00**
Order – Evap.			**0.95**		**Order – Evap.**			**0.75**

One of the most interesting results from calculating the orders of reaction is that the orders with respect to added nitrogen compounds are not the same between the aqueous and

evaporation reactions. For example, in the aqueous formation of C_{500}, the order with respect to the $[NH_4^+]$ is unity and the order in the evaporation reaction for the same chromophore is zero when there is sufficient $[NH_4^+]$. Similarly, there is no observed dependence on [GLY] for the evaporative formation of C_{520} when there is sufficient [GLY]. Yet, in the aqueous reaction this order is a fractional 0.4, which suggest many steps in the aqueous reaction. We spectulate that the observed differences in reaction orders for these two conditons are an indirect indication of the involvement of water in chromophore formation.

Table 8.3. Linear initial rates (in M s^{-1}) and rate constants (in M^{-1} s^{-1}) of the aqueous KLA reaction with AS and GLY. Rate constants were obtained by assuming an upper limit for the molar extinction coefficient of C_{500} and C_{520} ($\epsilon \sim 1 \times 10^5$ M^{-1} cm^{-1}) based on results from evaporation experiments. The reported rates are lower limit estimations.

N:KLA ratio	KLA + AS (C_{500})		KLA + GLY (C_{520})	
	R (M s^{-1})	k (L mol^{-1} s^{-1})	R (M s^{-1})	k (L mol^{-1} s^{-1})
(1:0.33)	2.8×10^{-12}	4.1×10^{-7}	2.0×10^{-10}	2.9×10^{-7}
(1:1)	9.2×10^{-12}	4.1×10^{-7}	$3.0 \times 10^{-10.}$	2.8×10^{-7}
(1:3)	3.1×10^{-11}	4.2×10^{-7}	4.5×10^{-10}	2.7×10^{-7}
(0.33:1)	3.4×10^{-12}	5.0×10^{-7}	1.0×10^{-10}	2.8×10^{-7}
(3:1)	3.9×10^{-11}	5.2×10^{-7}	9.3×10^{-10}	2.9×10^{-7}
	Average	**4.5×10^{-7}**		**2.8×10^{-7}**
	Std. Dev.	5.2×10^{-8}		7.2×10^{-9}

For the reaction with NH_4^+, the rate-limiting step may involve both H_2O and NH_4^+, in which case the reaction would depend on NH_4^+ directly in solution. If the chromophore formation directly involves a condensation step then evaporation will shift the equilibrium dramatically to the right. The concentration dependence observed in Fig. 8.10 c/f and an evaporation order of zero with respect to NH_4^+/GLY, respectively, may indicate that a non-dominant intermediate is the active reagent, or a reaction where the reduced nitrogen compound is catalytic. A known NH_4^+- and amino acid-catalyzed condensation reaction that occur with

carbonyls is aldol condensation. This type of catalytic reaction has been documented in atmospherically-relevant systems like glyoxal and actaldehyde, producing conjugated light-absorbing compounds [475-477].

The remarkable stability of the chromophores in water does not contradict the suggestion that condensation reactions are responsible for their formation. We acidified an aqueous solution of C_{500} with formic acid (HCOOH) until pH < 1. Even at low pH, no disintegration of the chromophore was observed. The aldol condensation products are stable under such conditions and only harsh treatment with base and heat will induce retro-aldol reactions. Similarly, secondary imines like Schiff bases are stable with respect to acid even at pH 1 [478], where the protonated form that absorbs in the visible wavelenth dominates. In contrast, the primary aldimines (C=NH) that are expected to form via the aldehyde + NH_4^+ reaction, at least in the initial steps, are reactive and are possibly converted to stable secondary aldimines through transimination if an amine tautomer is present [479].

We can also estimate rate coefficents for the aqueous browning reactions by assuming a certain value of the molar extinction coefficient (ϵ) for the resulting chromophore. This and previous work suggested that the chromophores are highly absorbing species, and assuming a typical maximum value of ϵ for a strong molecular absorber ($1 \times 10^5 \ M^{-1} \ cm^{-1}$) should give us the lower limit of the reaction rate coefficients. Table 8.3 shows that the rate coefficients for the formation of chromphores are at least $10^{-7} \ M^{-1} \ s^{-1}$. If we overestimate the extinction coeffient by a certain factor, then the rate coeffients will be proportionally larger. However, this factor is unlikely to exceed 10^2, suggesting that the rate constants are small in magnitude relative to typical bimolecular reaction rate constants. This result is qualitively consistent with the observation that chromophore production in water is a very slow process, taking several days to

afford complete reaction even at millimolar concentrations of the reactants. In the evaporation experiment, however, the full reaction is achieved in a matter of seconds to minutes, so the (effective) rate coefficients in this scenario are much larger and the reactions are more relevant for lifetimes of clouds, fogs, and aerosols in the atmosphere.

8.4.3. Chromophore structure analysis
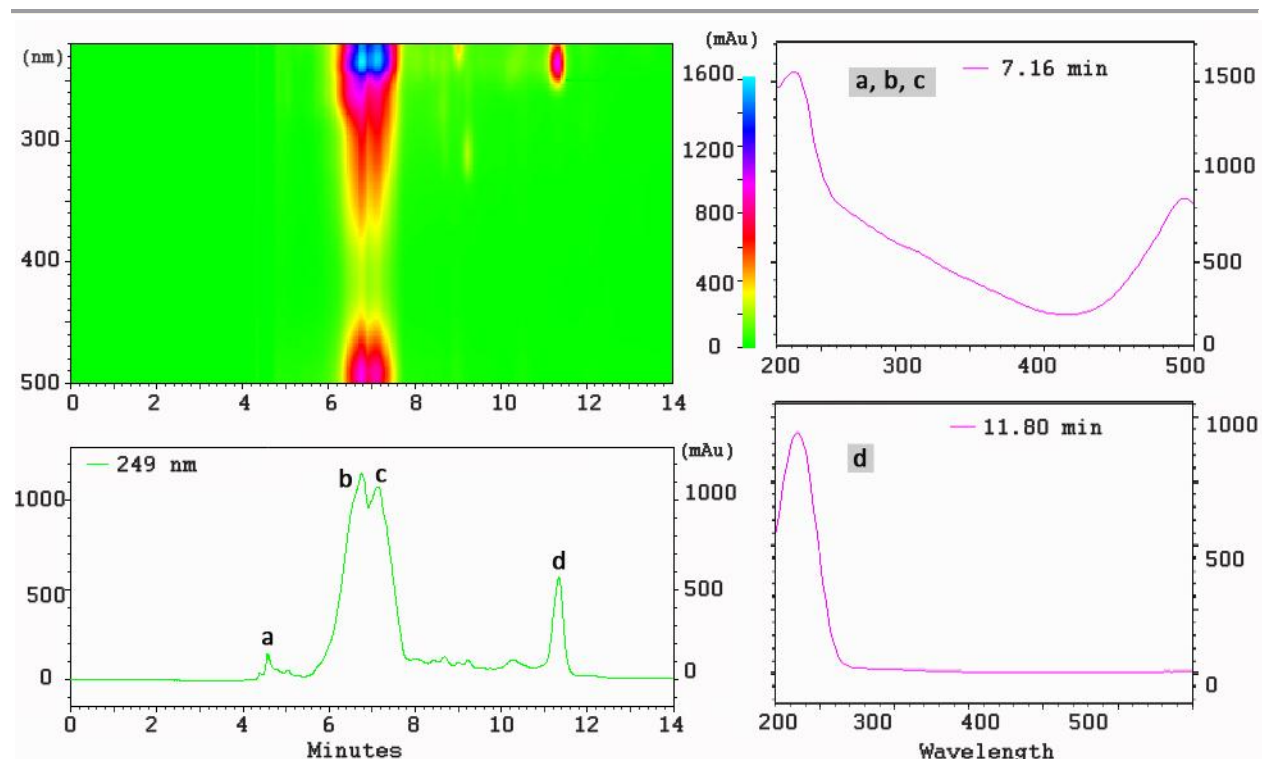
Figure 8.11. LC-UV chromatograms and spectra of selected analytes from a KLA/AS mixture. The upper left panel shows the 2D wavelength vs. retention time plot of the mixture. The lower left panel shows the chromatogram recorded at 249 nm. The right panels show characteristic absorption spectra corresponding to peaks (a – d) in the chromatogram.

The aged aqueous and evaporated/redissolved reaction mixture may contain multiple species, including the parent compound KLA, and separation by LC is necessary before structure analysis. In this section, we will focus on structure elucidation of only the C_{500} chromophore

from the KLA/AS reaction as the analyses techniques are time-consuming and the GLY-derived chromophores are expected to be similar in chemical structure.

Figure 8.11 shows LC-UV data for the reversed-phase separation of C_{500} formed from the aqueous KLA/AS reaction with an ACN/H_2O eluting solvent system. The chromatogram in the lower left indicate at least three dominant species are present. The absorbance spectra for the eluted fractions (a – c) contain the strong absorbance feature at 500 nm, indicating that they are associated with C_{500}. The spectrum for the (d) fraction corresponds to that of KLA because it has a strong absorbance band in the near UV due to the carbonyl $n \rightarrow \pi^*$ transition and no spectral features in the visible wavelengths. We note that the spectrum of fractions (a – c) also contain the carbonyl-like absorbance peak, indicating an either an intact ketone group or another UV-absorbing species.

The two dominant fractions (b, c) were inseparable with the C_{18} column and the ACN/H_2O eluent. Normal phase separation was not useful because C_{500} was not soluble in a non-polar organic solvent. Optimization of the column and the eluting solvent mixture in future work may afford better separation of the two dominant peaks. The small difference in retention times for these two compounds may indicate that they are either similar in structure (but two different neutral compounds), or an ionic pair. Curiously, these and other fractions seemingly do not contain the C_{430} chromophore (the 2D chromatogram is empty in this region), even though the aging reaction was performed in the aqueous phase where C_{430} is produced. The reason for this discrepancy is unclear and under investigation. The same LC-UV separation was done on the evaporated KLA/AS samples, also resulting in two convoluted dominant peaks. The main difference is that the fraction corresponding to KLA, (d), was negligible in magnitude due to more a complete reaction prompted by evaporation. The dominant fractions (b, c) corresponding

227

to C_{500} were collected for further analysis. All structure analysis studies henceforth refer to at least two dominant compounds (b) and (c).
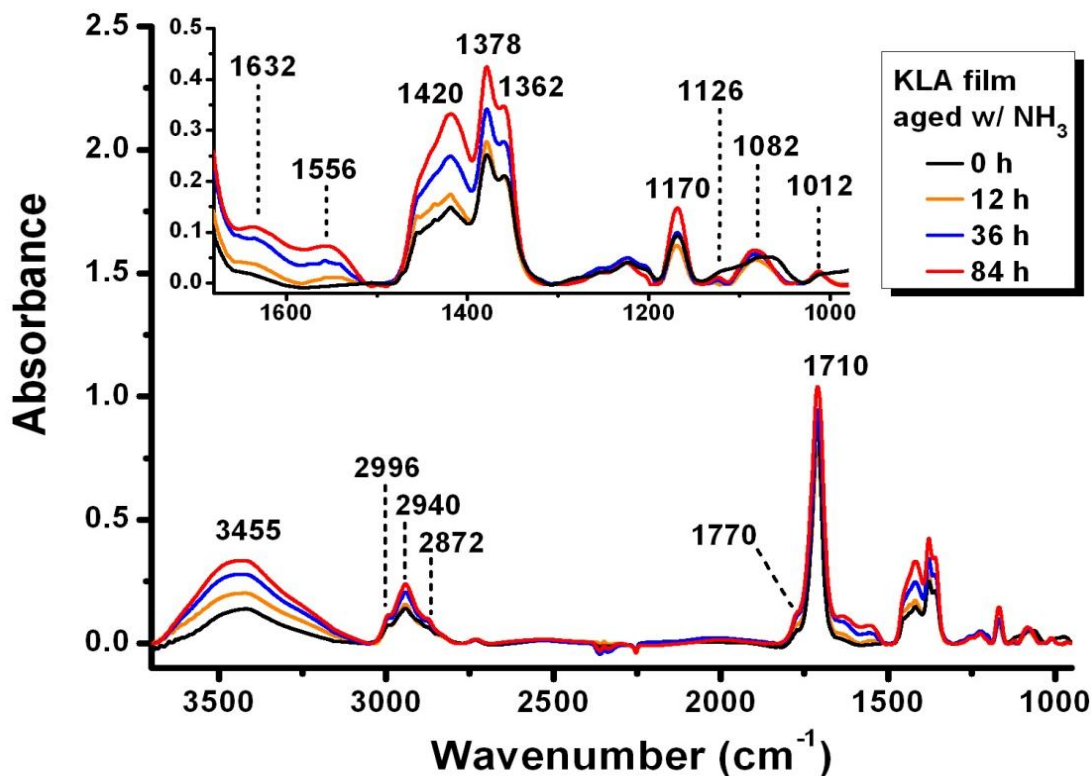
Figure 8.12. FT-IR spectra of a KLA film aged with humid NH_3 vapor at four time intervals. The inset panel magnifies the $950 - 1700$ cm^{-1} region. Proposed assignments for labeled bands are shown in Table 8.4.

FT-IR analysis was performed in the manner described in Section 8.3.4 and interpretations were made based on suggestions from ref [480]. Both sets of FT-IR experiments studied dehydrated films on ZnSe windows; therefore the nature of the chromophore or product mixture may be different than in the aqueous phase. Particularly, compounds like imines may be present in the film when they may be hydrated or hydrolyzed in water. The "surface aging" experiments, e.g., aging of a KLA film with humid NH_3 vapor, were monitored at 4 time intervals. The proposed FT-IR assignments are reported in Table 8.4. Figure 8.12 shows aliphatic

CH$_3$/CH$_2$ stretches (2800 – 3000 cm^{-1}) and bends (1300 – 1500 cm^{-1}) that are not sharp or well-resolved, suggesting a disordered KLA film. There is an OH stretching peak at ~ 3500 cm^{-1} that may indicate the H-bonded hydrated version of KLA or the OH of carboxylic acids. However, the relatively small width and symmetric shape of the C=O stretch at 1710 cm^{-1} suggests low acid contribution. The 1710 cm^{-1} band is characteristic of carbonyls. The aldehyde functionality is confirmed by the weak C(O)H stretch band at 2732 cm^{-1}.

Table 8.4. Proposed FT-IR assignments for KLA film aged with humid NH$_3$ vapor.

Band (cm^{-1})	height	width	Possible Assignment
3455	strong	v. broad	H-bonded OH or NH-intermolecular
2996	med.	broad	CH$_3$/CH$_2$ str,
2944	med.	broad	CH$_3$/CH$_2$ str,
2872	med.	broad	CH$_3$/CH$_2$ str,
2732	weak	broad	CHO str. of aldehydes
1770	med.	sharp	C=O of cyclic ketones?
1711	v. strong	sharp	Ketone/ald. C=O stretch
1632	med-str	broad	C=N str of imines?
1556	med-str	broad	N=N str of azos or N-H bend of imines?
1420	strong	broad	C-H deformation
1378	strong	sharp	C-H deformation
1362	strong	sharp	C-H deformation
1170	strong	sharp	C-C stretch
1126	weak	sharp	C-C rocking / or C-N stretch
1080	strong	broad	C-O stretch / or C-N stretch
1012	med	sharp	C-C skeletal vibration

As the film experiences aging by NH$_3$, several new bands appear at 1012, 1082, 1070, 1556 and 1632 cm^{-1} but are not sufficiently characteristic by themselves. The bands appear to be fairly broad, which may be due to the nature of the humid surface aging technique. The new peaks with higher diagnostic potential are the 1632 and 1556 cm^{-1} bands. In the absence of

aromatic CH stretches (> 3000 cm^{-1}), these bands may indicate nitrogen-containing bonds instead of the conjugated C=C stretch that would also appear in the 1610 – 1640 cm^{-1} spectral region. In particular, the 1632 cm^{-1} band may correspond to the C=N stretching mode, perhaps of imines [481]. Likely, this band does not correspond to the C=N moiety in heterocyclic nitrogen compounds like imidazoles or pyridines because we would also expect bands at 3000 – 3100 cm^{-1} signifying the production of an aromatic compound. The 1556 cm^{-1} band may correspond to an N-H bend or the N=N stretch of azo compounds [482, 483]. It is not clear whether the chemistry producing azo compounds can occur under these mild conditions; however, azo compounds have the same magnitude for molar extinction coefficients expected for the brown carbon. A more straightforward diagnosis of azo compounds may be obtained by Raman spectroscopy; however, the aged film exhibited strong fluorescence that prevented Raman measurements.
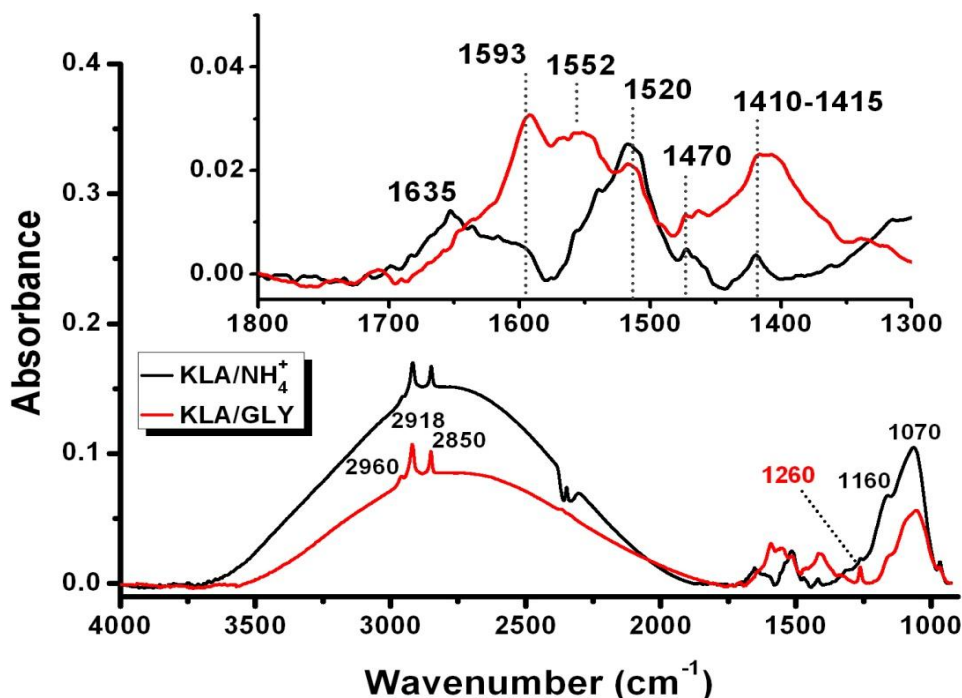
Figure 8.13. FT-IR spectra of separated and dried C$_{500}$ (KLA/NH$_4^+$) and C$_{520}$ (KLA/GLY) chromophores. Inset panel magnifies the 1300 – 1800 cm^{-1} region.

Figure 8.13 shows the FT-IR spectrum of C_{500} after concentration under vacuum, redissolution in D_2O, aerosolizing onto ZnSe windows and drying. The spectra of C_{520} from the GLY reaction are superimposed onto the data for comparison. The FT-IR spectra for the aged and dried residue has a large artifact band from approximately $1800 – 3700$ cm^{-1} that may have obscured weaker vibrational features and many of the features are broadened, presumably through interaction with incompletely-removed D_2O. However, several important observations can be made. The carbonyl C=O band is missing from the spectrum, suggesting that parent carbonyls have been completely separated by LC and that the chromophore no longer retains this functionality. The CH$_3$/CH$_2$ stretch bands appear to be sharp, perhaps due to a well-defined cyclic structure, and occur in the non-aromatic region.

For C_{500}, several bands are observed in both types of aging experiments, although for the aqueous aging experiment the shapes of these bands are much broader: $1070 – 1160$ cm^{-1}, ~ 1520 cm^{-1} and ~ 1630 cm^{-1}. The assignments are likely the same as those found in Table 8.4. For the GLY-aged chromophore, a red shift occurs for the major peaks (except for the CH$_3$/CH$_2$ stretches) which may be possibly due to conjugation with the neighboring C=O group from the amino-acid nitrogen-substitution at the carbonyl site. Importantly, a suggestion was made in *Bones et al (2010)* that the GLY-aged chromophore may be a protonated amino-acid linked Schiff base [64], which can be highly absorbing if there is enough conjugation [466]. The FT-IR spectrum of C_{520} has a strong band at 1593 cm^{-1}, which may signify a C=N bond linked to an amino acid that is consistent with this suggestion. The 1593 cm^{-1} band of C_{520} is comparable to that of the protonated retinal-lysine Schiff base, where the C=N frequency occurs in the 1578-1639 cm^{-1} window and D-substitution at the nitrogen site further shifts the frequency to toward the blue [484]. In general, the C=N band in amino acid-based Schiff bases are found in the 1600

– 1660 cm^{-1} range [481]. It is plausible based on the expected chemistry that the formation of a protonated Schiff base plays a role in the formation of the stable C$_{520}$ and C$_{500}$ chromophores.
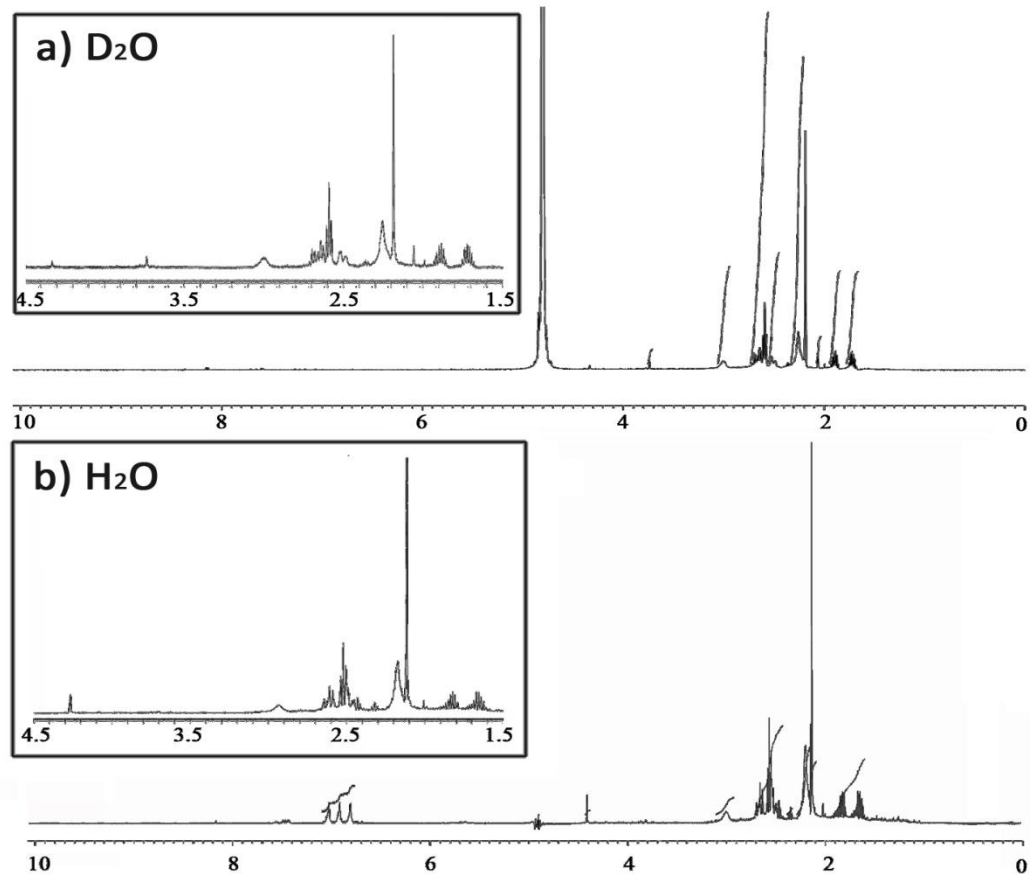
Figure 8.14. ^{1}H NMR spectra for the 0 – 10 ppm region of LC-separated C$_{500}$ in (a) D$_2$O and (b) in 90% H$_2$O/10% D$_2$O with water suppression. Inset panels for (a) and (b) show the magnified 1.5 – 4.5 ppm region. Protons that exchange with water only show up in (b). Peak resonances are reported in Table 8.5.

Another standard analytical technique for structure analysis is NMR spectroscopy. Figure 8.14 shows the ^{1}H NMR spectra for C$_{500}$ recorded in both (a) D$_2$O and (b) 90% H$_2$0/10% D$_2$O with water suppression. In contrast to the FT-IR experiments (studied with films), the resonances observed in NMR aqueous solutions may not correspond to water-sensitive compounds like the primary aldimine intermediates that are formed from the reaction of ammonia with aldehydes.

The molecules observed in NMR studies are likely isolatable in neutral aqueous environments, e.g., aldols, aldol condensates, cyclic compounds, or substituted imines. Table 8.5 reports the peak resonances and the proposed assignments based on Ref. [485]. No peak integration was reported for the ^1H spectra because they may have contribution from more than one compound.

Table 8.5. ^1H and ^{13}C proton-decoupled resonances in 90% H_2O/ 10% D_2O for separated C_{500} KLA/NH_4^+ chromophore. Muliplicities are abbreviated as: s (singlet) and m (multiplet). Spectra are shown in Fig. 8.14 (^1H) and Fig. 8.16 (^{13}C).

^1H peak (ppm)	Multiplicity	Proposed Assignment	^{13}C peak (ppm)	Proposed Assignment
1.70	m	alkyl - tertiary	26.6	cyclic CH_2
1.92	m	alkyl - tertiary	32.0	CH_3
2.12	*sharp* s	methyl	37.6	CH_2
2.25	*broad* s	-	42.7	CH
2.4 – 2.7	*unresolved*	-	49.9	N–C, CH, CH_2
2.91	*broad* m	-	69.8	CH_2-O
4.27	s	alcohol	179.5	COOH, N=CH<
6.93	s	Enol/OH exchange	215.5	cyclic ketone
7.03	s	C=O/COOH exchange	217.5	cyclic ketone
7.13	s	OH/COOH exchange		

In general, the peaks are well-resolved with no strong underlying structures in the alkyl (~ 1 – 3 ppm) region, signifying a high level of chemical purity. The aldehyde proton at ~ 9.7 ppm, which was observable in NMR spectra of KLA, is no longer present in the separated chromophore, suggesting that this aldehyde is one of the reaction sites. Many of these features in the C_{500} NMR spectra are also observed in the parent KLA, e.g. a multiplet that center at 1.9 ppm. Both this multiplet and its upfield neighbor are consistent with CH_2 or CH protons, as suggested by the *J* splitting patterns and the reference of KLA. Of the two sharp singlets corresponding to the two –CH_3 groups in KLA at 2.16 and 2.27 ppm, only one has survived (slightly shifted at 2.12 ppm). The other methyl group occurs at the correct position (2.25 ppm)

however the peak shape is considerably broadened. Structure interconversions may contribute to broadening the peak shape. It is possible one of the ketone methyl groups was converted into an enol, followed by subsequent cyclization. The multiplet in the 2.9 – 3.2 ppm region of the KLA spectrum is also present in the C_{500} spectrum; however, additional difficult-to-resolve resonances complicate this spectral range.
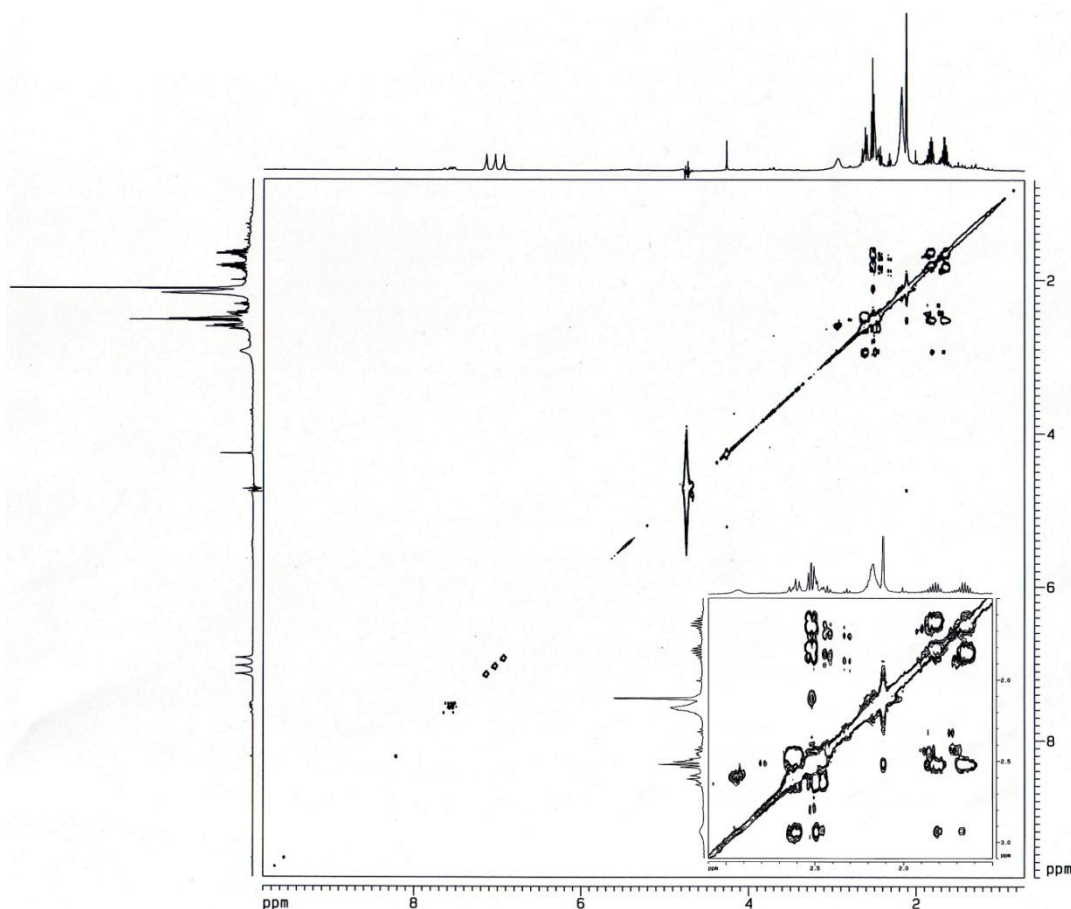
Figure 8.15. Proton-proton correlation spectroscopy (COSY) spectrum for the 0 – 10 ppm region of LC-separated C_{500} in 90% H_2O/10% D_2O with water suppression. Inset panel shows the magnified 1.5 – 3 ppm region. Symmetrical off-diagonal elements represent coupling between protons 3 bonds away. Non-symmetrical or singlet couplings are "noise" from coupling through space of neighboring protons.

Recording the spectrum in water (Fig. 8.14 b) was particulary instructive for identifying exhangeable protons. Three separate broad singlets appear in the 6.93 – 7.13 ppm range and one sharp singlet appears at 4.27 ppm. The singlet at 4.27 can be assigned to the proton of an alcohol because they are typically found in the 1 – 5 ppm region. The resonances at approximately 7 ppm are more difficult to assign. These resonances only appear in the H_2O spectrum and are therefore not consistent with aromatic protons, because even though aromatic protons appear in the 6.5 – 8 ppm region, they are not chemically-labile. The spacing between the three singlets around 7 ppm is uniform, yet these resonances are clearly singlets: the magnitude of the splitting ($J_{H,H} \sim 50$ Hz) is outside the range of proton-proton coupling, and the peak heights are not consistent with a typical distribution in a triplet (which would have 1:2:1 ratio of peak heights).

Furthermore, a 2D correlation spectroscopy (COSY) experiment, used to analyze coupling between protons 2 – 3 bonds away, offer definitive proof that all the exchangeable protons are singlets (Figure 8.15). The presence of symmetrical off-diagonal peaks in the spectrum directly correlates the coupled partners. Some non-symmetric peaks are the "noise" in the COSY spectra, which may arise from long-range coupling between partners that are close spatially but are not located 2 – 3 bonds away. The COSY spectrum is also useful for visualizing the spatial arrangement of a molecule. For example, the two upfield multiplets centered around 1.7 and 1.9 ppm are strongly coupled to each other in the COSY spectrum, and therefore, must be vicinal neighbors. Based on the possible aldol products shown in Scheme 8.3 (a – c), the structures shown in (a) and (b) are consistent with the COSY spectrum because there are two neighboring equivalent proton types (at non-primary carbon sites) and the two non-isolated CH_2 protons would give rise to multiplets. However, the aldehyde proton is absent which eleminates the structure in (a) as shown, but the imine form may still exist. The oxidized form of (a), shown

235

as (d) is also consistent with the chemical intuition that the aldehyde enol is the most reactive and with the observation of exchangeable protons discussed below.
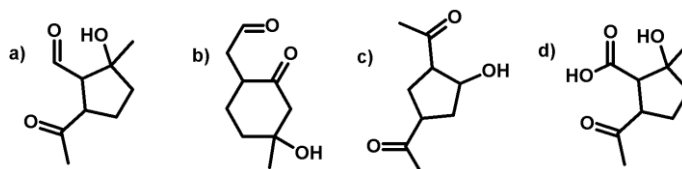
Scheme 8.3. Three (a – c) aldols that may be produced intramolecularly from KLA and (d) the carboxylic acid that is produced by oxidation of the aldehyde in (a).

The three exchangeable protons at ~ 7 ppm were not expected in the spectrum. Although close to resonances of imine protons (8 ppm), primary aldimines (i.e., compounds with the R(H)C=NH structure) are not likely to be observed because these compounds are not stable in water and therefore cannot belong to the hydrolysis-stable chromophore. For more stable Schiff bases (>C=NR$_1$), only the protonated form will offer proton resonances. The expected range for other exchangeable protons are: amines (0.5 – 3 ppm), carboxylic acids (10 – 14 ppm), and alcohols (1 – 5 ppm). Amides show up in this range (7 – 8 ppm) but are slow-exchanging and they are not expected based on the chemistry.

Thus, it is more likely that the broad trio of protons observed at ~ 7 ppm may arise due to fast structure interconversions of a particular dominant molecule. Mass spectrometry studies will later show that the dominant product structure is consistent with (d), which is the carboxylic acid form of (a), but is not the light-absorbing C$_{500}$. Although no carboxylic acid proton is observed in the expected range of 10 – 14 ppm, this resonance is particularly tricky in NMR and may appear at unexpected frequencies. If fast intramolecular proton exchanges between an NH or OH proton and a carboxylic acid proton occur, the signal of the carboxylic acid proton would shift significantly and may be incorrectly interpreted as absent. For fast proton exchanges, the hybrid proton may appear the average peak position of the two.

236

The NMR spectrum of the multifunctional carboxylic acid (d) cannot be found in a database; however, NMR spectra for representative parts of the molecules were available from the Advanced Industrial Science and Technology (AIST) Spectral Database for Organic Compounds (*http://riodb01.ibase.aist.go.jp/sdbs/cgi-bin/direct_frame_top.cgi*). The resonance in question for the 1,3-hydroxyacid moiety was referenced from the NMR spectrum of 2-hydroxy-2-methylpropanoic acid, which gave a broad COOH/OH exchange peak at 7.28 ppm. Therefore we assign in Table 8.5 the 7.13 ppm (most downfield) resonance to the OH/COOH hybrid proton. The 1,4-oxo-acid moiety was referenced from 2-oxopentanoic acid (another spatially close oxoacid), which gave a broad COOH-carbonyl exchange peak at 7.04 ppm. We assign the observed broad 7.03 proton to the enol/COOH hybrid proton. We note that some aliphatic oxyacids (like 3-acetylpropionic acid) do not exchange protons, possibly due to the isolated spatial configuration of the molecule. As (d) has the C=O group close to the COOH group, it is possible that this exchange happens similarly to the case of 2-oxopentanoic acid. The hydroxy-enol moiety did not have a suitable literature reference. However, enol protons appear at 14 ppm and can be surprisingly sharper than COOH protons. This hydroxyl-enol exchange may be responsible for the remaining resonance observed at 6.93 ppm for the enol/OH hybrid proton, although we note these two groups are far spatially. Although the NMR results qualitatively agree with HR-MS data, to be discussed later, the structure (d) does not absorb visible light.

One of the most straightforward structure analysis techniques is proton-decoupled ^{13}C NMR spectroscopy. Figure 8.16 shows the ^{13}C NMR spectrum for C_{500} recorded in H_2O/D_2O while referencing the ^{1}H spectrum for peak positions. Each ^{13}C resonance represents a carbon atom in a unique electronic environment and the proposed assignments are reported in Table 8.5. The alkyl resonances in the $10 - 30$ ppm region contains $4 - 5$ types of alkyl groups (primary to

tertiary progresses right to left) and one of these resonances at 27 ppm correspond to a 5-member ring CH_2 group. The resonances on the far left of the spectrum correlate to ketones (216 – 218 ppm); however, as they are more downfield than aliphatic ketones, they can be assigned to cyclic ketones. There appear to be one major and minor cyclic ketone isomer. Both the observations in the alkyl region and the ketone region supports that the aldol structure drawn in Scheme 8.3a is one of the dominant products and is consistent with ^{1}H and COSY results. However, these NMR results seem to be in conflict with FT-IR spectra, where the C=O band of ketones is no longer observed after aging and separation. The reason for this discrepancy is not clear but NMR data agrees with UV-Vis spectra, suggesting that the ketone functionality is intact in the chromophore. The absence of aldehydes in the expected region 190 – 200 ppm corroborates the observations from the ^{1}H spectrum, where aldehyde protons are also absent.
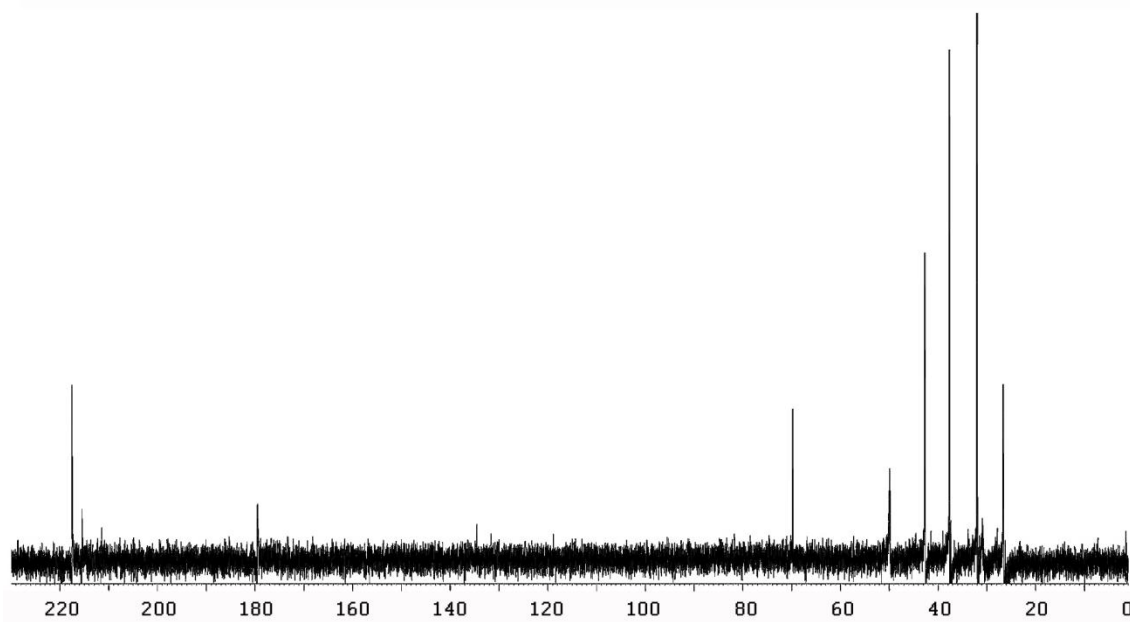
Figure 8.16. ^{13}C NMR proton-decoupled spectrum for the 0 – 230 ppm region of LC-separated C_{500} in 90% H_2O/10% D_2O. Peak resonances are reported in Table 8.5.

The resonance at ~ 180 ppm can be assigned to either carboxylic acid or imine carbons. Imine ^{13}C resonances, in particular, may be detected in the range 170 – 180 ppm [486]. The peak at ~180 ppm is not consistent with imidazoles or pyridines, whose C=N resonances are expected more upfield at 150 – 160 ppm. Furthermore, there has not been any evidence so far of these aromatic N-heterocyclic structures from ^{1}H NMR or FT-IR. The resonance at 70 ppm is most likely due to an alcohol functional group. The 50 ppm resonance may be assigned to a primary/secondary carbon atom attached to nitrogen by a single bond, although in some cases secondary/tertiary alkyl carbon can show up in this region. As azo compounds still cannot be ruled out, these ^{13}C resonances may suggest the possibility of a carbon atom bonded to an azo (C–N=N) group that does not have any ^{1}H resonance of its own.

Unfortunately, the dominant structures implicated by NMR may not be the species that absorb visible light. Based on this and previous work, the chromophore is more likely a minor species whose signals are suppressed by more dominant compounds in the IR and NMR analyses. Weak resonances in the 120 – 130 ppm region of the ^{13}C spectrum may provide useful clues on the nature of the minor species. The types of carbon that can be found in this region are the conjugated and aromatic carbons (–C=C–). As suspected, it may take substantial conjugation and nitrogen substitution to promote light absorbance in the visible region. However, we note that in FT-IR measurements, no aromatic CH stretches (> 3000 cm^{-1}) were discernible in the aged spectra. Although the work done so far has uncovered a wealth of information on the nature of the dominant products, this ^{13}C NMR spectrum may be the first insight gained on the minor conjugated species that more realistically contribute to light absorption.

One of the best tools for "needle in a haystack" type problems is HR-MS because this technique is extremely sensitive (detection at the nanogram level) and, when coupled with LC,
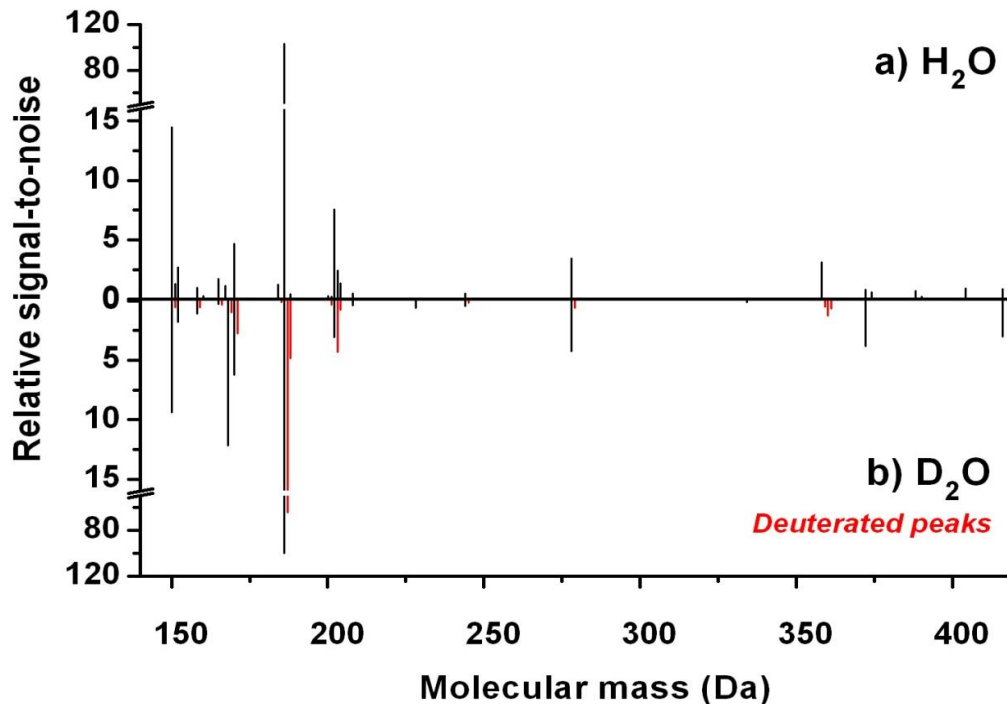
Figure 8.17. High-resolution mass spectra of the separated C_{500} chromophore, recorded in (a) 90% H_2O and (b) 90% D_2O solvents (with ACN making up the remainder). Deuterated peaks are shown in red.

can also offer high chemical specificity. The same H/D test was done for HR-MS samples, where the samples were dissolved in 90% H_2O/10% ACN and 90% D_2O/10% ACN and directly electrosprayed into the MS. Figure 8.17 shows a representative mass spectrum with peaks observed reproducibly in at least two of the four separated C_{500} samples. Deuterated peaks, shown in red, are common in the D_2O spectrum, indicating a significant number of exchangeable protons. The reported masses and molecular formulas have been converted to their non-ionic values by subtracting the contribution from a sodium ion or a proton. The masses of the deuterated peaks are different from their hydrogen counterparts by $\Delta\, m/z = 1.0063$ (D – H) and a different isotopic abundance pattern from the ^{13}C peaks that also appear at a nominal 1 Da offset from the parent peak.

240

Table 8.6. HR-MS data for the separated C_{500} chromophore, recorded in 90% H_2O and 90% D_2O solvents (with ACN making up the remainder). The relative signal-to-noise (S/N) ratios have been normalized to the largest peak $C_9H_{14}O_4$, which is the oxidized version of KLA ($C_9H_{14}O_3$). Deuterated peaks are highlighted in gray. Bolded/underlined table entries correspond to compounds shown in Scheme 8.4. DBE correspond to the total number of double bonds and rings, assuming trivalent nitrogen atoms.

Molecular Mass (Da)	S/N (H₂O)	S/N (D₂O)	# C	# H	#D	# O	#N	DBE
150.0681	14.51	9.40	9	10	0	2	0	5
151.0744		0.53	9	9	1	2	0	5
151.0997	1.30		9	13	0	1	1	4
152.0837	2.69	1.77	9	12	0	2	0	4
158.0943	0.98	1.06	8	14	0	3	0	2
159.1006		0.54	8	13	1	3	0	2
160.0736	0.27		7	12	0	4	0	2
165.0790	1.74	0.27	9	11	0	2	1	5
166.0853		0.35	9	10	1	2	1	5
<u>167.0946</u>	**1.14**		**9**	**13**	**0**	**2**	**1**	**4**
<u>168.0786</u>	**18.54**	**12.15**	**9**	**12**	**0**	**3**	**0**	**4**
169.0849		0.98	9	11	1	3	0	4
<u>170.0943</u>	**4.69**	**6.23**	**9**	**14**	**0**	**3**	**0**	**3**
171.1006		2.72	9	13	1	3	0	3
184.0736	1.26		9	12	0	4	0	4
185.0798		0.12	9	11	1	4	0	4
<u>185.1052</u>	**0.10**		**9**	**15**	**0**	**3**	**1**	**3**
<u>186.0892</u>	**100.00**	**100.00**	**9**	**14**	**0**	**4**	**0**	**3**
187.0955		64.87	9	13	1	4	0	3
188.0685	0.44		8	12	0	5	0	3
188.1018		4.82	9	12	2	4	0	3
200.1049	0.29		10	16	0	4	0	3
201.1001	0.21		9	15	0	4	1	3
201.1111		0.35	10	15	1	4	0	3
202.0630	4.27	2.82	12	10	0	3	0	8
202.0841	7.60	3.05	9	14	0	5	0	3
203.0693		1.12	12	9	1	3	0	8
203.0904		4.28	9	13	1	5	0	3
<u>203.1158</u>	**2.42**		**9**	**17**	**0**	**4**	**1**	**2**
204.0967		0.75	9	12	2	5	0	3
204.0998	1.37		9	16	0	5	0	2
208.0736	0.49	0.41	11	12	0	4	0	6
206.1123		0.60	9	14	2	5	0	2
216.0998	0.07		10	16	0	5	0	3

244.0947	0.50	0.43	11	16	0	6	0	4
245.1010		0.15	11	15	1	6	0	4
278.0862	3.43	4.23	8	14	0	7	4	4
279.0925		0.58	8	13	1	7	4	4
301.1678	**0.07**		**18**	**23**	**0**	**3**	**1**	**8**
319.1784	**0.05**		**18**	**25**	**0**	**4**	**1**	**7**
334.1125	0.09	0.10	11	18	0	8	4	5
358.1893	3.14		20	26	0	4	2	9
359.1955		0.49	20	25	1	4	2	9
360.2018		1.24	20	24	2	4	2	9
361.2081		0.67	20	23	3	4	2	9
388.1423	0.84	3.79	23	20	0	4	2	15
372.1784	**0.60**		**18**	**28**	**0**	**8**	**0**	**5**
388.1733	0.70		18	28	0	9	0	5
390.1890	0.26		18	30	0	9	0	4
404.1682	0.90		18	28	0	10	0	5
416.1431	0.86	3.00	17	24	0	10	2	7

The molecular formulas and their relative abundances are compiled in Table 8.6. The deuterated molecules are highlighted in gray in the table and double bond equivalency (DBE) values are reported in the last column. Table entries that are bolded and underlined are compounds whose chemical reactions are visualized in Scheme 8.4. DBE corresponds to the total number of double bonds and rings present in the molecule and was calculated from the molecular formula, with the assumption that the nitrogen atoms in the molecule are trivalent [2]. The peaks were normalized to the most dominant peak $C_9H_{14}O_4$, which is the either the oxidized version of KLA (ketolimononic acid) or its intramolecular aldol. The aldehyde moeity spontaneously oxidizes into the carboxylic acid in the presence of water, and the addition of AS may promote this oxidation. We note that although oxidation of the aldehyde is facile, the KLA was used immediately after synthesis and NMR analysis prior to experiment did not indicate COOH (10 – 13 ppm) nor COOH/OH hybrid ($\sim$ 7 – 9 ppm) protons in the KLA sample so the oxidized compounds are likely products formed from the reaction of KLA with dissolved oxygen, which

may be facilitated by NH_4^+. The signal of $C_9H_{14}O_4$ is higher than others by almost a factor of 10, which may actually correspond to a higher concentration in the mixture as NMR spectra seem to indicate a dominant major species. However, the large signal of this compound may also be due to a high ionization efficiency. Unpublished work by our collaborator Julia Laskin supports that this compound (shown encircled in Scheme 8.4) is expected to have high sodium affinity. The $C_9H_{14}O_4$ ketoacid may form a 6-member stabilization complex with Na^+ at the C=O and COOH sites. Upon deuteration, the exchangeable COOH proton is converted to COOD, and the deuterated peak is observed at roughly 80% of the parent signal.

Table 8.6 shows the KLA + AS reaction primarily generates monomer (C_9) or dimer (C_{18}) compounds. However, some observed products cannot be explained by self reactions of KLA and may be impurities or decomposition side products. An important observation is the scarcity of 2N compounds – especially for products originating from the KLA structure. This offers additional evidence that the KLA-derived chromophores are not 2N heterocycles like imidazoles. For C_9 and C_{18} compounds, we can trace the chemical reactions of observed HR-MS products from initial reactions of KLA.

Scheme 8.4 shows reactions stemming from KLA in water with consideration of reaction pathways promoted by NH_4^+ and evaporation. The parent KLA ($C_9H_{14}O_3$) and its cyclic intramolecular aldol with the same molecular formula are observed at roughly 5% relative abundance. Facile acid-catalyzed (or NH_4^+-catalyzed) oxidation of the aldehyde group produces the acid, which may be the dominant form in water and observed at 100% signal. Self reactions produces an aldol dimer $C_{18}H_{28}O_8$ (~ 0.6%) and further oxidation of this compound produces $C_{18}H_{28}O_9$, which may be a peroxide. These aldol dimers are likely to absorb radiation only in the near UV. Water elimination from the dominant product $C_9H_{14}O_4$ produces $C_9H_{12}O_3$, which is

also a stable and abundant (~ 18%) product. The reaction of the $C_9H_{12}O_3$ aldol condensate with NH_4^+ produces the imine (~ 1%). Many observed products shown in Table 8.6 are not included in Scheme 8.4; however, most of them are formed from similar aldol and NH_4^+ pathways.
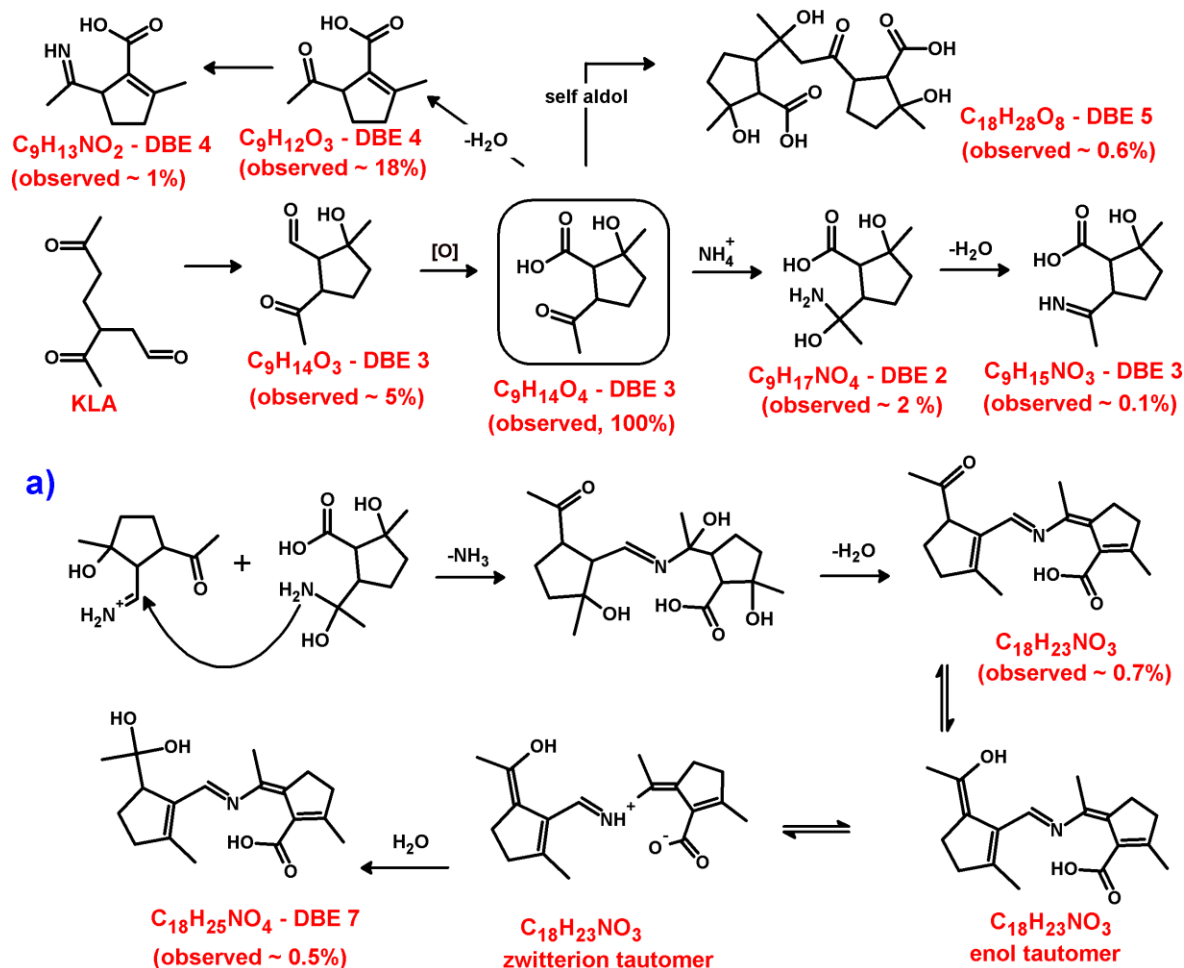
Scheme 8.4. Proposed reactions leading to the formation of select compounds observed in HR-MS. The observed compounds are reported in Table 8.6. The product with the highest signal in HR-MS is circled. Proposed reaction sequence (a) involves a transimination followed by loss of NH_3. The enol tautomer is the conjugated form of the $C_{18}H_{23}NO_3$ molecule (which may exist as a neutral molecule or zwitterion due to the H-bonding interaction of the imine-acid). Percent values shown in the figure and cited in the text correspond to the relative peak intensities listed in table 8.6.

Of all the molecules observed in HR-MS, the most likely candidate for the chromophore compound, which meets the requirements of having high DBE, 1 or more nitrogen compounds, a

244

KLA-based structure, and low relative abundance, is $C_{18}H_{23}NO_3$. This molecule, and its hydrated form $C_{18}H_{25}NO_4$, are observed at abundance < 1%, consistent with expectations. Proposed reaction sequence (a) in Scheme 8.4 suggests a mechanism toward the formation of $C_{18}H_{23}NO_3$. This 1-nitrogen C_{18} dimer with high DBE may be formed from coupling at the site of the imine with an elimination of ammonia, e.g. a *transimination* reaction. This type of reaction is known to occur with primary imines, as they are unstable, and documented in reactions of Schiff bases [487]. Protonation on the imine nitrogen is necessary for attack by the amine and carboxylic acids, which are abundant in the reaction pool, are efficient catatlysts for the transimination reaction [488]. Sequence (a) in Scheme 8.4 shows a reactive primary aldamine that is converted to a stable Schiff base by transimination a with a primary amine (e.g., the hydrated form of an imine, $C_9H_{17}NO_4 \sim 2\%$) coupled to the liberation of ammonia [479, 489]. In water, the hydrated form (an aminoalcohol) is expected and observed to be more abundant.

A study of transimination between several ketimines and aminoalcohols finds that water facilitates the reaction, which may not occur in organic solvents [486]. Condensation reactions (-H_2O) prompted by evaporation will produce the high-DBE C_{18} dimer $C_{18}H_{23}NO_3$. The enol tautomer of this product is fully conjugated. Both the imine/aminoacohol intermediate and proposed conjugated Schiff base product are minor species (< 1%) but the chromophore has high enough extinction coefficient to significantly influence the optical properties of the aged KLA. The proposed reaction sequence (a) offers a reasonable explanation to the formation of the $C_{18}H_{23}NO_3$ compound; however, further study is needed to describe the thermodynamics of the reaction to assess the feasibility.

The tentatively-identified Schiff base $C_{18}H_{23}NO_3$ may exist in the zwitterionic form, in which the imine group is protonated and the acid group is deprotonated. For an organic

compound containing both an imine group and a carboxylic acid group, strong intramolecular H-bonding may be lead to zwitterion formation by protonation of the imine by the acid [490]. In the case of $C_{18}H_{23}NO_3$, the H-bonding occurs via a 7-member ring. In visible light-absorbing Schiff bases like the protonated Lysine-retinal chromophore shown in Scheme 8.5a (DBE = 8, counting the Lysine COOH), a counterion such as a deprotonated carboxylic acid is needed to stabilize this protonated light-absorbing form [466, 491]. The proposed structure for C_{500} is shown in Scheme 8.5b. In the case of $C_{18}H_{23}NO_3$, either an intramolecular or intermolecular COO$^-$ group may serve as the counterion.
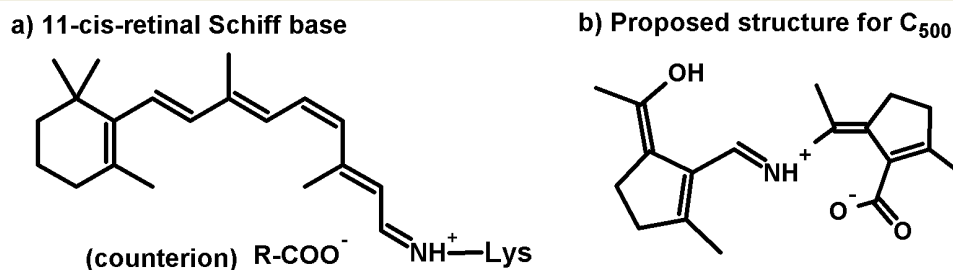
Scheme 8.5. Structures of (a) 11-cis-retinal-lysine Schiff base and (b) tentatively-identified C_{500}.

The proposed structure for $C_{18}H_{23}NO_3$ has conjugated double bonds, but compared to highly-colored carotenoid compounds, the pi-conjugation of the proposed structure may not be high enough by istelf to extend light absorption to the visible. Perhaps further interactions of this molecule with other compounds in the reaction mixture may explain the bathochromic shift. The observed UV-Vis absorbance maxima for the protonated Schiff base retinal chromophore that is not protein-bound is ~ 440 nm [492], whereas absorbance maximum for C_{500} is even higher at ~ 500 nm. The proposed structure of the C_{500} Schiff base has lower level of conjugation compared to retinal and therefore can be assumed that the free version of this molecule does not absorb past 400 nm. However, interactions with negative charges around the protonated C=NH$^+$ moeity may

produce a large red shift. For example, the interaction of the retinal Schiff base with negative charges in a protein pocket of a membrane can shift the abosorption maximum of the Schiff base almost 200 nm into the red [493]. It is possible that the interaction of deprotonated acid groups either within the molecule or in the reaction mixture may shift the absorption maximum of C_{500} into the visible wavelengths. Both of these chromophores have a double absorbance maximum, one in the ~ 350 - 450 nm region and one in the ~ 400 – 500 nm region, and very high extinction coefficients ($> 3 \times 10^4$ M^{-1} cm^{-1}) [466]. Furthermore, both NH_4^+-aged limonene/O_3 SOA and retinal Schiff bases (either amino acid bound or alkyl substituted) fluoresce with similar excitation/emission profiles (~ 350 nm excitation, ~ 450 – 500 nm emission) [64, 494].
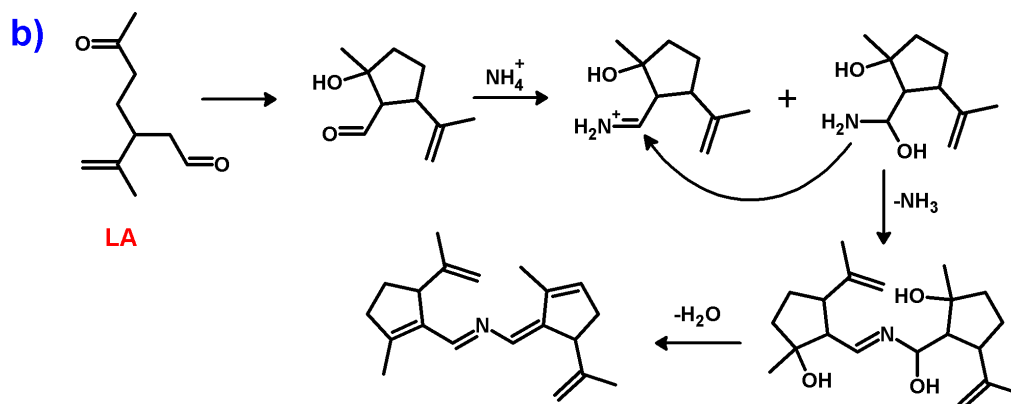
Scheme 8.6. Parallel reactions for LA as those shown in Scheme 8.4a for KLA.

A similar mechanism to reaction sequence (a) can be demonstrated for LA, shown in Scheme 8.6 as reaction sequence (b). In the case of LA, only one carbonyl group is intact after cyclization. This aldehyde can be converted to both the aminoalcohol and its dehydrated form, the imine; however, no other N-containing products are expected. The transimination reaction between these two N-containing compounds yields an unsaturated 1N product. However, due to the locations of the double bonds initially present in LA and the limited precursors, the product is

247

not fully-conjugated and cannot form a zwitterion. The extra ketone group in KLA is likely important because an aminoalcohol can form at the ketone site and the carboxylic acid can form at the aldehyde site after intramolecular cyclization. The transimination product for KLA is much more likely to absorb visible light due to higher conjugation and intramolecular charge transfer than the product from LA.

The structures and mechanism proposed in Scheme 8.4 are consistent with the clues provided by kinetics and structure analysis. The proposed mechanism of chromophore formation depends on the rate-limiting formation of the imine, which would be slow in water and accelerated by evaporation. The proposed reactions should be feasible in room temperature aqueous solutions at mild acidity, consistent with previous results that chromophore formation is most facile at pH $4 - 6$ [96]. The proposed protonated Schiff base chromophore structure is stable in water, and furthermore is not expected to degrade in acidic solution [478]. The proposed structure has an intact ketone group but no aldehyde group, which is consistent with NMR data. Additionally, this Schiff base may be zwitterionic or intermolecularly stabilized by abundant carboxylic acid compounds in the mixture, providing an explanation for the existence of a protonated imine moeity at neutral pH and the stability of the molecule at acidic pH. As the N-containing chromophore is a minor species and major species are colorless oxidation products, the apparent zero-order dependence on NH_4^+ in the evaporation reaction can be rationalized because complete reaction requires less than 10% by mole nitrogen. The chromophoric product is low in abundance, and its signals in NMR and FT-IR are overwhelmed by the major constituents like $C_9H_{14}O_4$. Nevertheless, evidence of minor conjugated species (^{13}C signals at ~ $120 - 130$ ppm and DBE) that contained a C=N group (suggested by FT-IR and NMR) supports the proposed structure.

8.4.5. Key points and future work

This unpublished work is the first report of the brown carbon forming reactions of KLA, the most abundant compound in limonene/O_3 SOA. This study characterized aqueous reaction kinetics and light absorption properties of the chromophore from both the NH_4^+- and GLY-mediated reactions. Importantly, a chromophore structure and mechanism of formation was proposed for the first time after obtaining clean vibrational and magnetic resonance data. The data implicate a protonated Schiff base structure for the chromophore, similar to the visible-light-absorbing compounds found in biological systems. Heterocyclic structures that have been suggested in the past were not consistent with findings.

However, although the proposed structure is supported by the available analytical data, definitive determinations of the nitrogen atom incorporation is needed. Future work in this area may involve ^{15}N labeling experiments to confirm the structure proposed here and provide quantitative estimations of chromophore concentrations. Additional studies that will be helpful in confirming the tentatively-identified structure include: tandem mass spectrometry, electronic calculations of structures and reactions, and direct synthesis of the proposed structure. As ketoaldehydes similar in structure to KLA are be found in other types of atmospheric organic mixtures, especially in the ozonolysis of many biogenic cyclic alkenes, these secondary brown carbon reactions may be broadly relevant in the atmosphere. Further studies of brown carbon reactions of SOA-relevant carbonyls are needed to provide estimates of the contribution of this reaction toward the total brown carbon budget.

8.5. Acknowledgments

Chapter 9: Conclusions

Organic aerosols (OA) have garnered recognition in the last few years as being an important component of atmospheric particular matter. Consequently, the number of conference papers and peer-reviewed publications on OA-related topics has grown exponentially in the past few years. Part of the motivation for studying OA was provided by the 2007 and previous IPCC reports that revealed our limited understanding of the role of aerosols in human-induced climate change. Another important motivation for studying OA continues to be driven by our poor understanding of the correlation between the health effects and chemical compositions of atmospheric particles. Yet another driving force is the significant paradigm shift surrounding the production of OA from abundant (but volatile) biogenic precursors like isoprene, which were not considered as important OA precursors in the past. The increased interested in OA has prompted large scale field campaigns, sophisticated laboratory investigations, and development of state-of-the-art equipment for the OA analysis.

Numerous field and modeling studies of ambient OA determined that secondary organic aerosols (SOA) are much more widespread than previously realized and can potentially affect many aspects of climate, chemistry, and human health. The scientific community made strong interdisciplinary efforts toward advancing the understanding of SOA sources, yields, and composition; however, the molecular composition was found to be too complex to characterize using traditional analytical techniques. Fortunately, emerging technology like high-resolution mass spectrometry (HR-MS), aerosol time-of-flight mass spectrometry, and single-particle laser spectroscopy became available in the last five years to facilitate this research.

This dissertation took advantage of HR-MS to contribute to the growing pool of knowledge regarding SOA composition and chemistry: particularly toward characterizing the

molecular composition of SOA from isoprene and the chemical aging of SOA as a route to brown carbon. Important conclusions from the works presented here include:

(a) *SOA composition is complex*. Even "simple" SOA created under controlled conditions in a smog chamber from a single precursor are composed of hundreds and possibly thousands of monomeric and oligomeric compounds. In the field, the composition is likely even more complex, although the oligomeric content may be much smaller.

(b) *SOA compounds are multifunctional*. The nature of the oxidation reactions that form low-volatility condensable compounds also give rise to numerous hydroxyl, carbonyl, carboxyl, nitrate, and other types of chemical functional groups. Most of the SOA compounds have 2 or more oxygen-containing functional groups per molecule. These functional groups may be located on vicinal carbon atoms, and influence each other, thus making it difficult to predict their properties *a priori*, e.g., from existing structure-activity relationships.

(c) *SOA composition is highly dependent on conditions present in the SOA generation stages.* The relative concentrations of water vapor, OH, O_3, NOx and VOC precursors have been demonstrated to drastically alter SOA composition. This dissertation discovered that high humidity conditions significantly hinder the formation of condensation oligomers in OA, and that dry environments high in NOx produce an abundance of aerosol-phase organic nitrates.

(d) *The most important oligomerization reaction is esterification.* Due to the abundant OH and COOH moieties found in SOA compounds, carbon-joining condensation reactions like oligomerization are prolific. Shortage of water vapor, for example under dry ambient conditions, accelerates these esterification reactions and promotes oligomer formation.

(e) ***2-methylglyceric acid is an important oligomer building block in isoprene SOA.*** It was previously suggested that this compound is a suitable tracer for ambient isoprene SOA. The HR-MS studies of large oligomers in isoprene SOA unambiguously confirmed that their backbones are made from 2-methylglyceric acid units. Other previously unrecognized oligomer building blocks have been identified in this dissertation.

(f) ***Semivolatile compounds contribute to SOA mass through heterogeneous chemistry.*** In the past few years, it was found that small volatile molecules like methylglyoxal can hydrate on aerosol surfaces and add to the total SOA mass. We determined that many other volatile and semivolatile compounds participate in this chemistry, particularly hydroxycarbonyls and small aldehydes, including the smallest aldehyde – formaldehyde.

(g) ***SOA compounds can be decomposed efficiently by direct photolysis.*** The abundant photolabile chemical groups existing in SOA (like carbonyls and organic nitrates) were shown to be efficiently photolyzed when SOA compounds were dissolved in water and exposed to solar radiation. We showed that these processes occur on time scales that are comparable to the lifetimes of clouds, fogs, and hydrated aerosols. The direct photolysis processes in dissolved SOA are only now getting recognized as an important mechanism of aerosol aging.

(h) ***Photolysis of organic nitrates in water can lead to heterocyclic nitrogen.*** We showed that SOA compounds produced under high-NOx conditions can undergo complex aqueous photochemistry leading to rather unusual nitrogen-containing compounds by unknown mechanisms. Such reactions produce photostable heterocyclic species containing two nitrogen atoms in the ring, which were observed for the first time in this dissertation.

(i)   *SOA composition is dramatically modified by aging with ammonia.* Abundant carbonyl compounds produce imine intermediates through reaction with ammonia. These intermediates produce a host of new products, amongst them conjugated nitrogen-containing brown carbon chromophores.

(j)   *Cloud/fog processing is an effective driver of SOA chemistry.* The evaporation of clouds and fogs, though common, had not been considered as a mechanism for promoting chemical transformations in the past. We showed that this evaporation can accelerate important condensation chemistry by orders of magnitude. This type of evaporative processing can produce long-chain oligomers, aldol products, and brown carbon compounds. In view of the highly dynamic nature of atmospheric liquid water (clouds and fogs appear and dissipate frequently) the evaporation-driven chemistry is likely to have global importance.

(k)   *SOA can be a significant source of secondary brown carbon.* The production of brown carbon via chemistry occurring directly in the atmosphere (as opposed to direct emissions) has only been discovered recently. We showed that natural products found in SOA, e.g. keto-limononaldehyde and similar compounds, can serve as precursors to the brown carbon, and proposed a mechanism of brown carbon formation. These investigations are ongoing.

The collection of works presented herein has provided a considerable amount of insight on the nature of the molecules and chemistry present in SOA. However, there are many important questions on the topic that are yet to be answered. The author of this dissertation views the following questions as interesting avenues for future research:

(i) *How, and to what extent, does anthropogenic pollution affect aerosol formation from biogenic precursors?* As mega-cities emerge, the perturbation of biosphere-atmosphere interactions from nitrogen-containing, sulfur containing, and other anthropogenic pollutants will increase. How will these increased NOx-, SOx- and NH_4^+ emissions modify global SOA, which is currently dominated by SOA from biogenic precursors? The effects of NOx on composition and yield of some types of SOA have been studied in laboratories and found to be quite complex. The nitrogen- and sulfur- containing products have been suggested to be abundant and have interesting chemical properties. The matters are further complicated by the recent realization of the importance of biogenically emitted amines in new particle formation, which also contribute to organic nitrogen compounds in aerosols. With the increasing importance of the organic nitrogen and organic sulfur compounds in the atmosphere, standard and reliable ways must be developed to measure these compounds quantitatively, and to unambiguously distinguish S- and N- compounds of anthropogenic and biogenic origin.

(ii) *How, and to what extent, does aqueous chemistry contribute to the formation and aging of aerosols?* The current state of the knowledge on the aqueous-phase production and loss mechanisms for atmospherically relevant organic compounds can be characterized as primitive. What makes this problem complicated is the high diversity in the amount of the liquid water content in atmospheric particles, which affects the rates and mechanisms of aqueous processes. In addition, the liquid water content of particles is highly dynamic, and it is therefore necessary to know the effects rapid evaporation has on aqueous rates and reaction products. Our group and others have demonstrated that aqueous phase processing of organics play a role in the modification and growth of SOA

mass in both dark and photochemical conditions. Ambient measurements and modeling studies support the importance of aqueous chemistry; however, a detailed understanding of the coupled atmospheric aqueous phase chemistry and cloud/fog physics is still needed. This type of pathway is yet to be fully appreciated in the field of aerosol chemistry.

(iii) *How do organic aerosol compounds affect human health?* The health effects of organic aerosols have been the subject of numerous recent studies and discussed in reviews, but the mechanism with which these compounds affect health is poorly understood. Aerosols contain a diverse mixture of compounds, some of them benign and some toxic or mutagenic. For example, alpha-beta unsaturated carbonyl compounds and nitro-aromatics have been shown to be hazardous to humans. Targeted studies of the correlation between the organic compounds identified by detailed HR-MS composition analyses and health should be able to identify the most important types of organic compounds responsible for the detrimental health effects of atmospheric particles.

(iv) *What underlying chemistry affects the optical properties of SOA?* The recent discovery of secondary brown carbon, which is produced by heterogeneous chemistry directly in the atmosphere, has already led to many active investigations in this area. It seems that the traditional view of light-scattering, climate-cooling, OA may be an oversimplification. At this time, the sources and chemistry of brown carbon are poorly understood, and need to be researched further through a combination of lab, field, and modeling studies. For example, it is not clear how stable the secondary brown carbon is with respect to atmospheric photooxidation, whether there is a connection between the

secondary brown carbon and humic like substances (HULIS), and what is its relative contribution in different locations.

(v) ***What underlying chemistry affects the physical properties of SOA?*** The phase of SOA compounds, which affects the dynamics of interactions of SOA with water, is a highly-debated topic in recent years. We have shown in this dissertation that even a subtle change in the reaction conditions through lowering relative humidity produces products that are more likely to form glasses in isoprene SOA. Is this a general observation for all types of OA? How does the history of particle formation affect its hygroscopic and cloud condensation properties? More work needs to be done to uncover the molecular changes responsible for the hygroscopic properties of SOA.

There are certain technological advances that would greatly improve the current understanding of OA. First, coupling HR-MS to a field-deployable instrument would overcome many obstacles that are related to aerosol collection and extraction. This type of instrument will enable scientists to characterize aerosols in real-time with a molecular level of detail at different locations in the world. Fortunately, with advances in electronics and machining, this type of technology is forthcoming (probably in the next several years) as progressively higher mass accuracy is achieved by mass spectrometers packaged in smaller sizes.

Second, as organic nitrogen and sulfur are starting to be appreciated as a significant fraction of the total nitrogen and sulfur, respectively, in aerosols, a reliable analytical method to quantify these compounds is needed. Unfortunately these compounds are hard to study for several reasons, e.g., it is difficult to study the organic signals amidst a large background of inorganic nitrogen and sulfur. Also, relatively weak bonds like O-N do not withstand even relatively mild ionization techniques like proton transfer ionization. It is highly desirable to

258

further develop field-deployable MS with softer ionization or specialized spectroscopy techniques sensitive to specific N-O, N-H or S-O spectral features.

Finally, a note on modeling, which provides important insights on SOA formation and enables useful predictions of future SOA burdens. Most air-pollution and chemical box models are based on existing kinetics measurements, as well as estimated reactions yields and rate constants, which come from structure-activity relationships and *ab initio* calculations. However, most models currently do not include physical processes like water evaporation from aqueous atmospheric droplets and some other models include oversimplified chemistry. For evaporation, when directly included, it is treated as a halt in chemistry instead of an acceleration in rates. Missing reactions and physical processes may explain why, sometimes, models underpredict SOA by an order of magnitude. These model upgrades would lead to more realistic calculations of SOA production; however, it is important to acknowledge that much work is to be done in the laboratory to obtain the kinetic data necessary to support these changes. As both the database of atmospheric chemical reactions and computational capability grows (though not at the same rate), the large-scale inclusion of relevant chemical and physical processes into models may be achievable in the next several years. As aerosol chemistry is a newer field, the next decade is sure to be exciting.

Bibliography

1.   Koch, B. P.; Dittmar, T., From mass to structure: an aromaticity index for high-resolution mass data of natural organic matter. *Rap. Comm. Mass. Spectr.* **2006,** *20*, (5), 926-932.

2.   Badertscher, M.; Bischofberger, K.; Munk, M. E.; Pretsch, E., A Novel Formalism To Characterize the Degree of Unsaturation of Organic Molecules. *Journal of Chemical Information and Computer Sciences* **2001,** *41*, (4), 889-893.

3.   Chen, Y.; Bond, T. C., Light absorption by organic carbon from wood combustion. *Atmos. Chem. Phys.* **2010,** *10*, (4), 1773-1787.

4.   Roach, P. J.; Laskin, J.; Laskin, A., Nanospray desorption electrospray ionization: an ambient method for liquid-extraction surface sampling in mass spectrometry. *Analyst* **2010,** *135*, (9), 2233-2236.

5.   Makarov, A., Electrostatic Axially Harmonic Orbital Trapping: A High-Performance Technique of Mass Analysis. *Anal. Chem.* **2000,** *72*, (6), 1156-1162.

6.   Twomey, S., Aerosols, clouds and radiation. *Atmospheric Environment, Part A: General Topics* **1991,** *25A*, (11), 2435-42.

7.   Finlayson-Pitts, B. J.; Hemminger, J. C., Physical Chemistry of Airborne Sea Salt Particles and Their Components. *J. Phys. Chem. A* **2000,** *104*, (49), 11463-11477.

8.   Solomon, S.; Qin, D.; Manning, M.; Chen, Z.; Marquis, M.; Averyt, K. B.; Tignor, M.; Miller, H. L. *Climate Change 2007: The Physical Science Basis. Contribution of Working Group I to the Fourth Assessment Report of the Intergovernmental Panel on Climate Change.*; IPCC: 2007.

9.   Hallquist, M.; Wenger, J. C.; Baltensperger, U.; Rudich, Y.; Simpson, D.; Claeys, M.; Dommen, J.; Donahue, N. M.; George, C.; Goldstein, A. H.; Hamilton, J. F.; Herrmann, H.; Hoffmann, T.; Iinuma, Y.; Jang, M.; Jenkin, M. E.; Jimenez, J. L.; Kiendler-Scharr, A.; Maenhaut, W.; McFiggans, G.; Mentel, T. F.; Monod, A.; Prevot, A. S. H.; Seinfeld, J. H.; Surratt, J. D.; Szmigielski, R.; Wildt, J., The formation, properties and impact of secondary organic aerosol: current and emerging issues. *Atm. Chem. Phys.* **2009,** *9*, (14/2), 5155-5236.

10. Solomon, S.; Daniel, J. S.; Neely, R. R.; Vernier, J. P.; Dutton, E. G.; Thomason, L. W., The Persistently Variable Background Stratospheric Aerosol Layer and Global Climate Change. *Science* **2011**.

11. Delfino, R., J.; Sioutas, C.; Malik, S., Potential role of ultrafine particles in associations between airborne particle mass and cardiovascular health. *Environ Health Perspect* **2005,** *113*, (8), 934-46.

12. Mauderly, J. L.; Chow, J. C., Health effects of organic aerosols. *Inhalation Toxicology* **2008,** *20*, (3), 257-288.

13. Kanakidou, M., Seinfeld, J. H., Pandis, S. N., Barnes, I., Dentener, F. J., Facchini, M. C., Van Dingenen, R., Ervens, B., Nenes, A., Nielsen, C. J., Swietlicki, E., Putaud, J. P., Balkanski, Y., Fuzzi, S., Horth, J., Moortgat, G. K., Winterhalter, R., Myhre, C. E. L., Tsigaridis, K., Vignati, E., Stephanou, E. G., and Wilson, J., Organic aerosol and global climate modelling: a review. *Atmos. Chem. Phys.* **2005,** *5*, 1053-1123.

14. Novakov, T.; Penner, J. E., Large contribution of organic aerosols to cloud-condensation-nuclei concentrations. *Nature* **1993,** *365*, (6449), 823-6.

15. Odum, J. R.; Hoffmann, T.; Bowman, F.; Collins, D.; Flagan, R. C.; Seinfeld, J. H., Gas/Particle Partitioning and Secondary Organic Aerosol Yields. *Environ. Sci. Technol.* **1996,** *30*, (8), 2580-2585.

16. Seinfeld, J. H.; Pankow, J. F., Organic atmospheric particulate material. *Annual Review of Physical Chemistry* **2003,** *54*, 121-140.

17. Atkinson, R., Atmospheric chemistry of VOCs and NOx. *Atmos. Environ.* **2000,** *34*, (12-14), 2063-2101.

18. Carlton, A. G.; Wiedinmyer, C.; Kroll, J. H., A review of secondary organic aerosol formation from isoprene. *Atmos. Chem. Phys.* **2009,** *9*, (14), 4987-5005.

19. Hoyle, C. R.; Boy, M.; Donahue, N. M.; Fry, J. L.; Glasius, M.; Guenther, A.; Hallar, A. G.; Huff Hartz, K.; Petters, M. D.; Petaja, T.; Rosenoern, T.; Sullivan, A. P., A review of the anthropogenic influence on biogenic secondary organic aerosol. *Atmos. Chem. Phys.* **2011,** *11*, (1), 321-343.

20. Müller, J.-F., Geographical Distribution and Seasonal Variation of Surface Emissions and Deposition Velocities of Atmospheric Trace Gases. *J. Geophys. Res.* **1992,** *97*, (D4), 3787-3804; doi:10.1029/91jd02757.

21. Finlayson-Pitts, B. J.; Pitts, J. N., *Chemistry of the Upper and Lower Atmosphere: Theory, Experiments, and Applications*. Academic Press: San Diego, CA, 2000.

22. Guenther, A.; Karl, T.; Harley, P.; Wiedinmyer, C.; Palmer, P. I.; Geron, C., Estimates of global terrestrial isoprene emissions using MEGAN (Model of Emissions of Gases and Aerosols from Nature). *Atm. Chem. Phys.* **2006,** *6*, (11, Pt. 1), 3181-3210.

23. Rinne, H. J. I.; Guenther, A. B.; Greenberg, J. P.; Harley, P. C., Isoprene and monoterpene fluxes measured above Amazonian rainforest and their dependence on light and temperature. *Atmos. Environ.* **2002,** *36*, (14), 2421-2426.

24. Claeys, M.; Graham, B.; Vas, G.; Wang, W.; Vermeylen, R.; Pashynska, V.; Cafmeyer, J.; Guyon, P.; Andreae, M. O.; Artaxo, P.; Maenhaut, W., Formation of secondary

organic aerosols through photooxidation of isoprene. *Science* **2004,** *303*, (5661), 1173-1176.

25. Pandis, S. N.; Paulson, S. E.; Seinfeld, J. H.; Flagan, R. C., Aerosol formation in the photooxidation of isoprene and beta -pinene. *Atmos. Environ.* **1991,** *25A*, (5-6), 997-1008.

26. Kleindienst, T. E., Lewandowski, M., Offenberg, J. H., Jaoui, M., Edney, E. O., Ozone-isoprene reaction: Re-examination of the formation of secondary organic aerosol. *Geophys. Res. Lett.* **2007,** *34*, (1).

27. Henze, D. K.; Seinfeld, J. H., Global secondary organic aerosol from isoprene oxidation. *Geophys. Res. Lett.* **2006,** *33*, (9), L09812, doi:10.1029/2006GL025976.

28. Paulot, F.; Crounse, J. D.; Kjaergaard, H. G.; Kuerten, A.; St. Clair, J. M.; Seinfeld, J. H.; Wennberg, P. O., Unexpected epoxide formation in the gas-phase photooxidation of isoprene. *Science* **2009,** *325*, (5941), 730-733.

29. Grosjean, D.; Williams, E. L.; Grosjean, E., Atmospheric chemistry of isoprene and of its carbonyl products. *Environ. Sci. Technol.* **1993,** *27*, (5), 830-840.

30. Paulot, F.; Crounse, J. D.; Kjaergaard, H. G.; Kroll, J. H.; Seinfeld, J. H.; Wennberg, P. O., Isoprene photooxidation: new insights into the production of acids and organic nitrates. *Atmos. Chem. Phys.* **2009,** *9*, 1479-1501.

31. Paulson, S. E., Richard C. Flagan, John H. Seinfeld, Atmospheric photooxidation of isoprene part I: The hydroxyl radical and ground state atomic oxygen reactions. *Int. J. Chem. Kinet.* **1992,** *24*, (1), 79-101.

32. Paulson, S. E., R. C. Flagan and J. H. Seinfeld, Atmospheric photooxidation of isoprene part II: The ozone-isoprene reaction. *Int. J. Chem. Kinet.* **1992,** *24*, (1), 103-125.

33. Kleindienst, T. E.; Lewandowski, M.; Offenberg, J. H.; Jaoui, M.; Edney, E. O., The formation of secondary organic aerosol from the isoprene plus OH reaction in the absence of NOx. *Atmos. Chem. Phys.* **2009,** *9*, (17), 6541-6558.

34. Paulot, F.; Crounse, J. D.; Kjaergaard, H. G.; Kurten, A.; St. Clair, J. M.; Seinfeld, J. H.; Wennberg, P. O., Unexpected Epoxide Formation in the Gas-Phase Photooxidation of Isoprene. *Science* **2009,** *325*, (5941), 730-733.

35. Claeys, M.; Wang, W.; Ion, A. C.; Kourtchev, I.; Gelencser, A.; Maenhaut, W., Formation of secondary organic aerosols from isoprene and its gas-phase oxidation products through reaction with hydrogen peroxide. *Atmos. Environ.* **2004,** *38*, (25), 4093-4098.

36. Surratt, J. D.; Murphy, S. M.; Kroll, J. H.; Ng, N. L.; Hildebrandt, L.; Sorooshian, A.; Szmigielski, R.; Vermeylen, R.; Maenhaut, W.; Claeys, M.; Flagan, R. C.; Seinfeld, J. H.,

Chemical composition of secondary organic aerosol formed from the photooxidation of isoprene. *J. Phys. Chem. A* **2006,** *110*, (31), 9665-9690.

37.   Szmigielski, R.; Surratt, J. D.; Vermeylen, R.; Szmigielska, K.; Kroll, J. H.; Ng, N. L.; Murphy, S. M.; Sorooshian, A.; Seinfeld, J. H.; Claeys, M., Characterization of 2-methylglyceric acid oligomers in secondary organic aerosol formed from the photooxidation of isoprene using trimethylsilylation and gas chromatography/ion trap mass spectrometry. *J. Mass. Spectrom.* **2007,** *42*, (1), 101-116.

38.   Nguyen, T. B.; Laskin, J.; Laskin, A.; Nizkorodov, S. A., Nitrogen containing organic compounds and oligomers in secondary organic aerosol formed by photooxidation of isoprene. *Environ. Sci. Technol.* **2011,** *45*, 6908-6918.

39.   Nguyen, T. B.; Roach, P. J.; Laskin, J.; Laskin, A.; Nizkorodov, S. A., Effect of humidity on the composition of isoprene photooxidation secondary organic aerosol *Atm. Chem. Phys.* **2011,** *11*, 6931-6944.

40.   Chan, A. W. H., Chan, M. N., Surratt, J. D., Chhabra, P. S., Loza, C. L., Crounse, J. D., Yee, L. D., Flagan, R. C., Wennberg, P. O., and Seinfeld, J. H., Role of aldehyde chemistry and NOx concentrations in secondary organic aerosol formation. *Atmos. Chem. Phys.* **2010,** *10*, 7169-7188.

41.   Edney, E. O.; Kleindienst, T. E.; Jaoui, M.; Lewandowski, M.; Offenberg, J. H.; Wang, W.; Claeys, M., Formation of 2-methyl tetrols and 2-methylglyceric acid in secondary organic aerosol from laboratory irradiated isoprene/NO_x/SO_2/air mixtures and their detection in ambient $PM_{2.5}$ samples collected in the eastern United States. *Atmos. Environ.* **2005,** *39*, (29), 5281-5289.

42.   Taraborrelli, D.; Lawrence, M. G.; Crowley, J. N.; Dillon, T. J.; Gromov, S.; Grosz, C. B. M.; Vereecken, L.; Lelieveld, J., Hydroxyl radical buffered by isoprene oxidation over tropical forests. *Nature Geosci* **2012,** *5*, (3), 190-193.

43.   Wang, W.; Kourtchev, I.; Graham, B.; Cafmeyer, J.; Maenhaut, W.; Claeys, M., Characterization of oxygenated derivatives of isoprene related to 2-methyltetrols in Amazonian aerosols using trimethylsilylation and gas chromatography/ion trap mass spectrometry. *Rapid Commun. Mass Spectrom.* **2005,** *19*, 1343-1351.

44.   Guenther, A.; Hewitt, C. N.; Erickson, D.; Fall, R.; Geron, C.; Graedel, T.; Harley, P.; Klinger, L.; Lerdau, M.; et al., A global model of natural volatile organic compound emissions. *J. Geophys. Res.* **1995,** *100*, (D5), 8873-92.

45.   Geron, C.; Rasmussen, R.; Arnts, R. R.; Guenther, A., A review and synthesis of monoterpene speciation from forests in the United States. *Atm. Environ.* **2000,** *34*, (11), 1761-1781.

46.   Brown, S. K.; Sim, M. R.; Abramson, M. J.; Gray, C. N., Concentrations of volatile organic compounds in indoor air - a review. *Indoor Air* **1994,** *4*, (2), 123-34.

263

47. Wainman, T.; Zhang, J.; Weschler, C. J.; Lioy, P. J., Ozone and limonene in indoor air: a source of submicron particle exposure. *Environ. Health Perspect.* **2000,** *108*, (12), 1139-1145.

48. Jaoui, M.; Corse, E.; Kleindienst, T. E.; Offenberg, J. H.; Lewandowski, M.; Edney, E. O., Analysis of Secondary Organic Aerosol Compounds from the Photooxidation of d-Limonene in the Presence of NOx and their Detection in Ambient PM2.5. *Environ. Sci. Technol.* **2006,** *40*, (12), 3819-3828.

49. Larsen, B. R.; Lahaniati, M.; Calogirou, A.; Kotzias, D., Atmospheric oxidation products of terpenes: a new nomenclature. *Chemosphere* **1998,** *37*, (6), 1207-1220.

50. Leungsakul, S., M. Jaoui and R. M. Kamens, Kinetic Mechanism for Predicting Secondary Organic Aerosol Formation from the Reaction of d-Limonene with Ozone. *Environ. Sci. Technol.* **2005,** *39*, 9583-9594.

51. Zhang, J.; Huff Hartz, K. E.; Pandis, S. N.; Donahue, N. M., Secondary Organic Aerosol Formation from Limonene Ozonolysis: Homogeneous and Heterogeneous Influences as a Function of NOx *J. Phys. Chem. A* **2006,** *110*, (38), 11053-11063.

52. Hakola, H.; Arey, J.; Aschmann, S. M.; Atkinson, R., Product formation from the gas-phase reactions of OH radicals and O3 with a series of monoterpenes. *J. Atmos. Chem.* **1994,** *18*, (1), 75-102.

53. Walser, M. L.; Desyaterik, Y.; Laskin, J.; Laskin, A.; Nizkorodov, S. A., High-resolution mass spectrometric analysis of secondary organic aerosol produced by ozonation of limonene. *Phys. Chem. Chem. Phys.* **2008,** *10*, (7), 1009-1022.

54. Bateman, A. P.; Nizkorodov, S. A.; Laskin, J.; Laskin, A., Time-resolved molecular characterization of limonene/ozone aerosol using high-resolution electrospray ionization mass spectrometry. *Phys. Chem. Chem. Phys.* **2009,** *11*, (36), 7931-7942.

55. Jaoui, M.; Kleindienst, T. E.; Lewandowski, M.; Offenberg, J. H.; Edney, E. O., Identification and Quantification of Aerosol Polar Oxygenated Compounds Bearing Carboxylic or Hydroxyl Groups. 2. Organic Tracer Compounds from Monoterpenes. *Environ. Sci. Technol.* **2005,** *39*, (15), 5661-5673.

56. Lim, H.-J.; Turpin, B. J., Origins of primary and secondary organic aerosol in Atlanta: results of time-resolved measurements during the Atlanta Supersite Experiment. *Environ. Sci. Technol.* **2002,** *36*, (21), 4489-4496.

57. Claeys, M.; Szmigielski, R.; Kourtchev, I.; Van der Veken, P.; Vermeylen, R.; Maenhaut, W.; Jaoui, M.; Kleindienst, T. E.; Lewandowski, M.; Offenberg, J. H.; Edney, E. O., Hydroxydicarboxylic Acids: Markers for Secondary Organic Aerosol from the Photooxidation of alpha -Pinene. *Environ. Sci. Technol.* **2007,** *41*, (5), 1628-1634.

58.   Abbatt, J. P. D.; Broekhuizen, K.; Pradeep Kumar, P., Cloud condensation nucleus activity of internally mixed ammonium sulfate/organic acid aerosol particles. *Atmos. Environ.* **2005,** *39*, (26), 4767-4778.

59.   Mikhailov, E.; Vlasenko, S.; Martin, S. T.; Koop, T.; Poschl, U., Amorphous and crystalline aerosol particles interacting with water vapor: conceptual framework and experimental evidence for restructuring, phase transitions and kinetic limitations. *Atmos. Chem. Phys.* **2009,** *9*, (24), 9491-9522.

60.   Norrish, R. G. W.; Bamford, C. H., Photodecomposition of aldehydes and ketones. *Nature* **1936,** *138*, 1016.

61.   Norrish, R. G. W.; Bamford, C. H., Photodecomposition of aldehydes and ketones. *Nature* **1937,** *140*, 195-6.

62.   Chacon-Madrid, H. J.; Donahue, N. M., Fragmentation vs. functionalization: chemical aging and organic aerosol formation. *Atmos. Chem. Phys.* **2011,** *11*, (20), 10553-10563.

63.   De Haan, D. O.; Hawkins, L. N.; Kononenko, J. A.; Turley, J. J.; Corrigan, A. L.; Tolbert, M. A.; Jimenez, J. L., Formation of Nitrogen-Containing Oligomers by Methylglyoxal and Amines in Simulated Evaporating Cloud Droplets. *Environ. Sci. Technol.* **2011,** *45*, (3), 984-991.

64.   Bones, D. L.; Henricksen, D. K.; Mang, S. A.; Gonsior, M.; Bateman, A. P.; Nguyen, T. B.; Cooper, W. J.; Nizkorodov, S. A., Appearance of strong absorbers and fluorophores in limonene-O3 secondary organic aerosol due to NH4+-mediated chemical aging over long time scales. *J. Geophys. Res.* **2010,** *115*, (D5), D05203, doi:10.1029/2009jd012864.

65.   Rincon, A. G.; Guzman, M. I.; Hoffmann, M. R.; Colussi, A. J., Thermochromism of Model Organic Aerosol Matter. *Journal of Physical Chemistry Letters* **2010,** *1*, (1), 368-373.

66.   Kalberer, M.; Paulsen, D.; Sax, M.; Steinbacher, M.; Dommen, J.; Prevot, A. S. H.; Fisseha, R.; Weingartner, E.; Frankevich, V.; Zenobi, R.; Baltensperger, U., Identification of polymers as major components of atmospheric organic aerosols. *Science* **2004,** *303*, (5664), 1659-1662.

67.   Hall, W. A.; Johnston, M. V., Oligomer content of a-pinene secondary organic aerosol. *Aerosol Sci. Technol.* **2011,** *45*, (1), 37 - 45.

68.   Tolocka, M. P.; Jang, M.; Ginter, J. M.; Cox, F. J.; Kamens, R. M.; Johnston, M. V., Formation of oligomers in secondary organic aerosol. *Environ. Sci. Technol.* **2004,** *38*, (5), 1428-1434.

69.   Surratt, J. D.; Kroll, J. H.; Kleindienst, T. E.; Edney, E. O.; Claeys, M.; Sorooshian, A.; Ng, N. L.; Offenberg, J. H.; Lewandowski, M.; Jaoui, M.; Flagan, R. C.; Seinfeld, J. H., Evidence for organosulfates in secondary organic aerosol. *Environ. Sci. Technol.* **2007,** *41*, (2), 517-527.

70.   Darer, A. I.; Cole-Filipiak, N. C.; O'Connor, A. E.; Elrod, M. J., Formation and Stability of Atmospherically Relevant Isoprene-Derived Organosulfates and Organonitrates. *Environ. Sci. Technol.* **2011,** *45*, (5), 1895-1902.

71.   Surratt, J. D.; Gomez-Gonzalez, Y.; Chan, A. W. H.; Vermeylen, R.; Shahgholi, M.; Kleindienst, T. E.; Edney, E. O.; Offenberg, J. H.; Lewandowski, M.; Jaoui, M.; Maenhaut, W.; Claeys, M.; Flagan, R. C.; Seinfeld, J. H., Organosulfate formation in biogenic secondary organic aerosol. *J. Phys. Chem. A* **2008,** *112*, (36), 8345-8378.

72.   Iinuma, Y.; Mueller, C.; Berndt, T.; Boege, O.; Claeys, M.; Herrmann, H., Evidence for the Existence of Organosulfates from beta -Pinene Ozonolysis in Ambient Secondary Organic Aerosol. *Environ. Sci. Technol.* **2007,** *41*, (19), 6678-6683.

73.   Froyd, K. D.; Murphy, S. M.; Murphy, D. M.; de Gouw, J. A.; Eddingsaas, N. C.; Wennberg, P. O., Contribution of isoprene-derived organosulfates to free tropospheric aerosol mass. *Proc. Natl. Acad. Sci.* **2010,** *107*, (50), 21360-21365.

74.   Noziere, B.; Ekstrom, S.; Alsberg, T.; Holmstrom, S., Radical-initiated formation of organosulfates and surfactants in atmospheric aerosols. *Geophys. Res. Lett.* **2010,** *37*, 6.

75.   Chan, M. N.; Surratt, J. D.; Claeys, M.; Edgerton, E. S.; Tanner, R. L.; Shaw, S. L.; Zheng, M.; Knipping, E. M.; Eddingsaas, N. C.; Wennberg, P. O.; Seinfeld, J. H., Characterization and Quantification of Isoprene-Derived Epoxydiols in Ambient Aerosol in the Southeastern United States. *Environ. Sci. Technol.* **2010,** *44*, (12), 4590-4596.

76.   Minerath, E. C.; Schultz, M. P.; Elrod, M. J., Kinetics of the Reactions of Isoprene-Derived Epoxides in Model Tropospheric Aerosol Solutions. *Environ. Sci. Technol.* **2009,** *43*, (21), 8133-8139.

77.   Laskin, A.; Smith, J. S.; Laskin, J., Molecular Characterization of Nitrogen-Containing Organic Compounds in Biomass Burning Aerosols Using High-Resolution Mass Spectrometry. *Environ. Sci. Technol.* **2009,** *43*, (10), 3764-3771.

78.   Wang, X. F.; Gao, S.; Yang, X.; Chen, H.; Chen, J. M.; Zhuang, G. S.; Surratt, J. D.; Chan, M. N.; Seinfeld, J. H., Evidence for High Molecular Weight Nitrogen-Containing Organic Salts in Urban Aerosols. *Environ. Sci. Technol.* **2010,** *44*, (12), 4441-4446.

79.   Nguyen, T. B.; Bateman, A. P.; Bones, D. L.; Nizkorodov, S. A.; Laskin, J.; Laskin, A., High-resolution mass spectrometry analysis of secondary organic aerosol generated by ozonolysis of isoprene. *Atmos. Environ.* **2010,** *44*, (8), 1032-1042.

80.   Saxena, P.; Hildemann, L. M., Water-soluble organics in atmospheric particles: A critical review of the literature and application of thermodynamics to identify candidate compounds. *J. Atmos. Chem.* **1996,** *24*, (1), 57-109.

81.   Jimenez, J. L.; Jayne, J. T.; Shi, Q.; Kolb, C. E.; Worsnop, D. R.; Yourshaw, I.; Seinfeld, J. H.; Flagan, R. C.; Zhang, X.; Smith, K. A.; Morris, J. W.; Davidovits, P., Ambient

aerosol sampling using the Aerodyne Aerosol Mass Spectrometer. *J. Geophys. Res.* **2003,** *108*, (D7), SOS 13/1-SOS 13/13.

82.   Nizkorodov, S. A.; Laskin, J.; Laskin, A., Molecular chemistry of organic aerosols through the application of high resolution mass spectrometry. *Phys. Chem. Chem. Phys.* **2011,** *13*, (9), 3612-3629.

83.   DeCarlo, P. F.; Kimmel, J. R.; Trimborn, A.; Northway, M. J.; Jayne, J. T.; Aiken, A. C.; Gonin, M.; Fuhrer, K.; Horvath, T.; Docherty, K. S.; Worsnop, D. R.; Jimenez, J. L., Field-Deployable, High-Resolution, Time-of-Flight Aerosol Mass Spectrometer. *Anal. Chem.* **2006,** *78*, (24), 8281-8289.

84.   Makarov, A.; Denisov, E.; Kholomeev, A.; Balschun, W.; Lange, O.; Strupat, K.; Horning, S., Performance Evaluation of a Hybrid Linear Ion Trap/Orbitrap Mass Spectrometer. *Anal. Chem.* **2006,** *78*, (7), 2113-2120.

85.   Marshall, A. G.; Hendrickson, C. L.; Jackson, G. S., Fourier Transform Ion Cyclotron Resonance Mass Spectrometry. In *Encyclopedia of Analytical Chemistry*, John Wiley & Sons, Ltd: 2006.

86.   Kim, S.; Rodgers, R. P.; Marshall, A. G., Truly "exact" mass: Elemental composition can be determined uniquely from molecular mass measurement at 0.1mDa accuracy for molecules up to 500 Da. *Int. J. Mass Spec.* **2006,** *251*, (2-3), 260-265.

87.   Bateman, A. P.; Walser, M. L.; Desyaterik, Y.; Laskin, J.; Laskin, A.; Nizkorodov, S. A., The Effect of Solvent on the Analysis of Secondary Organic Aerosol Using Electrospray Ionization Mass Spectrometry. *Environ. Sci. Technol.* **2008,** *42*, (19), 7341-7346.

88.   Bruins, A. P., Mechanistic aspects of electrospray ionization. *J. Chromatogr. A* **1998,** *794*, (1-2), 345-357.

89.   Andreae, M. O.; Gelencser, A., Black carbon or brown carbon? The nature of light-absorbing carbonaceous aerosols. *Atmos. Chem. Phys.* **2006,** *6*, (10), 3131-3148.

90.   Park, R. J.; Kim, M. J.; Jeong, J. I.; Youn, D.; Kim, S., A contribution of brown carbon aerosol to the aerosol light absorption and its radiative forcing in East Asia. *Atmos. Environ.* **2010,** *44*, (11), 1414-1421.

91.   Laskin, J.; Laskin, A.; Roach, P. J.; Slysz, G. W.; Anderson, G. A.; Nizkorodov, S. A.; Bones, D. L.; Nguyen, L. Q., High-resolution desorption electrospray ionization mass spectrometry for chemical characterization of organic aerosols. *Analyt. Chem.* **2010,** *82*, (5), 2048-2058.

92.   Gelencser, A.; Hoffer, A.; Kiss, G.; Tombacz, E.; Kurdi, R.; and Bencze, L., In-situ Formation of Light-Absorbing Organic Matter in Cloud Water. *J. Atmos. Chem.* **2003,** *45*, (1), 25-33.

93. De Haan, D. O.; Tolbert, M. A.; Jimenez, J. L., Atmospheric condensed-phase reactions of glyoxal with methylamine. *Geophys. Res. Lett.* **2009,** *36*, L11819; doi:10.1029/2009gl037441.

94. Sareen, N.; Schwier, A. N.; Shapiro, E. L.; Mitroo, D.; McNeill, V. F., Secondary organic material formed by methylglyoxal in aqueous aerosol mimics. *Atm. Chem. Phys.* **2010,** *10*, (3), 997-1016.

95. Shapiro, E. L.; Szprengiel, J.; Sareen, N.; Jen, C. N.; Giordano, M. R.; McNeill, V. F., Light-absorbing secondary organic material formed by glyoxal in aqueous aerosol mimics. *Atm. Chem. Phys.* **2009,** *9*, (7), 2289-2300.

96. Nguyen, T. B.; Lee, P. B.; Updyke, K. M.; Bones, D. L.; Laskin, J.; Laskin, A.; Nizkorodov, S. A., Formation of nitrogen- and sulfur-containing light-absorbing compounds accelerated by evaporation of water from secondary organic aerosols. *J. Geophys. Res.* **2012,** *117*, (D1), D01207; doi:10.1029/2011JD016944

97. Noziere, B.; Esteve, W., Light-absorbing aldol condensation products in acidic aerosols: Spectra, kinetics, and contribution to the absorption index. *Atmos. Environ.* **2007,** *41*, (6), 1150-1163.

98. Hecobian, A.; Zhang, X.; Zheng, M.; Frank, N.; Edgerton, E. S.; Weber, R. J., Water-soluble organic aerosol material and the light-absorption characteristics of aqueous extracts measured over the Southeastern United States. *Atmos. Chem. Phys.* **2010,** *10*, (13), 5965-5977.

99. Yang, M.; Howell, S. G.; Zhuang, J.; Huebert, B. J., Attribution of aerosol light absorption to black carbon, brown carbon, and dust in China - interpretations of atmospheric measurements during EAST-AIRE. *Atmos. Chem. Phys.* **2009,** *9*, (6), 2035-2050.

100. Kendrick, E., Mass scale based on CH_2 = 14.0000 for high-resolution mass spectrometry of organic compounds. *Anal. Chem.* **1963,** *35*, (13), 2146-54.

101. van Krevelen, D. W., Graphical-statistical method for the study of structure and reaction processes of coal. *Fuel* **1950,** *29*, 269-84.

102. Zhang, D.; Lei, W.; Zhang, R., Mechanism of OH formation from ozonolysis of isoprene: kinetics and product yields. *Chem. Phys. Lett.* **2002,** *358*, (3-4), 171-179.

103. Zelenyuk, A.; Yang, J.; Song, C.; Zaveri, R. A.; Imre, D., A New Real-Time Method for Determining Particles' Sphericity and Density: Application to Secondary Organic Aerosol Formed by Ozonolysis of alpha-Pinene. *Environ. Sci. Technol.* **2008,** *42*, (21), 8033-8038.

104. Bouchoux, G., Gas-phase basicities of polyfunctional molecules. Part 1: Theory and methods. *Mass Spectrom. Rev.* **2007,** *26*, (6), 775-835.

105. Warneke, C.; de Gouw, J. A.; Kuster, W. C.; Goldan, P. D.; Fall, R., Validation of Atmospheric VOC Measurements by Proton-Transfer- Reaction Mass Spectrometry Using a Gas-Chromatographic Preseparation Method. *Environ. Sci. Technol.* **2003,** *37*, (11), 2494-2501.

106. Inomata, S.; Tanimoto, H.; Kameyama, S.; Tsunogai, U.; Irie, H.; Kanaya, Y.; Wang, Z., Technical Note: Determination of formaldehyde mixing ratios in air with PTR-MS: laboratory experiments and field measurements. *Atmos. Chem. Phys.* **2008,** *8*, (2), 273-284.

107. Zhao, J.; Zhang, R., Proton transfer reaction rate constants between hydronium ion (H_3O^+) and volatile organic compounds. *Atmos. Environ.* **2004,** *38*, (14), 2177-2185.

108. Roach, P. J.; Laskin, J.; Laskin, A., Molecular Characterization of Organic Aerosols Using Nanospray-Desorption/Electrospray Ionization-Mass Spectrometry *Anal. Chem.* **2010,** *82*, (19), 7979-7986.

109. Fenn, J. B.; Mann, M.; Meng, C. K.; Wong, S. F.; Whitehouse, C. M., Electrospray ionization for mass spectrometry of large biomolecules. *Science* **1989,** *246*, (4926), 64-71.

110. Reemtsma, T., Determination of molecular formulas of natural organic matter molecules by (ultra-) high-resolution mass spectrometry: Status and needs. *J. Chromatogr. A* **2009,** *1216*, (18), 3687-3701.

111. Kebarle, P., A brief overview of the present status of the mechanisms involved in electrospray mass spectrometry. *J. Mass. Spectrom.* **2000,** *35*, (7), 804-817.

112. Takats, Z.; Wiseman, J. M.; Gologan, B.; Cooks, R. G., Mass Spectrometry Sampling Under Ambient Conditions with Desorption Electrospray Ionization. *Science* **2004,** *306*, (5695), 471-473.

113. Takáts, Z.; Wiseman, J. M.; Cooks, R. G., Ambient mass spectrometry using desorption electrospray ionization (DESI): instrumentation, mechanisms and applications in forensics, chemistry, and biology. *J. Mass. Spectrom.* **2005,** *40*, (10), 1261-1275.

114. Kind, T.; Fiehn, O., Seven golden rules for heuristic filtering of molecular formulas obtained by accurate mass spectrometry. *BMC Bioinformatics* **2007,** *8*, 1-20.

115. Morikawa, T.; Newbold, B. T., Analogous odd-even parities in mathematics and chemistry. *Khimiya (Sofiya, Bulgaria)* **2003,** *12*, (6), 445-449.

116. Fuentes, J. D.; Wang, D.; Bowling, D. R.; Potosnak, M.; Monson, R. K.; Goliff, W. S.; Stockwell, W. R., Biogenic hydrocarbon chemistry within and above a mixed deciduous forest. *J. Atm. Chem.* **2007,** *56*, (2), 165-185.

117. Paulson, S. E.; Flagan, R. C.; Seinfeld, J. H., Atmospheric photooxidation of isoprene. Part II. The ozone-isoprene reaction. *International Journal of Chemical Kinetics* **1992,** *24*, (1), 103-25.

118. Paulson, S. E.; Chung, M.; Sen, A. D.; Orzechowska, G., Measurement of OH radical formation from the reaction of ozone with several biogenic alkenes. *J. Geophys. Res. D* **1998,** *103*, (D19), 25533-25539.

119. Hasson, A. S.; Ho, A. W.; Kuwata, K. T.; Paulson, S. E., Production of stabilized Criegee intermediates and peroxides in the gas phase ozonolysis of alkenes. 2. Asymmetric and biogenic alkenes. *J. Geophys. Res. D* **2001,** *106*, (D24), 34143-34153.

120. Kamens, R. M.; Gery, M. W.; Jeffries, H. E.; Jackson, M.; Cole, E. I., Ozone-isoprene reactions: product formation and aerosol potential. *Int. J. Chem. Kinet.* **1982,** *14*, (9), 955-75.

121. Grosjean, D.; Williams, E. L., II; Grosjean, E., Atmospheric chemistry of isoprene and of its carbonyl products. *Environ. Sci. Technol.* **1993,** *27*, (5), 830-40.

122. Neeb, P.; Moortgat, G. K., Formation of OH radicals in the gas-phase reaction of propene, Isobutene, and isoprene with O_3: yields and mechanistic implications. *J. Phys. Chem. A* **1999,** *103*, (45), 9003-9012.

123. Lewin, A. G.; Johnson, D.; Price, D. W.; Marston, G., Aspects of the kinetics and mechanism of the gas-phase reactions of ozone with conjugated dienes. *Phys. Chem. Chem. Phys.* **2001,** *3*, (7), 1253-1261.

124. Gutbrod, R.; Kraka, E.; Schindler, R. N.; Cremer, D., A Kinetic and theoretical investigation of the gas-phase ozonolysis of isoprene: carbonyl oxides as an important source for OH radicals in the atmosphere. *J. Amer. Chem. Soc.* **1997,** *119*, (31), 7330-7342.

125. Kleindienst, T. E., Lewandowski, M., Offenberg, J. H., Jaoui, M., Edney, E. O., Ozone-isoprene reaction: Re-examination of the formation of secondary organic aerosol. *Geophys. Res. Lett.* **2007,** *34*, (1), L01805, doi:10.1029/2006GL027485.

126. Limbeck, A.; Kulmala, M.; Puxbaum, H., Secondary organic aerosol formation in the atmosphere via heterogeneous reaction of gaseous isoprene on acidic particles. *Geophys. Res. Lett.* **2003,** *30*, (19), 1996, doi:10.1029/2003GL017738.

127. Boege, O.; Miao, Y.; Plewka, A.; Herrmann, H., Formation of secondary organic particle phase compounds from isoprene gas-phase oxidation products: An aerosol chamber and field study. *Atm. Environ.* **2006,** *40*, (14), 2501-2509.

128. Surratt, J. D.; Lewandowski, M.; Offenberg, J. H.; Jaoui, M.; Kleindienst, T. E.; Edney, E. O.; Seinfeld, J. H., Effect of acidity on secondary organic aerosol formation from isoprene. *Environ. Sci. Technol.* **2007,** *41*, (15), 5363-5369.

129. Lim, H.-J.; Carlton, A. G.; Turpin, B. J., Isoprene forms secondary organic aerosol through cloud processing: model simulations. *Environ. Sci. Technol.* **2005,** *39*, (12), 4441-4446.

130. Altieri, K. E.; Carlton, A. G.; Lim, H.-J.; Turpin, B. J.; Seitzinger, S. P., Evidence for oligomer formation in clouds: reactions of isoprene oxidation products. *Environ. Sci. Technol.* **2006,** *40*, (16), 4956-4960.

131. Altieri, K. E.; Seitzinger, S. P.; Carlton, A. G.; Turpin, B. J.; Klein, G. C.; Marshall, A. G., Oligomers formed through in-cloud methylglyoxal reactions: Chemical composition, properties, and mechanisms investigated by ultra-high resolution FT-ICR mass spectrometry. *Atmos. Environ.* **2008,** *42*, (7), 1476-1490.

132. Ervens, B.; Carlton, A. G.; Turpin, B. J.; Altieri, K. E.; Kreidensweis, S. M.; Feingold, G., Secondary organic aerosol yields from cloud-processing of isoprene oxidation products. *Geophys. Res. Lett.* **2008,** *35*, (2), L02816, doi:10.1029/2007GL031828.

133. Liggio, J.; Li, S.-M.; Brook, J. R.; Mihele, C., Direct polymerization of isoprene and a-pinene on acidic aerosols. *Geophys. Res. Lett.* **2007,** *34*, (5), L05814, doi:10.1029/2006GL028468.

134. Docherty, K. S.; Wu, W.; Lim, Y. B.; Ziemann, P. J., Contributions of organic peroxides to secondary aerosol formed from reactions of monoterpenes with O_3. *Environ. Sci. Technol.* **2005,** *39*, (11), 4049-4059.

135. Bonn, B.; Von Kuhlmann, R.; Lawrence, M. G., High contribution of biogenic hydroperoxides to secondary organic aerosol formation. *Geophys. Res. Lett.* **2004,** *31*, (10), L10108, doi:10.1029/2003GL019172.

136. Jenkin, M. E., Modelling the formation and composition of secondary organic aerosol from alpha - and beta -pinene ozonolysis using MCM v3. *Atm. Chem. Phys.* **2004,** *4*, (7), 1741-1757.

137. Hasson, A. S.; Chung, M. Y.; Kuwata, K. T.; Converse, A. D.; Krohn, D.; Paulson, S. E., Reaction of Criegee intermediates with water vapor-an additional source of OH radicals in alkene ozonolysis? *J. Phys. Chem. A* **2003,** *107*, (32), 6176-6182.

138. Gaeb, S.; Turner, W. V.; Wolff, S.; Becker, K. H.; Ruppert, L.; Brockmann, K. J., Formation of alkyl and hydroxyalkyl hydroperoxides on ozonolysis in water and in air. *Atm. Environ.* **1995,** *29*, (18), 2401-7.

139. Neeb, P.; Sauer, F.; Horie, O.; Moortgat, G. K., Formation of hydroxymethyl hydroperoxide and formic acid in alkene ozonolysis in the presence of water vapor. *Atm. Environ.* **1997,** *31*, (15), 1417-1423.

140. Sauer, F.; Schafer, C.; Neeb, P.; Horie, O.; Moortgat, G. K., Formation of hydrogen peroxide in the ozonolysis of isoprene and simple alkenes under humid conditions. *Atm. Environ.* **1998,** *33*, (2), 229-241.

141. Mochida, M.; Katrib, Y.; Jayne, J. T.; Worsnop, D. R.; Martin, S. T., The relative importance of competing pathways for the formation of high-molecular-weight peroxides in the ozonolysis of organic aerosol particles. *Atm. Chem. Phys.* **2007,** *6*, (12, Pt. 2), 4851-4866.

142. Atkinson, R.; Carter, W. P. L., Kinetics and mechanisms of the gas-phase reactions of ozone with organic compounds under atmospheric conditions. *Chem. Rev.* **1984,** *84*, (5), 437-70.

143. Bateman, A. P.; Walser, M. L.; Desyaterik, Y.; Laskin, J.; Laskin, A.; Nizkorodov, S. A., The effect of solvent on the analysis of secondary organic aerosol using electrospray ionization mass spectrometry. *Environ. Sci. Technol.* **2008,** *42*, (19), 7341-7346.

144. Reinhold, M.; Meier, R. J.; de Koster, C. G., How feasible is matrix-assisted laser desorption/ionization time-of-flight mass spectrometry analysis of polyolefins? *Rap. Comm. Mass. Spectr.* **1998,** *12*, (23), 1962-1966.

145. Meot-Ner, M., The proton affinity scale, and effects of ion structure and solvation. *Int. J. Mass. Spectr.* **2003,** *227*, (3), 525-554.

146. Kim, S.; Kramer, R. W.; Hatcher, P. G., Graphical method for analysis of ultrahigh-resolution broadband mass spectra of natural organic matter, the Van Krevelen diagram. *Analyt. Chem.* **2003,** *75*, (20), 5336-5344.

147. Pellegrin, V., Molecular formulas of organic compounds. The nitrogen rule and degree of unsaturation. *Journal of Chemical Education* **1983,** *60*, (8), 626-33.

148. Meija, J., Mathematical tools in analytical mass spectrometry. *Analyt. Bioanalyt. Chem.* **2006,** *385*, (3), 486-499.

149. Heaton, K. J.; Sleighter, R. L.; Hatcher, P. G.; Hall, W. A. I.; Johnston, M. V., Composition domains in monoterpene secondary organic aerosol. *Environ. Sci. Technol.* **2009,** *43*, (20), 7797-7802.

150. Wozniak, A. S.; Bauer, J. E.; Sleighter, R. L.; Dickhut, R. M.; Hatcher, P. G., Technical Note: molecular characterization of aerosol-derived water soluble organic carbon using ultrahigh resolution electrospray ionization Fourier transform ion cyclotron resonance mass spectrometry. *Atm. Chem. Phys.* **2008,** *8*, (17), 5099-5111.

151. Hearn, J. D.; Smith, G. D., Reactions and mass spectra of complex particles using Aerosol CIMS. *Int. J. Mass. Spectr.* **2006,** *258*, (1-3), 95-103.

152. Heaton, K. J.; Dreyfus, M. A.; Wang, S.; Johnston, M. V., Oligomers in the Early Stage of Biogenic Secondary Organic Aerosol Formation and Growth. *Environ. Sci. Technol.* **2007,** *41*, (17), 6129-6136.

153. Gao, S.; Keywood, M.; Ng, N. L.; Surratt, J.; Varutbangkul, V.; Bahreini, R.; Flagan, R. C.; Seinfeld, J. H., Low-molecular-weight and oligomeric components in secondary

organic aerosol from the ozonolysis of cycloalkenes and a-pinene. *J. Phys. Chem. A* **2004,** *108*, (46), 10147-10164.

154.   Gao, S.; Ng, N. L.; Keywood, M.; Varutbangkul, V.; Bahreini, R.; Nenes, A.; He, J.; Yoo, K. Y.; Beauchamp, J. L.; Hodyss, R. P.; Flagan, R. C.; Seinfeld, J. H., Particle phase acidity and oligomer formation in secondary organic aerosol. *Environ. Sci. Technol.* **2004,** *38*, (24), 6582-6589.

155.   Tolocka, M. P.; Jang, M.; Ginter, J. M.; Cox, F. J.; Kamens, R. M.; Johnston, M. V., Formation of oligomers in secondary organic aerosol. *Environ. Sci. Technol.* **2004,** *38*, (5), 1428-1434.

156.   Baltensperger, U.; Kalberer, M.; Dommen, J.; Paulsen, D.; Alfarra, M. R.; Coe, H.; Fisseha, R.; Gascho, A.; Gysel, M.; Nyeki, S.; Sax, M.; Steinbacher, M.; Prevot, A. S. H.; Sjogren, S.; Weingartner, E.; Zenobi, R., Secondary organic aerosols from anthropogenic and biogenic precursors. *Faraday Discuss.* **2005,** *130*, 265-278.

157.   Reinhardt, A.; Emmenegger, C.; Gerrits, B.; Panse, C.; Dommen, J.; Baltensperger, U.; Zenobi, R.; Kalberer, M., Ultrahigh Mass Resolution and Accurate Mass Measurements as a Tool To Characterize Oligomers in Secondary Organic Aerosols. *Anal. Chem.* **2007,** *79*, (11), 4074-4082.

158.   Dommen, J.; Metzger, A.; Duplissy, J.; Kalberer, M.; Alfarra, M. R.; Gascho, A.; Weingartner, E.; Prevot, A. S. H.; Verheggen, B.; Baltensperger, U., Laboratory observation of oligomers in the aerosol from isoprene/NO_x photooxidation. *Geophys. Res. Lett.* **2006,** *33*, (13), L13805, doi:10.1029/2006GL026523.

159.   Gross, D. S.; Gaelli, M. E.; Kalberer, M.; Prevot, A. S. H.; Dommen, J.; Alfarra, M. R.; Duplissy, J.; Gaeggeler, K.; Gascho, A.; Metzger, A.; Baltensperger, U., Real-time measurement of oligomeric species in secondary organic aerosol with the aerosol time-of-flight mass spectrometer. *Analyt. Chem.* **2006,** *78*, (7), 2130-2137.

160.   Kalberer, M.; Paulsen, D.; Sax, M.; Steinbacher, M.; Dommen, J.; Prevot, A. S. H.; Fisseha, R.; Weingartner, E.; Frankevich, V.; Zenobi, R.; Baltensperger, U., Identification of polymers as major components of atmospheric organic aerosols. *Science* **2004,** *303*, (5664), 1659-62.

161.   Sato, K.; Hatakeyama, S.; Imamura, T., Secondary organic aerosol formation during the photooxidation of toluene: NO_x dependence of chemical composition. *J. Phys. Chem. A* **2007,** *111*, (39), 9796-9808.

162.   Loeffler, K. W.; Koehler, C. A.; Paul, N. M.; De Haan, D. O., Oligomer formation in evaporating aqueous glyoxal and methyl glyoxal solutions. *Environ. Sci. Technol.* **2006,** *40*, (20), 6318-6323.

163.   Perri, M. J.; Seitzinger, S.; Turpin, B. J., Secondary organic aerosol production from aqueous photooxidation of glycolaldehyde: laboratory experiments. *Atm. Environ.* **2009,** *43*, (8), 1487-1497.

164. Shilling, J. E.; Chen, Q.; King, S. M.; Rosenoern, T.; Kroll, J. H.; Worsnop, D. R.; DeCarlo, P. F.; Aiken, A. C.; Sueper, D.; Jimenez, J. L.; Martin, S. T., Loading-dependent elemental composition of a-pinene SOA particles. *Atm. Chem. Phys.* **2009,** *9*, (3), 771-782.

165. Hughey, C. A.; Hendrickson, C. L.; Rodgers, R. P.; Marshall, A. G.; Qian, K., Kendrick Mass Defect Spectrum: A Compact Visual Analysis for Ultrahigh-Resolution Broadband Mass Spectra. *Anal. Chem.* **2001,** *73*, (19), 4676-4681.

166. Kendrick, E., Mass scale based on $CH_2 = 14.0000$ for high-resolution mass spectrometry of organic compounds. *Analyt. Chem.* **1963,** *35*, (13), 2146-54.

167. Corrigan, A. L.; Hanley, S. W.; De Haan, D. O., Uptake of glyoxal by organic and inorganic aerosol. *Environ. Sci. Technol.* **2008,** *42*, (12), 4428-4433.

168. Barsanti, K. C.; Pankow, J. F., Thermodynamics of the formation of atmospheric organic particulate matter by accretion reactions - 2. Dialdehydes, methylglyoxal, and diketones. *Atm. Environ.* **2005,** *39*, (35), 6597-6607.

169. Kroll, J. H.; Ng, N. L.; Murphy, S. M.; Varutbangkul, V.; Flagan, R. C.; Seinfeld, J. H., Chamber studies of secondary organic aerosol growth by reactive uptake of simple carbonyl compounds. *J. Geophys. Res. D* **2005,** *110*, (D23), D23207, doi:10.1029/2005JD006004.

170. Liggio, J.; Li, S. M., Reversible and irreversible processing of biogenic olefins on acidic aerosols. *Atm. Chem. Phys.* **2008,** *8*, (7), 2039-2055.

171. Finlayson-Pitts, B. J.; Pitts, J. N., *Chemistry of the Upper and Lower Atmosphere: Theory, Experiments, and Applications*. Academic Press: San Diego, 2000; p 1040 pp.

172. Barsanti, K. C.; Pankow, J. F., Thermodynamics of the formation of atmospheric organic particulate matter by accretion reactions - Part 1: aldehydes and ketones. *Atm. Environ.* **2004,** *38*, (26), 4371-4382.

173. Schweitzer, F.; Magi, L.; Mirabel, P.; George, C., Uptake rate measurements of methanesulfonic acid and glyoxal by aqueous droplets. *J. Phys. Chem. A* **1998,** *102*, (3), 593-600.

174. Liggio, J.; Li, S.-M.; McLaren, R., Heterogeneous reactions of glyoxal on particulate matter: identification of acetals and sulfate esters. *Environ. Sci. Technol.* **2005,** *39*, (6), 1532-1541.

175. Liggio, J.; Li, S.-M.; McLaren, R., Reactive uptake of glyoxal by particulate matter. *J. Geophys. Res. D* **2005,** *110*, (D10), D10304, doi:10.1029/2004JD005113.

176. Carlton, A. G.; Turpin, B. J.; Lim, H. J.; Altieri, K. E.; Seitzinger, S., Link between isoprene and secondary organic aerosol (SOA): Pyruvic acid oxidation yields low

volatility organic acids in clouds. *Geophys. Res. Lett.* **2006,** *33*, (6), L06822, doi:10.1029/2005GL025374.

177. Atkinson, R.; Aschmann, S. M.; Arey, J.; Shorees, B., Formation of OH radicals in the gas phase reactions of O_3 with a series of terpenes. *J. Geophys. Res. D* **1992,** *97*, 6065–6073.

178. Kroll, J. H.; Hanisco, T. F.; Donahue, N. M.; Demerjian, K. L.; Anderson, J. G., Accurate, direct measurements of OH yields from gas-phase ozone-alkene reactions using an in situ LIF instrument. *Geophys. Res. Lett.* **2001,** *28*, (20), 3863-3866.

179. Orzechowska, G. E.; Paulson, S. E., Production of OH radicals from the reactions of C4-C6 internal alkenes and styrenes with ozone in the gas phase. *Atm. Environ.* **2002,** *36*, (3), 571-581.

180. Wilkins, C. K.; Clausen, P. A.; Wolkoff, P.; Larsen, S. T.; Hammer, M.; Larsen, K.; Hansen, V.; Nielsen, G. D., Formation of strong airway irritants in mixtures of isoprene/ozone and isoprene/ozone/nitrogen dioxide. *Environ. Health Perspect.* **2001,** *109*, (9), 937-941.

181. Van Cauwenberghe, K.; Van Vaeck, L.; Pitts, J. N., Jr., Physical and chemical transformations of organic pollutants during aerosol sampling. *Advances in Mass Spectrometry* **1980,** *8B*, 1499-507.

182. McDow, S. R.; Huntzicker, J. J., Vapor adsorption artifact in the sampling of organic aerosol: Face velocity effects. *Atm. Environ.* **1990,** *A24*, (10), 2563-2571.

183. Park, K.; Kittelson, D. B.; McMurry, P. H., A closure study of aerosol mass concentration measurements: comparison of values obtained with filters and by direct measurements of mass distributions. *Atm. Environ.* **2003,** *37*, (9-10), 1223-1230.

184. Turpin, B. J.; Lim, H.-J., Species contributions to PM2.5 mass concentrations: revisiting common assumptions for estimating organic mass. *Aerosol Sci. Technol.* **2001,** *35*, (1), 602-610.

185. Pang, Y.; Turpin, B.; Gundel, L., On the importance of organic oxygen for understanding organic aerosol particles. *Aerosol Sci. Technol.* **2006,** *40*, (2), 128-133.

186. Jaoui, M.; Corse, E. W.; Lewandowski, M.; Offenberg, J. H.; Kleindienst, T. E.; Edney, E. O., Formation of organic tracers for isoprene SOA under acidic conditions. *Atmos. Environ.* **2010,** *44*, (14), 1798-1805.

187. Alves, C.; Gonçalves, C.; Mirante, F.; Nunes, T.; Evtyugina, M.; Sánchez de la Campa, A.; Rocha, A.; Marques, M., Organic speciation of atmospheric particles in Alvão Natural Park (Portugal). *Environ. Monit. Assess.* **2010,** *168*, (1), 321-337.

188. Kalberer, M.; Sax, M.; Samburova, V., Molecular size evolution of oligomers in organic aerosols collected in urban atmospheres and generated in a smog chamber. *Environ. Sci. Technol.* **2006,** *40*, (19), 5917-5922.

189. Tuazon, E. C.; Atkinson, R., A product study of the gas-phase reaction of isoprene with the OH radical in the presence of NOx. *Int. J. Chem. Kinet.* **1990,** *22*, (12), 1221-1236.

190. Sprengnether, M.; Demerjian, K. L.; Donahue, N. M.; Anderson, J. G., Product analysis of the OH oxidation of isoprene and 1,3-butadiene in the presence of NO. *J. Geophys. Res.* **2002,** *107*, (D15), 4268-4281, doi:10.1029/2001JD000716

191. Werner, G.; Kastler, J.; Looser, R.; Ballschmiter, K., Organic nitrates of isoprene as atmospheric trace compounds. *Angew. Chem. Int. Edit.* **1999,** *38*, 1634-1637.

192. Aschmann, S. M.; Atkinson, R., Formation yields of methyl vinyl ketone and methacrolein from the gas-phase reaction of O_3 with isoprene. *Environ. Sci. Technol.* **1994,** *28*, (8), 1539-1542.

193. Tuazon, E. C.; Atkinson, R., A product study of the gas-phase reaction of methyl vinyl ketone with the OH radical in the presence of NOx. *Int. J. Chem. Kinet.* **1989,** *21*, 1141-1152.

194. Pankow, J. F., and Asher, W. E., SIMPOL.1: a simple group contribution method for predicting vapor pressures and enthalpies of vaporization of multifunctional organic compounds. *Atmos. Chem. Phys.* **2008,** *8*, 2773-2796.

195. Nash, D. G.; Baer, T.; Johnston, M. V., Aerosol mass spectrometry: An introductory review. *Int. J. Mass Spec.* **2006,** *258*, (1-3), 2-12.

196. Chhabra, P. S.; Flagan, R. C.; Seinfeld, J. H., Elemental analysis of chamber organic aerosol using an aerodyne high-resolution aerosol mass spectrometer. *Atmos. Chem. Phys.* **2010,** *10*, (9), 4111-4131.

197. Farmer, D. K.; Matsunaga, A.; Docherty, K. S.; Surratt, J. D.; Seinfeld, J. H.; Ziemann, P. J.; Jimenez, J. L., Response of an aerosol mass spectrometer to organonitrates and organosulfates and implications for atmospheric chemistry. *Proc. Natl. Acad. Sci.* **2010,** *107*, (15), 6670-6675.

198. Chen, Q.; Farmer, D. K.; Schneider, J.; Zorn, S. R.; Heald, C. L.; Karl, T. G.; Guenther, A.; Allan, J. D.; Robinson, N.; Coe, H.; Kimmel, J. R.; Pauliquevis, T.; Borrmann, S.; Pöschl, U.; Andreae, M. O.; Artaxo, P.; Jimenez, J. L.; Martin, S. T., Mass spectral characterization of submicron biogenic organic particles in the Amazon Basin. *Geophys. Res. Lett.* **2009,** *36*, (20), L20806, doi:10.1029/2009gl039880.

199. Shilling, J. E.; Chen, Q.; King, S. M.; Rosenoern, T.; Kroll, J. H.; Worsnop, D. R.; DeCarlo, P. F.; Aiken, A. C.; Sueper, D.; Jimenez, J. L.; Martin, S. T., Loading-dependent elemental composition of alpha-pinene SOA particles. *Atmos. Chem. Phys.* **2009,** *9*, (3), 771-782.

200. Heaton, K. J.; Dreyfus, M. A.; Wang, S.; Johnston, M. V., Oligomers in the early stage of biogenic secondary organic aerosol formation and growth. *Environ. Sci. Technol.* **2007,** *41*, (17), 6129-6136.

201. Gao, Y.; Hall, W. A.; Johnston, M. V., Molecular composition of monoterpene secondary organic aerosol at low mass loading. *Environ. Sci. Technol.* **2010,** *44*, (20), 7897-7902.

202. Sun, Y.; Zhang, Q.; Macdonald, A. M.; Hayden, K.; Li, S. M.; Liggio, J.; Liu, P. S. K.; Anlauf, K. G.; Leaitch, W. R.; Steffen, A.; Cubison, M.; Worsnop, D. R.; van Donkelaar, A.; Martin, R. V., Size-resolved aerosol chemistry on Whistler Mountain, Canada with a high-resolution aerosol mass spectrometer during INTEX-B. *Atmos. Chem. Phys.* **2009,** *9*, (9), 3095-3111.

203. Aiken, A. C.; Decarlo, P. F.; Kroll, J. H.; Worsnop, D. R.; Huffman, J. A.; Docherty, K. S.; Ulbrich, I. M.; Mohr, C.; Kimmel, J. R.; Sueper, D.; Sun, Y.; Zhang, Q.; Trimborn, A.; Northway, M.; Ziemann, P. J.; Canagaratna, M. R.; Onasch, T. B.; Alfarra, M. R.; Prevot, A. S. H.; Dommen, J.; Duplissy, J.; Metzger, A.; Baltensperger, U.; Jimenez, J. L., O/C and OM/OC ratios of primary, secondary, and ambient organic aerosols with high-resolution time-of-flight aerosol mass spectrometry. *Environ. Sci. Technol.* **2008,** *42*, (12), 4478-4485.

204. Surratt, J.; Chan, A. W. H.; Eddingsaas, N. C.; Chan, M.; Loza, C. L.; Kwan, A. J.; Hersey, S. P.; Flagan, R. C.; Wennberg, P. O.; Seinfeld, J. H., Reactive intermediates revealed in secondary organic aerosol formation from isoprene. *Proc. Natl. Acad. Sci.* **2010,** *107*, 6640-6645.

205. Reemtsma, T.; These, A.; Venkatachari, P.; Xia, X. Y.; Hopke, P. K.; Springer, A.; Linscheid, M., Identification of fulvic acids and sulfated and nitrated analogues in atmospheric aerosol by electrospray ionization Fourier transform ion cyclotron resonance mass spectrometry. *Anal. Chem.* **2006,** *78*, (24), 8299-8304.

206. Yinon, J.; McClellan, J. E.; Yost, R. A., Electrospray ionization tandem mass spectrometry collision-induced dissociation study of explosives in an ion trap mass spectrometer. *Rapid Commun. Mass Spectrom.* **1997,** *11*, (18), 1961-1970.

207. Levsen, K.; Schiebel, H. M.; Terlouw, J. K.; Jobst, K. J.; Elend, M.; Preib, A.; Thiele, H.; Ingendoh, A., Even-electron ions: a systematic study of the neutral species lost in the dissociation of quasi-molecular ions. *J. Mass. Spectrom.* **2007,** *42*, (8), 1024-1044.

208. Nunes, F. M.; Domingues, M. R.; Coimbra, M. A., Arabinosyl and glucosyl residues as structural features of acetylated galactomannans from green and roasted coffee infusions. *Carbohydr. Res.* **2005,** *340*, (10), 1689-1698.

209. Simoes, J.; Nunes, F. M.; Domingues, M. D. M.; Coimbra, M. A., Structural features of partially acetylated coffee galactomannans presenting immunostimulatory activity. *Carbohydr. Polym.* **2010,** *79*, (2), 397-402.

210. Quéméner, B.; Cabrera Pino, J. C.; Ralet, M.-C.; Bonnin, E.; Thibault, J.-F., Assignment of acetyl groups to O-2 and/or O-3 of pectic oligogalacturonides using negative electrospray ionization ion trap mass spectrometry. *J. Mass. Spectrom.* **2003,** *38*, (6), 641-648.

211. Ralet, M. C.; Cabrera, J. C.; Bonnin, E.; Quemener, B.; Hellin, P.; Thibault, J. F., Mapping sugar beet pectin acetylation pattern. *Phytochemistry* **2005,** *66*, (15), 1832-1843.

212. Madeira, P. J. A.; Rosa, A. M.; Xavier, N. M.; Rauter, A. P.; Florêncio, M. H., Electrospray ionization mass spectrometric analysis of newly synthesized α,β-unsaturated γ-lactones fused to sugars. *Rapid Commun. Mass Spectrom.* **2010,** *24*, 1049-1058.

213. Zhang, Q.; Anastasio, C.; Jimenez-Cruz, M., Water-soluble organic nitrogen in atmospheric fine particles (PM2.5) from northern California. *J. Geophys. Res.* **2002,** *107*, (D11), 4112, doi:10.1029/2001jd000870.

214. Duan, F.; Liu, X.; He, K.; Dong, S., Measurements and Characteristics of Nitrogen-Containing Compounds in Atmospheric Particulate Matter in Beijing, China. *Bull. Environ. Contam. Toxicol.* **2009,** *82*, (3), 332-337.

215. Lin, M., Walker, J., Geron, C., Khlystov, A., Organic nitrogen in PM$_{2.5}$ aerosol at a forest site in the Southeast US. *Atmos. Chem. Phys.* **2010,** *10*, (5), 2145–2157.

216. Lee, S. H.; Murphy, D. M.; Thomson, D. S.; Middlebrook, A. M., Nitrate and oxidized organic ions in single particle mass spectra during the 1999 Atlanta Supersite Project. *J. Geophys. Res.-Atmos.* **2003,** *108*, (D7), 8417-8425, doi: 10.1029/2001jd001455.

217. Apel, E. C.; Riemer, D. D.; Hills, A.; Baugh, W.; Orlando, J.; Faloona, I.; Tan, D.; Brune, W.; Lamb, B.; Westberg, H.; Carroll, M. A.; Thornberry, T.; Geron, C. D., Measurement and interpretation of isoprene fluxes and isoprene, methacrolein, and methyl vinyl ketone mixing ratios at the PROPHET site during the 1998 Intensive. *J. Geophys. Res.-Atmos.* **2002,** *107*, (D3), 4034-4049, doi:10.1029/2000jd000225.

218. Stroud, C. A.; Roberts, J. M.; Goldan, P. D.; Kuster, W. C.; Murphy, P. C.; Williams, E. J.; Hereid, D.; Parrish, D.; Sueper, D.; Trainer, M.; Fehsenfeld, F. C.; Apel, E. C.; Riemer, D.; Wert, B.; Henry, B.; Fried, A.; Martinez-Harder, M.; Harder, H.; Brune, W. H.; Li, G.; Xie, H.; Young, V. L., Isoprene and its oxidation products, methacrolein and methylvinyl ketone, at an urban forested site during the 1999 Southern Oxidants Study. *J. Geophys. Res.* **2001,** *106*, (D8), 8035-8046, doi:10.1029/2000jd900628.

219. Kroll, J. H.; Ng, N. L.; Murphy, S. M.; Flagan, R. C.; Seinfeld, J. H., Secondary organic aerosol formation from isoprene photooxidation. *Environ. Sci. Technol.* **2006,** *40*, (6), 1869-1877.

220. Henze, D. K., and J. H. Seinfeld, Global secondary organic aerosol from isoprene oxidation. *Geophys. Res. Lett.* **2006,** *33*, L09812, doi:10.1029/2006GL025976

221. Novakov, T.; Mueller, P. K.; Alcocer, A. E.; Otvos, J. W., Chemical composition of Pasadena aerosol by particle size and time of day. III. Chemical states of nitrogen and sulfur by photoelectron spectroscopy. *J. Colloid Interface Sci.* **1972,** *39*, (1), 225-234.

222. Hughey, C. A.; Rodgers, R. P.; Marshall, A. G., Resolution of 11,000 compositionally distinct components in a single electrospray ionization fourier transform ion cyclotron resonance Mass spectrum of crude oil. *Anal. Chem.* **2002,** *74*, (16), 4145-4149.

223. Zhang, H.; Surratt, J. D.; Lin, Y. H.; Bapat, J.; Kamens, R. M., Effect of relative humidity on SOA formation from isoprene/NO photooxidation: role of particle-phase esterification under dry conditions. *Atmos. Chem. Phys.* **2011,** *11*, 6411-6424.

224. Lim, Y. B.; Ziemann, P. J., Products and mechanism of secondary organic aerosol formation from reactions of n-alkanes with OH radicals in the presence of NOx. *Environ. Sci. Technol.* **2005,** *39*, (23), 9229-9236.

225. Warneck, P., Multi-phase chemistry of C_2 and C_3 organic compounds in the marine atmosphere. *J. Atmos. Chem.* **2005,** *51*, (2), 119-159.

226. Spaulding, R. S.; Schade, G. W.; Goldstein, A. H.; Charles, M. J., Characterization of secondary atmospheric photooxidation products: Evidence for biogenic and anthropogenic sources. *J. Geophys. Res.* **2003,** *108*, (D8), 4247, doi:10.1029/2002jd002478.

227. Matsunaga, S. N., Wiedinmyer, C., Guenther,A. B., Orlando, J. J., Karl,T., Toohey,D. W., Greenberg,J. P., and Kajii, Y., Isoprene oxidation products are a significant atmospheric aerosol component. *Atmos. Chem. Phys. Discuss.* **2005,** *5*, 11143–11156.

228. Lee, A.; Goldstein, A. H.; Kroll, J. H.; Ng, N. L.; Varutbangkul, V.; Flagan, R. C.; Seinfeld, J. H., Gas-phase products and secondary aerosol yields from the photooxidation of 16 different terpenes. *J. Geophys. Res.* **2006,** *111*, (D17), D17305, doi:10.1029/2006jd007050.

229. Hamilton, J. F.; Lewis, A. C.; Carey, T. J.; Wenger, J. C., Characterization of polar compounds and oligomers in secondary organic aerosol using liquid chromatography coupled to mass spectrometry. *Anal. Chem.* **2008,** *80*, (2), 474-480.

230. Barsanti, K. C.; Pankow, J. F., Thermodynamics of the formation of atmospheric organic particulate matter by accretion reactions - Part 3: Carboxylic and dicarboxylic acids. *Atmos. Environ.* **2006,** *40*, (34), 6676-6686.

231. Zhao, J.; Levitt, N. P.; Zhang, R.; Chen, J., Heterogeneous reactions of methylglyoxal in acidic media: implications for secondary organic aerosol formation. *Environ. Sci. Technol.* **2006,** *40*, (24), 7682-7687.

232. Healy, R. M.; Wenger, J. C.; Metzger, A.; Duplissy, J.; Kalberer, M.; Dommen, J., Gas/particle partitioning of carbonyls in the photooxidation of isoprene and 1,3,5-trimethylbenzene. *Atmos. Chem. Phys.* **2008,** *8*, (12), 3215-3230.

233. Liggio, J.; Li, S.-M.; McLaren, R., Heterogeneous reactions of glyoxal on particulate matter: identification of acetals and sulfate esters. *Environ. Sci. Technol.* **2005,** *39*, (6), 1532-1541.

234. Kroll, J. H.; Ng, N. L.; Murphy, S. M.; Varutbangkul, V.; Flagan, R. C.; Seinfeld, J. H., Chamber studies of secondary organic aerosol growth by reactive uptake of simple carbonyl compounds. *J. Geophys. Res.* **2005,** *110*, (D23), D23207, doi:10.1029/2005JD006004

235. Corrigan, A. L.; Hanley, S. W.; Haan, D. O., Uptake of glyoxal by organic and inorganic aerosol. *Environ. Sci. Technol.* **2008,** *42*, (12), 4428-4433.

236. Atkinson, R.; Arey, J., Atmospheric chemistry of biogenic organic compounds. *Acc. Chem. Res.* **1998,** *31*, (9), 574-583.

237. Williams, J.; Poschl, U.; Crutzen, P. J.; Hansel, A.; Holzinger, R.; Warneke, C.; Lindinger, W.; Lelieveld, J., An atmospheric chemistry interpretation of mass scans obtained from a proton transfer mass spectrometer flown over the tropical rainforest of Surinam. *J. Atmos. Chem.* **2001,** *38*, (2), 133-166.

238. Lim, H. J., Carlton, A. G., and Turpin, B. J, Isoprene forms secondary organic aerosol through cloud processing: model simulations. *Environ. Sci. Technol.* **2005,** *39*, 4441-4446.

239. Moortgat, G. K.; Grossmann, D.; Boddenberg, A.; Dallmann, G.; Ligon, A. P.; Turner, W. V.; Gaeb, S.; Slemr, F.; Wieprecht, W.; Acker, K.; Kibler, M.; Schlomski, S.; Baechmann, K., Hydrogen peroxide, organic peroxides and higher carbonyl compounds determined during the BERLIOZ campaign. *J. Atmos. Chem.* **2002,** *42*, (1-3), 443-463.

240. Lee, Y. N.; Zhou, X.; Kleinman, L. I.; Nunnermacker, L. J.; Springston, S. R.; Daum, P. H.; Newman, L.; Keigley, W. G.; Holdren, M. W.; Spicer, C. W.; Young, V.; Fu, B.; Parrish, D. D.; Holloway, J.; Williams, J.; Roberts, J. M.; Ryerson, T. B.; Fehsenfeld, F. C., Atmospheric chemistry and distribution of formaldehyde and several multioxygenated carbonyl compounds during the 1995 Nashville/Middle Tennessee Ozone Study. *J. Geophys. Res.* **1998,** *103*, (D17), 22449-22462, doi:10.1029/98jd01251.

241. Zhou, X.; Huang, G.; Civerolo, K.; Schwab, J., Measurement of atmospheric hydroxyacetone, glycolaldehyde, and formaldehyde. *Environ. Sci. Technol.* **2009,** *43*, (8), 2753-2759.

242. Matsunaga, S.; Mochida, M.; Kawamura, K., Growth of organic aerosols by biogenic semi-volatile carbonyls in the forestal atmosphere. *Atmos. Environ.* **2003,** *37*, (15), 2045-2050.

243. Seinfeld, J. H.; Erdakos, G. B.; Asher, W. E.; Pankow, J. F., Modeling the Formation of Secondary Organic Aerosol (SOA). 2. The Predicted Effects of Relative Humidity on Aerosol Formation in the alpha-Pinene-, beta-Pinene-, Sabinene-, delta 3-Carene, and Cyclohexene-Ozone Systems. *Environ. Sci. Technol.* **2001,** *35*, (9), 1806-1817.

244. de P. Vasconcelos, L. A.; Macias, E. S.; White, W. H., Aerosol composition as a function of haze and humidity levels in the Southwestern U.S. *Atmos. Environ.* **1994,** *28*, (22), 3679-3691.

245. Poulain, L., Wu, Z., Petters, M. D., Wex, H., Hallbauer, E., Wehner, B., Massling, A., Kreidenweis, S. M., and Stratmann, F., Towards closing the gap between hygroscopic growth and CCN activation for secondary organic aerosols - Part 3: influence of the chemical composition on the hygroscopic properties and volatile fractions of aerosols. . *Atmos. Chem. Phys.* **2010,** *10*, (8), 3775-3785.

246. Volkamer, R., Ziemann, P. J., and Molina, M. J., Secondary Organic Aerosol Formation from Acetylene (C2H2): seed effect on SOA yields due to organic photochemistry in the aerosol aqueous phase. *Atmos. Chem. Phys.* **2009,** *9*, 1907-1928.

247. Varutbangkul, V.; Brechtel, F. J.; Bahreini, R.; Ng, N. L.; Keywood, M. D.; Kroll, J. H.; Flagan, R. C.; Seinfeld, J. H.; Lee, A.; Goldstein, A. H., Hygroscopicity of secondary organic aerosols formed by oxidation of cycloalkenes, monoterpenes, sesquiterpenes, and related compounds. *Atmos. Chem. Phys.* **2006,** *6*, (9), 2367-2388.

248. Couvidat, F., and C. Seigneur, Modeling secondary organic aerosol formation from isoprene oxidation under dry and humid conditions. *Atmos. Chem. Phys.* **2011,** *11*, 893–909.

249. Liggio, J.; Li, S. M.; McLaren, R., Reactive uptake of glyoxal by particulate matter. *J. Geophys. Res.-Atmos.* **2005,** *110*, (D10), D10304.

250. Jang, M.; Kamens, R. M., Atmospheric Secondary Aerosol Formation by Heterogeneous Reactions of Aldehydes in the Presence of a Sulfuric Acid Aerosol Catalyst. *Environ. Sci. Technol.* **2001,** *35*, (24), 4758-4766.

251. Jang, M.; Carroll, B.; Chandramouli, B.; Kamens, R. M., Particle Growth by Acid-Catalyzed Heterogeneous Reactions of Organic Carbonyls on Preexisting Aerosols. *Environ. Sci. Technol.* **2003,** *37*, (17), 3828-3837.

252. Axson, J. L.; Takahashi, K.; De Haan, D. O.; Vaida, V., Gas-phase water-mediated equilibrium between methylglyoxal and its geminal diol. *Proc. Nat. Acad. Sci. USA* **2010,** *107*, (15), 6687-6692.

253. Loeffler, K. W.; Koehler, C. A.; Paul, N. M.; De Haan, D. O., Oligomer Formation in Evaporating Aqueous Glyoxal and Methyl Glyoxal Solutions. *Environ. Sci. Technol.* **2006,** *40*, (20), 6318-6323.

254. Tan, Y.; Carlton, A. G.; Seitzinger, S. P.; Turpin, B. J., SOA from methylglyoxal in clouds and wet aerosols: Measurement and prediction of key products. *Atmos. Environ.* **2010,** *44*, (39), 5218-5226.

255. Fu, T. M.; Jacob, D. J.; Heald, C. L., Aqueous-phase reactive uptake of dicarbonyls as a source of organic aerosol over eastern North America. *Atmos. Environ.* **2009,** *43*, (10), 1814-1822.

256. Jayne, J. T.; Duan, S. X.; Davidovits, P.; Worsnop, D. R.; Zahniser, M. S.; Kolb, C. E., Uptake of gas-phase aldehydes by water surfaces. *J. Phys. Chem.* **1992,** *96*, (13), 5452-5460.

257. Ewing, G. E., Thin Film Water. *J. Phys. Chem. B* **2004,** *108*, (41), 15953-15961.

258. Casale, M. T.; Richman, A. R.; Elrod, M. J.; Garland, R. M.; Beaver, M. R.; Tolbert, M. A., Kinetics of acid-catalyzed aldol condensation reactions of aliphatic aldehydes. *Atm. Environ.* **2007,** *41*, (29), 6212-6224.

259. Surratt, J. D., Murphy, S.M. , Kroll, J.H., Ng, N.L., Hildebrandt, L., Sorooshian, A., Szmigielski, R., Vermeylen, R., Maenhaut, W., Claeys, M., Flagan, R.C, and Seinfeld, J.H., Chemical Composition of Secondary Organic Aerosol Formed from the Photooxidation of Isoprene. *J. Phys. Chem. A* **2006,** *110*, (31), 9665-9690.

260. Iinuma, Y.; Boge, O.; Kahnt, A.; Herrmann, H., Laboratory chamber studies on the formation of organosulfates from reactive uptake of monoterpene oxides. *Phys. Chem. Chem. Phys.* **2009,** *11*, (36), 7985-7997.

261. Ghorai, S., Laskin, A., and Tivanski, A.V. , Evidence of Keto-enol Tautomerism in Deliquesced Malonic Acid Particles. *J. Phys. Chem. A* **2011,** *115*, 4373-4380.

262. Virkkula, A.; Van Dingenen, R.; Raes, F.; Hjorth, J., Hygroscopic properties of aerosol formed by oxidation of limonene, a-pinene, and b-pinene. *J. Geophys. Res.* **1999,** *104*, (D3), 3569-3579.

263. Cruz, C. N.; Pandis, S. N., Deliquescence and Hygroscopic Growth of Mixed Inorganic-Organic Atmospheric Aerosol. *Environ. Sci. Technol.* **2000,** *34*, (20), 4313-4319.

264. Malloy, Q. G. J.; Nakao, S.; Qi, L.; Austin, R.; Stothers, C.; Hagino, H.; Cocker, D. R., Real-Time Aerosol Density Determination Utilizing a Modified Scanning Mobility Particle Sizerâ€"Aerosol Particle Mass Analyzer System. *Aerosol Sci. Technol.* **2009,** *43*, (7), 673 - 678.

265. Bahreini, R.; Keywood, M. D.; Ng, N. L.; Varutbangkul, V.; Gao, S.; Flagan, R. C.; Seinfeld, J. H.; Worsnop, D. R.; Jimenez, J. L., Measurements of Secondary Organic Aerosol from Oxidation of Cycloalkenes, Terpenes, and m-Xylene Using an Aerodyne Aerosol Mass Spectrometer. *Environ. Sci. Technol.* **2005,** *39*, (15), 5674-5688.

266. Hewitt, C. N.; Hayward, S.; Tani, A., The application of proton transfer reaction-mass spectrometry (PTR-MS) to the monitoring and analysis of volatile organic compounds in the atmosphere. *Journal of Environmental Monitoring* **2003,** *5*, (1), 1-7.

267. Moore, C. B.; Weisshaar, J. C., Formaldehyde photochemistry. *Annual Review of Physical Chemistry* **1983,** *34*, (1), 525-555.

268. Atkinson, R.; Arey, J., Atmospheric degradation of volatile organic compounds. *Chem. Rev.* **2003,** *103*, (12), 4605-4638.

269. Dibble, T. S., Prompt chemistry of alkenoxy radical products of the double H-atom transfer of alkoxy radicals from isoprene. *J. Phys. Chem. A* **2004,** *108*, (12), 2208-2215.

270. Dibble, T. S., Intramolecular hydrogen bonding and double H-atom transfer in peroxy and alkoxy radicals from isoprene. *J. Phys. Chem. A* **2004,** *108*, (12), 2199-2207.

271. Kroll J. H., N. L. N., S. M. Murphy, R. C. Flagan, and J. H. Seinfeld, Secondary organic aerosol formation from isoprene photooxidation under high-NO x conditions. *Geophys. Res. Lett.* **2005,** *32*, L18808, doi:10.1029/2005GL023637

272. Aoki, N.; Inomata, S.; Tanimoto, H., Detection of C1-C5 alkyl nitrates by proton transfer reaction time-of-flight mass spectrometry. *Int. J. Mass Spec.* **2007,** *263*, (1), 12-21.

273. Perring, A. E.; Bertram, T. H.; Wooldridge, P. J.; Fried, A.; Heikes, B. G.; Dibb, J.; Crounse, J. D.; Wennberg, P. O.; Blake, N. J.; Blake, D. R.; Brune, W. H.; Singh, H. B.; Cohen, R. C., Airborne observations of total RONO2: new constraints on the yield and lifetime of isoprene nitrates. *Atmos. Chem. Phys.* **2009,** *9*, (4).

274. Perring, A. E.; Wisthaler, A.; Graus, M.; Wooldridge, P. J.; Lockwood, A. L.; Mielke, L. H.; Shepson, P. B.; Hansel, A.; Cohen, R. C., A product study of the isoprene+NO3 reaction. *Atmos. Chem. Phys.* **2009,** *9*, (14), 4945-4956.

275. Reinhardt, A.; Emmenegger, C.; Gerrits, B.; Panse, C.; Dommen, J.; Baltensperger, U.; Zenobi, R.; Kalberer, M., Ultrahigh mass resolution and accurate mass measurements as a tool to characterize oligomers in secondary organic aerosols. *Anal. Chem.* **2007,** *79*, (11), 4074-4082.

276. Virtanen, A.; Joutsensaari, J.; Koop, T.; Kannosto, J.; Yli-Pirila, P.; Leskinen, J.; Makela, J. M.; Holopainen, J. K.; Poschl, U.; Kulmala, M.; Worsnop, D. R.; Laaksonen, A., An amorphous solid state of biogenic secondary organic aerosol particles. *Nature* **2010,** *467*, (7317), 824-827.

277. Vaden, T. D.; Imre, D.; Beranek, J.; Shrivastava, M.; Zelenyuk, A., Evaporation kinetics and phase of laboratory and ambient secondary organic aerosol. *Proc. Natl. Acad. Sci.* **2010,** *108*, (6), 2190-2195.

278. Braud, C.; Devarieux, R.; Garreau, H.; Vert, M., Capillary electrophoresis to analyze water-soluble oligo(hydroxyacids) issued from degraded or biodegraded aliphatic polyesters. *Journal of Polymers and the Environment* **1996,** *4*, (3), 135-148.

279. Yu, Q.; Nauman, S.; Santerre, J. P.; Zhu, S., Photopolymerization behavior of di(meth)acrylate oligomers. *Journal of Materials Science* **2001,** *36*, (15), 3599-3605.

280. Hori, M.; Ohta, S.; Murao, N.; Yamagata, S., Activation capability of water soluble organic substances as CCN. *Journal of Aerosol Science* **2003,** *34*, (4), 419-448.

281. King, S. M.; Rosenoern, T.; Shilling, J. E.; Chen, Q.; Wang, Z.; Biskos, G.; McKinney, K. A.; Poschl, U.; Martin, S. T., Cloud droplet activation of mixed organic-sulfate particles produced by the photooxidation of isoprene. *Atmos. Chem. Phys.* **2010,** *10*, (8), 3953-3964.

282. Gonsior, M.; Peake, B. M.; Cooper, W. T.; Podgorski, D.; D'Andrilli, J.; Cooper, W. J., Photochemically Induced Changes in Dissolved Organic Matter Identified by Ultrahigh Resolution Fourier Transform Ion Cyclotron Resonance Mass Spectrometry. *Environ. Sci. Technol.* **2009,** *43*, (3), 698-703.

283. Mazzoleni, L. R.; Ehrmann, B. M.; Shen, X.; Marshall, A. G.; Collett, J. L., Water-Soluble Atmospheric Organic Matter in Fog: Exact Masses and Chemical Formula Identification by Ultrahigh-Resolution Fourier Transform Ion Cyclotron Resonance Mass Spectrometry. *Environ. Sci. Technol.* **2010,** *44*, (10), 3690-3697.

284. Yates, J. R.; Ruse, C. I.; Nakorchevsky, A., Proteomics by Mass Spectrometry: Approaches, Advances, and Applications. In *Annu. Rev. Biomed. Eng.*, Annual Reviews: Palo Alto, 2009; Vol. 11, pp 49-79.

285. Marshall, A. G.; Rodgers, R. P., Petroleomics: The Next Grand Challenge for Chemical Analysis. *Acc. Chem. Res.* **2004,** *37*, (1), 53-59.

286. Hall, W. A.; Johnston, M. V., Oligomer Content of alpha-Pinene Secondary Organic Aerosol. *Aerosol Sci. Technol.* **2011,** *45*, (1), 37-45.

287. Ong, S.-E.; Mann, M., Mass spectrometry-based proteomics turns quantitative. *Nat Chem Biol* **2005,** *1*, (5), 252-262.

288. Selby, D. S.; Guilhaus, M.; Murby, J.; Wells, R. J., Direct quantification of alkaloid mixtures by electrospray ionization mass spectrometry. *J. Mass. Spectrom.* **1998,** *33*, (12), 1232-1236.

289. Rizzarelli, P.; Zampino, D.; Ferreri, L.; Impallomeni, G., Direct Electrospray Ionization Mass Spectrometry Quantitative Analysis of Sebacic and Terephthalic Acids in Biodegradable Polymers. *Anal. Chem.* **2011,** *83*, (3), 654-660.

290. Oss, M.; Kruve, A.; Herodes, K.; Leito, I., Electrospray Ionization Efficiency Scale of Organic Compounds. *Anal. Chem.* **2010,** *82*, (7), 2865-2872.

291. Chalcraft, K. R.; Lee, R.; Mills, C.; Britz-McKibbin, P., Virtual Quantification of Metabolites by Capillary Electrophoresis-Electrospray Ionization-Mass Spectrometry: Predicting Ionization Efficiency Without Chemical Standards. *Anal. Chem.* **2009,** *81*, (7), 2506-2515.

292. Enke, C. G., A Predictive Model for Matrix and Analyte Effects in Electrospray Ionization of Singly-Charged Ionic Analytes. *Anal. Chem.* **1997,** *69*, (23), 4885-4893.

293. Leito, I.; Herodes, K.; Huopolainen, M.; Virro, K.; Künnapas, A.; Kruve, A.; Tanner, R., Towards the electrospray ionization mass spectrometry ionization efficiency scale of organic compounds. *Rapid Commun. Mass Spectrom.* **2008,** *22*, (3), 379-384.

294. Bouchoux, G.; Djazi, F.; Houriet, R.; Rolli, E., Gas-phase basicity of olefinic C5 and C6 carbonyl compounds. *J. Org. Chem.* **1988,** *53*, (15), 3498-3501.

295. Bouchoux, G.; Salpin, J.-Y., Gas-phase basicities of polyfunctional molecules. Part 2: Saturated basic sites. *Mass Spectrom. Rev.* **2011**, 1-38.

296. Mazarin, M.; Phan, T. N. T.; Charles, L., Using solvent-free sample preparation to promote protonation of poly(ethylene oxide)s with labile end-groups in matrix-assisted laser desorption/ionisation. *Rapid Commun. Mass Spectrom.* **2008**, *22*, (23), 3776-3782.

297. Guillemin, J.-C.; Decouzon, M.; Maria, P.-C.; Gal, J.-F.; Ma, O.; Yaez, M., Gas-Phase Basicities and Acidities of Ethyl-, Vinyl-, and Ethynylarsine. An Experimental and Theoretical Study. *J. Phys. Chem. A* **1997**, *101*, (49), 9525-9530.

298. Hennion, G. F.; DiGiovanna, C. V., Sterically Crowded Amines. IV. Secondary and Tertiary Bispropargylic Amines and Their Hydrogenation Products1. *J. Org. Chem.* **1965,** *30*, (8), 2645-2650.

299. Kabli, S.; van Beelen, E. S. E.; Ingemann, S.; Henriksen, L.; Hammerum, S., The proton affinities of saturated and unsaturated heterocyclic molecules. *Int. J. Mass Spec.* **2006,** *249-250*, 370-378.

300. Bouchoux, G.; Leblanc, D.; Mo, O.; Yanez, M., Structural Effects on the Intrinsic Basicities of alpha and beta-Unsaturated Lactones and Ketones. *J. Org. Chem.* **1997,** *62*, (24), 8439-8448.

301. Wolf, R.; Grutzmacher, H. F., The proton affinities of some alpha-beta-unsaturated esters and amides. *New J. Chem.* **1990,** *14*, 379-382.

302. Collett Jr, J.; Daube Jr, B.; Munger, J. W.; Hoffmann, M. R., Cloud water chemistry in Sequoia National Park. *Atmos. Environ.* **1989,** *23*, (5), 999-1007.

303. Keene, W. C.; Galloway, J. N., Organic acidity in precipitation of North America. *Atmos. Environ.* **1984,** *18*, (11), 2491-2497.

304. Capel, P. D.; Gunde, R.; Zuercher, F.; Giger, W., Carbon speciation and surface tension of fog. *Environ. Sci. Technol.* **1990,** *24*, (5), 722-727.

305. Duffin, K. L.; Henion, J. D.; Shieh, J. J., Electrospray and tandem mass spectrometric characterization of acylglycerol mixtures that are dissolved in nonpolar solvents. *Anal. Chem.* **1991,** *63*, (17), 1781-1788.

306. Koivusalo, M.; Haimi, P.; Heikinheimo, L.; Kostiainen, R.; Somerharju, P., Quantitative determination of phospholipid compositions by ESI-MS: effects of acyl chain length, unsaturation, and lipid concentration on instrument response. *J. Lipid Res.* **2001,** *42*, (4), 663-672.

307. Ehrmann, B. M.; Henriksen, T.; Cech, N. B., Relative Importance of Basicity in the Gas Phase and in Solution for Determining Selectivity in Electrospray Ionization Mass Spectrometry. *J. Am. Soc. Mass Spectrom.* **2008,** *19*, (5), 719-728.

308. Kebarle, P.; Peschke, M., On the mechanisms by which the charged droplets produced by electrospray lead to gas phase ions. *Anal. Chim. Acta* **2000,** *406*, (1), 11-35.

309. Hunter, E. P. L.; Lias, S. G., Evaluated Gas Phase Basicities and Proton Affinities of Molecules: An Update. *J. Phys. Chem. Ref. Data* **1998,** *27*, (3), 413-656.

310. Miller, T. M., *Atomic and molecular polarizabililies*. 92 ed.; CRC Press: Boca Raton, FL., 2012.

311. Miller, K. J., Additivity methods in molecular polarizability. *J. Am. Chem. Soc.* **1990,** *112*, (23), 8533-8542.

312. Chinthaka, S.; Rodgers, M., Sodium Cation Affinities of Commonly Used MALDI Matrices Determined by Guided Ion Beam Tandem Mass Spectrometry. *J. Am. Soc. Mass Spectrom.* **2012**, 1-14.

313. Tsang, Y.; Siu, F. M.; Ho, C. S.; Ma, N. L.; Tsang, C. W., Experimental validation of theoretical potassium and sodium cation affinities of amides by mass spectrometric kinetic method measurements. *Rapid Commun. Mass Spectrom.* **2004,** *18*, (3), 345-355.

314. Rodgers, M. T.; Armentrout, P. B., Absolute Binding Energies of Sodium Ions to Short Chain Alcohols, CnH2n+2O, n = 1-4, Determined by Threshold Collision-Induced Dissociation Experiments and Ab Initio Theory. *J. Phys. Chem. A* **1999,** *103*, (25), 4955-4963.

315. Verheggen, B.; Cozic, J.; Weingartner, E.; Bower, K.; Mertes, S.; Connolly, P.; Gallagher, M.; Flynn, M.; Choularton, T.; Baltensperger, U., Aerosol partitioning between the interstitial and the condensed phase in mixed-phase clouds. *J. Geophys. Res.* **2007,** *112*, (D23), D23202; doi:10.1029/2007jd008714.

316. Henning, S.; Bojinski, S.; Diehl, K.; Ghan, S.; Nyeki, S.; Weingartner, E.; Wurzler, S.; Baltensperger, U., Aerosol partitioning in natural mixed-phase clouds. *Geophys. Res. Lett.* **2004,** *31*, (6), L06101.

317. Facchini, M. C.; Fuzzi, S.; Zappoli, S.; Andracchio, A.; Gelencsér, A.; Kiss, G.; Krivácsy, Z.; Mészáros, E.; Hansson, H.-C.; Alsberg, T.; Zebühr, Y., Partitioning of the organic aerosol component between fog droplets and interstitial air. *J. Geophys. Res.* **1999,** *104*, (D21), 26821-26832.

318. Hoose, C.; Lohmann, U.; Bennartz, R.; Croft, B.; and Lesins, G., Global simulations of aerosol processing in clouds. *Atmos. Chem. Phys.* **2008,** *8*, 6939–6963.

319. Prenni, A. J.; Petters, M. D.; Kreidenweis, S. M.; DeMott, P. J.; Ziemann, P. J., Cloud droplet activation of secondary organic aerosol. *J. Geophys. Res.* **2007,** *112*, (D10), D10223; doi:10.1029/2006JD007963.

320. Gomez, A. E.; Wortham, H.; Strekowski, R.; Zetzsch, C.; Gligorovski, S., Atmospheric photo-sensitized heterogeneous and multiphase reactions: From outdoors to indoors. *Environ. Sci. Technol.* **2012,** *46*, (4), 1955–1963.

321. Jammoul, A.; Gligorovski, S.; George, C.; D'Anna, B., Photosensitized Heterogeneous Chemistry of Ozone on Organic Films. *J. Phys. Chem. A* **2008,** *112*, (6), 1268-1276.

322. Hu, K. S.; Darer, A. I.; Elrod, M. J., Thermodynamics and kinetics of the hydrolysis of atmospherically relevant organonitrates and organosulfates. *Atmos. Chem. Phys.* **2011,** *11*, (16), 8307-8320.

323. Pruppacher, H. R.; and Jaenicke, R., The processing of water vapor and aerosols by atmospheric clouds, a global estimate. *Atmos. Res.* **1995,** *38*, (1-4), 283-295.

324. Lin, B.; and Rossow, W. B., Seasonal Variation of Liquid and Ice Water Path in Nonprecipitating Clouds over Oceans. *J. Climate* **1996,** *9*, (11), 2890-2902.

325. Rehbein, P. J. G.; Jeong, C.-H.; McGuire, M. L.; Yao, X.; Corbin, J. C.; Evans, G. J., Cloud and Fog Processing Enhanced Gas-to-Particle Partitioning of Trimethylamine. *Environ. Sci. Technol.* **2011,** *45*, (10), 4346-4352.

326. Lim, Y. B.; Tan, Y.; Perri, M. J.; Seitzinger, S. P.; Turpin, B. J., Aqueous chemistry and its role in secondary organic aerosol (SOA) formation. *Atmos. Chem. Phys.* **2010,** *10*, (21), 10521-10539.

327. Ervens, B.; Turpin, B. J.; Weber, R. J., Secondary organic aerosol formation in cloud droplets and aqueous particles (aqSOA): a review of laboratory, field and model studies. *Atmos. Chem. Phys.* **2011,** *11*, (8), 11069-11102.

328. Chang, J. L.; Thompson, J. E., Characterization of colored products formed during irradiation of aqueous solutions containing H2O2 and phenolic compounds. *Atmos. Environ.* **2010,** *44*, (4), 541-551.

329. Yao, L.; Tritscher, T.; Praplan, A. P.; DeCarlo, P. F.; Temime-Roussel, B.; Quivet, E.; Marchand, N.; Dommen, J.; Baltensperger, U.; Monod, A., Aqueous phase processing of secondary organic aerosols. *Atmos. Chem. Phys. Discuss.* **2011,** *11*, (7), 21489-21532.

330. Albinet, A.; Minero, C.; Vione, D., Phototransformation processes of 2,4-dinitrophenol, relevant to atmospheric water droplets. *Chemosphere* **2010,** *80*, (7), 753-758.

331. Lee, A. K. Y.; Zhao, R.; Gao, S. S.; Abbatt, J. P. D., Aqueous-phase OH oxidation of glyoxal: application of a novel analytical approach employing aerosol mass spectrometry and complementary off-line techniques. *J. Phys. Chem. A* **2011,** *115*, (38), 10517-10526.

332. Tan, Y.; Perri, M. J.; Seitzinger, S. P.; Turpin, B. J., Effects of Precursor Concentration and Acidic Sulfate in Aqueous Glyoxal-OH Radical Oxidation and Implications for Secondary Organic Aerosol. *Environ. Sci. Technol.* **2009,** *43*, (21), 8105-8112.

333. Carlton, A. G.; Turpin, B. J.; Altieri, K. E.; Seitzinger, S.; Reff, A.; Lim, H.-J.; Ervens, B., Atmospheric oxalic acid and SOA production from glyoxal: Results of aqueous photooxidation experiments. *Atmos. Environ.* **2007,** *41*, (35), 7588-7602.

334. Altieri, K. E.; Carlton, A. G.; Lim, H. J.; Turpin, B. J.; Seitzinger, S. P., Evidence for Oligomer Formation in Clouds: Reactions of Isoprene Oxidation Products. *Environ. Sci. Technol.* **2006,** *40*, (16), 4956-4960.

335. Guzman, M. I.; Colussi, A. J.; Hoffmann, M. R., Photoinduced Oligomerization of Aqueous Pyruvic Acid. *J. Phys. Chem. A* **2006,** *110*, (10), 3619-3626.

336. Lee, A. K. Y.; Herckes, P.; Leaitch, W. R.; Macdonald, A. M.; Abbatt, J. P. D., Aqueous OH oxidation of ambient organic aerosol and cloud water organics: Formation of highly oxidized products. *Geophys. Res. Lett.* **2011,** *38*, (11), L11805; doi:10.1029/2011gl047439.

337. Collett, J. L.; Herckes, P.; Youngster, S.; Lee, T., Processing of atmospheric organic matter by California radiation fogs. *Atmos. Res.* **2008,** *87*, (3-4), 232-241.

338. Collett, J. L.; Bator, A.; Sherman, D. E.; Moore, K. F.; Hoag, K. J.; Demoz, B. B.; Rao, X.; Reilly, J. E., The chemical composition of fogs and intercepted clouds in the United States. *Atmos. Res.* **2002,** *64*, (1-4), 29-40.

339. Cappiello, A.; De Simoni, E.; Fiorucci, C.; Mangani, F.; Palma, P.; Trufelli, H.; Decesari, S.; Facchini, M. C.; Fuzzi, S., Molecular Characterization of the Water-Soluble Organic Compounds in Fogwater by ESIMS/MS. *Environ. Sci. Technol.* **2003,** *37*, (7), 1229-1240.

340. Herckes, P.; Lee, T.; Trenary, L.; Kang, G.; Chang, H.; Collett, J. L., Organic Matter in Central California Radiation Fogs. *Environ. Sci. Technol.* **2002,** *36*, (22), 4777-4782.

341. Herckes, P.; Chang, H.; Lee, T.; Collett, J., Air Pollution Processing by Radiation Fogs. *Water Air Soil Poll.* **2007,** *181*, (1), 65-75.

342. Jacob, D. J.; Waldman, J. M.; Munger, J. W.; Hoffmann, M. R., A field investigation of physical and chemical mechanisms affecting pollutant concentrations in fog droplets. *Tellus B* **1984,** *36B*, (4), 272-285.

343. Fuzzi, S.; Facchini, M. C.; Decesari, S.; Matta, E.; Mircea, M., Soluble organic compounds in fog and cloud droplets: what have we learned over the past few years? *Atmos. Res.* **2002,** *64*, (1-4), 89-98.

344. Fisak, J.; Tesar, M.; Rezacova, D.; Elias, V.; Weignerova, V.; Fottova, D., Pollutant concentrations in fog and low cloud water at selected sites of the Czech Republic. *Atmos. Res.* **2002,** *64*, (1-4), 75-87.

345. Zepp, R. G.; Hoigne, J.; Bader, H., Nitrate-induced photooxidation of trace organic chemicals in water. *Environ. Sci. Technol.* **1987,** *21*, (5), 443-450.

346. Torrents, A.; Anderson, B. G.; Bilboulian, S.; Johnson, W. E.; Hapeman, C. J., Atrazine Photolysis:Mechanistic Investigations of Direct and Nitrate-Mediated Hydroxy Radical Processes and the Influence of Dissolved Organic Carbon from the Chesapeake Bay. *Environ. Sci. Technol.* **1997,** *31*, (5), 1476-1482.

347. Talukdar, R. K.; Burkholder, J. B.; Hunter, M.; Gilles, M. K.; Roberts, J. M.; Ravishankara, A. R., Atmospheric fate of several alkyl nitrates. Part 2. UV absorption cross-sections and photodissociation quantum yields. *J. Chem. Soc., Faraday Trans.* **1997,** *93*, (16), 2797-2805.

348. Roberts, J. M.; Fajer, R. W., UV absorption cross sections of organic nitrates of potential atmospheric importance and estimation of atmospheric lifetimes. *Environ. Sci. Technol.* **1989,** *23*, (8), 945-951.

349. Barnes, I.; Becker, K. H.; Zhu, T., Near UV absorption spectra and photolysis products of difunctional organic nitrates: possible importance as NOx reservoirs. *J. Atmos. Chem.* **1993,** *17*, (4), 353-73.

350. Luke, W. T.; Dickerson, R. R.; Nunnermacker, L. J., Direct Measurements of the Photolysis Rate Coefficients and Henry's Law Constants of Several Alkyl Nitrates. *J. Geophys. Res.* **1989,** *94*, (D12), 14905-14921.

351. Volkamer, R.; Spietz, P.; Burrows, J.; Platt, U., High-resolution absorption cross-section of glyoxal in the UV-vis and IR spectral ranges. *J. Photochem. Photobiol., A* **2005,** *172*, (1), 35-46.

352. Bacher, C.; Tyndall, G. S.; Orlando, J. J., The Atmospheric Chemistry of Glycolaldehyde. *J. Atmos. Chem.* **2001,** *39*, (2), 171-189.

353. Chen, Y. Q.; Wang, W. J.; Zhu, L., Wavelength-dependent photolysis of methylglyoxal in the 290-440 nm region. *J. Phys. Chem. A* **2000,** *104*, (47), 11126-11131.

354. Chen, Y. Q.; Zhu, L., Wavelength-dependent photolysis of glyoxal in the 290-420 nm region. *J. Phys. Chem. A* **2003,** *107*, (23), 4643-4651.

355. Horowitz, A.; Meller, R.; Moortgat, G. K., The UV-VIS absorption cross sections of the alpha-dicarbonyl compounds: Pyruvic acid, biacetyl and glyoxal. *J. Photochem. Photobiol., A* **2001,** *146*, (1-2), 19-27.

356. Calvert, J. G.; Pitts, J. N., *Photochemistry*. John Wiley & Sons: New York-London-Sydney, 1966, 899 pp; p 899

357. Sun, Y. L.; Zhang, Q.; Anastasio, C.; Sun, J., Insights into secondary organic aerosol formed via aqueous-phase reactions of phenolic compounds based on high resolution mass spectrometry. *Atmos. Chem. Phys.* **2010,** *10*, (10), 4809-4822.

358. Bateman, A. P.; Nizkorodov, S. A.; Laskin, J.; Laskin, A., Photolytic processing of secondary organic aerosols dissolved in cloud droplets. *Phys. Chem. Chem. Phys.* **2011,** *13*, (26), 12199-12212.

359. Monod, A.; Chevallier, E.; Durand, J. R.; Doussin, J. F.; Picquet-Varrault, B.; Carlier, P., Photooxidation of methylhydroperoxide and ethylhydroperoxide in the aqueous phase under simulated cloud droplet conditions. *Atmos. Environ.* **2007,** *41*, (11), 2412-2426.

360. Ervens, B.; Gligorovski, S.; Herrmann, H., Temperature-dependent rate constants for hydroxyl radical reactions with organic compounds in aqueous solutions. *Phys. Chem. Chem. Phys.* **2003,** *5*, (9), 1811-1824.

361. Anastasio, C.; McGregor, K. G., Chemistry of fog waters in California's Central Valley: 1. In situ photoformation of hydroxyl radical and singlet molecular oxygen. *Atmos. Environ.* **2001,** *35*, (6), 1079-1089.

362. Ervens, B.; George, C.; Williams, J. E.; Buxton, G. V.; Salmon, G. A.; Bydder, M.; Wilkinson, F.; Dentener, F.; Mirabel, P.; Wolke, R.; Herrmann, H., CAPRAM 2.4 (MODAC mechanism): An extended and condensed tropospheric aqueous phase mechanism and its application. *J. Geophys. Res.* **2003,** *108*, (D14), 4426.

363. Jacob, D. J., Chemistry of OH in Remote Clouds and Its Role in the Production of Formic Acid and Peroxymonosulfate. *J. Geophys. Res.* **1986,** *91*, (D9), 9807-9826.

364. Fuentes, J. D.; Lerdau, M.; Atkinson, R.; Baldocchi, D.; Bottenheim, J. W.; Ciccioli, P.; Lamb, B.; Geron, C.; Gu, L.; Guenther, A.; Sharkey, T. D.; Stockwell, W., Biogenic hydrocarbons in the atmospheric boundary layer: A review. *Bull. Am. Meterol. Soc.* **2000,** *81*, (7), 1537-1575.

365. Guenther, A.; Karl, T.; Harley, P.; Wiedinmyer, C.; Palmer, P. I.; Geron, C., Estimates of global terrestrial isoprene emissions using MEGAN (Model of Emissions of Gases and Aerosols from Nature). *Atmos. Chem. Phys.* **2006,** *6*, 3181-3210.

366. Tie, X.; Madronich, S.; Walters, S.; Zhang, R.; Rasch, P.; Collins, W., Effect of clouds on photolysis and oxidants in the troposphere. *J. Geophys. Res.* **2003,** *108*, (D20), 4642; doi:10.1029/2003JD003659

367. Docherty, K. S.; Wu, W.; Lim, Y. B.; Ziemann, P. J., Contributions of Organic Peroxides to Secondary Aerosol Formed from Reactions of Monoterpenes with O3. *Environ. Sci. Technol.* **2005,** *39*, (11), 4049-4059.

368. Brinkmann, T.; Horsch, P.; Sartorius, D.; Frimmel, F. H., Photoformation of low-molecular-weight organic acids from brown water dissolved organic matter. *Environ. Sci. Technol.* **2003,** *37*, (18), 4190-4198.

369. Kujawinski, E. B.; Del Vecchio, R.; Blough, N. V.; Klein, G. C.; Marshall, A. G., Probing molecular-level transformations of dissolved organic matter: insights on photochemical degradation and protozoan modification of DOM from electrospray ionization Fourier transform ion cyclotron resonance mass spectrometry. *Mar. Chem.* **2004,** *92*, (1-4), 23-37.

370. Aiken, A. C.; Salcedo, D.; Cubison, M. J.; Huffman, J. A.; DeCarlo, P. F.; Ulbrich, I. M.; Docherty, K. S.; Sueper, D.; Kimmel, J. R.; Worsnop, D. R.; Trimborn, A.; Northway, M.; Stone, E. A.; Schauer, J. J.; Volkamer, R. M.; Fortner, E.; de Foy, B.; Wang, J.; Laskin, A.; Shutthanandan, V.; Zheng, J.; Zhang, R.; Gaffney, J.; Marley, N. A.; Paredes-Miranda, G.; Arnott, W. P.; Molina, L. T.; Sosa, G.; Jimenez, J. L., Mexico City aerosol analysis during MILAGRO using high resolution aerosol mass spectrometry at the urban supersite (T0) - Part 1: Fine particle composition and organic source apportionment. *Atmos. Chem. Phys.* **2009,** *9*, (17), 6633-6653.

371. Sun, Y. L.; Zhang, Q.; Schwab, J. J.; Demerjian, K. L.; Chen, W. N.; Bae, M. S.; Hung, H. M.; Hogrefe, O.; Frank, B.; Rattigan, O. V.; Lin, Y. C., Characterization of the sources and processes of organic and inorganic aerosols in New York city with a high-resolution time-of-flight aerosol mass apectrometer. *Atmos. Chem. Phys.* **2011,** *11*, (4), 1581-1602.

372. Kautzman, K. E.; Surratt, J. D.; Chan, M. N.; Chan, A. W. H.; Hersey, S. P.; Chhabra, P. S.; Dalleska, N. F.; Wennberg, P. O.; Flagan, R. C.; Seinfeld, J. H., Chemical Composition of Gas- and Aerosol-Phase Products from the Photooxidation of Naphthalene. *J. Phys. Chem. A* **2009,** *114*, (2), 913-934.

373. Roberts, J. M., The atmospheric chemistry of organic nitrates. *Atmos. Environ.* **1990,** *24*, (2), 243-287.

374. Kaufman, J. V. R.; Picard, J. P., The Furoxans. *Chem. Rev.* **1959,** *59*, (3), 429-461.

375. Kingston, D. G. I.; Hobrock, B. W.; Bursey, M. M.; Bursey, J. T., Intramolecular hydrogen transfer in mass spectra. III. Rearrangements involving the loss of small neutral molecules. *Chem. Rev.* **1975,** *75*, (6), 693-730.

376. Rebbert, R. E., Primary processes in the photolysis of ethyl nitrate. *J. Phys. Chem.* **1963,** *67*, (9), 1923-1925.

377. Gray, J. A.; Style, D. W. G., The photolysis of ethyl nitrate. *Trans. Faraday Soc.* **1953,** *49*, 52-57.

378. Vandaele, A. C.; Hermans, C.; Simon, P. C.; Carleer, M.; Colin, R.; Fally, S.; Merienne, M. F.; Jenouvrier, A.; Coquart, B., Measurements of the NO2 absorption cross-section from 42 000 cm-1 to 10 000 cm-1 (238-1000 nm) at 220 K and 294 K. *J. Quant. Spectros. Radiat. Transfer* **1998,** *59*, (3-5), 171-184.

379. Schneider, W.; Moortgat, G. K.; Tyndall, G. S.; Burrows, J. P., Absorption cross-sections of NO2 in the UV and visible region (200- 700 nm) at 298 K. *J. Photochem. Photobiol., A* **1987,** *40*, (2-3), 195-217.

380. Troe, J., Are Primary Quantum Yields of NO2 Photolysis at 398 nm Smaller than Unity? *Z. Phys. Chem.* **2000,** *214*, (5), 573-581.

381. Huie, R. E., The reaction kinetics of NO2. *Toxicology* **1994,** *89*, (3), 193-216.

382. Lee, Y. N.; Schwartz, S. E., Reaction kinetics of nitrogen dioxide with liquid water at low partial pressure. *J. Phys. Chem.* **1981,** *85*, (7), 840-848.

383. Lewis, R. S.; Deen, W. M., Kinetics of the Reaction of Nitric Oxide with Oxygen in Aqueous Solutions. *Chem. Res. Toxicol.* **1994,** *7*, (4), 568-574.

384. Williams, D. H. L., *Nitrosation*. Cambridge University Press: Cambridge, U.K. , 1988, 214 pp.

385. Wink, D. A.; Darbyshire, J. F.; Nims, R. W.; Saavedra, J. E.; Ford, P. C., Reactions of the bioregulatory agent nitric oxide in oxygenated aqueous media: Determination of the kinetics for oxidation and nitrosation by intermediates generated in the nitric oxide/oxygen reaction. *Chem. Res. Toxicol.* **1993,** *6*, (1), 23-27.

386. Umstead, M. E.; Lloyd, S. A.; Fleming, J. W.; Lin, M. C., Laser-induced reactions of NO2 in the visible region: I. Kinetic Modeling of Nitrobutane Formation

in the NO2-Isobutane System. *Appl. Phys. B: Lasers O.* **1985,** *38*, (4), 219-224.

387. Umstead, M. E.; Lin, M. C., Laser-induced reactions of NO2 in the visible region: III. Adamantane Nitration in the Liquid Phase. *Appl. Phys. B: Lasers O.* **1986,** *39*, (1), 61-63.

388. Demir, A. S.; Findik, H., The Reaction of Alkenes with AgNO2/TMSCL: The Synthesis of Oxadiazole-2-Oxides (Furoxans) Via Nitroso Nitrates. *Lett. Org. Chem.* **2005,** *2*, (7), 602-604.

389. Velazquez, C.; Rao, P. N. P.; McDonald, R.; Knaus, E. E., Synthesis and biological evaluation of 3,4-diphenyl-1,2,5-oxadiazole-2-oxides and 3,4-diphenyl-1,2,5-oxadiazoles as potential hybrid COX-2 inhibitor/nitric oxide donor agents. *Bioorg. Med. Chem.* **2005,** *13*, (8), 2749-2757.

390. Napolitano, A.; d'Ischia, M., New Insights into the Acid-Promoted Reaction of Caffeic Acid and Its Esters with Nitrite:Decarboxylation Drives Chain Nitrosation Pathways toward Novel Oxime Derivatives and Oxidation/Fragmentation Products Thereof. *J. Org. Chem.* **2002,** *67*, (3), 803-810.

391. Calvino, R.; Ferrarotti, B.; Serafino, A.; Gasco, A., Unsymmetrically substituted furoxans. 10. Acetylmethylfuroxans. *Heterocycles* **1985,** *23*, (8), 1955-60.

392. Nirode, W. F.; Luis, J. M.; Wicker, J. F.; Wachter, N. M., Synthesis and evaluation of NO-release from symmetrically substituted furoxans. *Bioinorg. Med. Chem. Lett.* **2006,** *16*, (8), 2299-2301.

393. Boule, P.; Bahnemann, D. W.; Robertson, P. K., *Environmental photochemistry*. Springer-Verlag: Berlin Heidelberg, 1999, 365 pp; p 365.

394. Cerecetto, H.; Gonzalez, M.; Khan, M., Benzofuroxan and furoxan. Chemistry and biology of bioactive heterocycles IV. In Springer Berlin / Heidelberg: 2007; Vol. 10, pp 265-308.

395. Hacker, N. P., Benzofuroxan photochemistry: direct observation of 1,2-dinitrosobenzene by steady state spectroscopy. A new photochromic reaction. *J. Org. Chem.* **1991,** *56*, (17), 5216-5217.

396. Murata, S.; Tomioka, H., Photochemistry of o-Nitrophenylazide in Matrices. The First Direct Spectroscopic Observation of o-Dinitrosobenzene. *Chem. Lett.* **1992,** *21*, (1), 57-60.

397. Himmel, H.-J. r.; Konrad, S.; Friedrichsen, W.; Rauhut, G., First Identification of an Aliphatic cis-Dinitroso Compound: A Combined Experimental and Quantum Chemical Study. *J. Phys. Chem. A* **2003,** *107*, (34), 6731-6737.

398. Kanakidou, M.; Seinfeld, J. H.; Pandis, S. N.; Barnes, I.; Dentener, F. J.; Facchini, M. C.; Van Dingenen, R.; Ervens, B.; Nenes, A.; Nielsen, C. J.; Swietlicki, E.; Putaud, J. P.; Balkanski, Y.; Fuzzi, S.; Horth, J.; Moortgat, G. K.; Winterhalter, R.; Myhre, C. E. L.; Tsigaridis, K.; Vignati, E.; Stephanou, E. G.; Wilson, J., Organic aerosol and global climate modelling: a review. *Atm. Chem. Phys.* **2005,** *5*, (4), 1053-1123.

399. Hartz, K. E. H.; Rosenoeron, T.; Ferchak, S. R.; Raymond, T. M.; Bilde, M.; Donahue, N. M.; Pandis, S. N., Cloud condensation nuclei activation of monoterpene and sesquiterpene secondary organic aerosol. *J. Geophys. Res. D* **2005,** *110*, (D14), D14208, doi:10.1029/2004JD005754.

400. van Reken, T. M.; Ng, N. L.; Flagan, R. C.; Seinfeld, J. H., Cloud condensation nucleus activation properties of biogenic secondary organic aerosol. *J. Geophys. Res. D* **2005,** *110*, (D7), D07206, doi:10.1029/2004JD005465.

401. Engelhart, G. J.; Asa-Awuku, A.; Nenes, A.; Pandis, S. N., CCN activity and droplet growth kinetics of fresh and aged monoterpene secondary organic aerosol. *Atmos. Chem. Phys.* **2008,** *8*, (14), 3937-3949.

402. Ervens, B.; Feingold, G.; Kreidenweis, S. M., Influence of water-soluble organic carbon on cloud drop number concentration. *J. Geophys. Res. D* **2005,** *110*, (D18), D18211, doi:10.1029/2004JD005634.

403. Roesler, E. L.; Penner, J. E., Can global models ignore the chemical composition of aerosols? *Geophys. Res. Lett.* **2010,** *37*, (24), L24809, doi:10.1029/2010GL044282.

404. Seinfeld, J. H.; Pandis, S. N., *Atmospheric Chemistry and Physics: From Air Pollution to Climate Change*. John Wiley & Sons, Inc.: New York, 1998; p 1326 pp.

405. Facchini, M. C.; Fuzzi, S.; Zappoli, S.; Andracchio, A.; Gelencser, A.; Kiss, G.; Krivacsy, Z.; Meszaros, E.; Hansson, H.-C.; Alsberg, T.; Zebuhr, Y., Partitioning of the organic aerosol component between fog droplets and interstitial air. *J. Geophys. Res. D* **1999,** *104*, (D21), 26821-26832.

406. Limbeck, A.; Paxbaum, H., Dependence of in-cloud scavenging of polar organic aerosol compounds on the water solubility. *J. Geophys. Res. D* **2000,** *105*, (D15), 19857-19867.

407. Carlton, A. G.; Turpin, B. J.; Altieri, K. E.; Seitzinger, S. P.; Mathur, R.; Roselle, S. J.; Weber, R. J., CMAQ model performance enhanced when in-cloud secondary organic aerosol is included: comparisons of organic carbon predictions with measurements. *Environ. Sci. Technol.* **2008,** *42*, (23), 8798-8802.

408. Huang, X. H. H.; Ip, H. S. S.; Yu, J. Z., Secondary organic aerosol formation from ethylene in the urban atmosphere of Hong Kong: a multiphase chemical modeling study. *J. Geophys. Res. D* **2011,** *116*, (D3), D03206, doi:10.1029/2010JD014121.

409. Pruppacher, H. R.; Klett, J. D., *Microphysics of Clouds and Precipitation*. 2nd edition ed.; Kluwer Academic: Boston, USA, 1997; Vol. 18, p 976.

410. Bator, A.; Collett, J. L., Jr., Cloud chemistry varies with drop size. *J. Geophys. Res. D* **1997,** *102*, (D23), 28071-28078.

411. Chate, D. M.; Devara, P. C. S., Acidity of raindrop by uptake of gases and aerosol pollutants. *Atm. Environ.* **2009,** *43*, (8), 1571-1577.

412. Barth, M. C., The importance of cloud drop representation on cloud photochemistry. *Atmos. Res.* **2006,** *82*, (1-2), 294-309.

413. Collett, J. L.; Bator, A.; Sherman, D. E.; Moore, K. F.; Hoag, K. J.; Demoz, B. B.; Rao, X.; Reilly, J. E., The chemical composition of fogs and intercepted clouds in the United States. *Atmos. Res.* **2002,** *64*, (1), 29-40.

414. Mancinelli, V.; Decesari, S.; Facchini, M. C.; Fuzzi, S.; Mangani, F., Partitioning of metals between the aqueous phase and suspended insoluble material in fog droplets. *Ann Chim* **2005,** *95*, (5), 275-90.

415. Waldman, J. M.; Munger, J. W.; Jacob, D. J.; Flagan, R. C.; Morgan, J. J.; Hoffmann, M. R., Chemical composition of acid fog. *Science* **1982,** *218*, (4573), 677-680.

416. Capel, P. D.; Gunde, R.; Zuercher, F.; Giger, W., Carbon speciation and surface tension of fog. *Environ. Sci. Technol.* **1990,** *24*, (5), 722-727.

417. Joos, F.; Baltensperger, U., A field study on chemistry, S(IV) oxidation rates and vertical transport during fog conditions. *Atm. Environ. A* **1991,** *25*, (2), 217-230.

418. Hoose, C.; Lohmann, U.; Bennartz, R.; Croft, B.; Lesins, G., Global simulations of aerosol processing in clouds. *Atm. Chem. Phys.* **2008,** *8*, (23), 6939-6963.

419. Pruppacher, H. R.; Jaenicke, R., The processing of water vapor and aerosols by atmospheric clouds, a global estimate. *Atmos. Res.* **1995,** *38*, (1-4), 283-295.

420. Rosenfeld, D.; Mintz, Y., Evaporation of rain falling from convective clouds as derived from radar measurements. *Journal of Applied Meteorology* **1988,** *27*, 209-215.

421. Lin, B.; Rossow, W. B., Seasonal variation of liquid and ice water path in nonprecipitating clouds over oceans. *Journal of Climate* **1996,** *9*, (11), 2890-2902.

422. De Haan, D. O.; Corrigan, A. L.; Tolbert, M. A.; Jimenez, J. L.; Wood, S. E.; Turley, J. J., Secondary organic aerosol formation by self-reactions of methylglyoxal and glyoxal in evaporating droplets. *Environ. Sci. Technol.* **2009,** *43*, (21), 8184-8190.

423. Bones, D. L.; Henricksen, D. K.; Mang, S. A.; Gonsior, M.; Bateman, A. P.; Nguyen, T. B.; Cooper, W. J.; Nizkorodov, S. A., Appearance of strong absorbers and fluorophores in limonene-O_3 secondary organic aerosol due to NH_4^+-mediated chemical aging over long time scales. *J. Geophys. Res. D* **2010,** *115*, (D5), D05203, doi:10.1029/2009JD012864.

424. Rizzi, G. P., Chemical structure of colored Maillard reaction products. *Food Rev. Int.* **1997,** *13*, (1), 1-28.

425. Trainic, M.; Abo Riziq, A.; Lavi, A.; Flores, J. M.; Rudich, Y., The optical, physical and chemical properties of the products of glyoxal uptake on ammonium sulfate seed aerosols. *Atm. Chem. Phys.* **2011,** *11*, (18), 9697-9707.

426. De Haan, D. O.; Corrigan, A. L.; Smith, K. W.; Stroik, D. R.; Turley, J. J.; Lee, F. E.; Tolbert, M. A.; Jimenez, J. L.; Cordova, K. E.; Ferrell, G. R., Secondary organic aerosol-forming reactions of glyoxal with amino acids. *Environ. Sci. Technol.* **2009,** *43*, (8), 2818-2824.

427. Galloway, M. M.; Chhabra, P. S.; Chan, A. W. H.; Surratt, J. D.; Flagan, R. C.; Seinfeld, J. H.; Keutsch, F. N., Glyoxal uptake on ammonium sulphate seed aerosol: reaction products and reversibility of uptake under dark and irradiated conditions. *Atm. Chem. Phys.* **2009,** *9*, (10), 3331-3345.

428. Yu, G.; Bayer, A. R.; Galloway, M. M.; Korshavn, K. J.; Fry, C. G.; Keutsch, F. N., Glyoxal in aqueous ammonium sulfate solutions: products, kinetics and hydration effects. *Environ. Sci. Technol.* **2011,** *45*, (15), 6336-6342.

429. Rincon, A. G.; Guzman, M. I.; Hoffmann, M. R.; Colussi, A. J., Optical absorptivity versus molecular composition of model organic aerosol matter. *J. Phys. Chem. A* **2009,** *113*, (39), 10512-10520.

430. Jaoui, M.; Edney, E. O.; Kleindienst, T. E.; Lewandowski, M.; Offenberg, J. H.; Surratt, J. D.; Seinfeld, J. H., Formation of secondary organic aerosol from irradiated a-pinene/toluene/NO_x mixtures and the effect of isoprene and sulfur dioxide. *J. Geophys. Res. D* **2008,** *113*, (D9), D09303, doi:10.1029/2007JD009426.

431.   Noziere, B.; Esteve, W., Light-absorbing aldol condensation products in acidic aerosols: Spectra, kinetics, and contribution to the absorption index. *Atmos. Environ.* **2007,** *41*, (6), 1150-1163.

432.   Noziere, B.; Voisin, D.; Longfellow, C. A.; Friedli, H.; Henry, B. E.; Hanson, D. R., The Uptake of methyl vinyl ketone, methacrolein, and 2-methyl-3-butene-2-ol onto sulfuric acid solutions. *J. Phys. Chem. A* **2006,** *110*, (7), 2387-2395.

433.   Zhao, J.; Levitt, N. P.; Zhang, R., Heterogeneous chemistry of octanal and 2,4-hexadienal with sulfuric acid. *Geophys. Res. Lett.* **2005,** *32*, (9), L09802, doi 10.1029/2004GL022200.

434.   Noziere, B.; Esteve, W., Organic reactions increasing the absorption index of atmospheric sulfuric acid aerosols. *Geophys. Res. Lett.* **2005,** *32*, (3), L03812, doi:10.1029/2004GL021942.

435.   Esteve, W.; Noziere, B., Uptake and reaction kinetics of acetone, 2-butanone, 2,4-pentanedione, and acetaldehyde in sulfuric acid solutions. *J. Phys. Chem. A* **2005,** *109*, (48), 10920-10928.

436.   Garland, R. M.; Elrod, M. J.; Kincaid, K.; Beaver, M. R.; Jimenez, J. L.; Tolbert, M. A., Acid-catalyzed reactions of hexanal on sulfuric acid particles: Identification of reaction products. *Atm. Environ.* **2006,** *40*, (35), 6863-6878.

437.   Gelencser, A.; Hoffer, A.; Kiss, G.; Tombacz, E.; Kurdi, R.; Bencze, L., In-situ formation of light-absorbing organic matter in cloud water. *J. Atm. Chem.* **2003,** *45*, (1), 25-33.

438.   Maksymiuk, C. S.; Gayahtri, C.; Gil, R. R.; Donahue, N. M., Secondary organic aerosol formation from multiphase oxidation of limonene by ozone: mechanistic constraints via two-dimensional heteronuclear NMR spectroscopy. *Phys. Chem. Chem. Phys.* **2009,** *11*, (36), 7810-7818.

439.   Dziedzic, P.; Bartoszewicz, A.; Cordova, A., Inorganic ammonium salts as catalysts for direct aldol reactions in the presence of water. *Tetrahedron Lett.* **2009,** *50*, (52), 7242-7245.

440.   Noziere, B.; Dziedzic, P.; Cordova, A., Inorganic ammonium salts and carbonate salts are efficient catalysts for aldol condensation in atmospheric aerosols. *Phys. Chem. Chem. Phys.* **2010,** *12*, (15), 3864-3872.

441.   Noziere, B.; Dziedzic, P.; Cordova, A., Products and kinetics of the liquid-phase reaction of glyoxal catalyzed by ammonium ions (NH_4^+). *J. Phys. Chem. A* **2009,** *113*, (1), 231-237.

442.   Chelf, J. H.; Martin, S. T., Water activity and equilibrium freezing temperatures of aqueous NH_4HSO_4 solutions from -30 to 25°C. *Geophys. Res. Lett.* **1999,** *26*, (15), 2391–2394, doi:10.1029/1999GL900436.

443. Martin, S. T., Phase Transitions of Aqueous Atmospheric Particles. *Chem. Rev.* **2000,** *100*, (9), 3403-3453.

444. Noziere, B.; Dziedzic, P.; Cordova, A., Formation of secondary light-absorbing "fulvic-like" oligomers: a common process in aqueous and ionic atmospheric particles? *Geophys. Res. Lett.* **2007,** *34*, (21), L21812, doi:10.1029/2007GL031300.

445. Schmitt-Kopplin, P.; Gelencser, A.; Dabek-Zlotorzynska, E.; Kiss, G.; Hertkorn, N.; Harir, M.; Hong, Y.; Gebefugi, I., Analysis of the unresolved organic fraction in atmospheric aerosols with ultrahigh-resolution mass spectrometry and nuclear magnetic resonance spectroscopy: organosulfates as photochemical smog constituents. *Analyt. Chem.* **2010,** *82*, (19), 8017-8026.

446. Chan, M. N.; Surratt, J. D.; Claeys, M.; Edgerton, E. S.; Tanner, R. L.; Shaw, S. L.; Zheng, M.; Knipping, E. M.; Eddingsaas, N. C.; Wennberg, P. O.; Seinfeld, J. H., Characterization and quantification of isoprene-derived epoxydiols in ambient aerosol in the Southeastern United States. *Environ. Sci. Technol.* **2010,** *44*, (12), 4590-4596.

447. Reemtsma, T.; These, A.; Venkatachari, P.; Xia, X.; Hopke, P. K.; Springer, A.; Linscheid, M., Identification of fulvic acids and sulfated and nitrated analogues in atmospheric aerosol by electrospray ionization Fourier transform ion cyclotron resonance mass spectrometry. *Analyt. Chem.* **2006,** *78*, (24), 8299-8304.

448. Surratt, J. D.; Kroll, J. H.; Kleindienst, T. E.; Edney, E. O.; Claeys, M.; Sorooshian, A.; Ng, N. L.; Offenberg, J. H.; Lewandowski, M.; Jaoui, M.; Flagan, R. C.; Seinfeld, J. H., Evidence for organosulfates in secondary organic aerosol. *Environ. Sci. Technol.* **2007,** *41*, (2), 517-527.

449. Gomez-Gonzalez, Y.; Surratt, J. D.; Cuyckens, F.; Szmigielski, R.; Vermeylen, R.; Jaoui, M.; Lewandowski, M.; Offenberg, J. H.; Kleindienst, T. E.; Edney, E. O.; Blockhuys, F.; Van Alsenoy, C.; Maenhaut, W.; Claeys, M., Characterization of organosulfates from the photooxidation of isoprene and unsaturated fatty acids in ambient aerosol using liquid chromatography/(-) electrospray ionization mass spectrometry. *J. Mass Spectrom.* **2008,** *43*, (3), 371-382.

450. Hawkins, L. N.; Russell, L. M.; Covert, D. S.; Quinn, P. K.; Bates, T. S., Carboxylic acids, sulfates, and organosulfates in processed continental organic aerosol over the southeast Pacific Ocean during VOCALS-REx 2008. *J. Geophys. Res. D* **2010,** *115*, (D13), D13201, doi:10.1029/2009JD013276.

451. Liggio, J.; Li, S.-M., Organosulfate formation during the uptake of pinonaldehyde on acidic sulfate aerosols. *Geophys. Res. Lett.* **2006,** *33*, (13), L13808, doi:10.1029/2006GL026079.

452. Iinuma, Y.; Mueller, C.; Berndt, T.; Boege, O.; Claeys, M.; Herrmann, H., Evidence for the existence of organosulfates from beta -pinene ozonolysis in ambient secondary organic aerosol. *Environ. Sci. Technol.* **2007,** *41*, (19), 6678-6683.

453. Iinuma, Y.; Boege, O.; Kahnt, A.; Herrmann, H., Laboratory chamber studies on the formation of organosulfates from reactive uptake of monoterpene oxides. *Phys. Chem. Chem. Phys.* **2009,** *11*, (36), 7985-7997.

454. Iinuma, Y.; Mueller, C.; Boege, O.; Gnauk, T.; Herrmann, H., The formation of organic sulfate esters in the limonene ozonolysis secondary organic aerosol (SOA) under acidic conditions. *Atmos. Environ.* **2007,** *41*, (27), 5571-5583.

455. Noziere, B.; Ekström, S.; Alsberg, T.; Holmström, S., Radical-initiated formation of organosulfates and surfactants in atmospheric aerosols. *Geophys. Res. Lett.* **2010,** *37*, (5), L05806, doi:10.1029/2009GL041683.

456. Darer, A. I.; Cole-Filipiak, N. C.; O'Connor, A. E.; Elrod, M. J., Formation and stability of atmospherically relevant isoprene-derived organosulfates and organonitrates. *Environ. Sci. Technol.* **2011,** *45*, (5), 1895-1902.

457. Minerath, E. C.; Elrod, M. J., Assessing the potential for diol and hydroxy sulfate ester formation from the reaction of epoxides in tropospheric aerosols. *Environ. Sci. Technol.* **2009,** *43*, (5), 1386-1392.

458. Minerath, E. C.; Casale, M. T.; Elrod, M. J., Kinetics feasibility study of alcohol sulfate esterification reactions in tropospheric aerosols. *Environ. Sci. Technol.* **2008,** *42*, (12), 4410-4415.

459. Ghorai, S.; Laskin, A.; Tivanski, A. V., Spectroscopic evidence of keto-enol tautomerism in deliquesced malonic acid particles. *J. Phys. Chem. A* **2011,** *115*, (17), 4373-4380.

460. Bateman, A. P.; Nizkorodov, S. A.; Laskin, J.; Laskin, A., High-resolution electrospray ionization mass spectrometry analysis of water-soluble organic aerosols collected with a particle into liquid sampler. *Analyt. Chem.* **2010,** *82*, (19), 8010-8016.

461. Pratt, K. A.; Prather, K. A., Mass spectrometry of atmospheric aerosols—recent developments and applications. Part II: On-line mass spectrometry techniques. *Mass Spectrom. Rev.* **2011**, n/a-n/a.

462. Noble, C. A.; Prather, K. A., Real-time single particle mass spectrometry: A historical review of a quarter century of the chemical analysis of aerosols. *Mass Spectrom. Rev.* **2000,** *19*, (4), 248-274.

463. Zahardis, J.; Geddes, S.; Petrucci, G. A., Improved Understanding of Atmospheric Organic Aerosols via Innovations in Soft Ionization Aerosol Mass Spectrometry. *Analyt. Chem.* **2011,** *83*, (7), 2409-2415.

464. Gioda, A.; Reyes-Rodríguez, G. J.; Santos-Figueroa, G.; Collett, J. L., Jr.; Decesari, S.; Ramos, M. d. C. K. V.; Bezerra Netto, H. J. C.; de Aquino Neto, F. R.; Mayol-Bracero, O. L., Speciation of water-soluble inorganic, organic, and total nitrogen in a background marine environment: cloud water, rainwater, and aerosol particles. *J. Geophys. Res. D* **2011,** *116*, (D5), D05203, doi:10.1029/2010JD015010.

465.   Debus, H., Ueber die einwirkung des ammoniaks auf glyoxal. *Justus Liebigs Annalen der Chemie* **1858,** *107*, (2), 199-208.

466.   Zhukovsky, E.; Oprian, D., Effect of carboxylic acid side chains on the absorption maximum of visual pigments. *Science* **1989,** *246*, (4932), 928-930.

467.   Binder, C. M.; Dixon, D. D.; Almaraz, E.; Tius, M. A.; Singaram, B., A simple procedure for C=C bond cleavage of aromatic and aliphatic epoxides with aqueous sodium periodate under ambient conditions. *Tetrahedron Letters* **2008,** *49*, (17), 2764-2767.

468.   Liu, S.-T.; Reddy, K. V.; Lai, R.-Y., Oxidative cleavage of alkenes catalyzed by a water/organic soluble manganese porphyrin complex. *Tetrahedron* **2007,** *63*, (8), 1821-1825.

469.   Griesbaum, K.; Dong, Y.; McCullough, K. J., Ozonolyses of Acetylenes: Trapping of a-Oxo Carbonyl Oxides by Carbonyl Compounds and Stabilization of a-Oxo Ozonides by Derivatizations. *J. Org. Chem.* **1997,** *62*, (18), 6129-6136.

470.   Yang, D.; Zhang, C., Ruthenium-Catalyzed Oxidative Cleavage of Olefins to Aldehydes. *J. Org. Chem.* **2001,** *66*, (14), 4814-4818.

471.   Gottlieb, H. E.; Kotlyar, V.; Nudelman, A., NMR Chemical Shifts of Common Laboratory Solvents as Trace Impurities. *J. Org. Chem.* **1997,** *62*, (21), 7512-7515.

472.   Griesbaum, K.; Hilb, M.; Bosch, J., Ozonides of mono-, bi- and tricyclic terpenes. *Tetrahedron* **1996,** *52*, (47), 14813-14826.

473.   Updyke, K. M.; Nguyen, T. B.; and Nizkorodov, S. A., Formation of brown carbon via reactions of gaseous ammonia with secondary organic aerosols from biogenic and anthropogenic precursors *Environ. Sci. Tech.; accepted* **2012**.

474.   Dziedzic, P.; Bartoszewicz, A.; Córdova, A., Inorganic ammonium salts as catalysts for direct aldol reactions in the presence of water. *Tetrahedron Letters* **2009,** *50*, (52), 7242-7245.

475.   Noziere, B.; Dziedzic, P.; Cordova, A., Products and Kinetics of the Liquid-Phase Reaction of Glyoxal Catalyzed by Ammonium Ions (NH(4)(+)). *J. Phys. Chem. A* **2009,** *113*, (1), 231-237.

476.   Noziere, B.; Cordova, A., A Kinetic and Mechanistic Study of the Amino Acid Catalyzed Aldol Condensation of Acetaldehyde in Aqueous and Salt Solutions. *J. Phys. Chem. A* **2008,** *112*, (13), 2827-2837.

477.   Nozière, B.; Dziedzic, P.; Córdova, A., Formation of secondary light-absorbing fulvic-like oligomers: A common process in aqueous and ionic atmospheric particles? *Geophys. Res. Lett.* **2007,** *34*, (21), L21812.

478. De Pont, J. J. H. H. M.; Daemen, F. J. M.; Bonting, S. L., Biochemical aspects of the visual process: VII. Equilibrium conditions in the formation of retinylidene imines. *Archives of Biochemistry and Biophysics* **1970,** *140*, (1), 267-274.

479. Jun, C.-H.; Moon, C. W.; Lee, D.-Y., Chelation-Assisted Carbon–Hydrogen and Carbon–Carbon Bond Activation by Transition Metal Catalysts. *Chemistry – A European Journal* **2002,** *8*, (11), 2422-2428.

480. Coates, J., Interpretation of Infrared Spectra, A Practical Approach. In *Encyclopedia of Analytical Chemistry*, John Wiley & Sons, Ltd: 2006.

481. Bicca Alencastro, R. D.; Badilescu, S.; Lussier, L. S.; Sandorfy, C.; Thanh, H. L.; Vocelle, D., Spectroscopic studies on the protonation of Schiff bases. *International Journal of Quantum Chemistry* **1990,** *38*, (2), 173-179.

482. Zimmermann, F.; Lippert, T. H.; Beyer, C. H.; Stebani, J.; Nuyken, O.; Wokaun, A., N=N Vibrational Frequencies and Fragmentation Patterns of Substituted 1-Aryl-3,3-Dialkyl-Triazenes: Comparison with Other High-Nitrogen Compounds. *Appl. Spectrosc.* **1993,** *47*, (7), 986-993.

483. Le Fevre, R.; O'Dwyer, M.; and Werner, R., The Stretching Frequency of the -N=N-Group. *Australian Journal of Chemistry* **1961,** *14*, (2), 315-317.

484. Rothschild, K. J.; Roepe, P.; Lugtenburg, J.; Pardoen, J. A., Fourier transform infrared evidence for Schiff base alteration in the first step of the bacteriorhodopsin photocycle. *Biochemistry* **1984,** *23*, (25), 6103-6109.

485. Solomons, T. W. G.; Fryhle, C. B., *Organic Chemistry*. 8 ed.; John Wiley & Sons, Inc.: Hoboken, NJ, 2004, 1255 pp.

486. Bafqiren, H.; Eddine, J. J., Water enables transimination between hindered ketimines and beta-aminoalcohols and selective protection of a vicinal diamine backbone. *Tetrahedron* **2010,** *66*, (34), 7028-7034.

487. Weng, S. H.; Leussing, D. L., Transimination kinetics of pyridoxal 5'-phosphate Schiff bases. *J. Am. Chem. Soc.* **1983,** *105*, (12), 4082-4090.

488. Hogg, J. L.; Jencks, D. A.; Jencks, W. P., Catalysis of transimination through trapping by acids and bases. *J. Am. Chem. Soc.* **1977,** *99*, (14), 4772-4778.

489. Tobias, P. S.; Kallen, R. G., Kinetics and equilibriums of the reaction of pyridoxal 5'-phosphate with ethylenediamine to form Schiff bases and cyclic geminal diamines. Evidence for kinetically competent geminal diamine intermediates in transimination sequences. *J. Am. Chem. Soc.* **1975,** *97*, (22), 6530-6539.

490. Carlton, L.; Staskun, B.; van Es, T., A nitrogen-15 NMR study of hydrogen bonding in 1-alkyl-4-imino-1,4-dihydro-3-quinolinecarboxylic acids and related compounds. *Magnetic Resonance in Chemistry* **2006,** *44*, (5), 510-514.

491. Sakmar, T. P.; Franke, R. R.; Khorana, H. G., Glutamic acid-113 serves as the retinylidene Schiff base counterion in bovine rhodopsin. *Proc. Natl. Acad. Sci.* **1989,** *86*, (21), 8309-8313.

492. Akita, H.; Tanis, S. P.; Adams, M.; Balogh-Nair, V.; Nakanishi, K., Nonbleachable rhodopsins retaining the full natural chromophore. *J. Am. Chem. Soc.* **1980,** *102*, (20), 6370-6372.

493. Seltzer, S., Models for bacteriorhodopsin-catalyzed dark cis-trans isomerization of bound retinal. *J. Am. Chem. Soc.* **1990,** *112*, (11), 4477-4483.

494. Irving, C. S.; Leermakers, P. A., Spectroscopic behavior of all-trans retinal and its Schiff bases in various media. The role of conformational perturbation. . *Photochem. Photobio.* **1968,** *7*, (6), 665-670.

495. Banerjee, D. K.; Budke, C. C., Spectrophotometric determination of traces of peroxides in organic solvents. *Anal. Chem.* **1964,** *36*, (4), 792-6.

496. Roehl, C. M.; Marka, Z.; Fry, J. L.; Wennberg, P. O., Near-UV photolysis cross sections of CH3OOH and HOCH2OOH determined via action spectroscopy. *Atmos. Chem. Phys.* **2007,** *7*, (3), 713-720.

497. Monteil-Rivera, F.; Radovic-Hrapovic, Z.; Halasz, A.; Paquet, L.; Ampleman, G.; Thiboutot, S.; and Hawari, J., Environmental Fate of Triethylene Glycol Dinitrate. *Environ. Eng. Sci.* **2011,** *28*, (1), 71-79.

498. Engelhardt, H.; Meister, J.; Kolla, P., Optimisation of post-column reaction detector for HPLC of explosives. *Chromatographia* **1993,** *35*, (1), 5-12.

499. Haag, W. R.; Spanggord, R. J.; Mill, T.; Podoll, R. T.; Chou, T.-W.; Tse, D. S.; Harper, J. C., Fate of diethylene glycol dinitrate in surface waters. *Chemosphere* **1991,** *23*, (2), 215-230.

500. Zellner, R.; Exner, M.; Herrmann, H., Absolute OH quantum yields in the laser photolysis of nitrate, nitrite and dissolved H2O2 at 308 and 351 nm in the temperature range 278-353 K. *J. Atmos. Chem.* **1990,** *10*, (4), 411-425.

501. Zafiriou, O. C.; Bonneau, R., Wavelength dependent quantum yield of OH radical from photolysis of nitrite ion in water *Photochem. Photobio.* **1987,** *45*, 723-727.

502. Gaffney, J. S.; Marley, N. A.; Cunningham, M. M., Measurement of the absorption constants for nitrate in water between 270 and 335 nm. *Environ. Sci. Technol.* **1992,** *26*, (1), 207-209.

503. Zuo, Y.; Deng, Y., The near-UV absorption constants for nitrite ion in aqueous solution. *Chemosphere* **1998,** *36*, (1), 181-188.

Appendices

Appendix A: Homologous Families in Isoprene/OH High-NOx SOA from Condensation and Addition Reactions

Table A1: Oligomers of the type $C_xH_yO_z + (C_4H_6O_3)_k$ formed from the homologous esterification of 2MGA ($C_4H_8O_4$) under high-NOx conditions are affected by humidity. The total oligomer signals ($k \geq 1$) of the members of several $C_xH_yO_z$ families are reported here for the dry vs. humid data. The length of the oligomer is reduced by approximately 3 monomer units in the humid, as compared to dry, conditions. The sums of the total oligomer signal, used to indicate the change in the extent of oligomerization, were also reported in Table 1 in the text as normalized values.

$C_2H_4O_3 + (C_4H_6O_3)_k$

k	Mass (Da)	Abundance (dry)	Abundance (humid)	C	H	O	N
0	76.016	10	12	2	4	3	0
1	178.048	12	5	6	10	6	0
2	280.079	19	12	10	16	9	0
3	382.111	26	7	14	22	12	0
4	586.175	23	7	22	34	18	0
5	688.206	19	4	26	40	21	0
6	790.238	12	0	30	46	24	0
7	892.27	4	0	34	52	27	0
Total Oligomer Signal		**114**	**34**				

$C_3H_4O_3 + (C_4H_6O_3)_k$

k	Mass (Da)	Abundance (dry)	Abundance (humid)	C	H	O	N
0	88.016	83	17	3	4	3	0
1	190.048	86	24	7	10	6	0
2	292.079	104	35	11	16	9	0
3	394.111	127	26	15	22	12	0
4	496.143	73	11	19	28	15	0
5	598.175	34	7	23	34	18	0
6	700.206	19	2	27	40	21	0
7	802.238	8	0	31	46	24	0
8	904.27	4	0	35	52	27	0
Total Oligomer Signal		**455**	**106**				

$C_3H_6O_2 + (C_4H_6O_3)_k$

k	Mass (Da)	Abundance (dry)	Abundance (humid)	C	H	O	N

k	Mass (Da)	Abundance (dry)	Abundance (humid)	C	H	O	N
0	74.037	10	8	3	6	2	0
1	176.068	26	19	7	12	5	0
2	278.1	36	22	11	18	8	0
3	380.132	37	18	15	24	11	0
4	482.164	36	27	19	30	14	0
5	584.195	32	15	23	36	17	0
6	686.227	28	6	27	42	20	0
7	788.259	19	0	31	48	23	0
8	890.29	10	0	35	54	26	0
9	992.322	2	0	39	60	29	0
Total Oligomer Signal		**225**	**107**				

$C_3H_6O_3 + (C_4H_6O_3)_k$

k	Mass (Da)	Abundance (dry)	Abundance (humid)	C	H	O	N
0	90.032	6	8	3	6	3	0
1	192.063	9	7	7	12	6	0
2	294.095	22	9	11	18	9	0
3	396.127	29	6	15	24	12	0
4	498.158	28	6	19	30	15	0
5	600.19	24	5	23	36	18	0
6	702.222	16	1	27	42	21	0
7	804.254	10	0	31	48	24	0
8	906.285	3	0	35	54	27	0
Total Oligomer Signal		**140**	**35**				

$C_4H_6O_3 + (C_4H_6O_3)_k$

k	Mass (Da)	Abundance (dry)	Abundance (humid)	C	H	O	N
0	102.032	7	5	4	6	3	0
1	204.063	98	61	8	12	6	0
2	306.095	92	28	12	18	9	0
3	408.127	99	26	16	24	12	0
4	510.158	69	14	20	30	15	0
5	612.19	43	7	24	36	18	0
6	714.222	27	2	28	42	21	0
7	816.254	10	0	32	48	24	0
8	918.285	8	0	32	48	24	0
Total Oligomer Signal		**445**	**137**				

$C_4H_8O_3 + (C_4H_6O_3)_k$

k	Mass (Da)	Abundance (dry)	Abundance (humid)	C	H	O	N
0	104.047	1	1	4	8	3	0

k	Mass (Da)	Abundance (dry)	Abundance (humid)	C	H	O	N
1	206.079	10	7	8	14	6	0
2	308.111	8	6	12	20	9	0
3	410.142	11	5	16	26	12	0
4	512.174	11	5	20	32	15	0
5	614.206	15	5	24	38	18	0
6	716.238	26	0	28	44	21	0
7	818.269	17	0	32	50	24	0
8	920.301	3	0	36	56	27	0
Total Oligomer Signal		**100**	**28**				

$C_4H_8O_4 + (C_4H_6O_3)_k$

k	Mass (Da)	Abundance (dry)	Abundance (humid)	C	H	O	N
0	120.042	269	285	4	8	4	0
1	222.074	191	218	8	14	7	0
2	324.106	153	117	12	20	10	0
3	426.137	102	60	16	26	13	0
4	528.169	59	47	20	32	16	0
5	630.201	43	20	24	38	19	0
6	732.232	31	5	28	44	22	0
7	834.264	14	0	32	50	25	0
8	936.296	4	0	36	56	28	0
Total Oligomer Signal		**598**	**467**				

$C_4H_7O_6N + (C_4H_6O_3)_k$

k	Mass (Da)	Abundance (dry)	Abundance (humid)	C	H	O	N
0	165.027	2	2	4	7	6	1
1	267.059	179	39	8	13	9	1
2	369.091	212	44	12	19	12	1
3	471.122	186	26	16	25	15	1
4	573.154	99	11	20	31	18	1
5	675.186	42	5	24	37	21	1
6	777.218	14	2	28	43	24	1
7	879.249	4	0	32	49	27	1
Total Oligomer Signal		**736**	**126**				

$C_5H_8O_4 + (C_4H_6O_3)_k$

k	Mass (Da)	Abundance (dry)	Abundance (humid)	C	H	O	N
0	132.042	9	10	5	8	4	0
1	234.074	49	26	9	14	7	0
2	336.106	67	50	13	20	10	0
3	438.137	66	29	17	26	13	0

k	Mass (Da)	Abundance (dry)	Abundance (humid)	C	H	O	N
4	540.169	46	13	21	32	16	0
5	642.201	32	6	25	38	19	0
6	744.232	21	0	29	44	22	0
7	846.264	7	0	33	50	25	0
8	948.296	3	0	37	56	28	0
Total Oligomer Signal		**291**	**124**				

$C_5H_8O_5 + (C_4H_6O_3)_k$
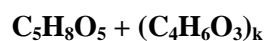
k	Mass (Da)	Abundance (dry)	Abundance (humid)	C	H	O	N
0	148.037	52	23	5	8	5	0
1	250.069	118	72	9	14	8	8
2	352.101	155	59	13	20	11	11
3	454.132	109	23	17	26	14	14
4	556.164	56	9	21	32	17	17
5	658.196	30	3	25	38	20	20
6	760.227	16	0	29	44	23	23
7	862.259	6	0	33	50	26	26
Total Oligomer Signal		**491**	**167**				

$C_6H_8O_4 + (C_4H_6O_3)_k$
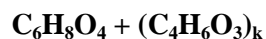
k	Mass (Da)	Abundance (dry)	Abundance (humid)	C	H	O	N
0	144.042	25	3	6	8	4	0
1	246.074	22	64	10	14	7	0
2	348.106	64	14	14	20	10	0
3	450.137	28	7	18	26	13	0
4	552.169	22	3	22	32	16	0
5	654.201	17	0	26	38	19	0
6	756.232	8	0	30	44	22	0
7	858.264	4	0	34	50	25	0
Total Oligomer Signal		**165**	**88**				

$C_6H_{10}O_5 + (C_4H_6O_3)_k$
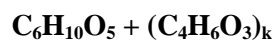
k	Mass (Da)	Abundance (dry)	Abundance (humid)	C	H	O	N
0	162.053	98	113	6	10	5	0
1	264.085	251	146	10	16	8	0
2	366.116	378	208	14	22	11	0
3	468.148	226	70	18	28	14	0
4	570.18	107	20	22	34	17	0
5	672.211	53	6	26	40	20	0
6	774.243	26	1	30	46	23	0
7	876.275	9	0	34	52	26	0

8	978.306	3	0		38	58	29	0
Total Oligomer Signal	**1151**	**564**					

C$_7$H$_{10}$O$_4$ + (C$_4$H$_6$O$_3$)$_k$
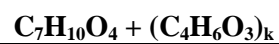
k	Mass (Da)	Abundance (dry)	Abundance (humid)	C	H	O	N
0	158.058	4	4	7	10	4	0
1	260.09	28	10	11	16	7	0
2	362.121	41	46	15	22	10	0
3	464.153	38	15	19	28	13	0
4	566.185	26	5	23	34	16	0
5	668.216	19	1	27	40	19	0
6	770.248	8	0	31	46	22	0
7	872.28	6	0	35	52	25	0
Total Oligomer Signal	**166**	**77**					

Appendix B: Physical and Thermochemical Data for Reference Compounds

Table B1: Compounds used for statistical analysis in Chapter 5 and their accompanying physical properties. Compounds are sorted by molecular mass. Data were taken from Ref [309] and references therein.

Heterocyclic Nitrogen (Imidazoles)	Mass (Da)	H/C	Adj. mass (Da)	PA (kJ/mol)	GB (kJ/mol)	Molecular Volume (Å^3)
Imidazole	68	1.33	91	942.8	909.2	5.9
2-Methyl-1H-imidazole	82	1.50	123	963.4	929.6	7.4
4-Methyl-1H-imidazole	82	1.50	123	952.8	920.9	7.4
1,4-Dimethyl-1H-imidazole	96	1.60	154	976.7	944.9	9.0
1,2-Dimethyl-1H-imidazole	96	1.60	154	984.7	952.6	9.0
1,5-Dimethyl-1H-imidazole	96	1.60	154	977.6	945.8	9.0
1H-Benzimidazole	118	0.86	101	953.8	920.5	11.7
1-Methyl-1H-benzimidazole	132	1.00	132	967.0	935.2	13.3
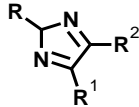
Heterocyclic Nitrogen (Pyrazoles)	Mass (Da)	H/C	Adj. mass (Da)	PA (kJ/mol)	GB (kJ/mol)	Molecular Volume (Å^3)
1H-Pyrazole	68	1.33	91	894.1	860.5	5.9
1-Methyl-1H-pyrazole	82	1.50	123	912.0	880.1	7.4
3-Methyl-1H-pyrazole	82	1.50	123	906.0	874.2	7.4
4-Methyl-1H-pyrazole	82	1.50	123	906.8	873.4	7.4
1,3-Dimethyl-1H-pyrazole	96	1.60	154	933.9	902.3	9.0
1,5-Dimethyl-1H-pyrazole	96	1.60	154	934.3	902.8	9.0
3,4-Dimethyl-1H-pyrazole	96	1.60	154	927.3	895.4	9.0
3,5-Dimethyl-1H-pyrazole	96	1.60	154	933.5	900.1	9.0
1,3,5-Trimethyl-1H-pyrazole	110	1.67	183	949.3	917.4	10.6
3,4,5-Trimethyl-1H-pyrazole	96	1.67	160	949.3	916.0	9.9
1-Methyl-3-phenyl-1H-pyrazole	144	1.00	144	932.6	900.8	15.7
1-Methyl-5-phenyl-1H-pyrazole	144	1.00	144	932.4	900.5	15.7
3,5-Diphenyl-1H-pyrazole	192	0.80	154	946.3	912.7	22.3
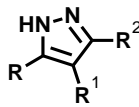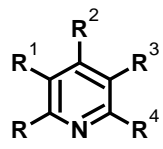
Pyridines	Mass (Da)	H/C	Adj. mass (Da)	PA (kJ/mol)	GB (kJ/mol)	Molecular Volume (Å^3)
Pyridine	79	1.00	79	930.0	898.1	8.2
2-Methylpyridine	93	1.17	109	949.1	917.3	9.7

	Mass (Da)	H/C	Adj. mass (Da)	PA (kJ/mol)	GB (kJ/mol)	Molecular Volume (Å³)
3-Methylpyridine	93	1.17	109	943.4	911.6	9.7
4-Methylpyridine	93	1.17	109	947.2	915.3	9.7
4-Vinylpyridine	105	1.00	105	944.1	912.3	11.2
2-Ethylpyridine	107	1.29	138	952.4	920.6	11.3
3-Ethylpyridine	107	1.29	138	947.4	915.5	11.3
4-Ethylpyridine	107	1.29	138	951.1	919.2	11.3
2,3-Dimethylpyridine	107	1.29	138	958.9	927.0	11.3
2,4-Dimethylpyridine	107	1.29	138	962.9	930.8	11.3
2,5-Dimethylpyridine	107	1.29	138	958.8	926.9	11.3
2,6-Dimethylpyridine	107	1.29	138	963.0	931.1	11.3
3,4-Dimethylpyridine	107	1.29	138	957.3	925.5	11.3
3,5-Dimethylpyridine	119	1.13	134	955.4	923.5	12.7
4-Isopropylpyridine	121	1.38	166	955.7	923.8	12.9
2-Propylpyridine	121	1.38	166	955.7	923.8	12.9
2,6-Diethylpyridine	135	1.44	195	972.3	940.4	14.4
4-tert-Butylpyridine	135	1.44	195	957.7	925.8	14.4
2-tert-Butylpyridine	135	1.44	195	961.7	929.8	14.4
4-Phenylpyridine	155	0.82	127	939.7	907.8	17.0
2-Hexylpyridine	163	1.55	252	963.6	931.7	17.6
2,4-Di-tert-butylpyridine	191	1.62	309	983.8	952.0	20.7
2,6-Di-tert-butylpyridine	191	1.62	309	982.9	951.0	20.7
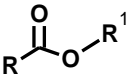
Saturated Esters (R-CO-O-R¹)	Mass (Da)	H/C	Adj. mass (Da)	PA (kJ/mol)	GB (kJ/mol)	Molecular Volume (Å³)
Methylformate	44	2.00	88	782.5	751.5	4.0
Ethylformate	74	2.00	148	799.4	768.4	6.5
Methylacetate	74	2.00	148	821.6	790.7	6.5
Propylformate	88	2.00	176	804.9	773.9	8.1
Isopropylformate	88	2.00	176	811.3	780.3	8.1
Ethylacetate	88	2.00	176	835.7	804.7	8.1
Methylpropanoate	88	2.00	176	830.2	799.2	8.1
Butylformate	102	2.00	204	806.0	775.0	9.6
Propylacetate	102	2.00	204	836.6	805.6	9.6
Isopropylacetate	102	2.00	204	836.6	805.6	9.6
Methylbutanoate	102	2.00	204	836.4	805.4	9.6
Methylisobutanoate	102	2.00	204	836.6	805.7	9.6
Methyl2,2-dimethylpropanoate	116	2.00	232	845.2	814.2	11.2
Methylcyclohexanecarboxylate	126	1.75	221	846.2	815.3	13.3
Methylcyclopropanecarboxylate	100	1.60	160	842.1	811.2	9.5
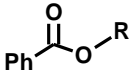
Unsaturated Esters (Ph-CO-O-R)	Mass (Da)	H/C	Adj. mass (Da)	PA (kJ/mol)	GB (kJ/mol)	Molecular Volume (Å³)

Methyltrans-2-butenoate	100	1.60	160	851.3	820.4	9.5
Methylbenzoate	136	1.00	136	850.5	819.5	13.8
Methyl2-methylbenzoate	150	1.11	167	858.3	827.3	15.4
Methyl3-methylbenzoate	150	1.11	167	857.7	826.8	15.4
Methyl4-methylbenzoate	150	1.11	167	861.5	830.6	15.4
Methyl4-hydroxybenzoate	152	1.00	152	863.4	832.5	14.7
Methyl3-hydroxybenzoate	152	1.00	152	850.0	819.1	14.7
Methyl4-formylbenzoate	164	0.89	146	832.9	801.9	16.2
Methyl4-methoxybenzoate	166	1.11	184	870.6	839.6	16.3
Methyl3-methoxybenzoate	134	1.11	149	856.7	825.8	14.5
Methyl2,5-dimethylbenzoate	148	1.20	178	864.7	833.7	16.1
Methyl2,4-dimethylbenzoate	148	1.20	178	868.2	837.2	16.1
Methyl3,5-dimethylbenzoate	148	1.20	178	864.3	833.4	16.1
Methyl2,4,6-trimethylbenzoate	160	1.27	204	866.3	835.3	17.4
Dimethylterephthalate	130	1.00	130	843.2	812.3	15.0
Dimethylisophthalate	146	1.00	146	843.5	814.3	15.9
4-Acetylphenylacetate	146	1.00	146	853.2	821.3	15.9
Vinylacetate	86	1.50	129	813.9	782.9	7.9
Methylacrylate	86	1.50	129	825.8	794.8	7.9
Methylmethacrylate	100	1.60	160	831.4	800.5	9.5
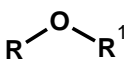
Alkyl Ethers $R \diagdown O \diagup R^1$	Mass (Da)	H/C	Adj. mass (Da)	PA (kJ/mol)	GB (kJ/mol)	Molecular Volume ($Å^3$)
Dimethylether	46	3.00	138	792.0	764.5	4.2
Ethylmethylether	60	2.67	160	808.6	781.2	5.7
Dipentylether	148	1.20	178	852.7	825.3	16.1
Diethylether	74	2.50	185	828.4	801.0	7.3
Methylpropylether	74	2.50	185	814.9	785.7	7.3
Butyl methylether	88	2.40	211	820.3	791.2	8.9
Methyltert-butylether	88	2.40	211	841.6	812.4	8.9
Ethylisopropylether	88	2.40	211	842.7	813.5	8.9
Isopropylmethylether	90	2.50	225	826.3	797.1	8.2
tert-Butylethylether	102	2.33	238	856.0	826.9	10.4
tert-Butylisopropylether	116	2.29	265	870.7	841.5	12.0
Dipropylether	102	2.33	238	837.9	810.5	10.4
Diisopropylether	102	2.33	238	855.5	828.1	10.4
Dibutylether	130	2.25	293	845.7	818.3	13.6
Di-sec-butylether	130	2.25	293	865.9	838.5	13.6
Di-tert-butylether	178	2.25	401	887.4	860.0	16.3
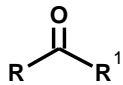
Saturated Ketones $R \diagdown \overset{O}{\underset{}{C}} \diagup R^1$	Mass (Da)	H/C	Adj. mass (Da)	PA (kJ/mol)	GB (kJ/mol)	Molecular Volume ($Å^3$)
5-Nonanone	142	2.00	284	853.7	821.9	15.0

	Mass (Da)	H/C	Adj. mass (Da)	PA (kJ/mol)	GB (kJ/mol)	Molecular Volume (Å^3)
Di-tert-butylketone	142	2.00	284	861.3	831.5	15.0
2,4-Dimethyl-3-pentanone	114	2.00	228	850.3	820.5	11.9
3,3-Dimethyl-2-butanone	116	2.00	232	840.1	808.2	11.2
2,2,4-Trimethyl-3-pentanone	128	2.00	256	856.9	825.0	13.4
2-Butanone	72	2.00	144	827.3	795.5	7.2
2-Pentanone	86	2.00	172	832.7	800.9	8.7
3-Pentanone	86	2.00	172	836.8	807.0	8.7
3-Methyl-2-butanone	86	2.00	172	836.3	804.4	8.7
3-Hexanone	100	2.00	200	843.2	811.3	10.3
4-Heptanone	114	2.00	228	845.0	815.3	11.9
Acetone	58	2.00	116	812.0	782.1	5.6
Cyclobutanone	70	1.50	105	802.5	772.7	7.0
Cyclopentanone	84	1.60	134	823.7	794.0	8.6
Cyclohexanone	98	1.67	163	841.0	811.2	10.2
Cycloheptanone	112	1.71	192	845.6	815.9	11.7
4-Methylcyclohexanone	128	1.71	219	844.9	813.0	12.6
Cyclooctanone	126	1.75	221	849.4	819.6	13.3
1-Cyclohexylethanone	142	1.75	249	841.4	809.5	14.2
Cyclononanone	172	1.78	306	852.6	822.8	16.7
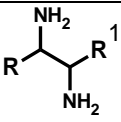
Diamines	Mass (Da)	H/C	Adj. mass (Da)	PA (kJ/mol)	GB (kJ/mol)	Molecular Volume (Å^3)
1,2-Ethanediamine	60	4.00	240	951.6	912.5	4.7
1,3-Propanediamine	74	3.33	247	987.0	940.0	6.3
1,4-Butanediamine	88	3.00	264	1005.6	954.3	7.8
1,5-Pentanediamine	102	2.80	286	999.6	946.2	9.4
1,2-Benzenediamine	108	1.33	144	896.5	865.8	10.4
1,3-Benzenediamine	108	1.33	144	929.9	899.2	10.4
1,4-Benzenediamine	108	1.33	144	905.9	874.0	10.4
Triethylenediamine	112	2.00	224	963.4	934.6	10.7
1,6-Hexanediamine	116	2.67	309	999.5	946.2	11.0
1,7-Heptanediamine	130	2.57	334	998.5	944.9	12.5
1,8-Naphthalenediamine	158	1.00	158	944.5	912.1	16.3

Primary Amines	Mass (Da)	H/C	Adj. mass (Da)	PA (kJ/mol)	GB (kJ/mol)	Molecular Volume (Å^3)
Methylamine	31	5.00	155	899.0	864.5	2.4
Ethylamine	45	3.50	158	912.0	878.0	4.0
Cyclopropylamine	57	2.33	133	904.7	869.9	5.4
Propylamine	59	3.00	177	917.8	883.9	5.5
Isopropylamine	59	3.00	177	923.8	889.0	5.5
Butylamine	73	2.75	201	921.5	886.6	7.1

tert-Butylamine	73	2.75	201	934.1	899.9	7.1
Isobutylamine	73	2.75	201	924.8	890.8	7.1
Pentylamine	87	2.60	226	923.5	889.5	8.7
Cyclohexylamine	99	2.17	215	934.4	899.6	10.1
Hexylamine	101	2.50	253	927.5	893.5	10.2
Benzylamine	107	1.29	138	913.3	879.4	11.3
Heptylamine	115	2.43	279	923.2	889.3	11.8
Octylamine	129	2.38	306	928.9	895.0	13.4
Cyclohexanemethanamine	113	2.14	242	926.6	895.8	11.7
2,2-Dimethylpropylamine	87	2.60	226	928.3	894.0	8.7

Secondary Amines $R\diagdown^{NH}\diagup R^1$	Mass (Da)	H/C	Adj. mass (Da)	PA (kJ/mol)	GB (kJ/mol)	Molecular Volume ($\mathring{A}^3$)
Dimethylamine	45	3.50	158	929.5	896.5	4.0
Diethylamine	73	2.75	201	952.4	919.4	7.1
Isopropylmethylamine	73	2.75	201	952.4	919.4	7.1
Allyldimethylamine	85	2.20	187	957.8	926.8	8.6
2-Methyl-2-butanamine	87	2.60	226	937.8	903.6	8.7
Ethylisopropylamine	87	2.60	226	960.0	926.7	8.7
Dipropylamine	101	2.50	253	962.3	929.3	10.2
Diisopropylamine	101	2.50	253	971.9	938.6	10.2
Dibutylamine	129	2.38	306	968.5	935.3	13.4
Di-sec-butylamine	129	2.38	306	980.7	947.5	13.4
Diisobutylamine	129	2.38	306	958.1	925.1	13.4

Tertiary Amines $R\diagdown_N^{R^1}\diagup R^2$	Mass (Da)	H/C	Adj. mass (Da)	PA (kJ/mol)	GB (kJ/mol)	Molecular Volume ($\mathring{A}^3$)
Trimethylamine	59	3.00	177	948.9	918.1	5.5
Ethyldimethylamine	73	2.75	201	960.1	929.1	7.1
Diethylmethylamine	87	2.60	226	971.0	940.0	8.7
Butyldimethylamine	101	2.50	253	969.2	938.2	10.2
Isobutyldimethylamine	101	2.50	253	968.7	937.8	10.2
Triethylamine	101	2.50	253	981.8	951.0	10.2
Methyldipropylamine	115	2.43	279	983.5	950.9	11.8
Diethylpropylamine	115	2.43	279	978.8	947.9	11.8
Cyclohexyldimethylamine	127	2.13	270	983.6	952.6	13.3
Tripropylamine	143	2.33	334	991.0	960.1	14.9
Tributylamine	185	2.25	416	998.5	967.6	19.6

Alcohols R–OH	Mass (Da)	H/C	Adj. mass (Da)	PA (kJ/mol)	GB (kJ/mol)	Molecular Volume (Å^3)
Methanol	16	4.00	64	754.3	724.5	2.6
Ethanol	30	3.00	90	776.4	746.0	4.2
1-Propanol	44	2.67	117	786.5	756.1	5.7
2-Propanol	46	3.33	153	793.0	762.6	5.9
1-Butanol	58	2.50	145	789.2	758.9	7.3
2-Butanol	58	2.50	145	815.7	784.6	7.3
2-Methyl-1-propanol	58	2.50	145	793.7	762.2	7.3
2-Methyl-2-propanol	58	2.50	145	802.6	772.2	7.3
2,2-Dimethyl-1-propanol	72	2.40	173	795.5	765.2	8.9
Cyclohexanemethanol	98	2.00	196	802.1	771.7	11.9

Carboxylic Acids	Mass (Da)	H/C	Adj. mass (Da)	PA (kJ/mol)	GB (kJ/mol)	Molecular Volume (Å^3)
Formic acid	14	2.00	28	742.0	710.3	3.4
Acetic acid	28	2.00	56	783.7	752.8	4.9
Propanoic acid	42	2.00	84	797.2	766.2	6.5
Methacrylic acid	54	1.50	81	816.7	785.7	7.9
Cyclopropanecarboxylic acid	54	1.50	81	821.4	790.4	7.9
3-Methyl-2-butenoic acid	68	1.60	109	822.9	791.9	9.5
cis-2-Methyl-2-butenoic acid	68	1.60	109	822.5	791.5	9.5
Cyclobutanecarboxylic acid	68	1.60	109	817.4	786.4	9.5
Cyclopentanecarboxylic acid	82	1.67	137	817.4	786.4	11.1
Benzoic acid	90	0.86	77	821.1	790.1	12.3
Cyclohexanecarboxylic acid	96	1.71	165	823.8	792.8	12.6
Toluic acid	104	1.00	104	829.8	798.8	13.8

314

Table B2: Hydrocarbons and oxygenated hydrocarbon compounds used for statistical analysis in Chapter 5and their accompanying average polarizability values. Compounds are sorted by number of carbon. Data were taken from Ref [310]and references therein.

Hydrocarbons	C	H	O	Mass	H/C	AM	Polarizability $(10^{24}$ cm$^3)$
methane	1	4	0	16	4.00	64	2.59
acetylene	2	2	0	26	1.00	26	3.33
ethylene	2	4	0	28	2.00	56	4.25
ethane	2	6	0	30	3.00	90	4.47
propyne	3	4	0	40	1.33	53	6.18
propene	3	6	0	42	2.00	84	6.26
cyclopropane	3	6	0	42	2.00	84	5.66
propane	3	8	0	44	2.67	117	6.29
1-butyne	4	6	0	54	1.50	81	7.41
1,3-butadiene	4	6	0	54	1.50	81	8.64
1-butene	4	8	0	56	2.00	112	7.97
trans-2-butene	4	8	0	56	2.00	112	8.49
2-methylpropene	4	8	0	56	2.00	112	8.29
butane	4	10	0	58	2.50	145	8.20
isobutane	4	10	0	58	2.50	145	8.14
1,3-cyclopentadiene	5	6	0	66	1.20	79	8.64
1-pentyne	5	8	0	68	1.60	109	9.12
trans-1,3-pentadiene	5	8	0	68	1.60	109	10.00
isoprene	5	8	0	68	1.60	109	9.99
cyclopentane	5	10	0	70	2.00	140	9.15
1-pentene	5	10	0	70	2.00	140	9.65
2-pentene	5	10	0	70	2.00	140	9.84
pentane	5	12	0	72	2.40	173	9.99
neopentane	5	12	0	72	2.40	173	10.20
benzene	6	6	0	78	1.00	78	10.00
1-hexyne	6	10	0	82	1.67	137	10.90
2-ethyl-1,3-butadiene	6	10	0	82	1.67	137	11.80
3-methyl-1,3-pentadiene	6	10	0	82	1.67	137	11.80
2-methyl-1,3-pentadiene	6	10	0	82	1.67	137	12.10
2,3-dimethyl-1,3-butadiene	6	10	0	82	1.67	137	11.80
cyclohexene	6	10	0	82	1.67	137	10.70
cyclohexane	6	12	0	84	2.00	168	11.00
1-hexene	6	10	0	82	1.67	137	11.65
hexane	6	14	0	86	2.33	201	11.90
toluene	7	8	0	92	1.14	105	11.80
1-heptyne	7	12	0	96	1.71	165	12.80
methylcyclohexane	7	14	0	98	2.00	196	13.10

315

	C	H	O	Mass	H/C	AM	Polarizability
1-heptene	7	14	0	98	2.00	196	13.51
heptane	7	16	0	100	2.29	229	13.61
styrene	8	8	0	104	1.00	104	15.00
ethylbenzene	8	10	0	106	1.25	133	14.20
o-xylene	8	10	0	106	1.25	133	14.90
p-xylene	8	10	0	106	1.25	133	13.70
m-xylene	8	10	0	106	1.25	133	14.20
ethylcyclohexane	8	16	0	112	2.00	224	15.90
n-octane	8	18	0	114	2.25	257	15.90
3-methylheptane	8	18	0	114	2.25	257	15.44
2,2,4-trimethylpentane	8	18	0	114	2.25	257	15.44
a-methylstyrene	9	10	0	118	1.11	131	16.05
isopropylbenzene	9	12	0	120	1.33	160	16.00
1,3,5-trimethylbenzene	9	12	0	120	1.33	160	15.50
isopropylcyclohexane	9	18	0	126	2.00	252	17.20
nonane	9	20	0	128	2.22	284	17.36
naphthalene	10	8	0	128	0.80	102	16.50
durene	10	14	0	134	1.40	188	17.30
tert-butylbenzene	10	14	0	134	1.40	188	17.20
tert-butylcyclohexane	10	20	0	140	2.00	280	19.80
decane	10	22	0	142	2.20	312	19.10
a-methylnaphthalene	11	10	0	142	0.91	129	19.35
ß-methylnaphthalene	11	10	0	142	0.91	129	19.52
Oxygenated hydrocarbons	**C**	**H**	**O**	**Mass**	**H/C**	**AM**	**Polarizability**
ethyleneglycol	2	6	2	62	3.00	186	5.70
propenal	3	4	1	56	1.33	75	6.38
acetone	3	6	1	58	2.00	116	6.33
allylalcohol	3	6	1	58	2.00	116	7.65
propionaldehyde	3	6	1	58	2.00	116	6.50
propionicacid	3	6	2	74	2.00	148	6.90
ethylformate	3	6	2	74	2.00	148	6.88
methylacetate	3	6	2	74	2.00	148	6.94
dimethylcarbonate	3	6	3	90	2.00	180	7.70
2-propanol	3	8	1	60	2.67	160	7.61
1-propanol	3	8	1	60	2.67	160	6.74
ethylmethylether	3	8	1	60	2.67	160	7.93
dimethoxymethane	3	8	2	76	2.67	203	7.70
ethyleneglycolmonomethylether	3	8	2	76	2.67	203	7.44
diketene	4	4	2	84	1.00	84	8.00
crotonaldehyde	4	6	1	70	1.50	105	8.50
methacrylaldehyde	4	6	1	70	1.50	105	8.30
biacetyl	4	6	2	86	1.50	129	8.20
aceticanhydride	4	6	3	102	1.50	153	8.90

butanal	4	8	1	72	2.00	144	8.20
methylethylketone	4	8	1	72	2.00	144	8.13
trans-2,3-epoxybutane	4	8	1	72	2.00	144	8.22
ethylacetate	4	8	2	88	2.00	176	8.62
1,4-dioxane	4	8	2	88	2.00	176	10.00
p-dioxane	4	8	2	88	2.00	176	8.60
2-methyl-1,3-dioxolane	4	8	2	88	2.00	176	9.44
butyricacid	4	8	2	88	2.00	176	8.58
methylpropionate	4	8	2	88	2.00	176	8.97
ethylether	4	10	1	74	2.50	185	10.20
1-butanol	4	10	1	74	2.50	185	8.88
2-methylpropanol	4	10	1	74	2.50	185	8.92
methylpropylether	4	10	1	74	2.50	185	8.86
ethyleneglycolmonoethylether	4	10	1	74	2.50	185	9.28
acetylacetone	5	8	2	100	1.60	160	10.50
diethylketone	5	10	1	86	2.00	172	9.93
methylpropylketone	5	10	1	86	2.00	172	9.93
ethylpropionate	5	10	2	102	2.00	204	10.41
methylbutanoate	5	10	2	102	2.00	204	10.41
diethylcarbonate	5	10	3	118	2.00	236	11.30
ethylpropylether	5	12	1	88	2.40	211	10.68
tetramethylorthocarbonate	5	12	4	136	2.40	326	13.00
phenol	6	6	1	94	1.00	94	11.10
ethylacetoacetate	6	10	3	130	1.67	217	12.90
cyclohexanol	6	12	1	100	2.00	200	11.56
amylformate	6	12	2	116	2.00	232	14.20
paraldehyde	6	12	3	132	2.00	264	17.90
propylether	6	14	1	102	2.33	238	12.80
1,1-diethoxyethane	6	14	2	118	2.33	275	13.20
1,2-diethoxyethane	6	14	2	118	2.33	275	11.30
anisole	7	8	1	108	1.14	123	13.10
cyclohexylmethylether	7	14	1	114	2.00	228	13.40
2,4-dimethyl-3-pentanone	7	14	1	114	2.00	228	13.50
pentylacetate	7	14	2	130	2.00	260	14.90
acetophenone	8	8	1	120	1.00	120	15.00
phenetole	8	10	1	122	1.25	153	14.90
ethylsorbate	8	12	2	140	1.50	210	17.20
tetramethylcyclobutane-1,3-dione	8	12	2	140	1.50	210	18.60
diethylsuccinate	8	14	4	174	1.75	305	16.80
butylether	8	18	1	130	2.25	293	17.20
ethylbenzoate	9	10	2	150	1.11	167	16.90
1-naphthaldehyde	11	8	1	156	0.73	113	19.75
2-naphthaldehyde	11	8	1	156	0.73	113	20.06

Table B3: Oligomers of the type $C_xH_yO_z + (C_2H_4O_2)_k$ formed from the homologous addition of glycolaldehyde ($C_2H_4O_2$) under high-NOx conditions may also be affected by humidity; however, there is a large uncertainty in the data. The length of the oligomer is largely unchanged in the dry vs. humid conditions. The sums of the total oligomer signal, used to indicate the change in the extent of oligomerization, were also reported in Table 1 in the text.

$C_3H_4O_2 + (C_2H_4O_2)_k$

k	Mass (Da)	Abundance (dry)	Abundance (humid)	C	H	O	N
0	72.021	2	3	3	4	2	0
1	132.042	9	10	5	8	4	0
2	192.063	9	7	7	12	6	0
3	252.085	15	5	9	16	8	0
Total Oligomer Signal		**32**	**21**				

$C_5H_6O_2 + (C_2H_4O_2)_k$

k	Mass (Da)	Abundance (dry)	Abundance (humid)	C	H	O	N
0	98.037	8	1	5	6	2	0
1	158.058	4	4	7	10	4	0
2	218.079	89	41	9	14	6	0
3	278.1	36	22	11	18	8	0
4	338.121	2	2	13	22	10	0
Total Oligomer Signal		**131**	**69**				

$C_5H_6O_4 + (C_2H_4O_2)_k$

k	Mass (Da)	Abundance (dry)	Abundance (humid)	C	H	O	N
0	130.027	2	3	5	6	4	0
1	190.048	86	24	7	10	6	0
2	250.069	118	72	9	14	8	0
3	310.09	6	4	11	18	10	0
4	370.111	1	0	13	22	12	0
Total Oligomer Signal		**212**	**101**				

$C_6H_8O_3 + (C_2H_4O_2)_k$

k	Mass (Da)	Abundance (dry)	Abundance (humid)	C	H	O	N
0	128.047	2	3	6	8	3	0
1	188.068	19	11	8	12	5	0
2	248.09	22	23	10	16	7	0
3	308.111	8	6	12	20	9	0
Total Oligomer Signal		**49**	**40**				

C$_6$H$_8$O$_4$ + (C$_2$H$_4$O$_2$)$_k$
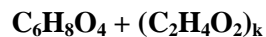
k	Mass (Da)	Abundance (dry)	Abundance (humid)	C	H	O	N
0	144.042	25	3	6	8	4	0
1	204.063	98	61	8	12	6	0
2	264.085	251	146	10	16	8	0
3	324.106	153	117	12	20	10	0
Total Oligomer Signal		**502**	**324**				

C$_7$H$_8$O$_4$ + (C$_2$H$_4$O$_2$)$_k$
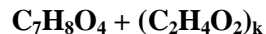
k	Mass (Da)	Abundance (dry)	Abundance (humid)	C	H	O	N
0	156.042	6	2	7	8	4	0
1	216.063	10	10	9	12	6	0
2	276.085	45	12	11	16	8	0
3	336.106	67	50	13	20	10	0
4	396.127	29	6	15	24	12	0
5	456.148	10	3	17	28	14	0
6	516.169	1	0	19	32	16	0
Total Oligomer Signal		**161**	**81**				

C$_7$H$_8$O$_5$ + (C$_2$H$_4$O$_2$)$_k$
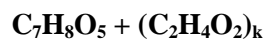
k	Mass (Da)	Abundance (dry)	Abundance (humid)	C	H	O	N
0	172.037	3	2	7	8	5	0
1	232.058	14	8	9	12	7	0
2	292.079	104	35	11	16	9	0
3	352.101	155	59	13	20	11	0
4	412.122	7	4	15	24	13	0
5	472.143	2	2	17	28	15	0
Total Oligomer Signal		**282**	**108**				

C$_7$H$_{10}$O$_5$ + (C$_2$H$_4$O$_2$)$_k$
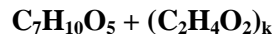
k	Mass (Da)	Abundance (dry)	Abundance (humid)	C	H	O	N
0	174.053	9	8	7	10	5	0
1	234.074	49	26	9	14	7	0
2	294.095	22	9	11	18	9	0
3	354.116	13	4	13	22	11	0
Total Oligomer Signal		**83**	**39**				

C$_8$H$_{10}$O$_3$ + (C$_2$H$_4$O$_2$)$_k$
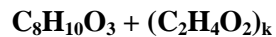
k	Mass (Da)	Abundance (dry)	Abundance (humid)	C	H	O	N
0	154.063	26	2	8	10	3	0

1	214.084	5	14	10	14	5	0
2	274.105	26	8	12	18	7	0
3	334.126	31	29	14	22	9	0
4	394.148	10	9	16	26	11	0
5	454.169	1	2	18	30	13	0
Total Oligomer Signal		**74**	**61**				

$C_8H_{10}O_5 + (C_2H_4O_2)_k$

k	Mass (Da)	Abundance (dry)	Abundance (humid)	C	H	O	N
0	186.053	11	4	8	10	5	0
1	246.074	22	64	10	14	7	0
2	306.095	92	28	12	18	9	0
3	366.116	378	208	14	22	11	0
4	426.137	102	60	16	26	13	0
5	486.158	4	28	18	30	15	0
6	546.18	2	0	20	34	17	0
Total Oligomer Signal		**599**	**388**				

$C_8H_{10}O_6 + (C_2H_4O_2)_k$

k	Mass (Da)	Abundance (dry)	Abundance (humid)	C	H	O	N
0	202.048	15	9	8	10	6	0
1	262.069	19	8	10	14	8	0
2	322.09	111	102	12	18	10	0
3	382.111	26	7	14	22	12	0
4	442.132	9	5	16	26	14	0
Total Oligomer Signal		**165**	**122**				

$C_9H_{12}O_4 + (C_2H_4O_2)_k$

k	Mass (Da)	Abundance (dry)	Abundance (humid)	C	H	O	N
0	184.074	17	4	9	12	4	0
1	244.095	19	7	11	16	6	0
2	304.116	7	85	13	20	8	0
3	364.137	14	46	15	24	10	0
4	424.158	8	2	17	28	12	0
5	484.179	4	2	19	32	14	0
Total Oligomer Signal		**51**	**143**				

$C_9H_{12}O_5 + (C_2H_4O_2)_k$

k	Mass (Da)	Abundance (dry)	Abundance (humid)	C	H	O	N
0	200.068	4	58	9	12	4	0

1	260.09	28	10	11	16	6	0
2	320.111	125	111	13	20	8	0
3	380.132	37	18	15	24	10	0
4	440.153	4	8	17	28	12	0
5	500.174	0	1	19	32	14	0
Total Oligomer Signal		**194**	**148**				

Appendix C: Interference of OH radicals in Direct Photolysis Experiments

OH-initiated chemistry may compete with direct photolysis experiments presented in Chapter 6. Sources of OH in aqueous solution of high-NOx SOA include the photolysis of peroxides (ROOH), nitrate ions, and nitrite ions. To gauge the OH production from peroxides in the control and photolyzed aqueous SOA samples, we performed iodo-colorimetric peroxide assays [367, 495] using H_2O_2 (Aldrich, 3 wt %) as a standard in the concentration range of $0 - 100$ μM. The results for the control and photolyzed samples were identical within error ~ 3.0 (±0.5) μM. The low concentration of peroxides in SOA is expected due to the suppression of HO_2 chemistry in the high-NOx oxidation. [21] We used the wavelength-dependent flux from our lamp (Fig. S2), the near UV absorption cross section of methyl hydroperoxide, [496] and a quantum yield of unity to estimate the rate of OH production from peroxides. The rate was low; photolysis of peroxides generated less than 0.6 μM in total over the entire timescale of the photolysis. Assuming prompt and complete reaction of OH with organics under 1:1 stoichiometry (~ 200 g/mol average molar mass of SOA compounds) we estimate < 0.1 % loss of organics resulting from peroxide photolysis and OH chemistry.

Likewise, negative ion mode IC measurements were used to estimate the rate of OH production from nitrate and nitrite ions present in solution. The measured concentrations of nitrate ($[NO_3^-]$ ~ 1.5 (±0.2) μM) and nitrite ions ($[NO_2^-]$ ~ 0.8 (±0.2) μM) were identical within error in control and photolyzed samples, indicating that photolysis of organic nitrates was not a significant source of these anions within 4 h irradiation. Our results agree with the available literature sources , which suggest the nitrite ion yield is negligible and the nitrate ion yield is below 0.1 in aqueous photolysis of organic nitrates at neutral pH. [497-499] Similar to the

estimation from peroxides, calculations using the known OH quantum yields [500, 501] and absorption cross sections [502, 503] for nitrate and nitrite ions, predicted small loss of organics from OH chemistry from the photolysis of nitrate (< 0.1%) and nitrite (< 0.2%) during the 4 h photolysis under our lamp flux. Considering all plausible sources for OH, we conclude that the contribution of OH chemistry to the changes in composition of aqueous isoprene SOA under the studied photolytic conditions are negligible (< 1%) assuming no OH recycling from the photolysis of organics.

Appendix D: Full List of Isoprene High-NOx SOA Compounds Decomposed and Produced by Aqueous Direct Photolysis and Hydrolysis

Table D1: Neutral composition and concentrations of compounds degraded from (a) photolysis and (b) hydrolysis experiments in Chapter 6. Entries highlighted in gray are observed in duplicate photolysis trials and average concentrations are reported. Peaks are sorted by increasing number of carbon. The rates of degradation for select compounds, listed in Table 2, in the main text are derived from linear fits of concentration vs. time profiles.

a. Photolysis Sample				Conc. 0h (μg mL^{-1})	Conc. 1h (μg mL^{-1})	Conc. 2h (μg mL^{-1})	Conc. 4h (μg mL^{-1})
C	H	O	N				
7	10	6	0	1.06	0.23	0.10	0.00
8	12	7	0	1.02	0.29	0.14	0.12
8	12	8	0	0.06	0.05	0.00	0.00
8	13	9	1	0.88	0.40	0.25	0.12
9	14	8	0	5.51	1.49	1.16	0.78
10	14	9	0	0.38	0.06	0.00	0.00
10	16	9	0	0.70	0.58	0.50	0.26
10	15	10	1	0.82	0.11	0.00	0.00
11	16	9	0	6.52	1.55	0.92	0.56
11	16	10	0	0.96	0.12	0.00	0.00
11	17	11	1	0.25	0.22	0.22	0.00
12	20	10	0	2.65	1.49	1.33	0.94
12	20	8	0	0.71	0.34	0.27	0.30
12	20	9	0	0.26	0.13	0.11	0.00
12	18	10	0	7.94	2.45	1.47	1.18
12	19	12	1	1.70	0.45	0.29	0.08
12	19	9	1	0.06	0.05	0.00	0.00
12	21	10	1	0.52	0.04	0.00	0.00
12	19	11	1	0.22	0.08	0.05	0.00
12	17	12	1	0.23	0.15	0.06	0.00
13	22	9	0	0.11	0.06	0.02	0.00
13	20	7	0	2.17	1.14	1.01	0.80
13	18	8	0	0.11	0.11	0.10	0.00
13	18	9	0	0.15	0.10	0.09	0.00
13	20	10	0	6.37	2.20	1.79	1.37
13	20	11	0	3.13	0.48	0.37	0.13
13	22	8	0	0.36	0.20	0.10	0.00
13	18	11	0	0.53	0.49	0.33	0.14
13	19	11	1	0.26	0.05	0.00	0.00
13	19	12	1	0.16	0.09	0.05	0.00
13	19	13	1	0.41	0.19	0.08	0.00

14	20	9	0	0.27	0.18	0.15	0.05
14	22	10	0	2.93	1.48	1.28	0.85
14	22	11	0	23.33	11.74	10.35	8.33
14	24	9	0	0.09	0.06	0.00	0.00
14	20	10	0	1.15	0.17	0.09	0.00
14	22	9	0	2.41	1.31	0.95	0.59
14	22	12	0	0.40	0.24	0.21	0.14
14	21	13	1	2.20	0.65	0.58	0.36
14	23	10	1	0.09	0.06	0.00	0.00
14	21	11	1	0.14	0.06	0.00	0.00
14	23	11	1	0.14	0.06	0.00	0.00
14	25	11	1	0.73	0.05	0.00	0.00
14	21	14	1	0.21	0.10	0.07	0.00
15	24	9	0	0.53	0.17	0.09	0.00
15	22	12	0	3.33	1.76	1.48	1.35
15	24	10	0	0.71	0.14	0.12	0.10
15	22	9	0	0.10	0.05	0.00	0.00
15	22	10	0	0.53	0.32	0.25	0.14
15	24	11	0	1.45	0.93	0.70	0.61
15	22	13	0	0.55	0.28	0.09	0.00
15	23	14	1	0.10	0.06	0.00	0.00
16	24	11	0	0.50	0.23	0.16	0.12
16	24	12	0	1.83	0.89	0.72	0.46
16	24	10	0	0.26	0.14	0.05	0.00
16	26	10	0	0.12	0.07	0.00	0.00
16	26	11	0	0.33	0.09	0.09	0.00
16	26	12	0	0.10	0.04	0.00	0.00
16	24	13	0	2.32	1.73	1.39	0.93
16	26	13	0	0.71	0.31	0.20	0.00
16	23	15	1	0.14	0.05	0.00	0.00
16	25	15	1	0.33	0.03	0.00	0.00
16	20	8	2	0.09	0.04	0.00	0.00
17	26	11	0	0.32	0.08	0.04	0.00
17	26	13	0	1.84	0.81	0.59	0.41
17	28	10	0	0.09	0.06	0.00	0.00
17	26	10	0	0.33	0.07	0.00	0.00
17	24	12	0	0.06	0.05	0.04	0.00
17	26	12	0	1.51	0.86	0.54	0.21
17	24	13	0	0.15	0.08	0.06	0.00
17	24	14	0	0.14	0.05	0.00	0.00
17	26	14	0	0.88	0.45	0.21	0.12
18	28	14	0	3.48	1.53	1.19	0.88
18	28	10	0	0.10	0.06	0.00	0.00

C	H	O	N				
18	28	12	0	0.73	0.15	0.00	0.00
18	28	13	0	1.48	0.28	0.26	0.15
18	28	11	0	0.09	0.04	0.00	0.00
18	30	11	0	0.10	0.05	0.00	0.00
18	26	12	0	0.08	0.05	0.00	0.00
18	28	12	0	0.59	0.18	0.14	0.00
18	26	14	0	0.19	0.11	0.08	0.00
18	26	15	0	0.07	0.04	0.00	0.00
19	28	13	0	0.10	0.04	0.00	0.00
19	30	13	0	0.17	0.04	0.00	0.00
19	28	14	0	0.11	0.11	0.06	0.00
19	30	14	0	0.34	0.13	0.00	0.00

b. Control Sample				Conc. 0h $(\mu g\ mL^{-1})$	Conc. 1h $(\mu g\ mL^{-1})$	Conc. 2h $(\mu g\ mL^{-1})$	Conc. 4h $(\mu g\ mL^{-1})$
C	H	O	N				
9	12	5	0	0.14	0.13	0.12	0.00
9	14	4	0	0.11	0.06	0.06	0.00
9	14	5	0	0.09	0.08	0.08	0.07
9	12	7	0	0.61	0.48	0.37	0.25
9	17	8	1	0.48	0.36	0.31	0.19
10	16	6	0	1.40	1.38	1.37	1.30
10	19	8	1	1.09	1.01	0.78	0.71
13	23	9	1	0.16	0.10	0.09	0.00
13	23	10	1	0.15	0.13	0.11	0.10
14	20	10	0	1.14	0.98	0.82	0.76
14	25	11	1	0.72	0.60	0.53	0.47
16	26	12	0	0.10	0.06	0.06	0.06
16	22	13	0	0.11	0.10	0.08	0.05

Table D2: Neutral composition and concentrations of compounds produced by (a) photolysis and (b) hydrolysis experiments in Chapter 6. Entries highlighted in gray are observed in duplicate photolysis trials and average concentrations are reported. Peaks are sorted by increasing number of carbon. The rates of degradation for select compounds, listed in Table 3, in the main text are derived from linear fits of concentration vs. time profiles.

a. Photolysis Sample				Conc. 0h ($\mu g\ mL^{-1}$)	Conc. 1h ($\mu g\ mL^{-1}$)	Conc. 2h ($\mu g\ mL^{-1}$)	Conc. 4h ($\mu g\ mL^{-1}$)
C	H	O	N				
3	4	5	2	0.00	0.22	0.36	0.49
5	12	4	0	0.00	0.04	0.16	0.26
5	11	6	1	0.00	0.12	0.40	0.61
5	6	7	2	0.35	1.38	1.48	1.93
6	14	6	0	0.00	0.09	0.12	0.14
6	8	4	0	0.04	0.13	0.22	0.45
6	6	8	2	0.17	0.78	0.89	1.43
7	12	6	0	0.00	0.14	0.18	0.52
7	12	5	0	0.00	0.55	1.16	2.04
7	12	4	0	0.00	0.15	0.17	0.17
7	10	5	0	0.03	0.33	0.79	1.04
7	8	9	2	0.09	0.67	0.82	1.20
7	10	9	2	0.30	2.39	3.74	5.44
7	8	8	2	0.00	0.44	0.50	0.78
8	12	4	0	0.00	0.12	0.17	0.24
8	12	6	0	0.60	1.81	3.08	4.59
8	16	3	0	0.00	0.09	0.22	0.22
8	16	4	0	0.00	0.09	0.11	0.19
8	14	5	0	0.00	0.14	0.16	0.17
8	10	5	0	0.03	0.05	0.19	0.86
8	12	5	0	0.11	0.56	0.59	0.82
8	14	6	0	0.00	0.16	0.20	0.23
8	15	6	1	0.00	0.07	0.14	0.18
8	15	7	1	0.00	0.08	0.13	0.15
8	15	6	1	0.00	0.04	0.14	0.32
8	10	8	2	0.16	1.07	1.40	1.57
8	10	10	2	0.42	2.86	4.07	5.85
9	16	7	0	0.00	0.32	0.42	0.59
9	12	3	0	0.00	0.03	0.07	0.32
9	14	3	0	0.00	0.03	0.06	0.21
9	16	5	0	0.00	0.14	0.15	0.23
9	12	6	0	0.05	0.16	0.20	0.23
9	14	6	0	3.45	4.46	5.97	6.87
9	12	7	0	0.08	0.29	0.40	0.43
9	12	10	2	0.39	5.37	8.01	12.03

C	H	O	N	0h	1h	2h	4h
9	12	11	2	0.00	0.08	0.13	0.16
10	16	5	0	0.24	0.55	0.74	1.00
10	20	4	0	0.12	0.67	1.29	1.70
10	20	5	0	0.00	0.13	0.17	0.34
10	14	7	0	0.55	0.68	0.80	1.22
10	18	5	0	0.00	0.04	0.07	0.18
10	18	6	0	0.00	0.07	0.07	0.12
10	14	8	0	0.38	1.09	1.13	1.81
10	12	10	2	0.00	0.21	0.34	0.43
10	14	10	2	0.00	0.52	1.04	1.18
11	16	6	0	0.16	0.28	0.48	0.54
11	16	8	0	1.23	1.99	3.12	5.42
11	18	7	0	0.17	0.37	0.42	0.49
11	14	9	2	0.00	0.19	0.20	0.26
12	18	5	0	0.00	0.16	0.26	0.35
12	18	6	0	0.05	0.09	0.12	0.16
12	18	8	0	1.16	1.29	1.33	1.49
12	18	9	0	3.45	4.15	4.61	4.73

| b. Control Sample | | | | Conc. 0h $(\mu g\ mL^{-1})$ | Conc. 1h $(\mu g\ mL^{-1})$ | Conc. 2h $(\mu g\ mL^{-1})$ | Conc. 4h $(\mu g\ mL^{-1})$ |
C	H	O	N				
8	14	7	0	3.36	3.76	3.82	3.83
12	14	8	0	0.13	0.15	0.19	0.20
12	18	8	0	1.15	1.17	1.27	1.41
12	20	10	0	3.46	3.73	3.91	4.22
15	22	11	0	0.58	0.68	0.74	0.89

Appendix E: Nitrogen and Sulfur Containing Organic Compounds in Evaporated Samples

Table E1. The list of nitrogen containing ions detected by positive ion mode ESI-MS in the SOA + AS solutions before and after evaporation/redissolution. Data were presented in Chapter 7. The formulas for the corresponding neutral compounds can be obtained from the positivie ions by subtracting one hydrogen or sodium atom.

SOA , nothing added, evaporated			
m/z	C	H	O	N
352.2816	19	39	3	1
494.2087	17	35	15	1

SOA + AS, evaporated			
m/z	C	H	O	N
360.1413	17	23	6	1
390.1604	13	27	12	1
392.1522	14	27	10	1
448.2017	16	33	13	1
450.1822	15	31	14	1
460.2026	17	33	13	1
462.2174	17	35	13	1
464.1971	16	33	14	1
478.2135	17	35	14	1
480.1921	16	33	15	1
484.2532	24	37	9	1
488.1975	18	33	14	1
490.2134	18	35	14	1
492.2290	18	37	14	1
506.2078	18	35	15	1
506.2438	19	39	14	1
508.2235	18	37	15	1
520.2600	20	41	14	1
522.2388	19	39	15	1
532.2593	21	41	14	1
534.2390	20	39	15	1

SOA + AS, evaporated			
m/z	C	H	O	N
536.2550	20	41	15	1
538.2342	19	39	16	1
548.2549	21	41	15	1
548.2910	22	45	14	1
550.1763	22	31	15	1

550.2341	20	39	16	1
550.2709	21	43	15	1
499.2316	19	37	17	1
552.2128	20	41	16	1
552.2497	10	16	7	2
277.1031	21	24	10	2
465.1504	20	40	9	2
475.2621	19	32	13	2
497.1977	20	32	14	2

Table E2. The list of sulfur containing ions detected by negative ion mode ESI-MS in the SOA + H_2SO_4 solutions before and after evaporation/redissolution. Data were presented in Chapter 7. The formulas for the corresponding neutral compounds can be obtained from the negative ions by adding one hydrogen atom.

SOA, nothing added				
m/z	C	H	O	S
---	---	---	---	---

SOA, nothing added, evaporated				
m/z	C	H	O	S
---	---	---	---	---

SOA + H_2SO_4 (pH = 4)				
m/z	C	H	O	S
285.0285	8	13	9	1
299.0441	9	15	9	1
315.0389	9	15	10	1
455.1234	17	27	12	1
467.1230	18	27	12	1
469.1385	18	29	12	1
471.1177	17	27	13	1
483.1537	19	31	12	1
485.1330	18	29	13	1
499.1489	19	31	13	1
501.1279	18	29	14	1

SOA + H_2SO_4 (pH = 4), evaporated				
m/z	C	H	O	S
251.0594	9	15	6	1
265.0387	9	13	7	1
267.0543	9	15	7	1
279.0542	10	15	7	1
281.0335	9	13	8	1
281.0698	10	17	7	1
285.0285	8	13	9	1
295.0493	10	15	8	1
297.0648	10	17	8	1
299.0441	9	15	9	1
311.1686	17	27	3	1
439.1279	17	27	11	1
451.1275	18	27	11	1
467.1230	18	27	12	1

m/z	C	H	O	S
469.1385	18	29	12	1
481.1385	19	29	12	1
485.1330	18	29	13	1

SOA + H₂SO₄ (pH = 2)

m/z	C	H	O	S
271.0127	7	11	9	1
285.0284	8	13	9	1
299.0441	9	15	9	1
315.0389	9	15	10	1
327.0388	10	15	10	1
329.0546	10	17	10	1
331.0337	9	15	11	1
441.1072	16	25	12	1
455.1227	17	27	12	1
457.1030	16	25	13	1
459.1176	16	27	13	1
467.1233	18	27	12	1
469.1028	17	25	13	1
469.1387	18	29	12	1
471.1178	17	27	13	1
481.1394	19	29	12	1
483.1180	18	27	13	1
483.1547	19	31	12	1
485.1337	18	29	13	1
487.1126	17	27	14	1
487.1492	18	31	13	1
497.1341	19	29	13	1
499.1127	18	27	14	1
499.1488	19	31	13	1
501.1288	18	29	14	1
503.1446	18	31	14	1
513.1276	19	29	14	1
513.1653	20	33	13	1

SOA + H₂SO₄ (pH = 2), evaporated

m/z	C	H	O	S
223.0280	7	11	6	1
225.0437	7	13	6	1
235.0280	8	11	6	1
237.0436	8	13	6	1
239.0229	7	11	7	1
249.0438	9	13	6	1

251.0229	8	11	7	1
251.0593	9	15	6	1
253.0386	8	13	7	1
263.0231	9	11	7	1
263.0593	10	15	6	1
265.0385	9	13	7	1
267.0179	8	11	8	1
267.0543	9	15	7	1
277.0387	10	13	7	1
279.0543	10	15	7	1
281.0335	9	13	8	1
285.0284	8	13	9	1
293.0337	10	13	8	1
295.0491	10	15	8	1
297.0285	9	13	9	1
299.0441	9	15	9	1
311.0441	10	15	9	1
313.0233	9	13	10	1
327.0388	10	15	10	1
377.0218	10	17	11	2
423.0961	16	23	11	1
463.1280	19	27	11	1
465.1075	18	25	12	1
467.1233	18	27	12	1
469.1028	17	25	13	1